STUDIES IN PENETRATION MECHANICS

FINAL REPORT

R. C. BATRA

October 1992

U. S. ARMY RESEARCH OFFICE

CONTRACT NO. DAAL03-89-K-0050

UNIVERSITY OF MISSOURI - ROLLA
ROLLA, MO 65401

DISCLAIMER NOTICE

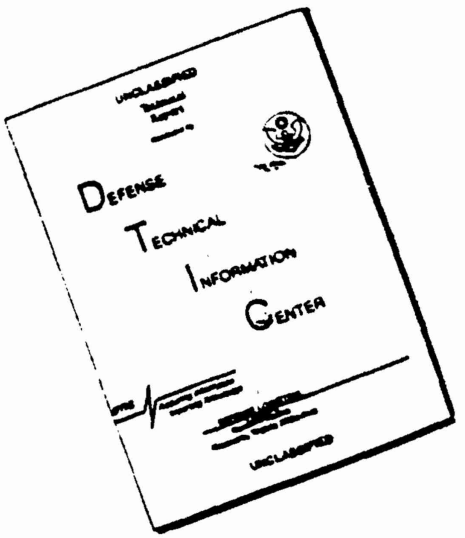

THIS DOCUMENT IS BEST QUALITY AVAILABLE. THE COPY FURNISHED TO DTIC CONTAINED A SIGNIFICANT NUMBER OF PAGES WHICH DO NOT REPRODUCE LEGIBLY.

MASTER COPY KEEP THIS COPY FOR REPRODUCTION PURPOSES

REPORT DOCUMENTATION PAGE

Form Approved
OMB No. 0704-0188

1. AGENCY USE ONLY (Leave blank)	2. REPORT DATE	3. REPORT TYPE AND DATES COVERED
	October 1992	

4. TITLE AND SUBTITLE
Studies in Penetration Mechanics

5. FUNDING NUMBERS
DAAL03-89-K-0050

6. AUTHOR(S)
Romesh C. Batra

7. PERFORMING ORGANIZATION NAME(S) AND ADDRESS(ES)
University of Missouri - Rolla
Rolla, MO 65401-0249

8. PERFORMING ORGANIZATION REPORT NUMBER

9. SPONSORING/MONITORING AGENCY NAME(S) AND ADDRESS(ES)
U. S. Army Research Office
P. O. Box 12211
Research Triangle Park, NC 27709-2211

10. SPONSORING/MONITORING AGENCY REPORT NUMBER
ARO 26443.16-EG

11. SUPPLEMENTARY NOTES
The view, opinions and/or findings contained in this report are those of the author(s) and should not be construed as an official Department of the Army position, policy, or decision, unless so designated by other documentation.

12a. DISTRIBUTION/AVAILABILITY STATEMENT
Approved for public release; distribution unlimited.

12b. DISTRIBUTION CODE

13. ABSTRACT (Maximum 200 words)

Steady state axisymmetric deformations of a thick thermoviscoplastic target being penetrated by a cylindrical penetrator also made of a thermoviscoplastic material have been studied. The materials of the target and the penetrator have been assumed to exhibit strain-rate hardening and thermal softening.

In the second set of studies, the penetrator has been taken to be rigid, and the effect of friction at the target/penetrator interface, elasticity of the target material, and different flow rules used to model the target material have been analyzed.

An engineering model capable of analyzing deformations of a viscoplastic target being penetrated by a rigid cylindrical rod has been developed. Various predictions from the model are found to match well with those from the finite element solution of the problem.

14. SUBJECT TERMS
Steady state penetration, axisymmetric deformations, material elasticity, frictional force

15. NUMBER OF PAGES
157

16. PRICE CODE

17. SECURITY CLASSIFICATION OF REPORT	18. SECURITY CLASSIFICATION OF THIS PAGE	19. SECURITY CLASSIFICATION OF ABSTRACT	20. LIMITATION OF ABSTRACT
UNCLASSIFIED	UNCLASSIFIED	UNCLASSIFIED	UL

TABLE OF CONTENTS

I. STATEMENT OF THE PROBLEM STUDIED

Factors that play a significant role during the penetration of metal targets by projectiles include material properties, impact velocity, projectile shape, target support position, and relative dimensions of the target and the projectile. Recently, emphasis has been placed on kinetic energy penetrators, which for terminal ballistic purposes may be considered as long metal rods traveling at high speeds. For impact velocities in the range of 2 to 10 km/sec, compressible hydrodynamic flow equations can be used to describe adequately the impact and penetration phenomena, because large stresses occurring in hypervelocity impact permit one to neglect the rigidity and compressibility of the striking bodies. Models, which require the use of the Bernoulli equation or its modification to describe this hypervelocity impact, have been proposed by Birkhoff *et al.*[1] and Pack and Evans.[2] At ordnance velocities (0.5 to 2 km/sec), material strength becomes an important parameter. Allen and Rogers[3] modified the Pack and Evans[2] flow model by representing the strength as a resistive pressure. This idea was taken further by Alekseevskii[4] and Tate,[5,6] who considered separate resistive pressures for the penetrator and the target. These resistive pressures are empirically determined quantities, and the predicted results depend strongly upon the assumed values of these pressures. As described lucidly by Wright[7] in his survey article on long rod penetrators, Tate's model is difficult to use for quantitative purposes, because the strength parameters depend upon the velocity of impact and the particular combination of materials involved. Wright and Frank[8] recently re-examined Tate's theory and derived expressions for the resistive pressures in terms of mass densities, yield strengths of the penetrator and target materials, and penetrator speed. They postulated the expression

$$F_t = A_t(a\Sigma_t + b\rho_t\dot{p}^2 + c\rho_t A_t^{1/2}\ddot{p}) \qquad (1)$$

for the force F_t delivered to the target during the nearly steady portion of the penetration process. In equation (1) A_t is the cross-sectional area of the cavity, Σ_t is the yield stress for the target material in a quasistatic simple tension or compression test, ρ_t equals the mass density of the target material, $\dot{p}$ and $\ddot{p}$ equal, respectively, the axial velocity and axial acceleration of the target/penetrator interface, and a, b, and c are nondimensional numbers that depend on material parameters. Dehn[9] assumed

$$F_t = a + b\dot{p} + c\dot{p}^2 \qquad (2)$$

and gave values of a, b, and c in terms of material parameters for the target. Strictly speaking, the modified Bernoulli's equation is valid only when the flow fields are steady. Batra and Wright[10] studied numerically the steady state penetration of a rigid/perfectly plastic target by a hemispherical nosed rigid cylindrical rod and found a = 3.9, and b = 0.0773. Batra[11,12] subsequently accounted for strain hardening, strain-rate hardening, and thermal softening, as well as different nose shapes, and found that the coefficients varied by a factor of at least three, depended strongly on the nose shape, and decreased for a more

pointed shape.

The one-dimensional theories ignore the lateral motion, plastic flow, and the detailed dynamic effects. The paper by Backman and Goldsmith[13] is an authoritative and superb review of the open literature on ballistic penetration, containing 278 reference citations from the 1800's to 1977. They describe different physical mechanisms involved in the penetration and perforation processes, and also discuss a number of engineering models. Jonas and Zukas[14] reviewed various analytical methods for the study of kinetic energy projectile-armor interaction at ordnance velocities and placed particular emphasis on three-dimensional numerical simulation of perforation. Anderson and Bodner[15] have recently reviewed engineering models for penetration and some of the major advances in hydrocode modeling of penetration problems. Three books,[16,17,18] published during the past few years, include extensive discussions of the engineering models, experimental techniques, and analytical modeling of ballistic perforation.

Manganello and Abbott,[19] Wingrove and Wulf,[20] and Recht[21] observed that the penetration resistance of some armor materials is reduced, even though these materials exhibit increased static mechanical strength. During penetration of such targets the formation of adiabatic shear bands leads to a sharp drop in shear yield stress after the formation of a plug, and the penetration resistance of the target is severely reduced. It has been suggested[22,23] that the material in the shear band melts. Woodward[24] has proposed a model for adiabatic shear plugging failure of targets. He considered the penetration of ductile metal targets impinged upon by a sharp conical projectile and assumed that the penetration is achieved by radial expansion of a hole in the plate from zero to the penetrator radius. Wingrove's[25] experiments show that sharp corners of flat-ended projectiles cause deformation in a narrow zone of the target, and hemispherical and ogive nose shapes progressively broaden the deformation pattern. Because of the formation of the thermally-softened shear zone and the difference in fracture behavior for breakout, flat-ended projectiles penetrate materials susceptible to adiabatic shear with greater ease than do radiused projectiles.

Awerbuch,[26] Awerbuch and Bodner,[27] Ravid and Bodner,[28] and Ravid, Bodner, and Holcman[29] have developed models with which to analyze the normal perforation of metallic plates by projectiles. The penetration process is presumed to occur in several interconnected stages, with plug formation and ejection being the principal mechanism of plate perforation. They presumed a kinematically admissible flow field and found the unknown parameters by minimizing the plastic dissipation. They characterized the procedure as being "a modification of the upper bound theorem of plasticity to include dynamic effects". Even if such a theorem were valid, it is hard to tell how close such a bound might be to the solution of the problem. These authors have included the dependence of the yield stress upon the strain rate and studied a purely mechanical problem.

Recht[30] has adapted the Taylor[31] model of mushrooming to the situation in which the

penetrator is allowed to move into the target, and both erosion and shear mass loss are allowed in the penetrator. The principal difficulty is the specification of velocities for the plastic waves in the projectile and the target in order to obtain a unique solution for the rate of interface movement. Brooks[32] and Brooks and Erickson[33] have demonstrated transitions in behavior such that, at increased velocities, it is possible to observe a reduced depth of penetration over a range of velocities. The transition is related to the degree of radial constraint offered by the surrounding target material and its ability to restrict projectile deformation. The transition velocity depends strongly upon the projectile tip geometry. Above the transition velocity, the deformation is described as "jetting" to illustrate a similarity in behavior to shaped charge jets. Forrestal *et al.*[34] have used the cavity expansion model to predict the penetration depths for relatively rigid projectiles striking deformable semi-infinite targets.

An important and still totally unresolved problem is that of selecting the most appropriate constitutive relation for the penetrator and target materials. The constitutive relation employed should adequately model the material response over the range of deformations expected to occur in the problem. However, the computed values of the deformation fields generally depend strongly upon the constitutive assumptions made. A way out of this dilemma is to choose a constitutive relation, solve the problem, check to see if the constitutive assumptions are valid over the range of computed deformations, and, if necessary, solve the problem again with the modified constitutive relation. In the last few years, many new theories[35,36,37] of large deformation elasto-plasticity have been proposed. We use three such theories to analyze the steady state penetration problem.

The work conducted under this contract involved the analysis of the steady state axisymmetric penetration problems with the objectives of delineating important material and kinematic variables that should be included in simpler penetration models, and, if possible, propose such a model.

II. SUMMARY OF RESULTS

When both the penetrator and target materials are assumed to be thermally softening, but strain and strain-rate hardening, the bottom part of the target/penetrator interface was found to be ellipsoidal rather than hemispherical.[38] The peak pressures near the stagnation point in the penetrator and target regions approached 4.58 σ_{op} and 14 σ_{ot}, respectively, for σ_{op}/σ_{ot} = 3.06. Here σ_{op} and σ_{ot} equal, respectively, the yield stress in a quasistatic simple compression test for the penetrator and target materials. The axial force on the penetrator equalled 8.91F, 11.52F, and 14.5F ($F = \pi r_0^2 \sigma_{op}$) for stagnation point speeds of 450 m/s, 500 m/s, and 550 m/s, respectively. A significant contribution to the resisting force is made by the consideration of strain-rate hardening effects. When the penetrator and target materials are modeled as rigid/perfectly plastic,[39] the resistive pressure terms in the modified Bernoulli's equation were found to depend upon the ratio of the mass densities of the target and the penetrator, as well as on the penetration speed.

The consideration of elastic deformations of the target reduced the peak value of the hydrostatic pressure acting at the stagnation point, the axial resisting force experienced by the rigid penetrator, and the target resistance parameter appearing in the modified Bernoulli equation by nearly 28%, 25%, and 25%, respectively, as compared to those for a rigid/perfectly plastic target.[40]

When the flow rules due to Litonski-Batra, Bodner-Partom, and Brown, Kim, and Anand were calibrated against a hypothetical compression test performed at a nominal strain-rate of 3300 sec^{-1} and then used to study the steady state axisymmetric deformations of a target, the three constitutive relations gave nearly the same value of the resisting force acting on the penetrator, temperature rise of material particles in the vicinity of the target/penetrator interface, and other macroscopic measures of deformation, such as the effective stress and the effective strain-rate.[41] However, when the Litonski-Batra and the Bodner-Partom flow rules are calibrated against a simple shear test, the Bodner-Partom model gave a very high value of the hydrostatic pressure at the target/penetrator interface as compared to that given by the Litonski-Batra flow rule.[42]

The transverse isotropy of the target material affected significantly its deformations and the resisting force it exerts on the penetrator.[43]

III. BRIEF REVIEW OF THE COMPLETED WORK

We[38] have studied axisymmetric deformations of a thermoviscoplastic rod penetrating a thick thermoviscoplastic target when their deformations appear steady to an observer situated at the stagnation point and moving with it. Both the rod and the target material are assumed to exhibit strain-rate hardening and thermal softening, and the contact between them at the common interface is smooth. We have plotted in Fig. 1 the shapes of the free surface of the deformed penetrator, and the target/penetrator interface for three values of the speed of the stagnation point. In order to elucidate the dependence of the location of the stagnation point upon the speeds of penetration, the ordinate is measured from the bottom surface of the target region studied. The stagnation point moves away from the free surface of the deformed penetrator as the speed of penetration is increased. Also, with the increase in the speed of penetration, the distance between the free surface of the undeformed penetrator and the deformed penetrator particles moving rearward increases. The shape of the target/penetrator interface also depends strongly upon the penetration speed. The peak values of the temperature rise θ, second invariant I of the strain-rate tensor $\underline{D}$ and the hydrostatic pressure p, and where they occur are influenced by the values of the strain-rate hardening exponents m_p and m_t for the penetrator and target, respectively. This is evidenced by the information provided in Table 1.

One of the challenging problems in penetration mechanics is to find constitutive relations that are valid over a wide range of strains, strain rates, and temperatures likely to

Table 1. Effect of m_p and m_t on θ_{max}, I_{max}, and p_{max} in the penetrator target regions*

Values	θ_{max} (°C)		I_{max}		p_{max} (x_s, v_s^2)	
of m	Penetrator	Target	Penetrator	Target	Penetrator	Target
m_p = 0.025 m_t = 0.025	232.2 (0.17,0.06)	189.5 (0.479,0.05)	5.25 (1.135,1.01)	4.185 (1.096,0.175)	0.8975 (0.0,0.0)	1.017 (0.148,-0.012)
m_p = 0.005 m_t = 0.025	199.8 (0.165,0.04)	167.1 (0.464,0.04)	4.26 (1.193,0.96)	4.108 (1.074,0.164)	0.9409 (0.0,0.0)	1.005 (0.149,-0.004)
m_p = 0.0 m_t = 0.025	193.07 (0.165,0.03)	164.15 (0.525,0.04)	4.11 (0.052,0.02)	4.174 (1.26,0.26)	0.9562 (0.0,0.0)	0.9951 (0.113,0.002)
m_p = 0.025 m_t = 0.005	229.9 (0.15,-0.02)	183.2 (0.48,0.02)	5.27 (1.134,1.02)	4.595 (1.86,0.77)	0.8957 (0.0,0.0)	0.978 (0.15,-0.014)
m_p = 0.025 m_t = 0.0	230.7 (0.165,0.034)	186.03 (0.526,0.04)	4.2815 (0.052,0.02)	4.128 (1.26,0.27)	0.9509 (0.0,0.0)	0.9454 (0.1129,0.001)

*The coordinates of points where θ, I, and p assume maximum values are parenthetically noted.

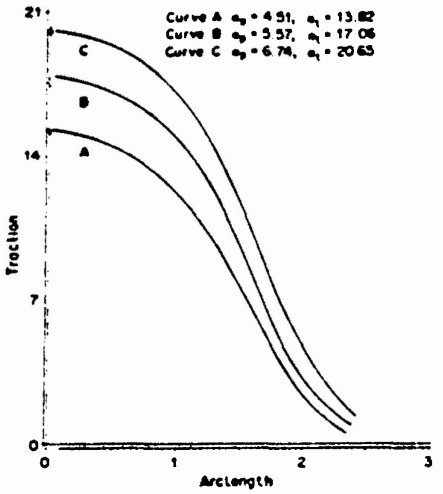

FIG. 1 Distribution of the mean normal tractions on the target/penetrator interface for three different speeds of penetration.

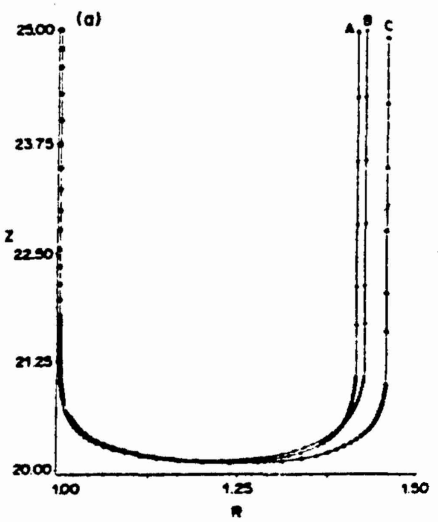

FIG. 1 (a). Shapes of the free surface for three different speeds of penetration.

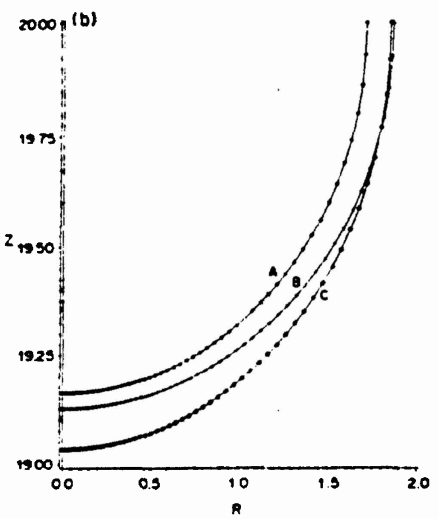

FIG. 1 (b). Shapes of the target/penetrator interface for three different speeds of penetration.

occur in the deforming penetrator and target regions. Compounding the difficulty is the observation that different deformation mechanisms are active at various temperatures and strain rates, and the mechanisms themselves are temperature and time dependent. Another complicating factor is the microstructural changes such as the generation/annihilation of dislocations, development of texture, dynamic recovery and recrystallization, nucleation and growth of microcracks and voids, and the development of shear bands, that occur during the plastic deformation of a material. One way to account for these microstructural changes at a macroscopic level is to use the theory of internal variables proposed by Coleman and Gurtin.[44] We[41] used three such constitutive relations, namely, the Litonski-Batra (LB) flow rule, the Bodner-Partom (BP) flow rule, and the Brown-Kim-Anand (BKA) flow rule. The material parameters in these constitutive relations were evaluated by solving numerically an

initial-boundary-value problem corresponding to plane strain compression of a block made of the target material and deformed at an average strain-rate of 3300 s^{-1} and ensuring that the effective stress vs. the logarithmic strain curves for the three constitutive relations are nearly identical. With these values of material parameters, the analysis of steady state axisymmetric deformations of the target by a hemispherical nosed rigid penetrator gave the following results.

Figure 2 depicts the distribution of the normal stress, temperature rise θ, and the

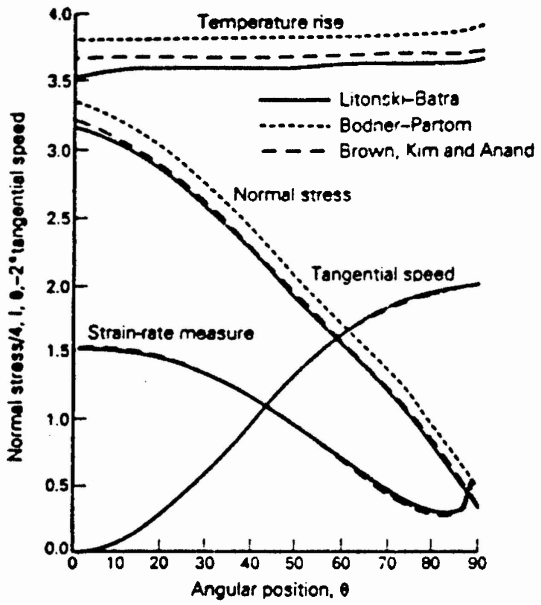

FIG. 2 Comparison of the variation of normal stress, strain rate measure, tangential speed, and the temperature rise at target particles abutting the penetrator nose surface for the three constitutive relations.

tangential speed on the penetrator nose surface and the second invariant I of the deviatoric strain-rate tensor at the centroids of elements abutting the nose surface for $\alpha = 10$, which corresponds to the penetrator speed of 718 m/s. Here $\alpha = \rho v_0^2/\sigma_0$, ρ being the mass density of the target, σ_0 its yield stress in a quasistatic simple compression test, and v_0 the speed of the penetrator. The quantities plotted are nondimensional, obtained by scaling stresses by σ_0, speed by v_0, time by r_0/v_0 where r_0 is the radius of the penetrator, and the temperature rise by 108.9° C. It is clear that the three models give essentially identical results; the maximum difference between the temperature rise computed at any point on the surface with the three flow rules is nearly 30° C for an average temperature rise of 400° C. The

nondimensional axial resisting force experienced by the penetrator was found to be 8.19, 8.84, and 8.26 for the LB, BP, and BKA flow rules, respectively. The values of (I,θ) at the stagnation point for the LB, BP, and BKA flow rules equalled (1.52, 3.53), (1.52, 3.80), and (1.53, 3.67), respectively.

An integration of the balance of linear momentum along the central streamline (r = 0) gives

$$\frac{1}{2}\alpha v^2 + p - s_{zz} - 2\int_0^z \frac{\partial \sigma_{rz}}{\partial r}\,dz = -\sigma_{zz}(0). \qquad (1)$$

Figure 3 shows the contribution from the various terms for $\alpha = 10$. The three models give

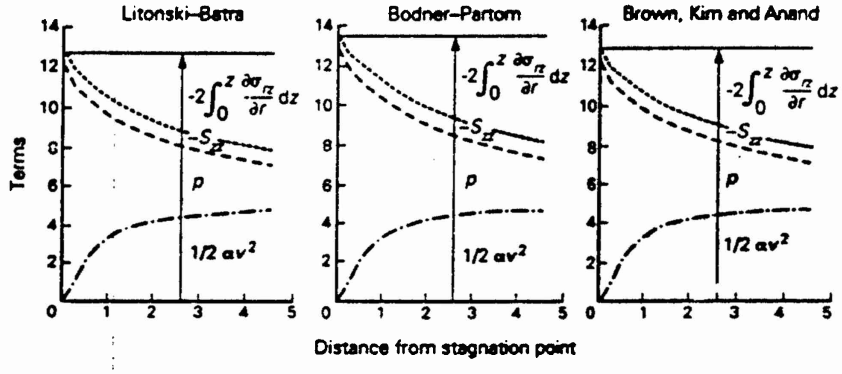

FIG. 3 Contribution of various terms in the nondimensionalized Bernoulli equation along the central stream line.

nearly the same value of the kinetic energy $\frac{1}{2}\alpha v^2$, and the deviatoric stress s_{zz}. The value of the hydrostatic pressure p for the BP model is uniformly more than that for the other two models, and each model predicts a substantial contribution from transverse gradients of the shear stress. The value of the strength parameter for the target in Tate's equation was found to be 7.71, 8.46, and 7.89 for the LB, BP, and BKA models, respectively.

We[40] studied the effect of the elasticity of the target material and the penetrator nose shape by modeling the target material as elastic/perfectly plastic. The dependence of the nondimensional peak pressure p_{max} that occurs at the stagnation point, and of the nondimensional axial resisting force F experienced by the penetrator upon α is exhibited in Fig. 4. Here r_a and r_0 equal, respectively, the semimajor and semiminor axes of the ellipsoidal nose of the rigid cylindrical penetrator. For each nose shape, the consideration of elastic effects lowers the value of p_{max} by about 2, and of F by 1.8. Whereas p_{max} depends upon α rather strongly, the dependence of F upon α is quite weak. Assuming that material points for which

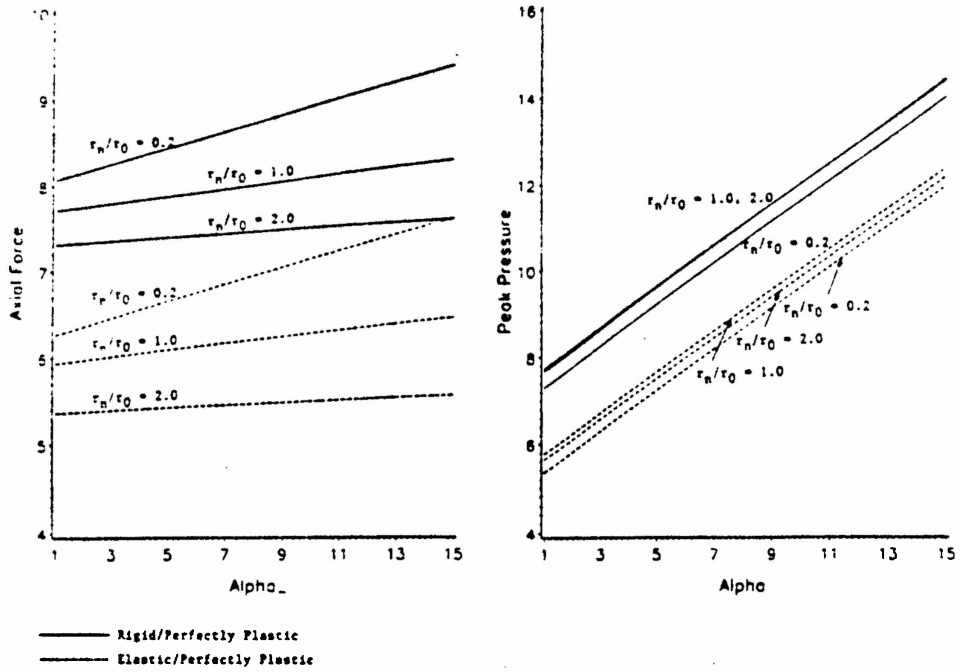

Fig. 4 Dependence of the peak pressure at the stagnation point and the axial resisting force experienced by the penetrator upon α

$$\alpha(\underline{s}^2) = \frac{2}{3} \tag{2}$$

are deforming plastically and those for which the stress state lies inside the surface are deforming elastically, one can determine the elastic/plastic boundary. Results plotted in Fig. 5 suggest that less of the material ahead of the penetrator nose tip and to the sides of the

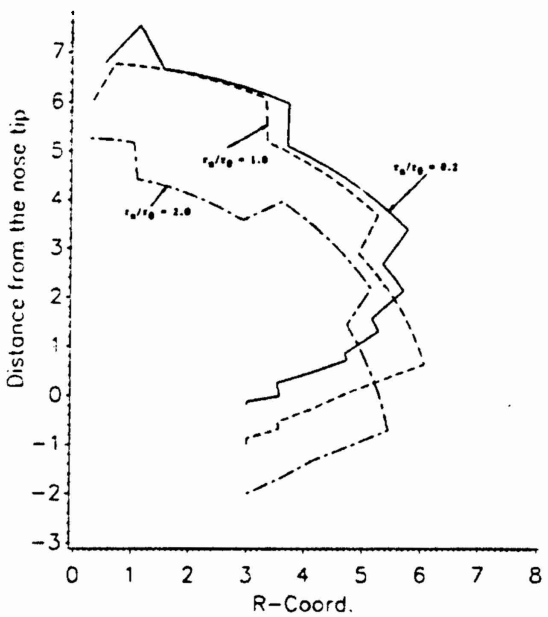

Fig. 5 . Elastic-plastic boundary for three different nose shapes, and α = 10

rigid rod is deformed plastically for the ellipsoidal nosed penetrator as compared to the other two nose shapes considered. The distance of the elastic-plastic boundary from the penetrator nose tip is found to be 5.4, 6.8, and 7.7, respectively, according as the penetrator nose shape is ellipsoidal, hemispherical, or blunt. Tate[45] presumed that a material particle was deforming either elastically or plastically, and based on his solenoid flow model, he found the axial distance of the elastic-plastic boundary from the stagnation point to be 6.71, which compares well with our computed values.

We[46] have used the velocity field computed in the preceding problem to develop an engineering model of target penetration. The deforming target region is divided into two parts, one ahead of the penetrator nose center and the other behind it. In each, the presumed velocity field satisfies the condition of isochoric deformations, essential boundary conditions, and the velocity compatibility condition across the interface between the two regions. The unknown parameters in the velocity field are determined by minimizing the error in the satisfaction of the balance of linear momentum. As shown in Fig. 6, the

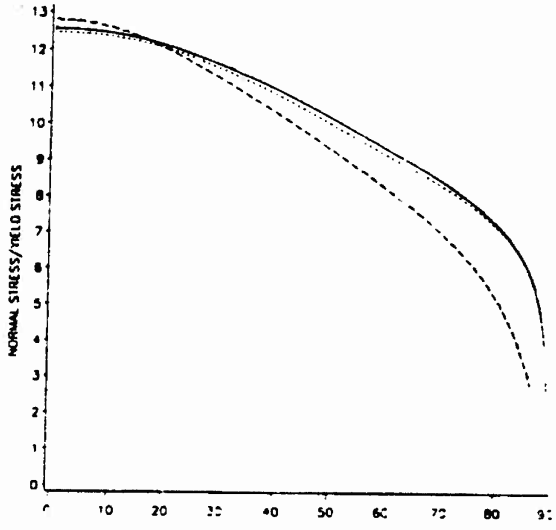

Fig. 6 Distribution of the normal traction on the penetrator nose. —— One term solution; ----- three terms solution; - - - FEM solution.

computed normal traction on the penetrator nose surface matches well with that obtained from the finite element solution near the penetrator nose center, but the two differ at points near the nose periphery, probably because of the differences in the values of the hydrostatic pressure. However, the dependence of the axial resisting force F upon α in the two cases, *viz.*,

$$F = 8.575 + 0.197\alpha, \quad \text{FEM solution,} \tag{3.1}$$

$$F = 8.717 + 0.243\alpha, \quad \text{engineering model,} \tag{3.2}$$

is virtually identical for $0 \leq \alpha \leq 10$.

By using an analogy between the flow of a fluid around a cylinder and that of the target material around the penetrator nose, we evaluated μ and β in the following expression (4) for the frictional force f_t between the target and the penetrator.[47]

$$f_t = -\mu v^{\beta} f_n \underset{\sim}{v}/v, \qquad v^2 = v_r^2 + v_z^2, \qquad f_n = \underset{\sim}{n} \cdot \underset{\sim}{\sigma}\underset{\sim}{n}, \tag{4}$$

where $\underset{\sim}{n}$ is a unit outward normal and $\underset{\sim}{\sigma}$ is the Cauchy stress tensor. Figure 7 depicts the

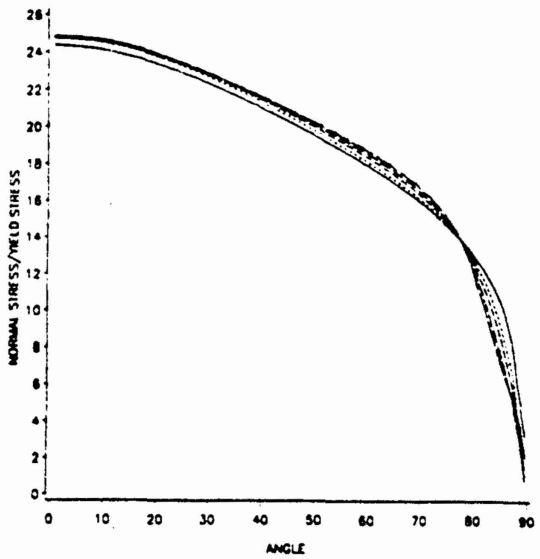

Fig. 7. Distribution of the normal traction on the hemispherical nose of the penetrator for different values of the coefficient μ of friction.

distribution of the normal traction f_n on the hemispherical nose surface of the penetrator for $\alpha = 6.5$, $\beta = 1.5$, and $\mu = 0.0$, 0.1, 0.2, 0.3, and 0.4. We note that the hydrostatic pressure, which seems to be less sensitive to the value of μ, makes a significant contribution to f_n. Thus, the value and the distribution of the normal tractions on the penetrator nose surface change very little when μ is increased from 0.0 to 0.4. Whatever little change does occur, the general trend is that f_n increases near the nose tip and decreases near the nose periphery with an increase in the value of μ.

IV. LIST OF PUBLICATIONS

1. T. Gobinath and R. C. Batra, Analysis of a Steady State Axisymmetric Penetration Problem, in Computational Techniques for Impact, Penetration and Perforation of Solids, L. E. Schwer, N. J. Salamon, and W. K. Liu, eds., ASME Press, pp. 235-247, 1989.

2. R. C. Batra and Pei-Rong Lin, Histories of Stress, Strain-Rate, Temperature, and Spin in Steady State Deformations of a Thermoviscoplastic Rod Striking a Hemispherical Rigid Cavity, Int. J. Eng. Sci., 28, 93-98, 1990.

3. T. Gobinath, Finite Element Solution of Steady State Axisymmetric Penetration Problems, Ph.D. Dissertation, University of Missouri - Rolla, Feb. 1990.

4. R. C. Batra and Xingju Chen, An Approximate Analysis of Steady State Axisymmetric Deformations of Viscoplastic Targets, Int. J. Engr. Science, 28, 1347-1358, 1990.

5. A. Adam, Effect of Viscoplastic Flow Rules and Transverse Isotropy on Steady State Penetration of Thick Targets, M.S. Thesis, University of Missouri - Rolla, December, 1990.

6. R. C. Batra and T. Gobinath, Steady State Axisymmetric Deformations of a Thermoviscoplastic Rod Penetrating a Thick Thermoviscoplastic Target, Int. J. Impact Engng., 11, 1-31, 1991.

7. T. Gobinath and R. C. Batra, A Steady State Axisymmetric Penetration Problem for Rigid Perfectly Plastic Materials, Int. J. Engng. Sci., 29, 1315-1331, 1991.

8. R. C. Batra and A. Adam, Effect of Viscoplastic Flow Rules on Steady State Penetration of Thermoviscoplastic Targets, Int. J. Engr. Sci., 29, 1391-1408, 1991.

9. R. C. Batra and A. Adam, Steady State Penetration of Transversely Isotropic Rigid/Perfectly Plastic Targets, Computers and Structures, 42, 489-495, 1992.

10. R. Jayachandran and R. C. Batra, Steady State Penetration of Elastic Perfectly Plastic Targets, Acta Mechanica, 92, 9-27, 1992.

11. R. Jayachandran and R. C. Batra, Steady State Axisymmetric Deformations of a Thick Elastic-Thermoviscoplastic Target, Int. J. Engr. Sci., 30, 1009-1026, 1992.

12. R. C. Batra and R. Jayachandran, Effect of Constitutive Models on Steady State Axisymmetric Deformations of Thermoelastic-Viscoplastic Targets, Int. J. Impact Engng., 12, 209-226, 1992.

13. X. Chen and R. C. Batra, Effect of Frictional Force on the Steady State Axisymmetric Deformations of a Viscoplastic Target, Acta Mechanica (in press).

14. R. Jayachandran, Analysis of Steady State Axisymmetric Penetration Problems by the Finite Element Method Using a Mixed Formulation, Ph.D. Dissertation, University of Missouri - Rolla, Oct. 1991.

V. LIST OF PRESENTATIONS

1. T. Gobinath and R. C. Batra, Analysis of a Steady State Axisymmetric Penetration Problem, ASME Winter Annual Meeting, San Francisco, December 10-15, 1989.

2. R. C. Batra, Steady State Penetration Problems, Seminar, National Cheng-Kung University, Tainan, Taiwan, July 1989.

3. R. C. Batra, Steady State Penetration Problems, Seminar, National Chung-Hsing University, Taichung, Taiwan, July 1989.

4. T. Gobinath, Nonlinear Finite Element Analysis of a Steady State Axisymmetric Penetration Problem, Seminar, University of Missouri - Rolla, September 1989.

5. R. C. Batra, Finite Element Solution of Three Impact Problems, NASA Lewis Research Center, Cleveland, OH, October 1989.

6. A. Adam, Effect of Viscoplastic Flow Rules and Transverse Isotropy on Steady State Penetration of Thick Targets, Seminar, University of Missouri - Rolla, November 1990.

7. R. Jayachandran, Steady State Penetration of Elastic Perfectly Plastic Targets, Seminar, University of Missouri - Rolla, February 1991.

8. R. C. Batra, X. Chen, and R. Jayachandran, Effect of Material Elasticity and Frictional Forces on the Steady State Axisymmetric Deformations of a Thick Target, Army Symp. Solid Mechanics, Plymouth, November 1991.

9. X. Chen, Effect of Frictional Force on the Steady State Axisymmetric Deformations of a Viscoplastic Target, Seminar, University of Missouri - Rolla, March 1992.

VI. DEGREES AWARDED

T. Gobinath, Ph.D., May 1990
A. Adam, M.S., January 1991
R. Jayachandran, Ph.D., December 1991

VII. PARTICIPATING SCIENTIFIC PERSONNEL

R. C. Batra
T. Gobinath
A. Adam
R. Jayachandran
X. Chen
Z. Peng

VIII. BIBLIOGRAPHY

1. G. Birkhoff, D. P. McDougall, E. M. Pugh, and G. Taylor, Proc. Phys. Soc. Lond. 57 147 (1945).
2. D. C. Pack and W. M. Evans, Proc. Phys. Soc. Lond. B64 298 (1951).
3. W. A. Allen and J. W. Rogers, J. Franklin Inst. 272 275 (1961).
4. V. P. Alekseevskii, Combst. Explo. Shock Waves, 2 63 (1966).
5. A. Tate, J. Mech. Phys. Sol., 15 387 (1967).
6. A. Tate, J. Mech. Phys. Sol., 17 141 (1969).
7. T. W. Wright, A Survey of Penetration Mechanics for Long Rods, in Lecture Notes in Engineering, v. 3, Computational Aspects of Penetration Mechanics, J. Chandra and J. Flaherty, eds., Springer-Verlag, New York, 1984.
8. T. W. Wright and K. Frank, Approaches to Penetration Mechanics, in Impact: Effects of Fast Transient Loading (W. J. Ammann, W. K. Liu, J. A. Studer, and T. Zimmerman, Eds.), A. A. Balkema, Rotterdam, 1988.
9. J. Dehn, Int. J. Impact Engng., 5 239 (1987).
10. R. C. Batra and T. W. Wright, Int. J. Eng. Sci., 24 41 (1986).
11. R. C. Batra, Int. J. Eng. Sci., 25 1131 (1987).
12. R. C. Batra, Comp. Mechs., 3 1 (1988).
13. M. E. Backman and W. Goldsmith, Int. J. Eng. Sci., 16 1 (1978).
14. G. H. Jonas and J. A. Zukas, Int. J. Eng. Sci, 16 879 (1978).
15. C. E. Anderson and S. R. Bodner, The Status of Ballistic Impact Modeling, Proc. 3rd TACOM Armor Coordinating Conf., Feb. 17-19, 1987, Monterey, CA.
16. E. W. Billington and A. Tate, The Physics of Deformation and Flow, McGraw-Hill, New York (1981).
17. J. A. Zukas, T. Nicholas, H. F. Swift, L. B. Greszczuk, and D. R. Curran, Impact Dynamics, John Wiley, New York (1982).
18. J. A. Zukas (ed.), High Velocity Impact Dynamics, John Wiley & Sons, Inc., New York, 1990.
19. S. J. Manganello and K. H. Abbott, J. Mats., 7 231 (1972).
20. A. L. Wingrove and G. L. Wulf, J. Aust. Inst. Met., 18 167 (1973).
21. R. F. Recht, I. Mech. E., 3rd Int. Conf. on High Pressure, Scotland (May 1970).
22. T. A. C. Stock and K. R. L. Thompson, Met. Trans., 1 219 (1970).
23. A. J. Bedford, A. L. Wingrove, and K. R. L. Thompson, J. Aust. Inst. Met., 19 61 (1974).
24. R. L. Woodward, Int. J. Mech. Sci., 20 599 (1978).
25. A. L. Wingrove, Met. Trans., 4 1829 (1973).
26. J. Awerbuch, Technion-Israel Institute of Technology, MED Report No. 28 (1970).
27. J. Awerbuch and S. R. Bodner, Int. J. Solids Structures, 10 671 (1974).
28. M. Ravid and S. R. Bodner, Int. J. Eng. Sci., 21 577 (1983).
29. M. Ravid, S. R. Bodner, and I. Holcman, Int. J. Eng. Sci., 25 473 (1987).
30. R. F. Recht, Int. J. Eng. Sci., 16 809 (1978).
31. G. I. Taylor, Proc. R. Soc., A 194 289 (1948).

32. P. N. Brooks, Defense Research Establishment, Valcartier, Canada, Rept. DREV R-4001/74 (Oct. 1974).
33. P. N. Brooks and W. N. Erickson, Defense Research Establishment, Valcartier, Canada, Rept. DREV R-643/72 (Nov. 1971).
34. M. J. Forrestal, K. Okajima, and V. K. Luk, Penetration of 6061-T651 Aluminum Targets with Rigid Long Rods, Proc. 1st Joint SES/ASME-AMD Conf., Univ. of California at Berkeley, June 1988.
35. E. H. Lee, J. Appl. Mech., 36 1 (1969).
36. L. Anand, J. Appl. Mech., 47 439 (1980).
37. Y. F. Dafalias, Acta Mech., 69, 119 (1987).
38. R. C. Batra and T. Gobinath, Int. J. Impact Engng., 11 1 (1991).
39. T. Gobinath and R. C. Batra, Int. J. Engng. Sci., 29 1315 (1991).
40. R. Jayachandran and R. C. Batra, Acta Mechanica, 92, 9 (1992).
41. R. C. Batra and R. Jayachandran, Int. J. Impact Engng., 12, 209 (1992).
42. R. C. Batra and A. Adam, Int. J. Engng. Sci., 29 1391 (1991).
43. R. C. Batra and A. Adam, Computers and Structures, 42, 489 (1992).
44. B. D. Coleman and M. E. Gurtin, J. Chem. Phys., 47, 597 (1967).
45. A. Tate, Int. J. Mech. Sci., 28, 535 (1986).
46. R. C. Batra and X. Chen, Int. J. Engng. Sci., 28 1347 (1990).
47. X. Chen and R. C. Batra, Acta Mechanica (in press).

IX. APPENDIX

A copy of each of the following papers is included in the appendix.

1. Steady state axisymmetric deformations of a thermoviscoplastic rod penetrating a thick thermoviscoplastic target

2. A steady state axisymmetric penetration problem for rigid/perfectly plastic materials

3. Steady state penetration of transversely isotropic rigid/perfectly plastic targets

4. Steady state penetration of elastic perfectly plastic targets

5. Steady state axisymmetric deformations of a thick elastic-thermoviscoplastic target

6. Effect of viscoplastic flow rules on steady state penetration of thermoviscoplastic targets

7. Effect of constitutive models on steady state axisymmetric deformations of thermoelastic-viscoplastic targets

8. Histories of stress, strain-rate, temperature, and spin in a steady state deformation of a thermoviscoplastic rod striking a hemispherical rigid cavity

9. An approximate analysis of steady state axisymmetric deformations of viscoplastic targets

Int. J. Impact Engng Vol. 11, No. 1, pp. 1–31, 1991
Printed in Great Britain

0734-743X/91 $3.00 + 0.00

STEADY STATE AXISYMMETRIC DEFORMATIONS OF A THERMOVISCOPLASTIC ROD PENETRATING A THICK THERMOVISCOPLASTIC TARGET

R. C. BATRA and T. GOBINATH

Department of Mechanical and Aerospace Engineering and Engineering Mechanics, University of Missouri-Rolla, Rolla, MO 65401-0249, U.S.A.

(*Received* 21 *February* 1990; *and in revised form* 18 *July* 1990)

Summary—The coupled nonlinear partial differential equations governing the thermomechanical and axisymmetric deformations of a cylindrical rod penetrating into a thick target, also made of a rigid/viscoplastic material, are solved by the finite element method. It is assumed that the deformations of the target and the penetrator as seen by an observer situated at the stagnation point and moving with it are independent of time. Both the rod and the target material are assumed to exhibit strain-rate hardening and thermal softening, and the contact between the penetrator and the target at the common interface is smooth. An effort has been made to assess the effect of the strain-rate hardening and thermal softening on the deformations of the target and the penetrator. It is found that the axial resisting force experienced by the penetrator, the shape and location of the free surface of the deformed penetrator and the target penetrator interface, and normal tractions on this common interface depend rather strongly upon the speed of the stagnation point and hence on the speed of the striking rod. Results presented graphically include the distribution of the velocity field, the temperature change, the hydrostatic pressure and the second-invariant of the strain-rate tensor.

In an attempt to help establish desirable testing regimes for determining constitutive relations appropriate for penetration problems, we also find histories of the effective stress, hydrostatic pressure, temperature and the second invariant of the strain-rate tensor experienced by four penetrator and two target particles.

NOTATION

v	velocity of a rod particle
ρ	mass density
q	heat flux
U	specific internal energy
$\boldsymbol{D}$	strain-rate tensor
$\boldsymbol{\sigma}$	Cauchy stress tensor
$\boldsymbol{s}$	deviatoric stress tensor
p	hydrostatic pressure
θ	temperature change
k	thermal conductivity
c	specific heat
σ_0	yield stress in simple compression
b, m	strain-rate sensitivity parameters
γ	thermal softening coefficient
t	a unit tangent vector
n	a unit normal vector
h	heat transfer coefficient
grad	gradient operator
div	divergence operator
I^2	second invariant of $\boldsymbol{D}$
α, β	non-dimensional numbers

1. INTRODUCTION

When a fast moving long rod strikes a very thick target, the deformations of the rod and the target appear to be time independent to an observer situated at the stagnation point and moving with it after the rod has penetrated into the target through a distance equal to a few rod diameters. This steady state lasts until the stagnation point reaches close to the other end of the target. Thus, for thick targets, the duration of the steady state portion

of the penetration process is a significant part of the total time taken to perforate through the target. For very high striking speeds, the deformations of the target and the penetrator can be assumed to be governed by purely hydrodynamic incompressible flow processes. In this approach, the only significant material property is the ratio of mass densities of the target and the penetrator, and the same penetration depth is predicted for all impact velocities. Tate [1,2] and Alekseevskii [3] modified this model by incorporating the effects of the material strengths of the projectile and the target and representing them as some multiple of the uniaxial yield stress of the material, but the multiplying factor was not specified. These and other limitations of the one-dimensional models have been discussed by Wright [4], and more recently by Wright and Frank [5]. Pidsley [6], who studied the penetration of a copper rod into an aluminum target, found that during the steady state portion of the penetration process these strength parameters equalled $2.4(\sigma_H)_t$ and $-(0.7)(\sigma_H)_p$ for the target and the penetrator, respectively. Here σ_H is the Hugoniot elastic limit. He explained that the negative value for the rod strength is due to the yield strength of the rod being lower than that of the target.

The reader is referred to the paper by Backman and Goldsmith [7] for a review of the open literature on ballistic penetration until 1977. It describes various physical mechanisms involved in the penetration and perforation processes, and also discusses a number of engineering models. Other recent review articles and books include those by Wright and Frank [5], Anderson and Bodner [8], Zukas *et al.* [9], Blazynski [10], and Macauley [11]. Ravid and Bodner [12] have proposed a five-stage penetration model applicable to two-dimensional analysis of rigid projectiles penetrating deformable targets. Various unknowns in the assumed kinematically admissible velocity field are found by using an upper bound theorem of plasticity modified to include dynamic effects. The penetration model proposed by Ravid *et al.* [13] also accounts for the shock effects and plastic deformation in the component bodies. Forrestal *et al.* [14] have recently applied the cavity expansion model to study the penetration of rigid projectiles into geological materials.

With the main objective of providing some guidelines for selecting and improving upon the previously used kinematically admissible fields in engineering models of penetration, Batra and Wright [15] initiated the study of an idealized steady state penetration problem. It simulates the penetration of a very long (semi-infinite) rod into an infinite target when all of the flow fields appear steady to an observer situated on the penetrator nose tip and moving with it and the target/penetrator interface is smooth. They studied the problem of a deformable target, assumed to be made of a rigid/perfectly plastic material and a rigid cylindrical penetrator with a hemispherical nose. Subsequently, Batra [16,17] found that the nose shape affected significantly the resisting force experienced by the penetrator and also studied the case when the target material exhibited work-hardening, strain-rate hardening and thermal softening effects. Batra and Lin [18–20], and Lin and Batra [21] studied the steady state axisymmetric deformations of a semi-infinite cylindrical penetrator striking a known semi-infinite cavity in an infinite and rigid target, and also computed the histories of the effective stress, temperature, second invariant of the strain-rate tensor and the plastic spin. Gobinath and Batra [22] have recently analysed the steady state axisymmetric penetration problem in which both the target and the penetrator are made of a rigid perfectly plastic material. Since most penetrator and target materials exhibit strain-rate hardening and thermal softening effects, we extend the previous work [22] to incorporate these effects. The problem is very challenging because of the presence in it of two *a priori* unknown surfaces, namely, the target penetrator interface and the free surface of the penetrator material flowing backwards. The shapes and locations of these surfaces are strongly influenced by the value of the strain-rate hardening exponent for the penetrator and a little by the value of the strain-rate hardening exponent for the target. The speed of penetration also affects noticeably the shapes of the target penetrator interface.

We note that there is no fracture or failure criterion incorporated in our work. Thus both the penetrator and target materials are presumed to undergo unlimited plastic deformations. It is hoped that the details of the kinematic and stress fields provided herein

will help propose better estimates of the kinematic fields in engineering models of steady state penetration process. Also the histories of the stress, temperature, the second invariant of the strain-rate tensor and the plastic spin for four penetrator and two target particles given herein should help establish desirable testing regimes for practical problems, and help assess the efficacy of different plasticity theories for the penetration problem.

2. FORMULATION OF THE PROBLEM

We use a cylindrical coordinate system, with origin at the stagnation point and moving with it at a uniform speed v_s, and positive z-axis pointing towards the undeformed portion of the rod, to describe the deformations of the target and the penetrator. The equations governing their deformations are

$$\operatorname{div} \mathbf{v} = 0, \tag{1}$$

$$\operatorname{div} \boldsymbol{\sigma} = \rho \dot{\mathbf{v}}, \tag{2.1}$$

$$= \rho(\mathbf{v} \cdot \operatorname{grad})\mathbf{v}, \tag{2.2}$$

$$-\operatorname{div} \mathbf{q} + \operatorname{tr}(\boldsymbol{\sigma}\mathbf{D}) = \rho(\mathbf{v} \cdot \operatorname{grad})U, \tag{3}$$

$$2\mathbf{D} = \operatorname{grad} \mathbf{v} + (\operatorname{grad} \mathbf{v})^T. \tag{4}$$

These equations are written in the Eulerian description of motion. Equation (1) expresses the balance of mass, Eqn (2) the balance of linear momentum, and Eqn (3) the balance of internal energy. Here $\mathbf{v}$ is the velocity of a material particle, $\boldsymbol{\sigma}$ the Cauchy stress at the present location of a material particle, ρ the mass density, $\mathbf{q}$ the heat flux, and U the specific internal energy. A dot superimposed over a character implies its material time derivative, and the operators grad and div signify the gradient and the divergence operators defined in the present configuration. In writing Eqn (1) we have assumed that the deformations of the target and the penetrator are isochoric, and in Eqn (3) all of the plastic working rather than 90–95% of it as asserted by Farren and Taylor [23] is assumed to be converted into heat.

For constitutive relations, which are characteristic of the target and the penetrator materials, we take

$$\boldsymbol{\sigma} = -p\mathbf{1} + \frac{\sigma_0}{\sqrt{3}I}(1 + bI)^m(1 - \gamma\theta)\mathbf{D}, \qquad \mathbf{D} \neq \mathbf{0}, \tag{5}$$

$$\mathbf{D} = \mathbf{0} \quad \text{if } \operatorname{tr}(\mathbf{s})^2 < \tfrac{2}{3}\sigma_0^2(1 - \gamma\theta)^2, \tag{6}$$

$$\mathbf{s} = \boldsymbol{\sigma} + p\mathbf{1}, \tag{7}$$

$$\mathbf{q} = -k \operatorname{grad} \theta, \tag{8}$$

$$U = c\theta, \tag{9}$$

$$2I^2 = \operatorname{tr}(\mathbf{D}^2). \tag{10}$$

In these equations, p is the hydrostatic pressure not determined by the deformation history of a material particle because we have assumed the target and penetrator materials to be incompressible, $\mathbf{1}$ is the unit tensor, σ_0 the yield stress in a quasistatic simple tension or compression test, I^2 the second invariant of the strain-rate tensor, b and m characterize the strain-rate hardening of the material, γ describes its thermal softening, θ equals the absolute temperature of a material particle, $\mathbf{s}$ is the deviatoric stress tensor, k the thermal conductivity and c the specific heat. Both k and c are assumed to be independent of the temperature. From Eqns (5) and (7), we get

$$(\tfrac{1}{2}\operatorname{tr} \mathbf{s}^2)^{1/2} = \frac{\sigma_0}{\sqrt{3}}(1 + bI)^m(1 - \gamma\theta). \tag{11}$$

This can be viewed as a generalized von Mises yield criterion when the flow stress, given by the right-hand side of Eqn (11), at a material particle depends upon its strain-rate and

the temperature change. That the flow stress decreases linearly with the temperature rise has been observed by Bell [24], and Lindholm and Johnson [25]. The range of temperatures studied by these investigators is not as large as that likely to occur here. We add that Tate [26] also used a linear thermal softening law in his study of the penetration problem.

Rewriting Eqn (5) as

$$\boldsymbol{\sigma} = -[\tilde{p} + \alpha(\theta - \theta_0)K]\mathbf{1} + \frac{\sigma_0}{\sqrt{3}I}(1 + bI)^m(1 - \gamma\theta)\mathbf{D}, \tag{12}$$

where α and K equal, respectively, the coefficient of thermal expansion and the bulk modulus of the material, we see that Eqn (5) embodies implicitly thermal stresses caused by the non-uniform temperature rise at different material particles. In Eqn (12), $\tilde{p}$ is not determined by the deformation history of a material particle and the addition of a determinate term to it gives rise to p in Eqn (5) which is taken to be an independent variable throughout this work.

Substitution for $\boldsymbol{\sigma}$, $\mathbf{q}$, and U from Eqns (5), (8) and (9) into Eqns (2.2) and (3) gives the following field equations:

$$-\operatorname{grad} p + \sigma_0 \operatorname{div}[(1 + bI)^m(1 - \gamma\theta)\mathbf{D}/\sqrt{3}I] = \rho(\mathbf{v}\cdot\operatorname{grad})\mathbf{v} \tag{13}$$

$$k \operatorname{div}(\operatorname{grad}\theta) + 2\sigma_0 I(1 + bI)^m(1 - \gamma\theta)/\sqrt{3} = \rho c(\mathbf{v}\cdot\operatorname{grad})\theta. \tag{14}$$

The nonlinear coupled Eqns (13) and (14), and Eqn (1) subject to the appropriate boundary conditions are to be solved for the fields of the velocity $\mathbf{v}$, pressure p and temperature θ in the deforming target and penetrator regions. Even though governing equations for the target and penetrator regions are the same, the values of material parameters σ_0, b, m, γ, ρ, k and c need not have the same values for the target and penetrator materials. In order to solve Eqns (1), (13) and (14), we need to know the domains over which they apply. This in turn requires a knowledge of the shapes and locations of the target penetrator interface Γ_i and the free surface Γ_f of the deformed penetrator. Both these surfaces are unknown *a priori*. For the time being, we presume that Γ_i and Γ_f are known. Subsequently, we discuss how to find these surfaces.

It is convenient to introduce non-dimensional variables, indicated below by a superimposed bar, as follows:

$$\bar{\boldsymbol{\sigma}} = \boldsymbol{\sigma}/\rho v_s^2, \quad \bar{p} = p/\rho v_s^2, \quad \alpha = \rho v_s^2/\sigma_0, \quad \theta_0 = v_s^2/c,$$
$$\bar{\mathbf{v}} = \mathbf{v}/v_s, \quad \bar{r} = r/r_0, \quad \bar{z} = z/r_0, \quad \bar{\theta} = \theta/\theta_0,$$
$$\bar{\gamma} = \gamma\theta_0, \quad \beta = k/(\rho c v_s r_0), \quad \bar{b} = b v_s r_0, \quad \bar{h} = h/\rho c v_s. \tag{15}$$

We note that v_s is the same for the target and the penetrator, but the values of other variables need not be the same. When non-dimensionalizing a quantity for the target (penetrator), the value of the material parameter for the target (penetrator) is used. An advantage of the non-dimensionalization (15) is that the governing equations for the penetrator and the target look alike. In Eqn (15), r_0 is the radius of the undeformed cylindrical penetrator, the pair (r, z) denotes the cylindrical coordinates of a point, θ_0 is the reference temperature, h is the heat transfer coefficient between the penetrator material and air, and the non-dimensional number α gives the magnitude of the inertia forces relative to the flow stress of the material. Rewriting Eqns (1), (13) and (14) in terms of non-dimensional variables, dropping the superimposed bars, and denoting the gradient and divergence operators in non-dimensional coordinates by grad and div, we arrive at the following set of equations:

$$\operatorname{div}\mathbf{v} = 0, \tag{16}$$

$$-\operatorname{grad} p + \operatorname{div}[(1 + bI)^m(1 - \gamma\theta)\mathbf{D}/\sqrt{3}I\alpha] = (\mathbf{v}\cdot\operatorname{grad})\mathbf{v}, \tag{17}$$

$$\beta \operatorname{div}(\operatorname{grad}\theta) + 2I(1 + bI)^m(1 - \gamma\theta)/(\sqrt{3}\alpha) = (\mathbf{v}\cdot\operatorname{grad})\theta. \tag{18}$$

For the boundary conditions, we take

$$\boldsymbol{t}\cdot(\boldsymbol{\sigma n})=0 \qquad \text{on } \Gamma_i, \tag{19.1}$$

$$\boldsymbol{n}\cdot\boldsymbol{\sigma}_t\boldsymbol{n}=\frac{\rho_p}{\rho_t}\boldsymbol{n}\cdot\boldsymbol{\sigma}_p\boldsymbol{n} \qquad \text{on } \Gamma_i, \tag{19.2}$$

$$\boldsymbol{v}\cdot\boldsymbol{n}=0 \qquad \text{on } \Gamma_i, \tag{19.3}$$

$$\theta_p=(\theta_{0t}/\theta_{0p})\theta_t \qquad \text{on } \Gamma_i, \tag{19.4}$$

$$\left(\rho\beta\frac{\partial\theta}{\partial n}\right)_t=\left(\rho\beta\frac{\partial\theta}{\partial n}\right)_p \qquad \text{on } \Gamma_i, \tag{19.5}$$

$$\boldsymbol{\sigma n}=0 \qquad \text{on } \Gamma_f, \tag{19.6}$$

$$\boldsymbol{v}\cdot\boldsymbol{n}=0 \qquad \text{on } \Gamma_f, \tag{19.7}$$

$$-\beta\frac{\partial\theta}{\partial n}=h(\theta-\theta_a) \qquad \text{on } \Gamma_f, \tag{19.8}$$

where $\boldsymbol{n}$ is a unit outward normal to the surface, $\boldsymbol{t}$ is a unit tangent to the surface, θ_a is the air temperature and subscripts p and t signify the quantity for the penetrator and the target, respectively. We note that boundary conditions (19.3) and (19.7) which signify that Γ_i and Γ_f are streamlines are not required for a complete specification of the problem provided that these surfaces are known. Since these surfaces are not known, we presume their shapes, solve the problem without using (19.2) and (19.7), and then use these conditions to ensure that the presumed Γ_i and Γ_f are correct. The procedure for adjusting Γ_i and Γ_f if (19.2) and (19.7) are not satisfied within the prescribed tolerance is described in Section 4.

At target particles far away from Γ_i, we take

$$|\boldsymbol{v}+\boldsymbol{e}_z|\to 0 \qquad \text{as } (r^2+z^2)^{1/2}\to\infty, \tag{20.1}$$

$$|\boldsymbol{\sigma n}|\to 0 \qquad \text{as } z\to\infty, \tag{20.2}$$

$$\left|\frac{\partial\theta}{\partial n}\right|\to 0 \qquad \text{as } z\to\infty. \tag{20.3}$$

That is, target particles at a large distance from Γ_i appear to be moving at a uniform speed to an observer situated at the stagnation point. Equations (20.2) and (20.3) state that the fields of surface tractions and heat flux vanish at target particles behind the stagnation point and far from it. On the penetrator cross-section far from the stagnation point,

$$|\boldsymbol{v}+(v_p-1)\boldsymbol{e}_z|\to 0 \qquad \text{as } z\to\infty, \tag{21.1}$$

$$|\theta-\theta_a|\to 0 \qquad \text{as } z\to\infty, \tag{21.2}$$

and on the deformed penetrator material at the outlet,

$$|\boldsymbol{\sigma n}|\to 0 \qquad \text{as } (r^2+z^2)^{1/2}\to\infty, \tag{21.3}$$

$$\left|\frac{\partial\theta}{\partial n}\right|\to 0 \qquad \text{as } (r^2+z^2)\to\infty. \tag{21.4}$$

Equations (21.1) and (21.2) state that the end of the penetrator far from the stagnation point is moving in the negative z-direction with a uniform speed of (v_p-1) relative to the observer at the stagnation point and is at a uniform temperature θ_a. Equations (21.3) and (21.4) state that the surface of the deformed penetrator near the outlet is traction free and there is no heat exchange between them and the material on the other side of the outlet surface. Ideally, one should specify the rate of decay of quantities in Eqns (20.1) through (20.3), and (21.1) through (21.4). However, at this time, there is little hope of proving any existence or uniqueness theorem for the stated problem and we, therefore, gloss over the issue. Herein we assume that the problem defined by Eqns (16)–(21) has a solution and seek an approximation to that solution by the finite element method.

3. FINITE ELEMENT FORMULATION OF THE PROBLEM

Unless one uses infinite elements, a numerical solution of the problem necessitates that we consider a finite region and know the shapes of the free surface Γ_f and the target penetrator interface Γ_i. We presume Γ_i and Γ_f and study deformations of the penetrator over the region ABGHIJA shown in Fig. 1 and of the target on the region BCDEFGB also shown in Fig. 1. The figure depicts a finite element discretization of the domain; the mesh is very fine in the darker regions. We note that the finite domains for the penetrator and the target considered here are larger than the penetrator region studied by Batra and Lin [18–19] and the target regions examined by Batra [15–17].

The boundary conditions (19.1), (19.3) and (19.4) apply on the target/penetrator interface BG and (19.6) and (19.8) on the penetrator free surface JIH. We recall that conditions (19.2) and (19.7) are used to verify the accuracy of the assumed surfaces Γ_i and Γ_f. On the axis of symmetry ABC, we impose

$$\sigma_{rz} = 0, \qquad v_r = 0, \qquad \frac{\partial \theta}{\partial r} = 0. \tag{22}$$

The boundary conditions (20) and (21) at the far surface of the penetrator and the target are replaced by the following conditions on the bounding surfaces of the finite region being analysed:

$$v_z = 1, \qquad v_r = 0, \qquad \theta = \theta_a \qquad \text{on the bounding surfaces CD and DEF.} \tag{23.1}$$

$$\sigma_{zz} = 0, \qquad v_r = 0, \qquad \frac{\partial \theta}{\partial z} = 0 \qquad \text{on FG.} \tag{23.2}$$

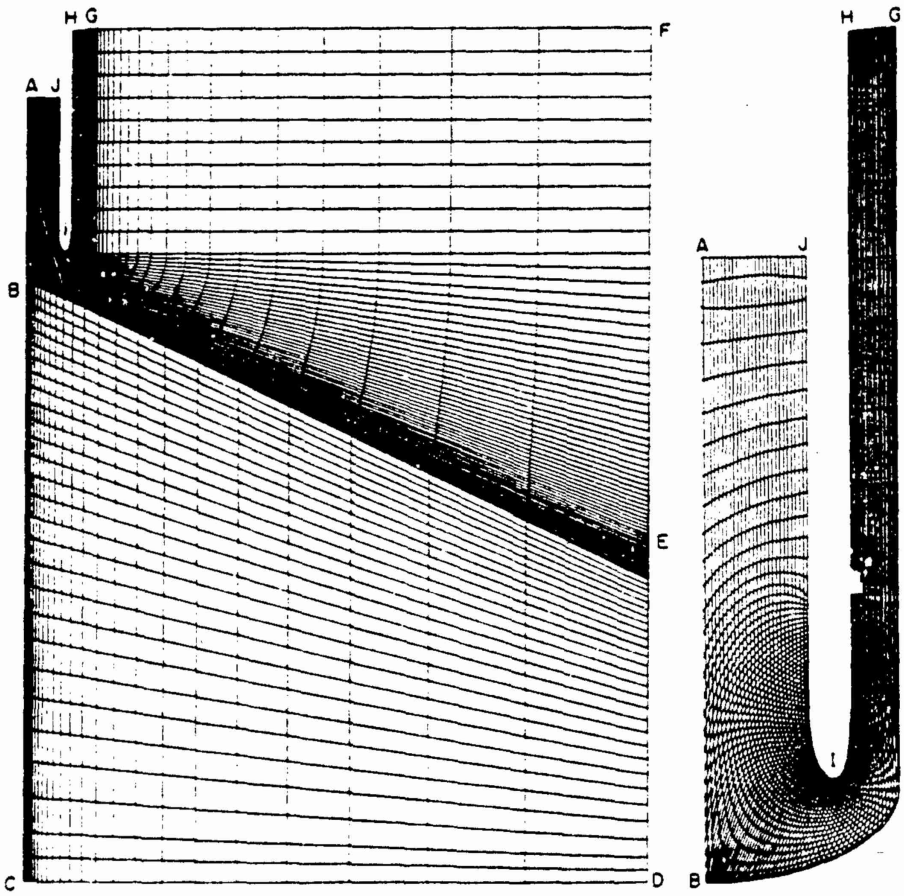

FIG. 1. The finite region studied and its discretization.

$$v_z = v_e, \qquad v_r = 0, \qquad \frac{\partial \theta}{\partial z} = 0 \qquad \text{on the outlet surface GH.} \tag{23.3}$$

$$v_z = -(v_p - 1), \qquad v_r = 0, \qquad \theta = \theta_a \qquad \text{on the surface AJ.} \tag{23.4}$$

The value of v_e is computed so as to satisfy the balance of mass.

Referring the reader to one of the books [27–29] for details of deriving a weak formulation of the problem, we simply note that a weak formulation of the problem defined on the target region R_t by Eqns (16)–(18), and boundary conditions (19.1), (22), (23.1) and (23.2) is that equations

$$\int_{R_t} \lambda(\operatorname{div} \boldsymbol{v})\, dV = 0 \tag{24.1}$$

$$\int_{R_t} p(\operatorname{div} \boldsymbol{\phi})\, dV - \int_{R_t} \mu_t(I, \theta, \alpha)[\boldsymbol{D}: (\operatorname{grad} \boldsymbol{\phi}) + (\operatorname{grad} \boldsymbol{\phi})^T]\, dV$$
$$= \int_{R_t} [(\boldsymbol{v}\cdot\operatorname{grad})\boldsymbol{v}]\cdot\boldsymbol{\phi}\, dV - \int_{\Gamma_t} (\boldsymbol{n}\cdot\boldsymbol{\sigma}\boldsymbol{n})(\boldsymbol{\phi}\cdot\boldsymbol{n})\, dS \tag{24.2}$$

$$\beta_t \int_{R_t} (\operatorname{grad}\theta\cdot\operatorname{grad}\eta)\, dV + \int_{R_t} [(\boldsymbol{v}\cdot\operatorname{grad})\theta]\eta\, dV = \int_{R_t} \eta Q_t(I, \theta, \alpha)\, dV - \int_{\Gamma_t} \beta\eta \frac{\partial\theta}{\partial n}\, dS \tag{24.3}$$

where

$$\mu_t(I, \theta, \alpha) = (1 + bI)^m(1 - \gamma\theta)/(2\sqrt{3}\, I\alpha), \tag{25.1}$$

$$Q_t(I, \theta, \alpha) = 2I(1 + bI)^m(1 - \gamma\theta)/\sqrt{3}\,\alpha. \tag{25.2}$$

hold for arbitrary smooth functions λ, $\boldsymbol{\phi}$ and η defined on R_t such that $\boldsymbol{\phi} = \boldsymbol{\theta}$ on CD and DEF, $\phi_r = 0$ on BC and FG, and $\eta = 0$ on CD and DEF. If at a boundary point a component of the trial solution is prescribed, the corresponding component of the test function is taken to vanish there. In Eqn (24.2) $\boldsymbol{A}:\boldsymbol{B} = \operatorname{tr}(\boldsymbol{A}\boldsymbol{B}^T)$ for linear transformations $\boldsymbol{A}$ and $\boldsymbol{B}$. A similar set of equations can be derived for the penetrator region. Note that for the penetrator region the second term on the right-hand side of Eqn (24.3) will be replaced by

$$-\int_{\Gamma_t} \beta\eta \frac{\partial\theta}{\partial n}\, dS + \int_{\Gamma_t} h(\theta - \theta_a)\eta\, dS. \tag{25.3}$$

Because of the boundary condition (19.4), we use the following iterative scheme to solve the problem. We estimate θ in R_p and R_t, solve equations (24.1), (24.2) and a similar set of equations for the penetrator for the fields of $\boldsymbol{v}$ and p in R_p and R_t, (cf. Section 4.1 below), use these values of $\boldsymbol{v}$ in Eqn (24.3) and a similar equation for the penetrator to solve these for θ in $R_p \cup R_t$. Thus the boundary conditions (19.4) and (19.5) requiring the continuity of the temperature and the normal component of the heat flux across the target penetrator interface Γ_t are satisfied. The computed value of θ is compared with the estimated value and the aforementioned process is repeated until the difference between the two at every node point is less than the prescribed tolerance. The nonlinear equations (24.1) and (24.2) are solved iteratively for p and $\boldsymbol{v}$. At the ith iteration, equations

$$\int_{R_t} \lambda(\operatorname{div} \boldsymbol{v}^i)\, dV = 0, \tag{26.1}$$

$$\int_{R_t} p^i(\operatorname{div} \boldsymbol{\phi})\, dV - \int_{R_t} \mu(I^{i-1}, \theta, \alpha)\{\boldsymbol{D}^i: [\operatorname{grad} \boldsymbol{\phi} + (\operatorname{grad} \boldsymbol{\phi})^T]\}\, dV$$
$$= \int_{R_t} [(\boldsymbol{v}^{i-1}\cdot\operatorname{grad})\boldsymbol{v}^i]\cdot\boldsymbol{\phi}\, dV - \int_{\Gamma_t} (\boldsymbol{n}\cdot\boldsymbol{\sigma}^{i-1}\boldsymbol{n})(\boldsymbol{\phi}\cdot\boldsymbol{n})\, dS \tag{26.2}$$

are solved for $\boldsymbol{v}^i$ and p^i. The iterative process is stopped when, at each nodal point,

$$\|\boldsymbol{v}^i - \boldsymbol{v}^{i-1}\| \le \varepsilon[\|\boldsymbol{v}^{i-1}\|] \tag{26.3}$$

where $\|v\|^2 = v_r^2 + v_z^2$, and ε is a preassigned small number. Since Eqn (26.2) is linear in p, its values are not included in the convergence criterion (26.3).

4. COMMENTS ON COMPUTATIONAL ASPECTS OF THE PROBLEM

Batra [17] and Batra and Lin [19] used 6-noded triangular elements to analyse steady state thermomechanical deformations of the target and the penetrator, respectively, while assuming that the other body was rigid. Thus, they approximated the velocity and pressure fields by piecewise quadratic and piecewise linear fields over R_p and R_t. Each of these fields is continuous across inter-element boundaries. The convergence rate of the iterative scheme used to solve Eqns (24.1) and (24.2) deteriorated significantly once the value of α_p or α_t exceeded 5. We note that for higher values of α_p and α_t, the convective part of the acceleration plays a dominant role and the finite element mesh required to obtain a satisfactory solution of Eqns (24) by the Galerkin approximation [29] needs to be very fine. This difficulty was overcome by adding an artificial viscosity to the diffusive terms in Eqns (24) and using 4-noded quadrilateral elements in which the pressure field is taken to be constant and the velocity field bilinear. The value of the artificial viscosity ν to be added in each element depends upon the values of ν and μ, defined by Eqn (25.1), at the centroid of the element and the dimensions (h_r, h_z) of the element. Here h_r and h_z equal, respectively, the largest distances in the r and z directions between the midpoints of the sides of a quadrilateral. Following Brooks and Hughes [30], we take

$$\nu = \nu_r + \nu_z, \tag{27.1}$$

$$\nu_r = h_r(\coth \nu_1 - 1/\nu_1)/2, \tag{27.2}$$

$$\nu_z = h_z(\coth \nu_2 - 1/\nu_2)/2, \tag{27.3}$$

$$\nu_1 = v_r^c h_r/\mu(I^c, \theta^c, \alpha), \qquad \nu_2 = v_z^c h_z/\mu(I^c, \theta^c, \alpha), \tag{27.4}$$

when solving Eqn (24.2), and

$$\nu_1 = v_r^c h_r \beta, \qquad \nu_2 = v_z^c h_z/\beta \tag{27.5}$$

when solving Eqn (24.3). In these equations, the superscript c signifies that the quantity is evaluated at the centroid of an element. Brooks and Hughes [30] have shown that adding artificial viscosity is equivalent to using the Petrov–Galerkin approximation of Eqn (24).

4.1 Solution algorithm

Assume the shapes and locations of the target/penetrator interface Γ_i and the free surface Γ_f of the deformed penetrator. Estimate the temperature field θ over the regions R_p and R_t occupied by the penetrator and the target. Solve Eqns (24.1) and (24.2) for (v, p) on R_t and a similar set of equations on R_p with the boundary condition (19.3). Thus $\phi \cdot n = 0$ on Γ_i and the contribution from the surface integral term on the right-hand side of Eqn (24.2) vanishes. Equations (19.2) and (19.7) are used to ascertain the accuracy of Γ_i and Γ_f. Emphasis is placed on finding Γ_f first, and once Γ_f has been determined, Γ_i is found always ensuring that Γ_f is still reasonably correct and if necessary, Γ_f is adjusted. During the adjustment of Γ_i nodes on it are moved in a direction perpendicular to it by an amount proportional to $(f_p^n - f_t^n)$ where f_p^n and f_t^n equal, respectively, the normal force on the penetrator and target particles abutting Γ_i. A check is made to ensure that the elements adjoining Γ_i are not severely distorted after the nodes on Γ_i have been shifted. The algorithm for modifying Γ_f, if necessary, is given below in Section 4.2.

After the mechanical problem has been satisfactorily solved, the computed velocity field is used to solve the thermal problem for the combined domain $R_p \cup R_t$. Thus the boundary conditions (19.4) and (19.5) are trivially satisfied. The second term in Eqn (25.3) results in the satisfaction of the boundary condition (19.8). The computed values of θ are compared with the estimated values and, if necessary, the solution process is repeated until the prespecified convergence criteria have been met.

4.2 Adjustment of the free surface

The algorithm used to adjust the free surface Γ_f is the same as that given by Gobinath and Batra [22] and is included herein for completeness. Referring to Fig. 2, let point Q on Γ_f be downstream from P on Γ_f. Assume that the computed velocity v_p is tangent to Γ_f at P and v_Q does not satisfy $v_Q \cdot n = 0$. In order to find the new location of point Q, we draw a circular arc that passes through points P and Q and is tangent to v_p at P. Let C be the center of this circular arc. Point Q is moved along CQ to Q* such that P and Q* lie on a circular arc with v_p and v_Q being tangent to the circle at P and Q*. Points downstream from Q are moved to an intermediate location before this rule is applied to them. Let R be a point neighboring Q and downstream from it. R is moved to R_1 such that the vector R_1Q^* equals the vector RQ. The final location R^* of R_1 is then found in the same way as Q* was determined and by assuming that the velocity of R_1 is v_R. Since point J is on Γ_f, the algorithm can be applied starting from J.

4.3 Mesh regeneration

After the position of Γ_f has been determined, the finite element mesh on R_p is regenerated by solving on it the Poisson equation

$$\nabla^2\phi = P(r, z)$$

under the essential boundary conditions $\phi = r$ and $\phi = z$ at nodes on the boundary ∂R_p. Here P is the control function [31–34] that helps generate an appropriately graded mesh. The points of intersection of the equipotential curves through nodes on the boundary define the new locations of interior nodes.

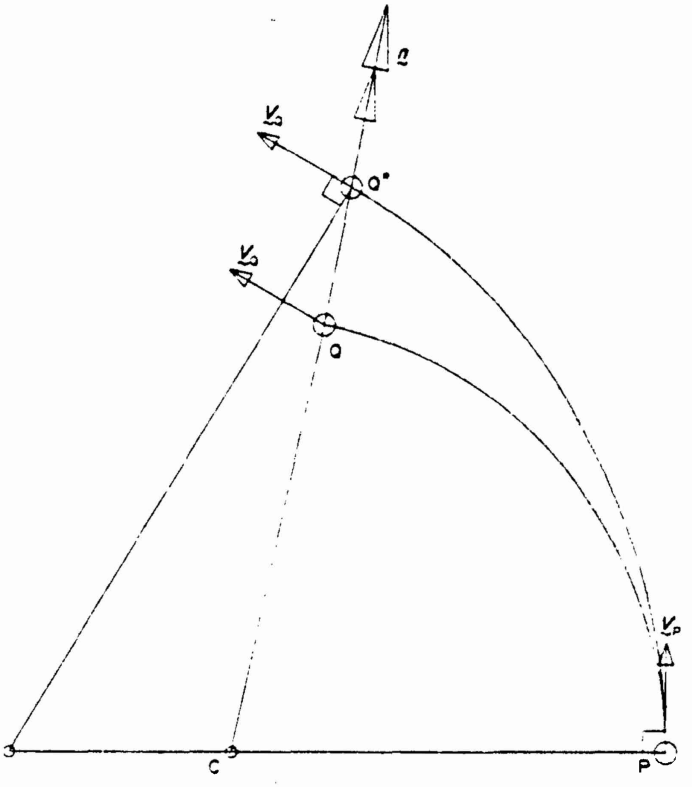

FIG. 2. Illustration of the algorithm to adjust Γ_f.

5. DISCUSSION OF RESULTS

Except when we study the effect of varying the value of a material parameter, we assign the following values to different parameters for the penetrator and target materials:

$$\rho_p = \rho_t = 7800 \text{ kg m}^3, \quad r_0 = 10 \text{ mm},$$
$$\sigma_{0p} = 350 \text{ MPa}, \quad \sigma_{0t} = 114.3 \text{ MPa},$$
$$m_p = 0.025, \quad m_t = 0.025,$$
$$b_p = 10\,000 \text{ s}, \quad b_t = 10\,000 \text{ s},$$
$$\gamma_p = 0.000555/^\circ\text{C}, \quad \gamma_t = 0.000772/^\circ\text{C},$$
$$c_p = 473 \text{ J kg}^{-1}{}^\circ\text{C}^{-1}, \quad c_t = 395 \text{ J Kg}^{-1}{}^\circ\text{C}^{-1},$$
$$k_p = 48 \text{ Wm}^{-1}{}^\circ\text{C}^{-1}, \quad k_t = 111 \text{ Wm}^{-1}{}^\circ\text{C}^{-1},$$
$$h = 20 \text{ Wm}^{-2}{}^\circ\text{C}^{-1}, \quad \theta_a = 0.$$

We recall that subscripts p and t signify the quantity for the penetrator and the target, respectively. For an assigned value of v_s, the value of v_p is estimated from the relation [1]

$$\tfrac{1}{2}(v_p - 1)^2 + Y_p = (R_t + \tfrac{1}{2})(\rho_t/\rho_p) \tag{28}$$

where Y_p and R_t represent strength parameters for the penetrator and target, respectively. Pidsley [6], for a copper penetrator and an aluminum target, estimated these parameters to equal $(-0.7)(\sigma_H)_p$ and $2.4(\sigma_H)_t$, respectively, where σ_H is the Hugoniot elastic limit. In his 1967 paper, Tate [1] found $R_t = 3.5(\sigma_H)_t$ and in a recent paper [25] he gave

$$\begin{aligned} Y_p &= 1.7\sigma_{0p}, \\ R_t &= \sigma_{0t}[2/3 + \ln(0.57E_t/\sigma_{0t})], \end{aligned} \tag{29}$$

where E_t is Young's modulus for the target material. Batra and Chen [36] used a semianalytical method to analyse the steady state axisymmetric deformations of a viscoplastic target being penetrated by a rigid hemispherical nosed penetrator and found that

$$R_t = 9.43\sigma_{0t}.$$

In terms of dimensional variables, we need to know $(R_t - Y_p)$ rather than the values of R_t and Y_p to find v_p from Eqn (28).

In all of the results presented below the solution for the velocity and temperature fields was assumed to have converged when, at each nodal point, the value of these quantities during two successive iterations differed by no more than 5%. The free surface was taken to have converged when at each node point on it, $|\mathbf{v}\cdot\mathbf{n}|$ was less than 0.02. The iterative process to compute the target/penetrator interface was stopped when the values of the normal tractions f_n^p and f_n^t at each node point on Γ_i differed from their mean values by less than 5%. We discuss below results for different speeds of the penetrator, and for different values of the strain-rate hardening exponent m and the coefficient of thermal softening γ.

5.1 *Results for* $v_s = 500$ m/s

Figure 3 depicts the computed velocity field in the penetrator and target regions for $v_s = 500$ m/s. The penetrator speed, as computed from Eqn (28), equals 1041 m s. The plots clearly show that the velocity at points on the free surface and the target/penetrator interface is along the tangent to these surfaces. In order to show this effect clearly, the velocity field in only a part of the deforming region is shown. The computed velocity field establishes the validity of the iterative technique outlined above to find the shapes of the free surface and the target/penetrator interface. A least squares fit to the bottom surface of the

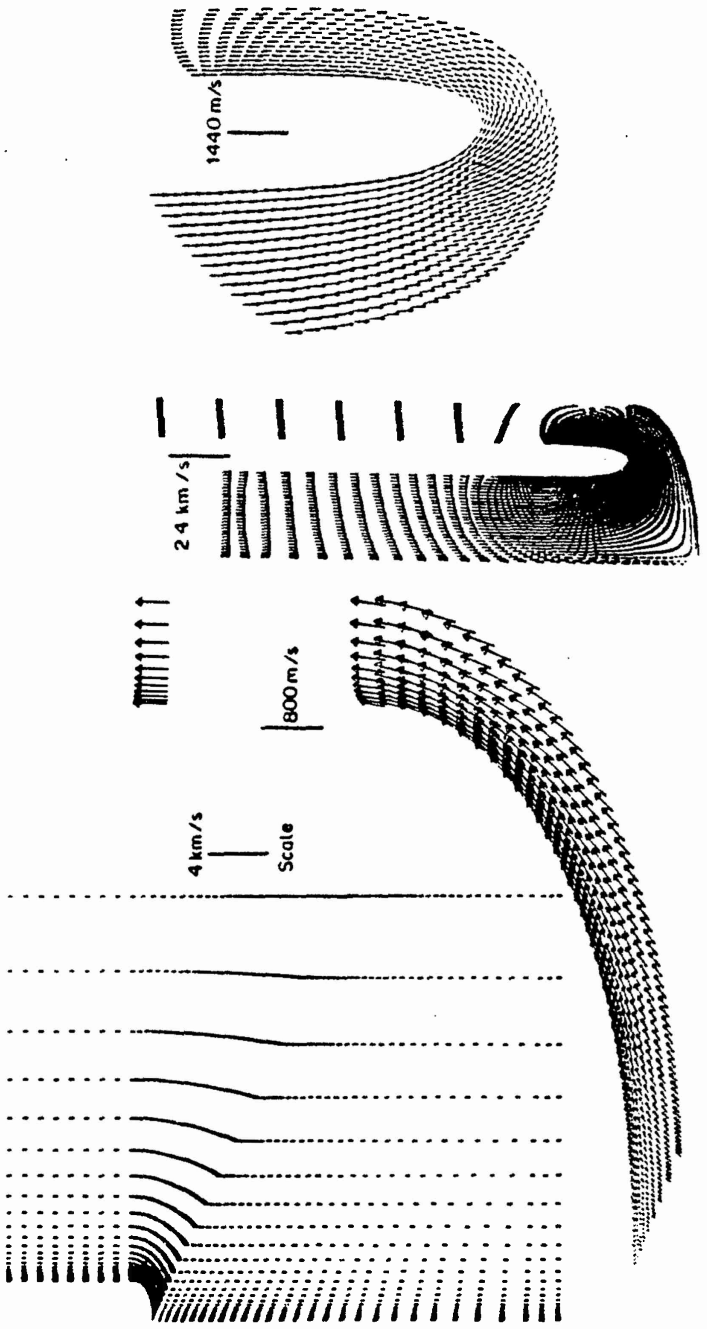

FIG. 3. Velocity field in the deforming penetrator and target regions. A blow up of the region where the flow is turning is also shown.

target/penetrator interface Γ_i can be represented by the equation

$$\frac{r^2}{1.861^2} + \frac{(z-0.874)^2}{0.874^2} = 1. \tag{30}$$

It is interesting to note that Tate [37] found the equation of the bottom surface of Γ_i to be

$$\frac{3}{4}\frac{r^2}{a^2} + \frac{(z-a)^2}{a^2} = 1. \tag{31}$$

A possible reason for the difference in the value of the coefficient for the first term is the lower value of v_s considered here.

If the penetrator speed is less than the limiting velocity and there is no perforation of the target, Eqn (30) will give approximately the shape of the bottom surface of the cylindrical cavity in the target. We note that the computed shape of Γ_i does not match well with the hemispherical cavity considered by Batra and Lin [19] in their study of the deformations of a thermoviscoplastic rod striking a rigid cavity. The thickness $0.38r_0$ of the outlet region computed by Batra and Lin [19] for $x_p = 5.6$ is comparable to $0.42r_0$ found herein. At the penetrator and target particles that lie to the rear of the bottom-most point of the free

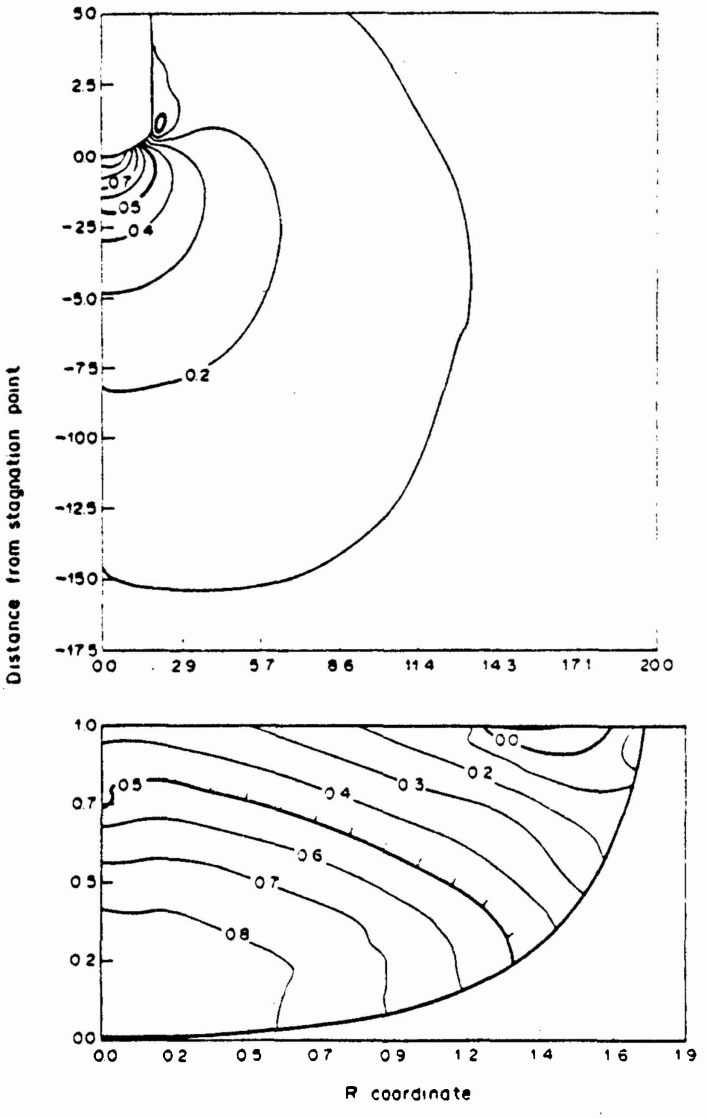

FIG. 4. Contours of the hydrostatic pressure in the penetrator and target regions for $v_s = 500$ m s.

surface, the flow quickly becomes essentially parallel to the axis of the penetrator. Target particles that lie ahead of the penetrator/target interface and within one penetrator radius from it have a noticeable radial component of velocity. The velocity field for other values of v_s was found to be similar to that shown in Fig. 3.

Figure 4 shows contours of the hydrostatic pressure in the penetrator and target regions. Recalling that the non-dimensionalization is with respect to ρv_s^2, and $v_s = 500$ m/s, these values need to be multiplied by 5.6 and 17.1 for the penetrator and target, respectively,

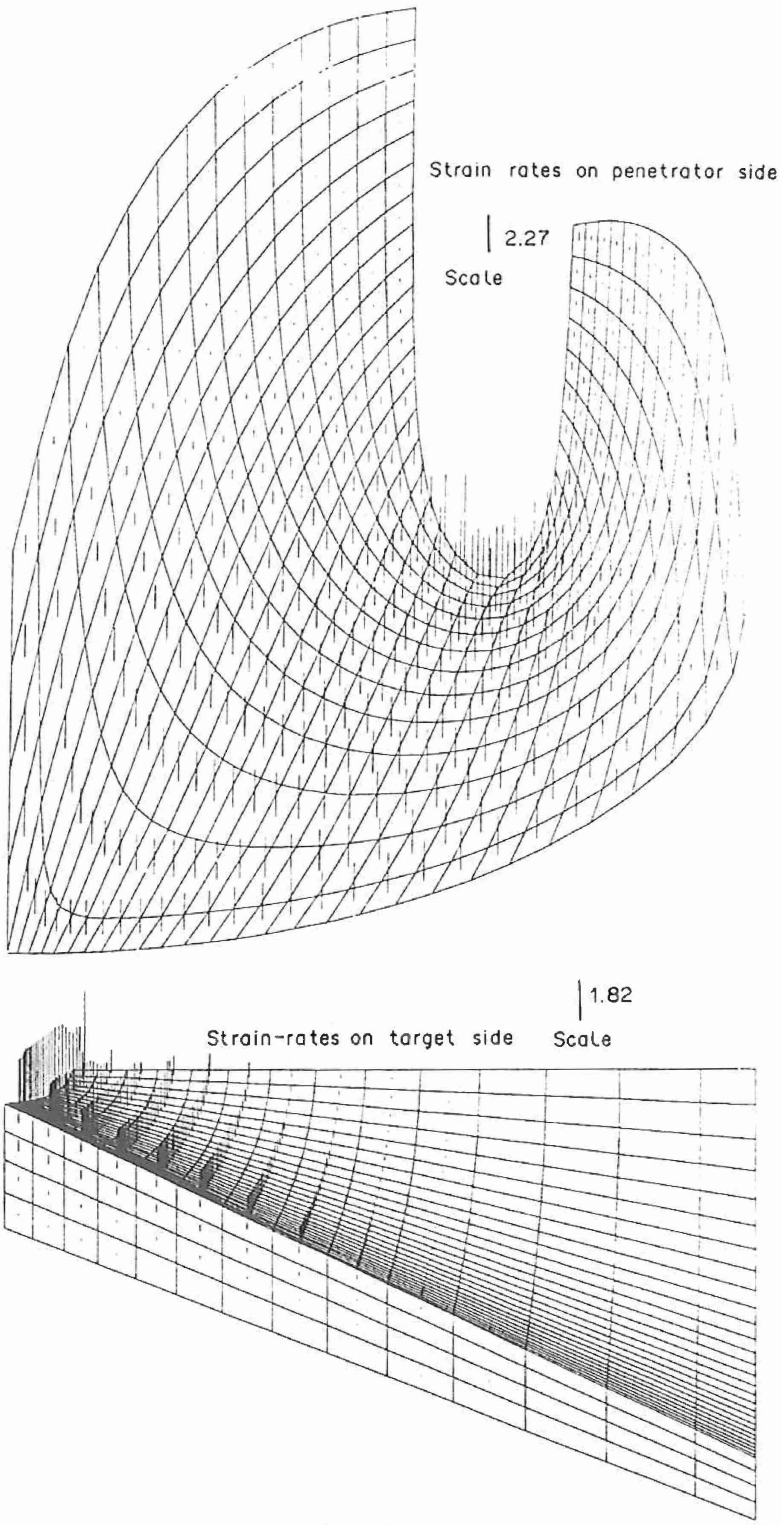

FIG. 5. Distribution of the strain-rate invariant I in the deforming penetrator and target regions for $v_s = 500$ m/s.

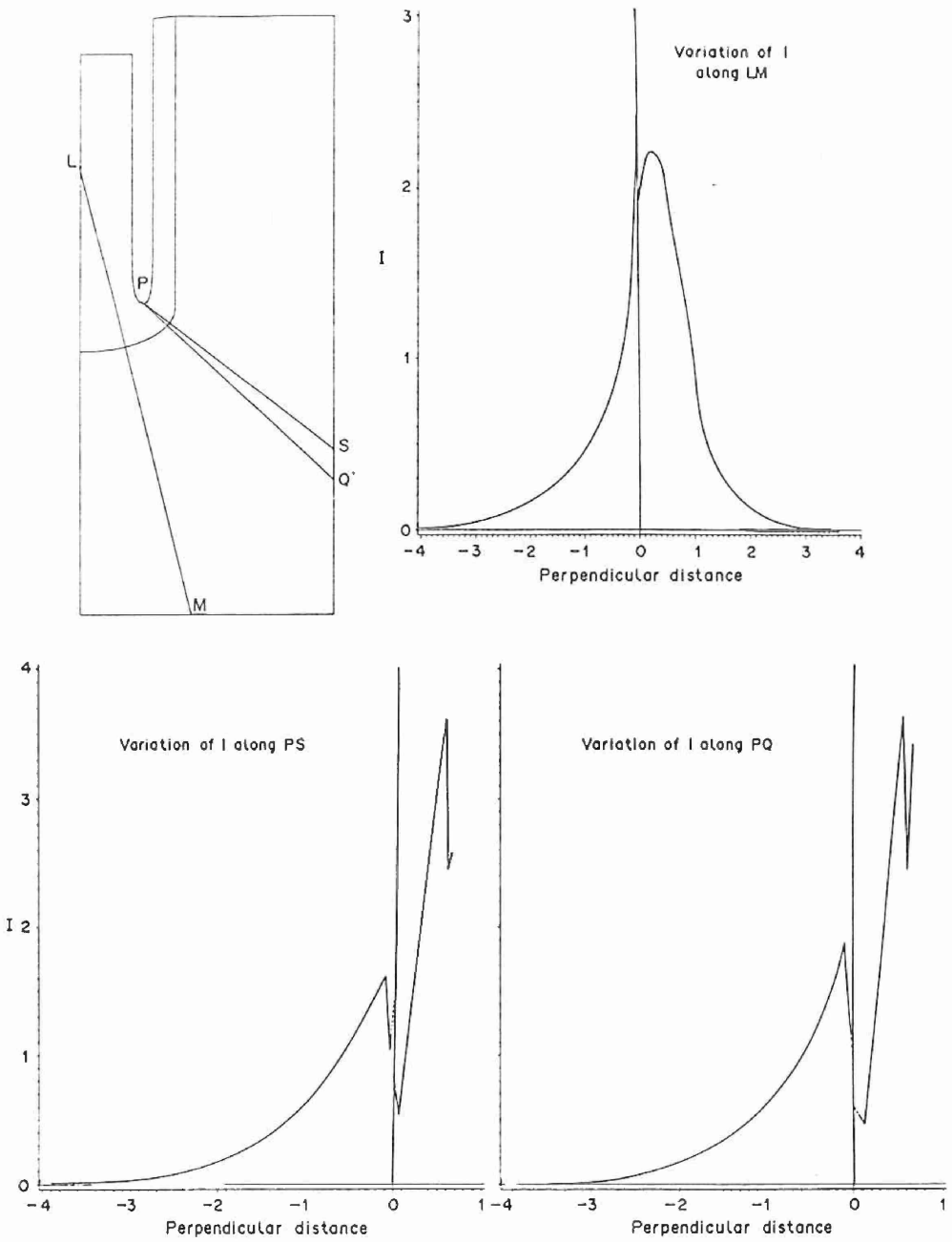

FIG. 6. Variation of 2nd invariant I of the strain-rate tensor along three arbitrary lines LM, PQ, and PS perpendicular to Γ_i ($v_s = 500$ m/s).

to get values of p as a multiple of corresponding σ_0. The maximum values of the non-dimensional hydrostatic pressure were found to be 0.8975 and 1.017 for the penetrator and the target, respectively. These equal 5.03 σ_{0p} and 17.39σ_{0t}, respectively. When the penetrator and the target materials are modeled as rigid/perfectly plastic, Gobinath and Batra [38] found for $v_s = 500$ m/s, the peak pressures in the penetrator and target to be 5.06σ_{0p} and 15.68σ_{0t} near the stagnation point. It seems that the consideration of strain-rate hardening and thermal softening effects has virtually no effect on the value of the peak hydrostatic pressure in the penetrator but increases its value in the target region. We note that for the rigid ellipsoidal nosed penetrator ($r_n/r_0 = 2.0$) and rigid/thermoviscoplastic target, Batra [16] computed the maximum value of p to be $12\sigma_{0t}$ for $\alpha_t = 5.0$ and for the thermoviscoplastic rod upset at the bottom of a rigid hemispherical cavity, Batra and Lin [19] found p_{max} to be $3\sigma_{0p}$ for $\alpha_p = 5.0$. Pidsley [6] who studied the penetration of a copper rod into a steel target by using the HELP code, computed p_{max} to be 5.53σ_{0p} and 4.33σ_{0t}

for $\alpha_p = 7.84$ and $\alpha_t = 1.92$, respectively, during the steady state portion of the penetration process.

The distribution of I in the deforming penetrator and target regions is shown in Fig. 5. Note that the scales in the two regions are different but the values of I in each case are to be multiplied by v_s/r_0 to get the dimensional values of I. Thus peak strain-rates of the order of 10^5/s occur in the penetrator and the target. As for the thermoviscoplastic target striking a rigid hemispherical cavity [19] significant deformations of the penetrator occur within the hemispherical region of radius nearly 1.0 and centered at the bottom-most point of the free surface. Note that the values of I near the stagnation point are quite high both

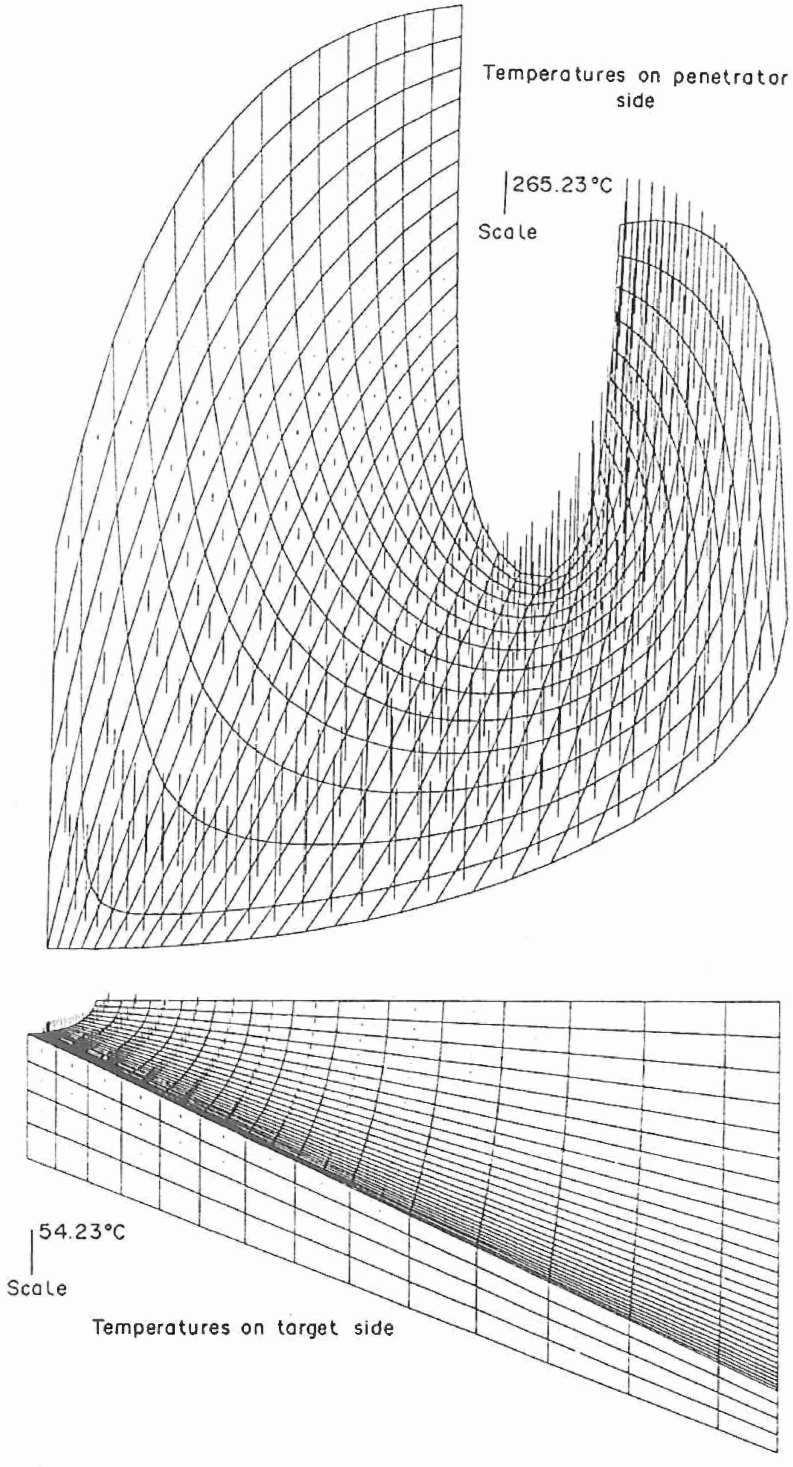

FIG. 7. Distribution of the temperature rise in the deforming penetrator and target regions ($v_s = 500$ m/s).

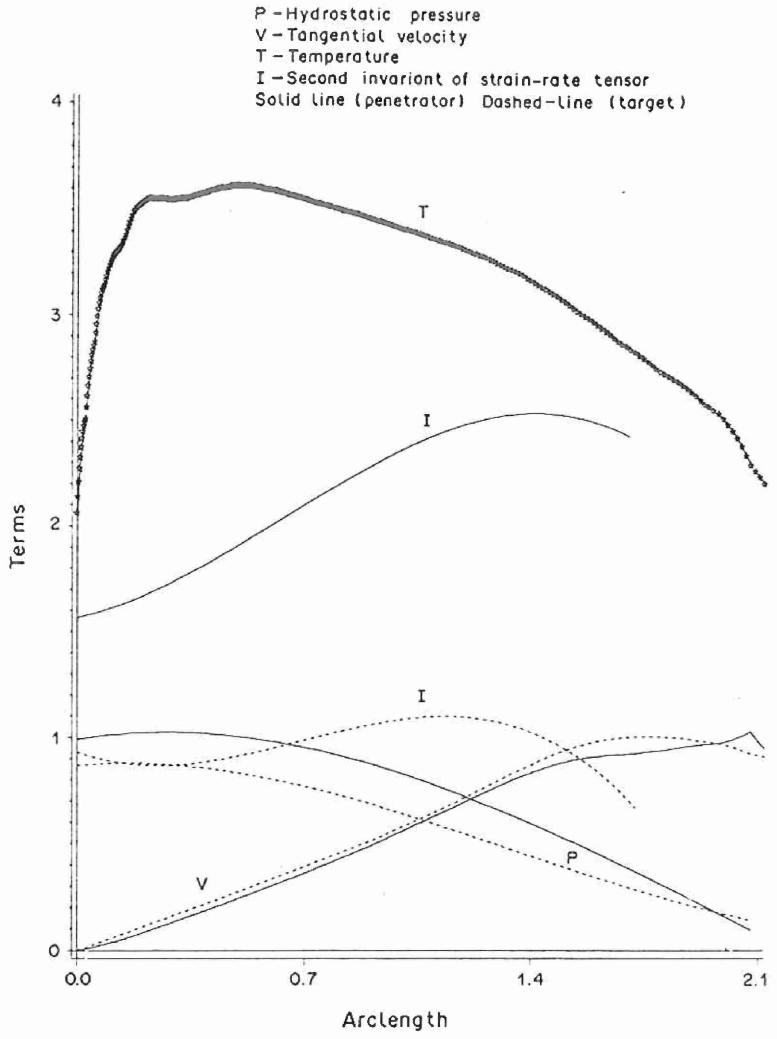

FIG. 8. Distribution of the hydrostatic pressure, tangential velocity, 2nd invariant I of the strain–rate tensor $\boldsymbol{D}$, and the temperature rise on the target/penetrator interface ($v_s = 500$ m/s).

in the target and penetrator regions. Whereas peak values of I in the deforming penetrator region occur at points near the free surface where the flow is reversing, those in the target occur at points adjoining the common interface Γ_i. Peak values of I in the penetrator and target equal 5.25 at the point (1.135, 1.01), 3.75 at the point (1.106, 0.17), respectively. In dimensional units these equal, respectively, 0.2625×10^6/s and 0.1875×10^6/s.

In order to examine whether or not sharp gradients of I occur across the target/penetrator interface Γ_i, we have plotted in Fig. 6 the variation of I along lines LM, PQ and PS which are arbitrarily selected and shown in the figure. The distribution of I along these three lines exhibits similar behavior in that the values of I are discontinuous across Γ_i and the value of I at the target particle abutting Γ_i is higher than that for the penetrator particle occupying the same spatial position. The maximum value of I within the deforming target region occurs at a point slightly away from Γ_i. For points on line LM, I_{max} for the target is higher than that for the penetrator particles, but the converse holds for points on lines PQ and PS. Since the tangential velocity of target and penetrator particles abutting Γ_i are nearly the same, for normal tractions to be continuous across Γ_i, normal derivatives of v on Γ_i must be discontinuous if target and penetrator particles are made of different materials. This provides a justification for the jump in the value of I as one crosses Γ_i. Recalling that the hydrostatic pressure contributes significantly to the normal tractions, it is not necessary that I be sharply discontinuous across Γ_i for the normal tractions on the two sides of Γ_i to match with each other.

Figure 7 depicts the temperature distribution in the deforming penetrator and target regions. Note that the scales for the two plots are different. As for the values of the

strain-rate invariant I, high temperatures occur in the deforming penetrator region near the stagnation point and points adjoining the free surface. Because of the high speed of material particles, a considerable amount of heat is transferred by convection. For this reason, the temperature decreases rather slowly as one moves downstream along the target penetrator interface or along any other streamline such as the free surface of the penetrator. The maximum temperature rise in the penetrator and target is found to be 232°C at the point (0.17, 0.66) and 191°C at the point (0.479, 0.05), respectively. This is considerably less than that found when either the penetrator (504°C) or the target (605°C) is regarded as rigid for nearly the same value of v_s. One possible explanation for this is that the external work done in the present problem is used to deform both the penetrator and the target, whereas in the previous studies referred to, all of the external work was used to deform either the penetrator or the target. Along the axial line the temperature decreases slowly within the penetrator but quite rapidly in the target.

Figure 8 shows the distribution of the non-dimensional hydrostatic pressure, second invariant I of the strain-rate tensor, tangential velocity and the temperature rise at points on the target/penetrator interface Γ_i. The temperature values are to be multiplied by 52.8°C to get their dimensional counterparts. It is clear that on Γ_i, the maximum value of the temperature occurs at a point slightly away from the stagnation point. Even though the values of the non-dimensional and dimensional pressures on the penetrator and target sides of the common interface Γ_i are nearly the same, their values as a multiple of the flow stress are not because of the difference in the values of the flow stresses for the penetrator and target regions. The slight difference in the value of the tangential velocities of the target and penetrator particles situated at the same spatial position on Γ_i reveals that there is some slippage between the two. This is consistent with our assumptions of only the normal velocity and normal tractions being continuous across Γ_i.

On the axial line, uniaxial strain conditions prevail, approximately. Thus the magnitude of the deviatoric stress s_{zz} should equal 2/3 the effective stress, which equals $\sqrt{3}$ times the right-hand side of Eqn (11). As shown in Fig. 9(a), the difference between s_{zz} and $2/3\sigma_e$ is less than 4% on the penetrator side and less than 0.3% on the target side. Also depicted in the figure are contributions of various terms in Eqn (32), obtained by integrating the equation of motion along the central streamline $r = 0$

$$\tfrac{1}{2}v^2 + p - s_{zz} - 2\int_0^z \frac{\partial \sigma_{rz}}{\partial r}\,dz = -\sigma_{zz}(0). \tag{32}$$

This equation holds both for the penetrator and the target, and z is measured from the stagnation point. Even though $\sigma_{zz}(0)$ for the target and the penetrator should equal each other, the two do not match in our plot because the solution was taken to have converged when the normal tractions on the penetrator and target sides differed from the mean normal tractions by, at most, 5%. Note that the integral term in Eqn (32) contributes significantly to the total as we move away from the stagnation point. This was pointed out by Wright [4] and has also been verified by Pidsley [6]. We add that while computing σ_{zz} from the computed velocity and temperature fields, contributions from the artificial viscosity were not considered. Figure 9(b) depicts the variation of the second invariant I of the strain-rate tensor and the temperature rise θ on the axial line. The temperature on the target side falls off rather rapidly as one moves away from the stagnation point. However, within the penetrator, the maximum value of the temperature rise occurs at a point away from the stagnation point. Even though the maximum value of I on the target axial line occurs near the stagnation point and is much higher than that on the penetrator axial line, θ_{max} for the penetrator particles is larger than θ_{max} for the target. This is due to the differences in the value of their heat capacities and flow stresses. A possible explanation for the discontinuity in the values of I as one crosses the target/penetrator interface is the same as that given above for lines LM, PQ and PS.

5.2 *Effect of the speed of penetration*

Figure 10 depicts the distribution of the mean normal tractions on the target/penetrator

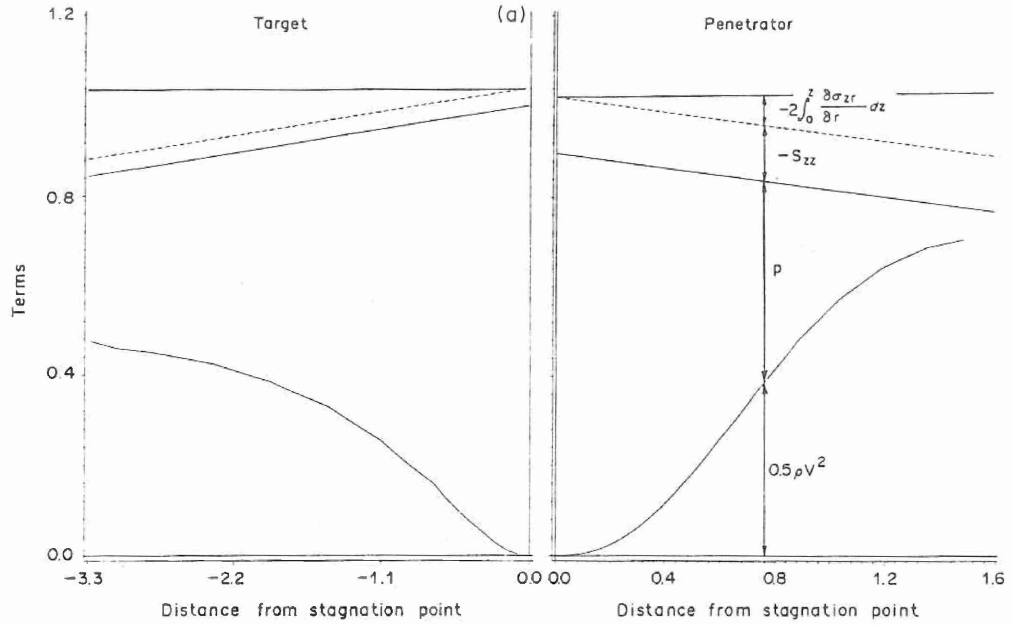

FIG. 9(a). Contributions of various terms in the Bernoulli equation along the central streamline ($v_s = 500$ m/s).

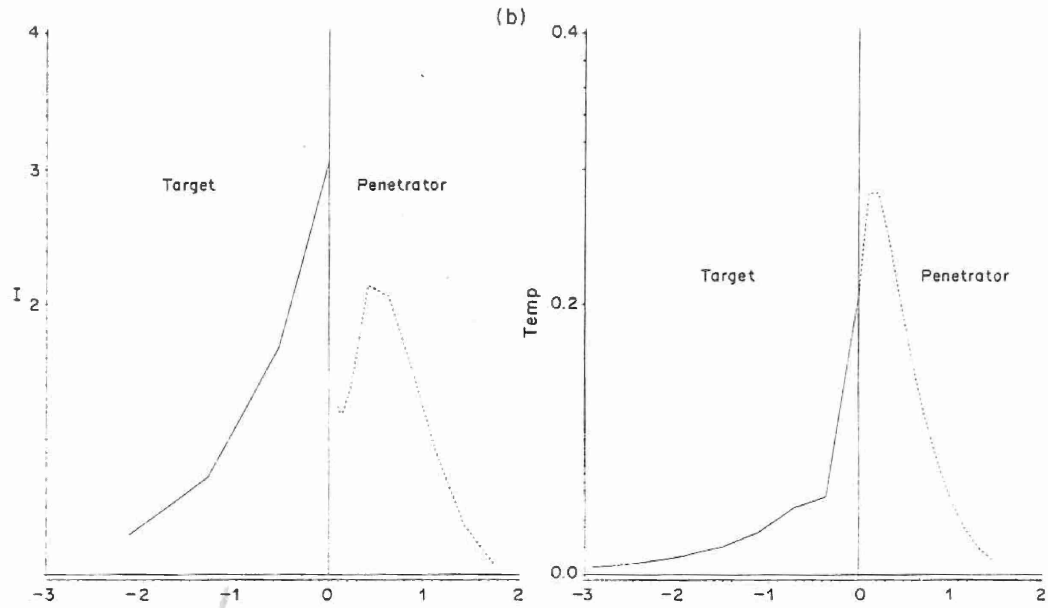

FIG. 9(b). Distribution of the 2nd invariant I of the strain–rate tensor $\boldsymbol{D}$ and the temperature rise along the central streamline ($v_s = 500$ m/s).

interface for $v_s = 450$ m/s, 500 m/s and 550 m/s. The values of (α_p, α_t) corresponding to these values of v_s equal (4.51, 13.82), (5.57, 17.06), and (6.74, 20.65), respectively. The values of the penetrator speed for these values of v_s equal 850 m/s, 1041 m/s and 1234 m/s, respectively. These plots elucidate that the normal tractions on the common interface increase sharply with the penetration speed. The normal tractions diminish to nearly zero values for non-dimensional values of arc length on Γ_i exceeding 2.0. We note that these curves are similar to that given by Gobinath and Batra [22] who assumed the penetrator and target materials to be rigid/perfectly plastic and solved the problem for $v_s = 400$ m/s. The axial resisting force experienced by the penetrator for the three values of v_s considered herein equalled 8.91, 11.52, and 14.51, respectively. These numbers need to be multiplied by $\pi r_0^2 \sigma_{0p}$ to get the corresponding dimensional values of the axial force acting on the penetrator. We have plotted the shapes of the free surface and the target/penetrator interface

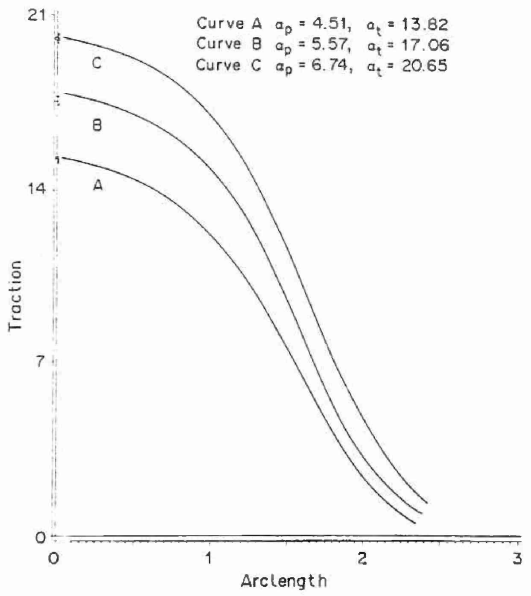

FIG. 10. Distribution of the mean normal tractions on the target/penetrator interface for three different speeds of penetration.

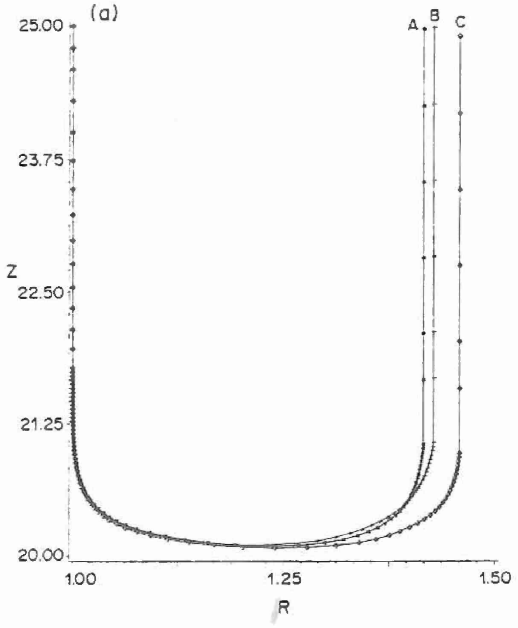

FIG. 10(a). Shapes of the free surface for three different speeds of penetration.

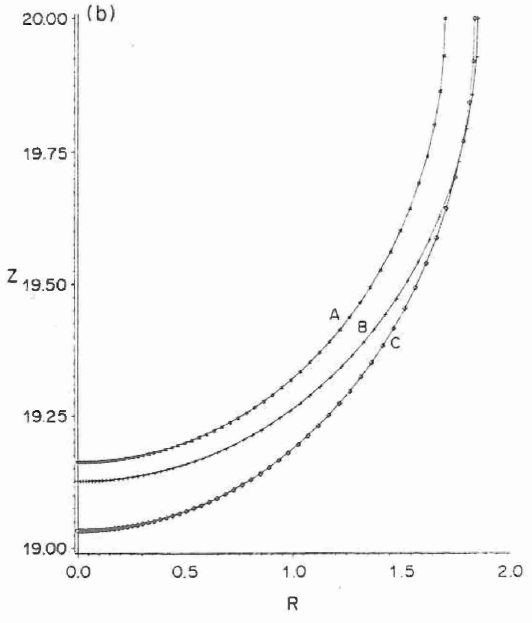

FIG. 10(b). Shapes of the target/penetrator interface for three different speeds of penetration.

for the three values of v_s stated above in Figs 10(a) and 10(b), respectively. In order to elucidate the dependence of the location of the stagnation point upon the speeds of penetration, the ordinate is measured from the bottom surface (CD in Fig. 1) of the target region considered. The stagnation point moves away from the free surface of the deformed penetrator as the speed of penetration is increased. Also with the increase in the speed of penetration, the distance between the free surface of the undeformed penetrator and the deformed penetrator particles moving rearwards increases. The shape of the target/penetrator interface also depends strongly upon the penetration speed.

5.3 *Effect of the strain–rate hardening exponent* m

Figures 11, 11(a) and 11(b) depict the distribution of the mean normal tractions on the target/penetrator interface Γ_i, its shape and the shape of the free surface Γ_f for three different

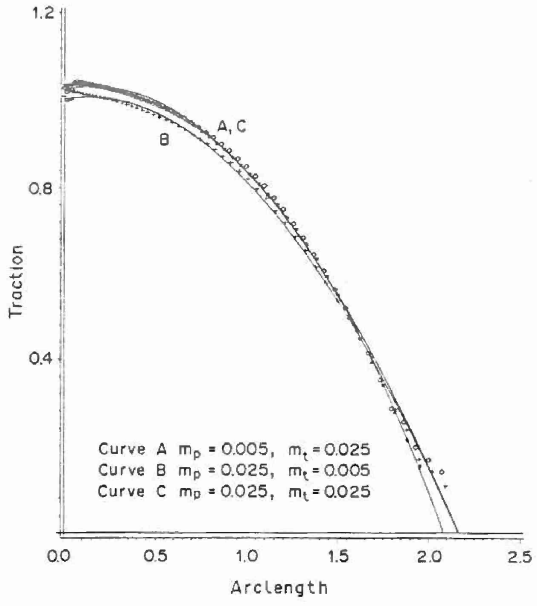

FIG. 11. Distribution of the mean normal tractions on the target/penetrator interface for three different strain–rate hardening exponents.

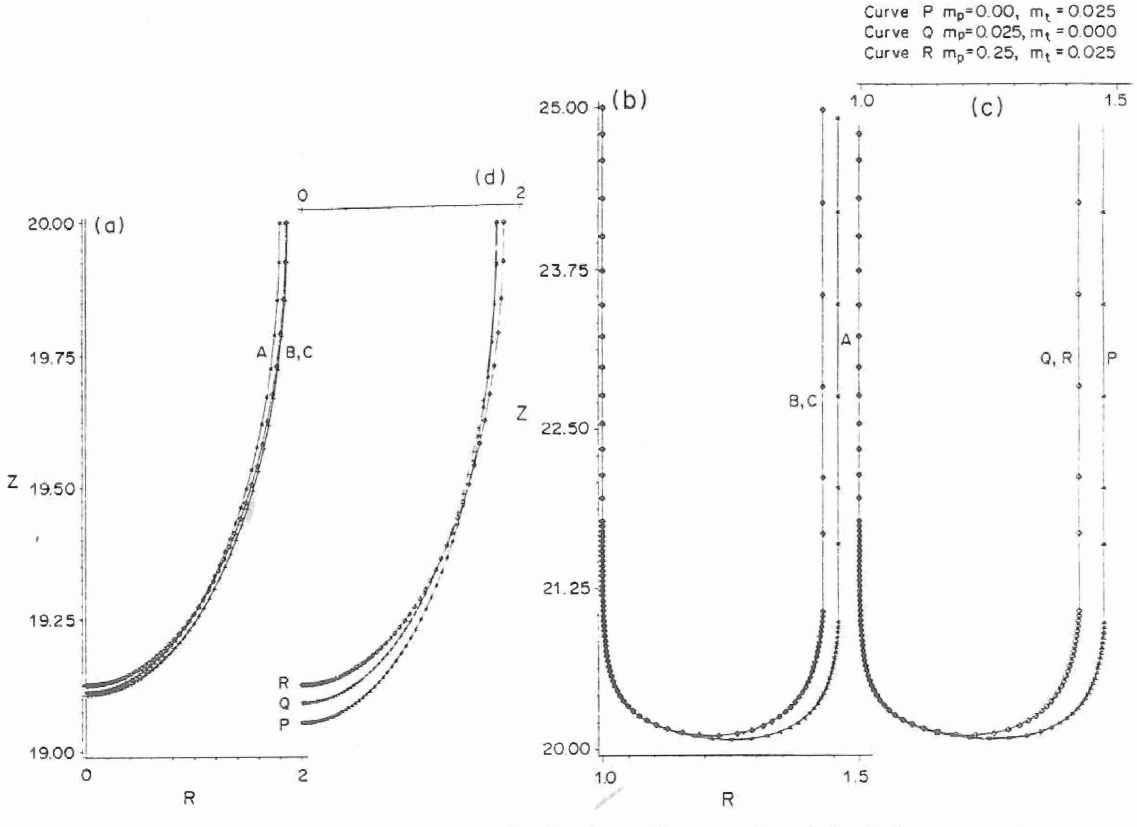

FIG. 11(a). Shapes of target/penetrator interface for three different strain–rate hardening exponents.

FIG. 11(b). Shapes of free surface for three different strain–rate hardening exponents.

FIG. 11(c). Comparison of shapes of free-surface for three different combinations of material model.

FIG. 11(d). Comparison of shapes of target/penetrator interface for three different combinations of material model.

combinations of the values of the strain-rate hardening exponent m and $c_s = 500$ m s. When the value of m for the penetrator is kept fixed at 0.025 and the value of m for the target is changed from 0.025 to 0.005, there is hardly any change in the shape of the free surface. However, the shape of Γ_i and the distribution of normal tractions on it do change some, though not significantly, when m_t is reduced from 0.025 to 0.005. In Fig. 11(b), the free surfaces are plotted to a large scale so as to magnify differences, if any, in their shapes for different values of m. The change in the value of m_p from 0.025 to 0.005 while m_t is kept fixed at 0.025 does influence significantly the shape of the free surface and to a somewhat less extent, the shape of the target/penetrator interface and the distribution of normal tractions on it. The stagnation point moves away a little bit from the free surface when the value of m is changed from 0.025 to 0.005 either for the penetrator or the target. The peak values of θ, I, and p and where they occur are influenced by the values of m_p and m_t as evidenced by the information provided in Table 1.

When either the penetrator or the target is modeled as rigid/perfectly plastic material and the other body as viscoplastic with $m = 0.025$, the shapes of the free surfaces and the corresponding intermediate surfaces are shown in Figs 11(c) and 11(d), respectively. The vertical scale in these figures represents the distance measured from the bottom-most point of the target region studied so that vertical displacements, if any, of the stagnation point could be determined. When either one of the two materials is modeled as rigid perfectly plastic, the stagnation point moves downward, the displacement for $m_p = 0$ being twice of that for $m_t = 0$. The shapes of the free surface of the deformed penetrator remain unaltered when either m_t is 0.025 or 0.0 and does not change noticeably when m_p is decreased from 0.025 to 0.0.

5.4 *Effect of the thermal-softening coefficient γ*

When the value of the thermal softening coefficient γ for either the target or the penetrator was doubled keeping that for the other part unchanged, the distributions of the mean normal tractions on the target/penetrator interface Γ_i, its shape and the shape of the free surface Γ_f were essentially unaltered. Therefore, these plots are not included in the paper. The values of θ_{max}, p_{max}, I_{max} in the penetrator and target regions do not change much when γ is doubled either for the target or the penetrator. We note that a similar effect was observed by Batra [17] who analysed the steady state penetration of a rigid cylindrical rod into a thick thermoviscoplastic target.

5.5 *Effect of different ratios of mass densities*

Results presented in this section are for the case when the penetrator and target materials are modeled as rigid/perfectly plastic. Figure 12 shows the shapes of the target/penetrator interface Γ_i and the distribution of normal tractions on it for $\rho_t/\rho_p = 1.25$, 1.0, and 0.75. The ordinate in Fig. 12(a) is the vertical distance from the bottom surface CD of the target region considered and the scales along the horizontal and vertical axes are quite different. The expanded scale along the horizontal axis is meant to magnify the small differences in the shapes of Γ_i when ρ_t/ρ_p is varied. We note that in these computations ρ_p was kept fixed. The plots of normal tractions on Γ_i reveal that the largest normal tractions occur for $\rho_t/\rho_p = 1.25$ and least for $\rho_t/\rho_p = 0.75$ and the change seems to depend continuously upon ρ_t/ρ_p. Thus, for the same penetrator material, the pressure at the stagnation point will increase with an increase in the mass density of the target. Similarly for a fixed target material, higher density penetrators would result in smaller values of the pressure at the stagnation point.

6. HISTORIES OF THE STRESS, STRAIN-RATE INVARIANT, HYDROSTATIC PRESSURE AND THE SPIN TENSOR

One of the unresolved problems in penetration mechanics is the selection for the material of the penetrator and the target constitutive relations that adequately model their response over the range of deformations anticipated to occur in a problem. In an attempt to help

TABLE 1. EFFECT OF m_p AND m_t ON θ_{max}, I_{max} AND p_{max} IN THE PENETRATOR TARGET REGIONS*

Values of m	θ_{max} (°C)		I_{max}		$p_{max}(x_p, v_t^2)$	
	Penetrator	Target	Penetrator	Target	Penetrator	Target
$m_p = 0.025$ $m_t = 0.025$	232.2 (0.17, 0.06)	189.5 (0.479, 0.05)	5.25 (1.135, 1.01)	4.185 (1.096, 0.175)	0.8975 (0.0, 0.0)	1.017 (0.148, −0.012)
$m_p = 0.005$ $m_t = 0.025$	199.8 (0.165, 0.04)	167.1 (0.464, 0.04)	4.26 (1.193, 0.96)	4.108 (1.074, 0.164)	0.9409 (0.0, 0.0)	1.005 (0.149, −0.004)
$m_p = 0.0$ $m_t = 0.025$	193.07 (0.165, 0.03)	164.15 (0.525, 0.04)	4.11 (0.052, 0.02)	4.174 (1.26, 0.26)	0.9562 (0.0, 0.0)	0.9951 (0.113, 0.002)
$m_p = 0.025$ $m_t = 0.005$	229.9 (0.15, −0.02)	183.2 (0.48, 0.02)	5.27 (1.134, 1.02)	4.5915 (1.86, 0.77)	0.8957 (0.0, 0.0)	0.978 (0.15, −0.014)
$m_p = 0.025$ $m_t = 0.0$	230.7 (0.165, 0.034)	186.03 (0.526, 0.04)	4.2815 (0.052, 0.02)	4.128 (1.26, 0.27)	0.9509 (0.0, 0.0)	0.9454 (0.1129, 0.001)

* The coordinates of points where θ, I and p assume maximum values are parenthetically noted.

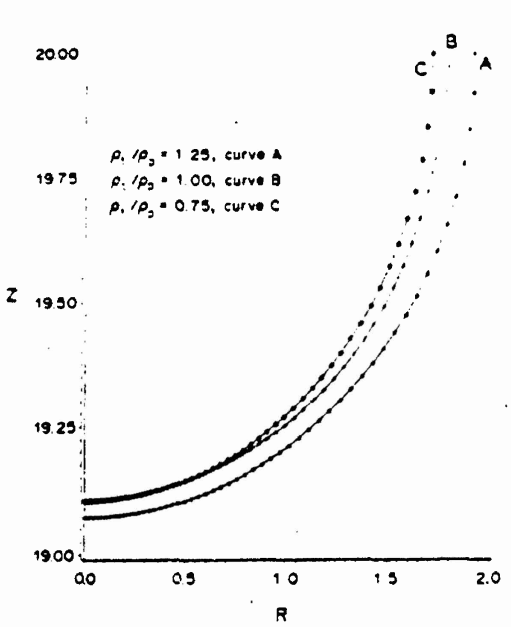

FIG. 12(a). Shapes of the target/penetrator interface for three different values of ρ_t/ρ_p.

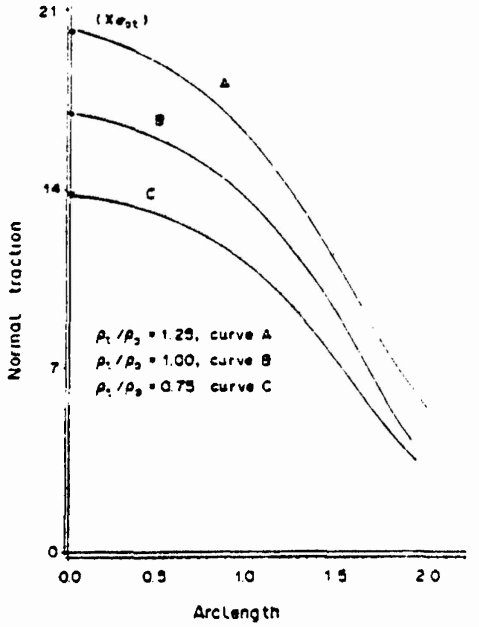

FIG. 12(b). Distribution of the mean normal tractions on the target/penetrator interface for three different values of ρ_t/ρ_p.

determine which one of the many recently proposed theories (e.g. Refs [39–42]) of large deformation elastoplasticity is most appropriate for a penetration problem, we give below histories of the effective stress, second invariant of the strain-rate tensor, the temperature and the spin for a few typical target and penetrator particles. These time histories should also help establish desirable testing regimes for practical problems.

The first step in finding histories of a field variable at a material particle is to find the streamline for that particle. Streamlines originating from four locations, viz. A(0.1, 5.88), B(0.15, 5.88), C(0.90, 5.88), and D(0.95, 5.88) within the deforming penetrator region and two locations, i.e. E (0.10, −3.12) and F(0.15, −3.12) within the deforming target region are plotted in Fig. 13. That the four streamlines originating from points C, D, E, and F do not intersect or merge together is clear from the enlarged view of the portion enclosed in the box. In the following discussion, we identify the histories of the material particle that once occupied, say, the place A as histories of the variable for the material particle A.

6.1 *Histories of field variables for penetrator particles*

Figure 14 depicts the location of the four particles at different times. The time is reckoned from the instant when particles A, B, C, and D occupied the places (0.10, 5.88), (0.15, 5.88), (0.90, 5.88), and (0.95, 5.88), respectively. The radial and axial components of the velocity at different times for these four particles are plotted in Fig. 15. As particles A and B approach the region surrounding the stagnation point at $t = 5$, their velocities in the radial direction increase sharply and those in the axial direction decrease to zero. Material particles C and D adjoining the free surface of the penetrator reach near the bottom-most point on the free surface at time $t = 2.8$. The radial velocity of these particles which was initially zero increases sharply, and becomes maximum when they are close to the bottom-most point on the free surface. It is followed by a rapid decrease to a small value which gradually becomes zero. Recalling that the velocities plotted are those relative to the velocity of the stagnation point, the sharp jump in the value of v_z for these particles corresponds to the reversal in their direction of motion after they move past the bottom of the free surface. In Fig. 16 we have plotted the histories of the non-dimensional temperature and the second invariant I of the strain-rate tensor. For points A and B

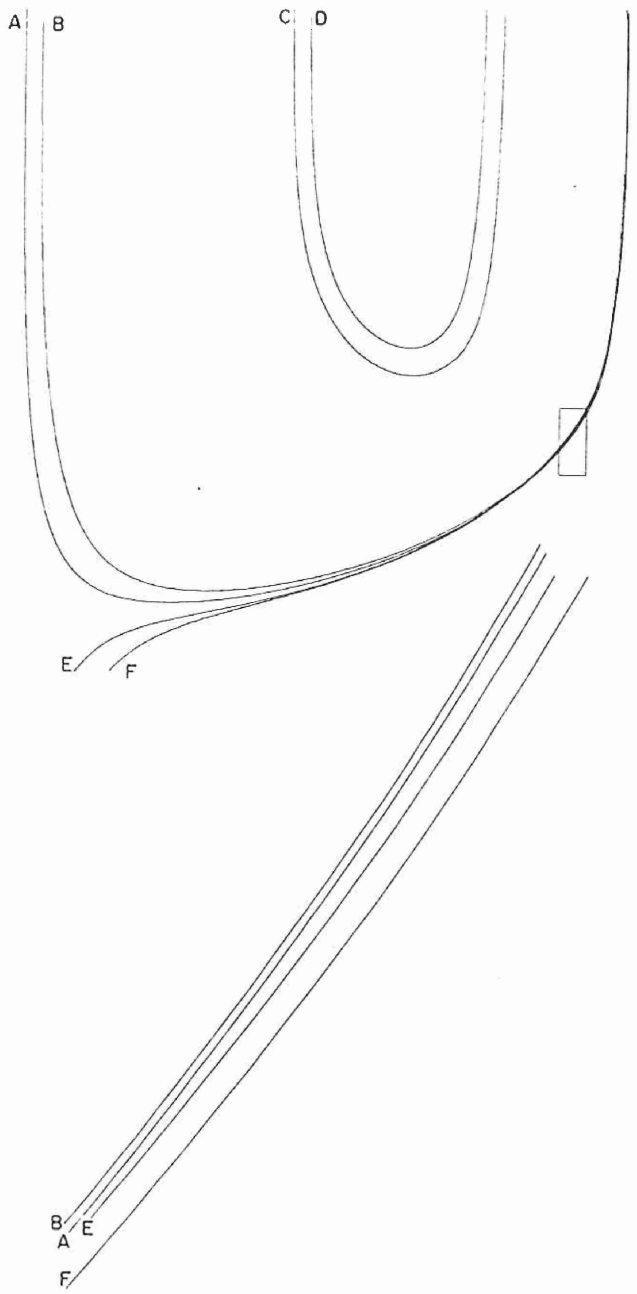

FIG. 13. Streamlines emanating from four points of the penetrator region and two points of the target region.

adjoining the axial line, peak values of the temperature rise are higher than those for points C and D, but the peak values of I for points C and D are higher than those for points A and B. Peak values of the second invariant I of the strain-rate tensor at points A and B are much lower than those for points C and D. Peak values of θ and I at points A and B occur when they are near the stagnation point. As these points move far away from the stagnation point, the value of I decreases rapidly but that of θ decreases slowly due to the convective transport of heat. For points C and D near the free surface, peak values of θ and I occur simultaneously soon after they cross over to the right of their bottom-most positions. Note that the values of I and θ increase at points C and D rapidly as they approach the bottom-most point on the free surface. Whereas the values of I drop quite rapidly, their temperature is still high because of the convective transport of heat. Figure 17 shows histories of the effective stress S_e, defined as the right-hand side of Eqn (11), and the hydrostatic pressure at these four particles. For particles C and D the hydrostatic pressure is negligibly small. This is to be expected since these particles always stay close

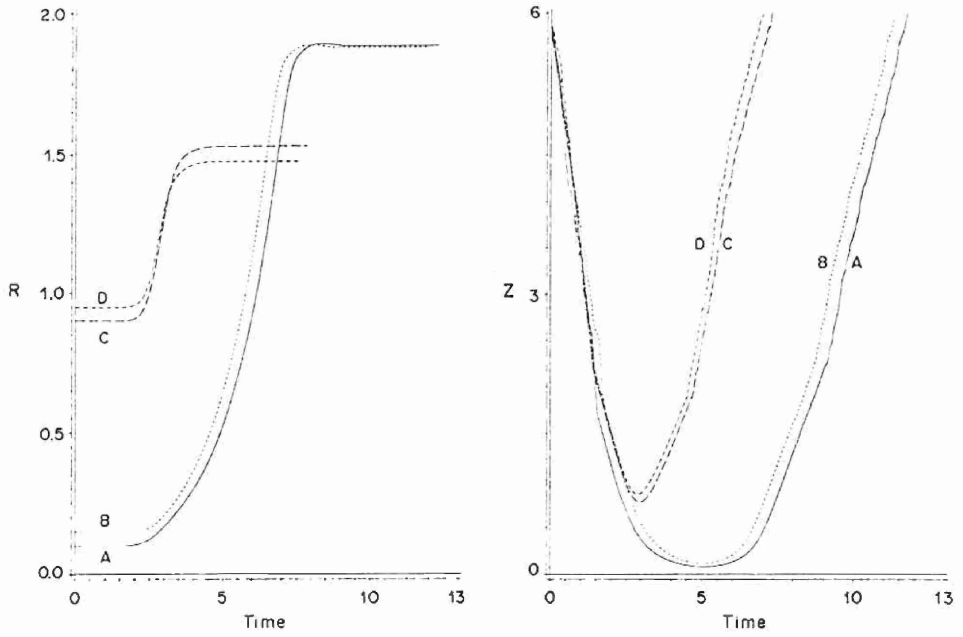

FIG. 14. The variation of r-, z-coordinate of four penetrator particles at different times.

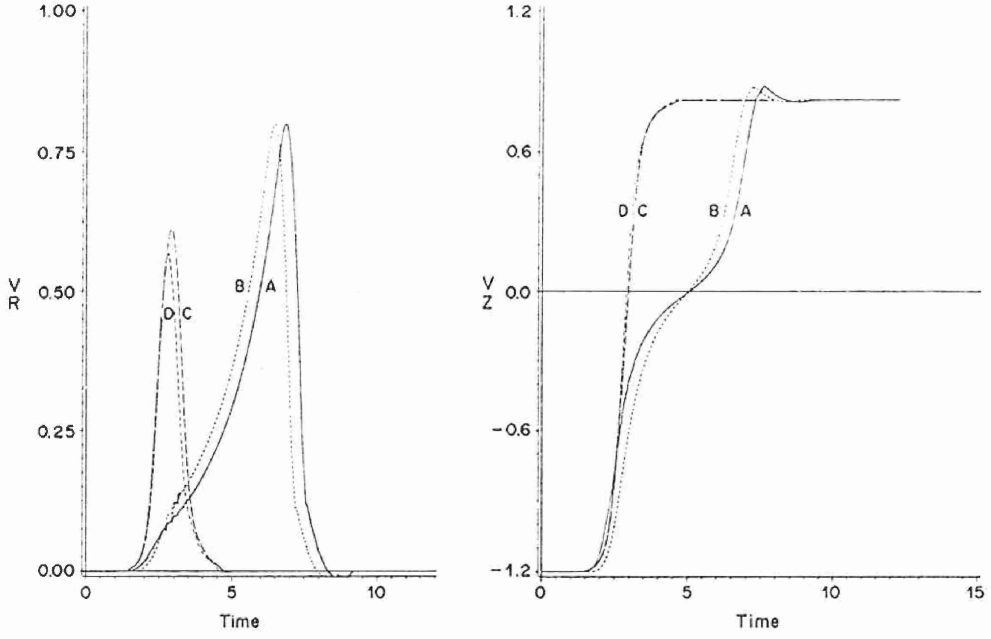

FIG. 15. Histories of the radial and axial components of velocity for four penetrator particles.

to the free surface of the penetrator. Note that the peak values of S_e at all four points considered is nearly the same. Since the material particles are undergoing plastic deformation, the effective stress must satisfy the yield condition (11). The variation in the effective stress at these points is due to the change in the values of I and θ. At points C and D, the peak values of I, θ, and S_e occur at the same time thereby implying that the strain–rate hardening effects dominate over the thermal softening effects. For $t \geq 5$ when the values of I have become essentially zero, the effective stress drops because of the softening caused by the heating of the material points. For material particles A and B, whereas I_{max} occurs at $t \simeq 2.8$, the maximum value of S_e occurs at $t \simeq 2.2$. Recalling the history of the temperature plotted in Fig. 16, we see that θ_{max} occurs at $t \simeq 4.5$ and the values of θ at $t \simeq 2.8$ are higher than those at $t \simeq 2.2$. The higher value of the thermal softening effect at $t \simeq 2.8$ reduces the value of S_e as compared to that at $t \simeq 2.2$.

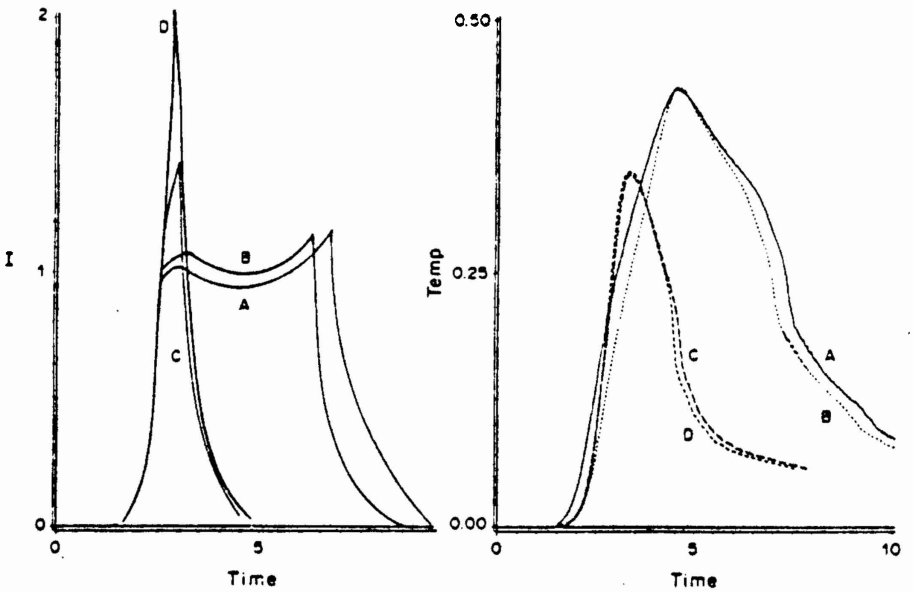

FIG. 16. Histories of the temperature rise and 2nd invariant I of the strain-rate tensor for four penetrator particles.

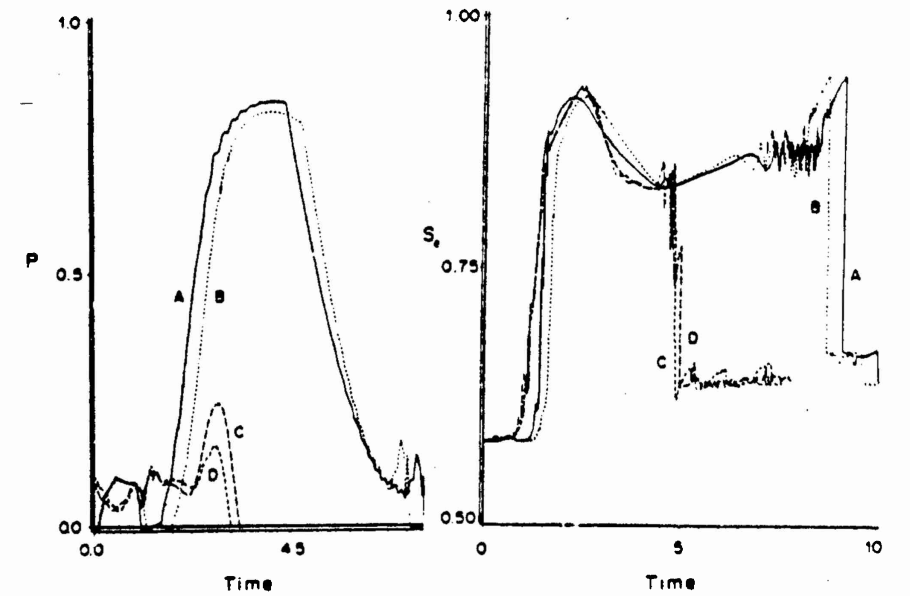

FIG. 17. Histories of the hydrostatic pressure and effective stress for four penetrator particles.

Because of the assumptions of axisymmetric deformations, there is only one non-zero component of spin. The histories of the spin for the four penetrator particles, plotted in Fig. 18, reveal that the material particle C that is near the free surface has the highest value of spin. The peak value of the plastic spin for the material particle C is twice that for each of the other three particles. This peak value of the spin at C occurs when it has crossed-over to the right of its bottom-most position and is flowing rearwards.

6.2 Histories of field variables for target particles

In Fig. 19 we have plotted the r- and z-coordinates of the target material particles for different values of time t; their positions at time $t=0$ were E(0.10, −3.12) and

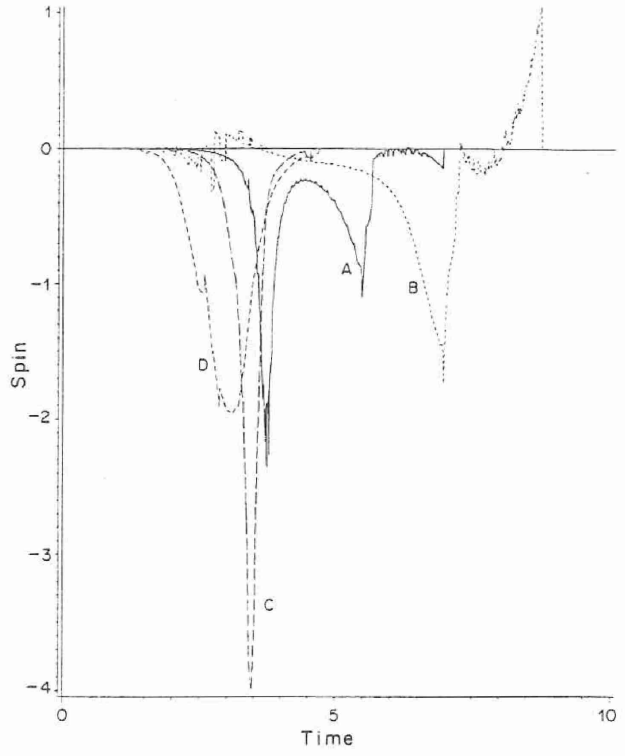

FIG. 18. Histories of the spin of four penetrator particles.

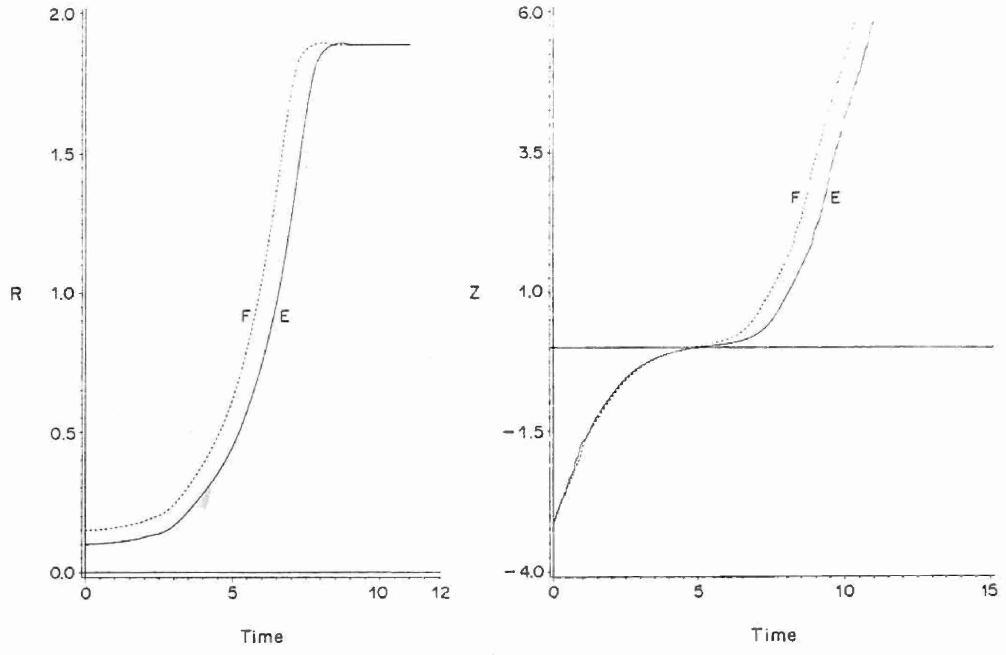

FIG. 19. Variation of r-, z-coordinates of two different target particles at different times.

F(0.15, −3.12), respectively. The radial and axial components of the velocity of these particles are plotted in Fig. 20. As these particles approach the region surrounding the stagnation point, their radial velocity increases sharply and subsequently drops to zero equally fast. The axial velocity of these particles relative to that of the stagnation point decreases and then increases as these points leave the area near the stagnation point. For $t \geq 9$, these particles are moving essentially vertically and parallel to the target/penetrator interface. The histories of the second invariant I of the strain–rate tensor and the temperature rise θ are plotted in Fig. 21. The peak values of θ at these two points occur at the same value of time. However, the peak values of I occur a little bit later. The rate

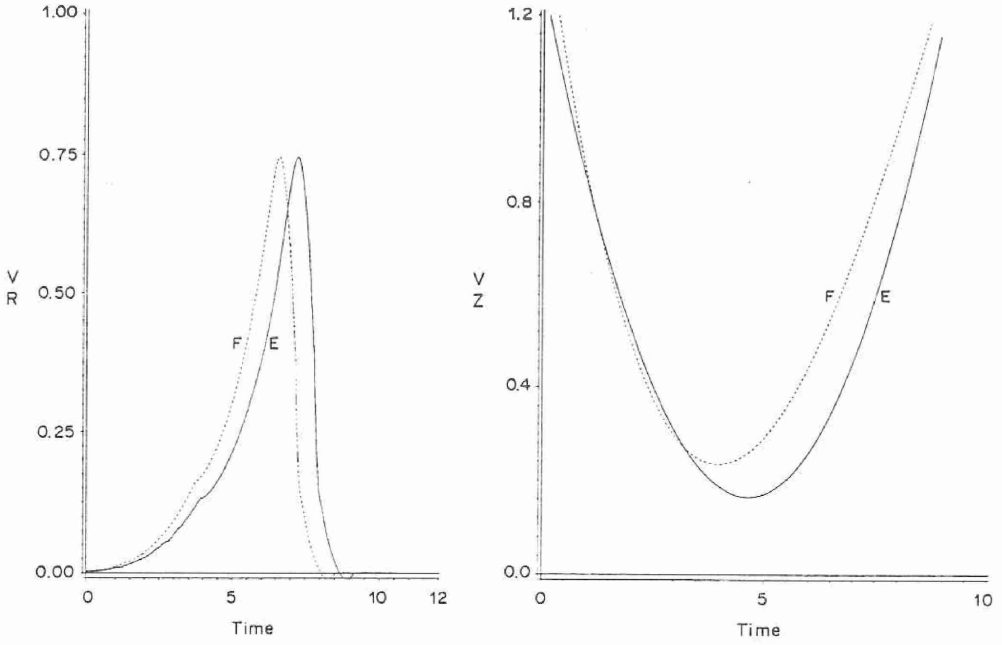

FIG. 20. Histories of the radial and axial components of velocity for two target particles.

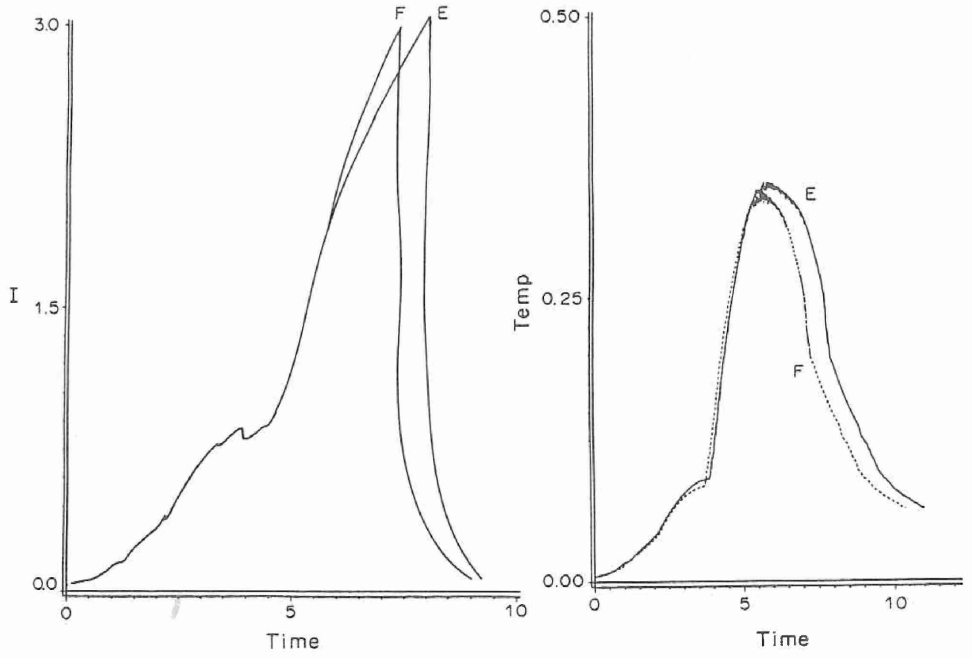

FIG. 21. Histories of the temperature rise and 2nd invariant I of two target particles.

of increase of temperature at these particles is much higher than the rate of increase of I, but I decreases much more rapidly than the temperature does because of the convective transport of heat. The histories of the hydrostatic pressure p and the effective stress S_e shown in Fig. 22 reveal that the pressure attains its maximum value when points E and F reach the zone surrounding the stagnation point at time $t \simeq 4.5$. Note that the maximum values of I and θ occur at these points when they have moved quite a bit away from the stagnation point. The effective stress at these points does not vary much because the thermal softening caused by their getting heated up seems to balance out the strain–rate hardening. The histories of the plastic spin, plotted in Fig. 23, suggest that of the two target particles considered, the one farther from the axial line has the higher values of the spin. The highest value of the spin occurs just before these particles arrive near the stagnation point. Also, when the particles start turning upwards along the target/penetrator interface,

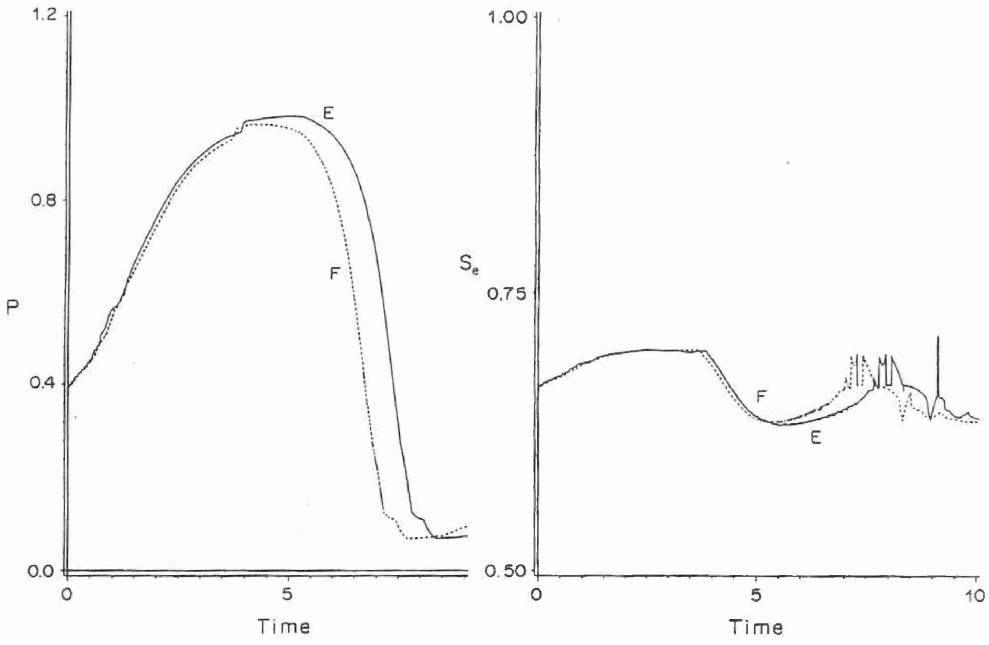

FIG. 22. Histories of the hydrostatic pressure and effective stress for two target particles.

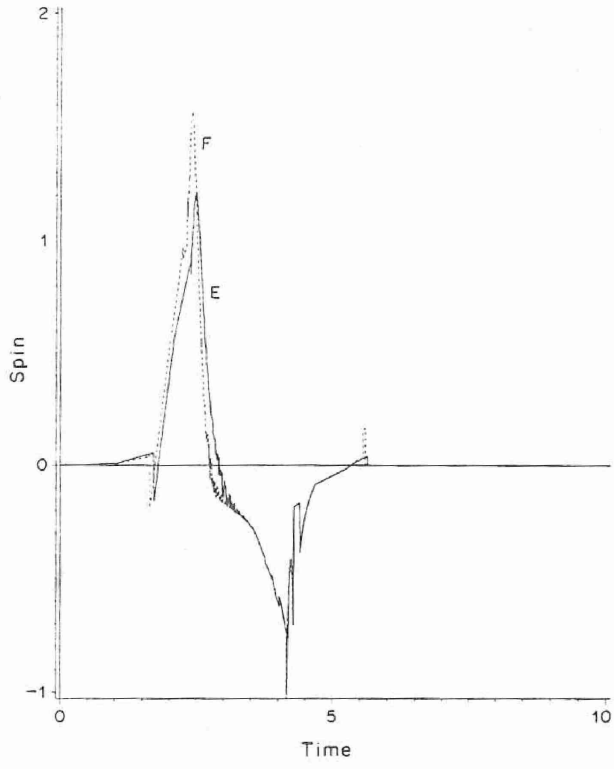

FIG. 23. Histories of the spin of two target particles.

their spin, now of opposite sign, is equally large in magnitude. The peak values of the spin are comparable in magnitude to the peak values of I for these particles.

7. CONCLUSIONS

We have analysed steady state axisymmetric deformations of a long cylindrical thermoviscoplastic rod penetrating into a thick thermoviscoplastic target. Also studied is the effect, on the deformations of the rod and the target, of the penetration speed, values

of the strain-rate hardening exponent and the coefficient of thermal softening. The bottom part of the target/penetrator interface Γ_i is a part of an ellipsoid rather than a hemisphere. For $v_s = 500$ m/s, the peak pressures in the penetrator near the stagnation point approach $5.6\sigma_{0p}$ and that in the target $14\sigma_{0t}$ when $\sigma_{0p}/\sigma_{0t} = 3.06$ where σ_{0p} and σ_{0t} equal the yield stress in a quasistatic simple compression test for the penetrator and target materials, respectively. The peak values of 232°C of the temperature rise in the penetrator and 191°C in the target are significantly lower than those found when either of the two materials is considered as rigid. Along the axial line the temperature decreases slowly in the penetrator but quite rapidly in the target. The normal tractions on the common interface Γ_i increase sharply with the increase in the penetration speed. Also the axial resisting force acting on the penetrator equalled 8.91, 11.52 and 14.51 F ($F = \pi r_0^2 \sigma_{0p}$) for stagnation point speeds of 450, 500 and 550 m/s, respectively. The corresponding values of the penetrator speed are 850, 1041 and 1234 m/s, respectively. A significant contribution to the resisting force is made by the consideration of the strain-rate hardening effects. The value of the strain-rate hardening exponent for the penetrator affects more the shapes of the free surface Γ_f of the deformed penetrator and the target/penetrator interface Γ_i than the value of the strain-rate hardening exponent for the target. The values of the thermal softening coefficient for the penetrator and target have minimal effect on the shapes of Γ_i and Γ_f and the distribution of normal tractions on Γ_f. The computed histories of the stress, second invariant of the strain-rate tensor, temperature, and the plastic spin for four penetrator and two target particles indicate that for the material parameters selected and the three speeds considered here, there is no likelihood of any material instability developing in the sense that the effective stress at these material particles is decreasing while their temperatures and values of the second invariant I of the strain-rate tensor are increasing. Also no narrow layers with sharp gradients of I were found on either side of Γ_i for the various cases studied. It is very likely that either the penetration speeds considered herein were not high enough for these effects to manifest themselves or the materials selected for the penetrator and the target were such that no localization of deformation could occur in regions surrounding Γ_i. The peak values of the plastic spin for the penetrator particles close to the free surface are nearly twice the peak values of the second-invariant I of the strain-rate tensor for them. Also for the two target particles close to the target/penetrator interface, peak values of the plastic spin are comparable to the peak values of I for them. It seems that plasticity theories which account appropriately for values of the plastic spin comparable to the values of the strain-rate tensor should be very suitable for analysing steady state axisymmetric problems.

Acknowledgements—This work was supported by the U.S. Army Research Office Contract DAAL-03-89-K-0050 to the University of Missouri-Rolla. Most of the computations were performed at the University of Illinois Supercomputer centre. We are indebted to a referee for many useful comments.

REFERENCES

1. A. TATE, A theory for the deceleration of long rods after impact. *J. Mech. Phys. Solids* **15**, 387–399 (1967).
2. A. TATE, Further results in the theory of long rod penetration. *J. Mech. Phys. Solids* **17**, 141–150 (1969).
3. V. P. ALEKSEEVSKII, Penetration of a rod into a target at high velocity. *Comb. Expl. and Shock Waves* **2**, 63–66 (1966). (Translation from Russian, Faraday Press, New York.)
4. T. W. WRIGHT, A survey of penetration mechanics for long rods, in *Lecture Notes in Engineering*, Vol. 3, Computational Aspects of Penetration Mechanics (edited by J. CHANDRA and J. FLAHERTY). Springer-Verlag, New York (1983).
5. T. W. WRIGHT and K. FRANK, Approaches to penetration problems. SMIRT Symposium, No. 14, Impact, Lausanne, Switzerland (1987).
6. P. D. PIDSLEY, A numerical study of long rod impact onto a large target. *J. Mech. Phys. Solids* **32**, 315–333 (1984).
7. M. E. BACKMAN and W. GOLDSMITH, The mechanics of penetration of projectiles into targets. *Int. J. Engng Sci.* **16**, 1–99 (1978).
8. C. E. ANDERSON and S. R. BODNER, The status of ballistic impact modeling. *Int. J. Impact Engng* **7**, 9–35 (1988).
9. J. A. ZUKAS *et al.* *Impact Dynamics*. Wiley-Interscience, New York (1982).
10. T. Z. BLAZYNSKI, in *Materials at High Strain Rates* (edited by T. Z. BLAZYNSKI). Elsevier, London, New York (1987).

11. M. MACAULEY, *Introduction to Impact Engineering*. Chapman and Hall, London, New York (1987).
12. M. RAVID and S. R. BODNER, Dynamic perforation of viscoplastic plates by rigid projectiles. *Int. J. Engng Sci.* **21**, 577–591 (1983).
13. M. RAVID, S. R. BODNER and I. HOLCMAN, Analysis of very high speed impact. *Int. J. Engng Sci.* **25**, 473–482 (1987).
14. M. J. FORRESTAL, K. OKAJIMA and V. K. LUK, Penetration of 6061-T651 aluminum targets with rigid long rods. *J. Appl. Mech.* **55**, 755–760 (1988).
15. R. C. BATRA and T. W. WRIGHT, Steady state penetration of rigid perfectly plastic targets. *Int. J. Engng Sci.* **24**, 41–54 (1986).
16. R. C. BATRA, Steady state penetration of viscoplastic targets. *Int. J. Engng Sci.* **25**, 1131–1141 (1987).
17. R. C. BATRA, Steady state penetration of thermoviscoplastic targets. *Comp. Mech.* **3**, 1–12 (1988).
18. R. C. BATRA and PEI-RONG LIN, Steady state deformations of a rigid perfectly plastic rod striking a rigid cavity. *Int. J. Engng Sci.* **26**, 183–192 (1988).
19. R. C. BATRA and P. R. LIN, Steady state axisymmetric deformations of a thermoviscoplatic rod striking a hemispherical rigid cavity. *Int. J. Impact Engng* **8**, 99–113 (1989).
20. R. C. BATRA and P. R. LIN, Histories of stress, temperature and spin in steady state deformations of a thermoviscoplastic rod striking a hemispherical rigid cavity. *Int. J. Engng. Sci.* **28**, 93–98 (1990).
21. P. R. LIN and R. C. BATRA, Histories of stress, strain-rate, temperature and spin in steady state penetration problems. *Int. J. Engng Sci.* **27**, 1155–1165 (1989).
22. T. GOBINATH and R. C. BATRA, Analysis of a steady state axisymmetric penetration problem, in *Computational Techniques for Contact, Impact, Penetration and Perforation of Solids* (edited by L. E. SCHWER, N. J. SALAMON and W. K. LIU), *ASME, AMD*, Vol. 103, 235–247 (1989).
23. W. D. FARREN and G. I. TAYLOR, The heat developed during plastic extrusion of metal. *Proc. R. Soc. London Ser. A* **107**, 422–429 (1925).
24. J. F. BELL, *Physics of Large Deformation of Crystalline Solids*. Springer-Verlag, New York, Berlin, Heidelberg (1968).
25. U. S. LINDHOLM and G. R. JOHNSON, Strain-rate effects in metals at large strain-rates, in *Material Behavior Under High Stresses and Ultrahigh Loading Rates* (edited by V. WEISS), pp. 61–79. Plenum Press, New York (1983).
26. A. TATE, A theoretical estimate of temperature effects during rod penetration. *9th Ballistic Symposium*, pp. 2.307–2.314 (1987).
27. E. BECKER, G. CAREY and J. T. ODEN, *Finite Elements—An Introduction*. Prentice-Hall, Englewood Cliffs (1982).
28. O. C. ZIENKIEWICZ, *The Finite Element Method*. McGraw-Hill, London (1977).
29. T. J. R. HUGHES, *The Finite Element Method: Linear Static and Dynamic Finite Element Analysis*. Prentice-Hall, Englewood Cliffs, New Jersey (1987).
30. A. N. BROOKS and T. J. R. HUGHES, Streamline upwind Petrov–Galerkin formulations for convection dominated flows with particular emphasis on the incompressible Navier–Stokes equations. *Comput. Methods Appl. Mech. Engng* **32**, 199–259 (1982).
31. D. J. BENSON, An efficient, accurate, simple ALE method for nonlinear finite element programs. *Comput. Methods Appl. Mech. Engng* **72**, 305–350 (1989).
32. G. CAREY and J. T. ODEN, *Finite Elements—Computational Aspects*, Vol. 3. Prentice-Hall, Englewood Cliffs, New Jersey (1981).
33. J. E. THOMPSON, Z. U. A. WARSI and C. W. MASTIN, *Numerical Grid Generation, Foundations and Application*. Elsevier, New York (1985).
34. J. E. THOMPSON, Z. U. A. WARSI and C. W. MASTIN, Boundary-fitted coordinate systems for numerical solution for partial differential equations—A Review. *J. Comput. Phys.* **47**, 1–108 (1982).
35. A. TATE, Long rod penetration models—Part II. Extensions to the hydrodynamic theory of penetration. *Int. J. Mech. Sci.* **28**, 599–612 (1986).
36. R. C. BATRA and XINGJU CHEN, An approximate analysis of steady state axisymmetric deformations of viscoplastic targers. *Int. J. Engng Sci.*, in press.
37. A. TATE, A simple hydrodynamic model for the strain field in a target by the penetration of a high speed long rod projectile. *Int. J. Engng Sci.* **16**, 858 (1978).
38. T. GOBINATH and R. C. BATRA, Steady state penetration of a rigid perfectly plastic rod into a rigid perfectly plastic target, submitted for publication.
39. E. H. LEE, Elastic-plastic deformations at finite strains. *J. Appl. Mech.* **36**, 1 (1969).
40. L. ANAND, Constitutive equations for rate-independent, isotropic, elastic-plastic solids exhibiting pressure-sensitive yielding and plastic dilatancy. *J. Appl. Mech.* **47**, 439 (1980).
41. S. NEMAT-NASSER, Micromechanically based finite plasticity. *Proc. Symp. Plasticity Today* (edited by A. SAWCZUK). Elsevier, London (1983).
42. Y. F. DAFALIAS, A simple illustration of the plastic spin concept and its role in finite plastic transformation. Proc. Current Theories of Plasticity and Their Applications, University of Oklahoma-Norman (1984).

Int. J. Engng Sci Vol. 29, No. 10, pp. 1315–1331, 1991
Printed in Great Britain.

0020-7225/91 $3.00 + 0.00

A STEADY STATE AXISYMMETRIC PENETRATION PROBLEM FOR RIGID/PERFECTLY PLASTIC MATERIALS

T. GOBINATH† and R. C. BATRA

Department of Mechanical and Aerospace Engineering and Engineering Mechanics, University of Missouri–Rolla, Rolla, MO 65401-0249, U.S.A.

Abstract—The axisymmetric deformations of an eroding long cylindrical rod made of a rigid/perfectly plastic material penetrating at a uniform rate into a thick rigid/perfectly plastic target are studied by the finite element method. It is assumed that the deformations appear steady to an observer situated at the stagnation point and moving with it, and that the contact between the target and the penetrator at the common interface is smooth. It is found that the resisting force experienced by the penetrator, the shape of the target/penetrator interface, and the distribution of normal tractions on it depend rather strongly upon the square of the penetration speed and also upon the ratio of the mass density of the penetrator to that of the target. In an attempt to help establish desirable testing regimes for practical problems we have also computed time histories of the hydrostatic pressure, second invariant of the strain-rate tensor and the spin for four typical penetrator and two typical target particles.

INTRODUCTION

We study that phase of the penetration process in which the penetrator and target deformations appear steady to an observer located at the stagnation point and moving with it. This situation occurs when a very long cylindrical rod strikes a rather huge target and has penetrated a few rod diameters into it. Until the time either most of the rod has been eroded or the stagnation point reaches near the other end of the target, the penetration process can be regarded as being nearly steady and may constitute a significant part of the total penetration process. For moderately high striking speeds, Tate [1, 2] and Alekseevskii [3] modified the purely hydrodynamic approach by including the effects of the material strengths of the projectile and the target and representing them as some multiple of the yield strengths of the corresponding materials. However, the multiplying factor was unresolved in the theories. Hidsley [4] recently computed the values of the strength parameters for a copper rod penetrating into an aluminum target to be 2.4 (σ_H), and $(-0.7)(\sigma_{t.})_p$ for the target and the penetrator, respectively. Here σ_H equals the Hugoniot elastic limit of the material. He justified the negative value for the rod strength because of its yield stress being lower than that of the target.

The review paper of Backman and Goldsmith [5] provides a comprehensive summary of the work done on ballistic penetration until 1977, and discusses various physical mechanisms involved in the penetration and perforation processes and their engineering models. Also during the last decade engineering models of target penetration have been proposed by Ravid and Bodner [6], Ravid *et al.* [7], and Forrestal [8]. Some of the books on the subject are by Zukas *et al.* [9], Blazynski [10], Billington and Tate [11], and MaCauley [12].

In previous studies [13–19] Batra and his coworkers have analyzed the steady state penetration problem in which either the penetrator or the target was considered as rigid. Here we study the case when both deform and their materials can be modeled as rigid/perfectly plastic. As in [13–19], the contact between the penetrator and the target at the common interface is assumed to be smooth and no fracture or failure criterion is included. However, the effect of the penetration speed and the ratio of the mass densities of the penetrator and target on their deformations is investigated. We add that the problem studied herein is more challenging than those studied earlier in [13–19] because of the presence in it of two *a priori* unknown free surfaces, one the target/penetrator interface and the other the free surface of the penetrator material flowing backwards. Also the convective part of the acceleration plays a dominant role which requires the use of either an appropriately graded mesh or the use of

†Present address: EGS ADEPT, 25900 Greenfield, Oakpark, MI 48237, U.S.A.

artificial viscosity or both. The kinematic and stress fields found herein should help select improved kinematic fields in other approximate theories of penetration mechanics and also check results from simpler engineering theories of penetration.

An other outstanding problem in penetration mechanics is the selection of the appropriate constitutive models for the penetrator and target materials. In order to assess which one of the many recently proposed theories [20–23] of large deformation elastoplasticity is appropriate, and also help establish desirable testing regimes for practical problems, we compute histories of the second-invariant of the strain-rate tensor and the plastic spin for four penetrator and two target particles.

FORMULATION OF THE PROBLEM

We use the Eulerian description of motion and a cylindrical coordinate system with origin at the stagnation point and moving with it at a uniform speed v_s to describe the deformations of the penetrator and the target. The positive z-axis is taken to point towards the undeformed portion of the rod. Also we work in terms of non-dimensional variables indicated below by a superimposed bar.

$$\bar{\sigma} = \sigma/\rho v_s^2, \quad \bar{p} = p/\rho v_s^2, \quad \alpha = \rho v_s^2/\sigma_0,$$
$$\bar{\mathbf{v}} = \mathbf{v}/v_s, \quad \bar{r} = r/r_0, \quad \bar{z} = z/r_0. \tag{1}$$

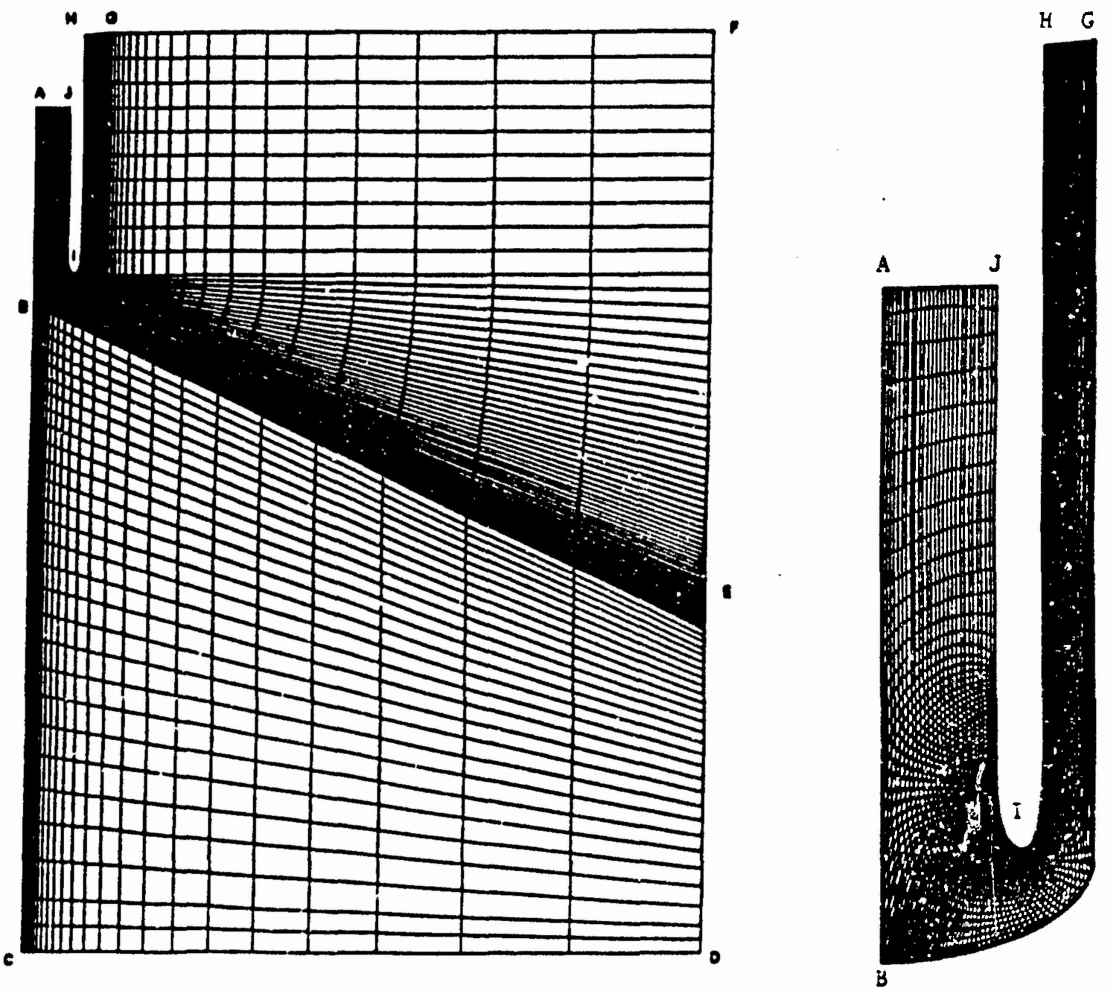

Fig. 1. The finite region studied and its discretization.

Here and below, σ is the Cauchy stress tensor, ρ the hydrostatic pressure not determined by the deformation history because the deformations are assumed to be isochoric, $\mathbf{v} = (v_r, v_z)$ is the velocity of a material particle, and r_0 is the radius of the undeformed cylindrical portion of the penetrator. The non-dimensional parameter α equals the magnitude of the inertia forces relative to the flow stress of the material. When non-dimensionalizing a quantity for the penetrator and the target, the value of the corresponding material parameter is used in equation (1). An advantage of the non-dimensionalization (1) is that the equations governing the deformations of the penetrator and target look alike. Hereafter we use only non-dimensional variables and drop the superimposed bars. The governing equations can be written as

$$\operatorname{div} \mathbf{v} = 0, \tag{2.1}$$

$$\operatorname{div} \boldsymbol{\sigma} = (\mathbf{v} \cdot \operatorname{grad})\mathbf{v}, \tag{2.2}$$

$$\boldsymbol{\sigma} = -p\mathbf{1} + \frac{1}{\alpha\sqrt{3}} I\mathbf{D}, \tag{2.3}$$

$$2\mathbf{D} = \operatorname{grad} \mathbf{v} + (\operatorname{grad} \mathbf{v})^T, \tag{2.4}$$

$$2I^2 = \operatorname{tr}(\mathbf{D}^2). \tag{2.5}$$

Equation (2.1) expresses the balance of mass, (2.2) the balance of linear momentum, and equation (2.3) is the constitutive relation for the penetrator and target materials. Recall that the value of α will be different for them. $\mathbf{D}$, given by equation (2.4), is the strain-rate tensor and its second invariant is denoted by I. Equations (2.1) and the one obtained by substituting (2.3) into (2.2) are the field equations to be solved for p and $\mathbf{v}$ under the appropriate boundary conditions.

A numerical solution of the problem usually necessitates that we consider only a finite region which for the Eulerian description of motion is also referred to as the control volume. The finite regions for the penetrator and target studied are depicted in Fig. 1, which also shows its finite element discretization. In the dark regions, a very fine finite element mesh is used. For the boundary conditions, we take

$$\mathbf{t} \cdot (\boldsymbol{\sigma}\mathbf{n}) = 0 \quad \text{on } \Gamma_i, \tag{3.1}$$

$$\mathbf{n} \cdot \boldsymbol{\sigma}_t \mathbf{n} = (\rho_p/\rho_t)\mathbf{n} \cdot \boldsymbol{\sigma}_p \mathbf{n} \quad \text{on } \Gamma_i, \tag{3.2}$$

$$\mathbf{v} \cdot \mathbf{n} = 0 \quad \text{on } \Gamma_i, \tag{3.3}$$

$$\boldsymbol{\sigma}\mathbf{n} = \mathbf{0} \quad \text{on } \Gamma_f, \tag{3.4}$$

$$\mathbf{v} \cdot \mathbf{n} = 0 \quad \text{on } \Gamma_f, \tag{3.5}$$

$$\sigma_{rz} = 0, \quad v_r = 0 \quad \text{on the axis of symmetry } ABC, \tag{3.6}$$

$$v_z = 1, \quad v_r = 0 \quad \text{on the boundary surfaces } CD \text{ and } DEF, \tag{3.7}$$

$$\sigma_{zz} = 0, \quad v_r = 0 \quad \text{on } FG, \tag{3.8}$$

$$v_z = v_e, \quad \sigma_{rz} = 0 \quad \text{on the outlet surface } GH, \tag{3.9}$$

$$v_z = -(v_p - 1), \quad v_r = 0 \quad \text{on the inlet surface } AJ. \tag{3.10}$$

Here Γ_i is the target/penetrator interface BG, and Γ_f is the free surface JIH of the deformed penetrator. The condition (3.1) expresses the assumption that the contact between the penetrator and target is frictionless, therefore, the tangential tractions there vanish. This seems reasonable since a thin layer of the material at the interface either melts or is severely degraded by adiabatic shear. The boundary condition (3.2) states that the normal tractions across the common interface Γ_i are continuous, and equation (3.3) implies that Γ_i is a streamline. If Γ_i were known, then either (3.2) or (3.3) is required. Here we use (3.2) to verify that the assumed shape of Γ_i is reasonably correct as discussed in the next section. The boundary condition (3.4) asserts that Γ_f is a free surface, and equation (3.5) implies that it is a streamline. Equation (3.5)

is used to ensure that the assumed shape of Γ_f is close to the actual one. The boundary condition (3.6) follows from the assumption that the deformations are axisymmetric. Since the distances of CD and DF from Γ_i exceed 30 r_0, and significant target deformations occur in the target region distance at most $2r_0$ from Γ_i, it is reasonable to assume that target particles on the bounding surfaces CD and DF do not deform. If the surfaces FG and GH were situated at infinite distances from the stagnation point B, then the boundary conditions (3.8) and (3.9) on them will hold exactly. Since these surfaces are situated at a distance of nearly $7r_0$ from B, the boundary conditions (3.8) and (3.9) are good approximations. The value of v_e in equation (3.9) is estimated by using the balance of mass for the penetrator region. The boundary condition (3.10) states that the end AJ of the rod has not deformed and is moving downward with a uniform speed. For an assigned value of v_s, v_p is estimated from the relation [1]

$$\frac{1}{2}(v_p - 1)^2 + Y_p = \left(R_t + \frac{1}{2}\right)\left(\frac{\rho_t}{\rho_p}\right) \tag{4}$$

where Y_p and R_t represent strength parameters for the penetrator and target materials. In his 1967 paper Tate [1] found $R_t = 3.5(\sigma_H)_t$ and in a recent paper [24] he gave $Y_p = 1.7\sigma_{0p}$, $R_t = \sigma_{0t}(2/3 + \ln(0.57E_t/\sigma_{0t}))$, where E_t is Young's modulus for the target material. Batra and Chen [25] used a semianalytical method to analyze the steady state axisymmetric deformations of a viscoplastic target being penetrated by a rigid hemispherical nosed penetrator and found that

$$R_t = 9.43\sigma_{0t}.$$

In terms of dimensional variables, we need to know $(R_t - Y_p)$ rather than the values of R_t and Y_p to find v_p from equation (4).

COMPUTATIONAL CONSIDERATIONS

The aforestated problem was solved by the following iterative technique. Assume Γ_i and Γ_f. Then the regions R_p (shown in Fig. 1 by the closed curve ABGHIJA) and R_t (shwn in Fig. 1 by the closed curve BCDEFGB) occupied, respectively, by the deformating penetrator and target material are well defined. The governing equations (2) under the boundary conditions (3.1), (3.3), (3.4), (3.6), (3.9), and (3.10) are solved to find the fields of $(\mathbf{v}, p)$ for the penetrator, and equations (2) under the boundary conditions (3.1), (3.3), (3.6), (3.7), and (3.8) are solved to find the fields of $(\mathbf{v}, p)$ for the target. The boundary conditions (3.2) and (3.5) are used to verify that the assumed Γ_i and Γ_f are reasonably correct. We first adjust Γ_f, and then Γ_i always ensuring that Γ_f is still correct and, if necessary, Γ_f is readjusted. During the modification of Γ_i, nodes on it are moved in a direction perpendicular to Γ_i by an amount proportional to $(f_p^n - f_t^n)$. Here f_p^n and f_t^n equal, respectively, the normal force on a penetrator and target particle on Γ_i.

The algorithm developed by Batra and Lin [16] to adjust Γ_f was modified to increase its efficiency and has been described by Gobinath and Batra [26]. After new shapes of Γ_i and Γ_f have been determined, a check is made to ensure that the elements adjoining these surfaces have not been severely distorted. If necessary, a new mesh is generated by solving on R_p and R_t the Laplace equation $\nabla^2\phi = 0$ under the essential boundary conditions $\phi = r$ and $\phi = z$. The intersection of the equipotential curves gives the new location of the nodes.

We used 9-noded quadrilateral macroelements each of which was divided into four 4-noded quadrilateral elements called microelements. In each micro-element the velocity field was assumed to be bilinear and pressure constant. The variables corresponding to the central node were eliminated prior to the assembly of the global stiffness matrix. An artificial viscosity ν given by [27]

$$\nu = \nu_r + \nu_z, \tag{5.1}$$

$$\nu_r = h_r(\coth \nu_1 - 1/\nu_1)/2, \tag{5.2}$$

$$\nu_z = h_z(\coth \nu_2 - 1/\nu_2)/2, \tag{5.3}$$

$$\nu_1 = \sqrt{3}\, v_r^c h_r I^c/\alpha, \qquad \nu_2 = \sqrt{3}\, v_z^c h_z I^c/\alpha, \tag{5.4}$$

was added to $\alpha/\sqrt{3}\,I$ in equation (2.3). In these equations h_r and h_z equal, respectively, the largest distances in the r and z directions between the midpoints of the sides of a quadrilateral, and the superscript c denotes that the quantity is evaluated at the centroid of an element. Brooks and Hughes [27] have shown that adding artificial viscosity is equivalent to using the Petrov–Galerkin approximation of equations (2.2)–(2.5).

DISCUSSION OF RESULTS

Recalling that the governing equations for the velocity field are nonlinear, the solution was assumed to have converged when, at each nodal point, the value of the speed computed during two successive iterations differed by no more than 5%. The convergence criterion used for the free surface Γ_f was that at each node point on Γ_f, $|\mathbf{v}\cdot n| \le 0.02$, and that for Γ_i

$$|f_p^n - f_{i1}^n| \le 0.025[|f_p^n| + |f_{i1}^n|], \tag{6}$$

at each node point on it. These convergence criteria are stronger than the global norms of errors sometimes employed.

Results for different speeds of penetration

We set

$$\rho_p = \rho_t = 7800\ \text{kg/m}^3, \qquad \sigma_{typ} = 350\ \text{MPa}, \qquad \sigma_{ytr} = 114.3\ \text{MPa}, \tag{7}$$

and compute results for $v_s = 400$ m/s, 500 m/s and 600 m/s. The corresponding values of (α_p, α_t) are (3.57, 10.92), (5.57, 17.06), and (8.02, 24.57), respectively. Values of v_p, as computed from equation (4), with $R_t - Y_p = 164.35$ MPa, equal 850 m/s, 1041 m/s and 1234 m/s for the three values of v_s considered herein. Since $\alpha_t \approx 3\alpha_p$, the inertia forces play a more dominant role for the target deformations as compared to that for the deformations of the penetrator. Figure 2 depicts the shapes of the free surface Γ_f and the target/penetrator interface Γ_i for these three values of v_s. In these plots the ordinate is the vertical distance from the bottom-most surface CD of the target region studied in order to decipher the vertical movement of Γ_i and Γ_f. When plotting Γ_f, the horizontal scale has been enlarged enormously to magnify the small differences in the shapes of the free surface for the three values of v_s. The

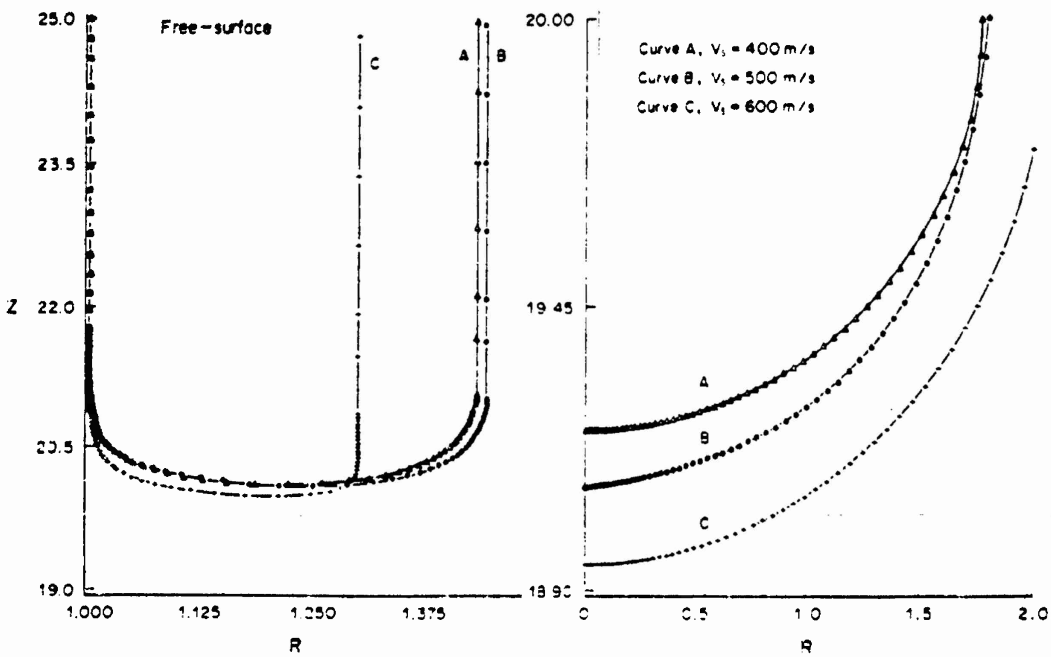

Fig. 2. Shapes of the free surface of the deformed penetrator and the target/penetrator interface for three different speeds.

shapes of Γ_i in the vicinity of the stagnation point seem to be independent of v_s. A least squares fit to the curve for $v_s = 600$ m/s has the equation

$$\frac{r^2}{2.061^2} + \frac{(z-1.05)^2}{1.05^2} = 1. \tag{8}$$

It is interesting to note that Tate [28] found the equation of the bottom surface of Γ_i to be

$$\frac{r^2}{(1.155a)^2} + \frac{(z-a)^2}{a^2} = 1.$$

A possible reason for the difference in the value of the coefficient for the first term is the lower value of v_s considered here.

The mean normal tractions at the common interface Γ_i for the three values of v_s are plotted in Fig. 3. Also shown in the figure is a least squares fit to the data points (F_a, α_i) where F_a is the non-dimensional axial resisting force experienced by the penetrator; the corresponding dimensional force equals $(\pi r_0^2 \sigma_{0p}) F_a$. It was found that the quadratic curve

$$F_a = 5.323 + 1.101\alpha_i + 0.031\alpha_i^2, \quad 10.92 \le \alpha_i \le 24.57, \tag{9}$$

provided a better fit to the computed data than a straight line. Batra and Lin [16] who studied the deformations of a rigid/perfectly plastic cylindrical rod upset at the bottom of a rigid cavity $z = 0.04r^4$ found $F_a = -2.2 + 2.15\alpha_p$, $1.8 \le \alpha_p \le 6$. In each of these cases, the values of F_a depend rather noticeably upon α_i and/or α_p. The normal tractions on Γ_i increase significantly with an increase in v_s. The general shapes of these curves especially near the stagnation point do not vary, and they are shifted upwards with an increase in v_s. For values of the non-dimensional arc length exceeding 2, the normal tractions on Γ_i become exceedingly small. At the stagnation point, the normal traction on Γ_i equals $(-\sigma_{zz})$, and since uniaxial strain conditions prevail on the axial line, $s_{zz} = (\sigma_{zz} + p)$ equals $(2/3\sigma_0)$ there. For penetrator and target particles on the axial line and situated within $2r_0$ of the stagnation point, computed values of $|s_{zz} - 2\sigma_0/3|$ were less than 0.02. Since $\sigma_{zz} \gg \sigma_0$ at the stagnation point, the hydrostatic pressure p_0 there provides a predominant contribution to σ_{zz}. The least squares fit

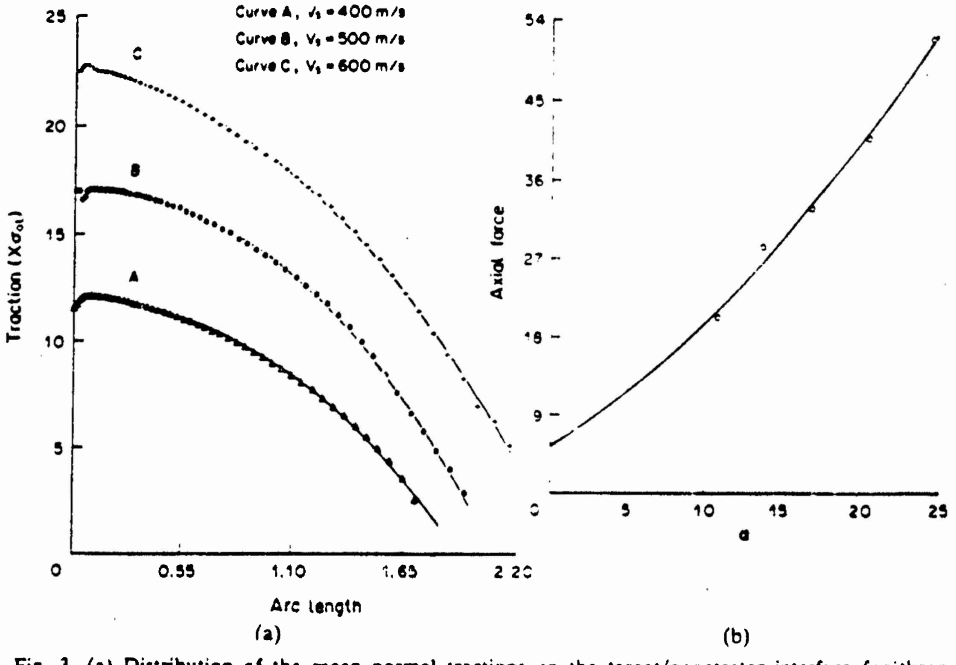

Fig. 3. (a) Distribution of the mean normal tractions on the target/penetrator interface for three different speeds. (b) Dependence of the axial resisting force experienced by the penetrator upon the non-dimensional number α_i.

to the data points (p_{0p}, α_p), (p_{0t}, σ_t), have the equations

$$p_{0p} = (0.1084 + 0.884\alpha_p)\sigma_{0p}, \tag{10.1}$$

$$p_{0t} = (4.005 + 0.683\alpha_t)\sigma_{0t}, \tag{10.2}$$

for the penetrator and the target respectively.

Recalling that equations,

$$\frac{1}{2}\rho_p(v_p - v_s)^2 + Y_p = \frac{1}{2}\rho_t v_s^2 + R_t = -(\sigma_{zz})_s, \tag{11}$$

proposed by Alekseevskii [3] and Tate [1], where Y_p and R_t equal the resistive pressure terms due to the strength of the material, $(\sigma_{zz})_s$ is the value of σ_{zz} at the stagnation point B, and quantities are dimensional, hold on the axial line we can find the values of R_t and Y_p. The computed values of R_t and Y_p for the three penetration speeds studied are listed in Table 1.

Table 1

v_s (m/s)	R_t $(x\sigma_{0t})$	Y_p $(x\sigma_{0p})$
400	6.19	1.553
500	8.46	2.293
600	10.29	2.89

We should caution the reader that equations (10.1) and (10.2) were obtained by a least squares fit to the data. Substitution from (10.1) and (10.2) into (11) and setting $(s_{zz})_s = 2/3\sigma_{0p}$ or $2/3\sigma_{0t}$ may yield values of Y_p and R_t that are slightly different from those listed in the table.

Results for different ratios of mass densities

In Fig. 4(a) are plotted the shapes of the free surface of the deformed penetrator and of the target/penetrator interface for $\rho_t/\rho_p = 1.25$, 1.0 and 0.75. The ordinate is the vertical distance from the bottom surface CD of the target region considered. In these computations ρ_p was kept fixed and v_s was set equal to 500 m/s. For $\rho_t/\rho_p = 0.75$, the bottom portion of the free surface is slightly above that for $\rho_t/\rho_p = 1.0$, and for $\rho_t/\rho_p = 1.25$, the bottom part of the free surface moves a little below that for $\rho_t/\rho_p = 1.0$. The curvature of the free surface where the flow turns upwards also seems to depend on ρ_t/ρ_p. The stagnation point does not move much when ρ_t/ρ_p is changed from 1.00 to 0.75 implying thereby that the thickness of the deforming penetrator material between the target/penetrator interface and the free surface of the deformed penetrator, especially near the axial line, is larger for $\rho_t/\rho_p = 0.75$ as compared to that for $\rho_t/\rho_p = 1.0$. When ρ_t/ρ_p is changed from 1.0 to 1.25, both the stagnation point and the bottom part of the free surface Γ_f move lower and since the former moves by a larger distance, the thickness of the deforming penetrator material between Γ_t and Γ_f increases again. The normal tractions on Γ_t, plotted in Fig. 4(b), reveal that the largest normal tractions occur for $\rho_t/\rho_p = 1.25$ and least for $\rho_t/\rho_p = 0.75$ and the change seems to depend continuously upon ρ_t/ρ_p. Thus, for the same penetrator material, the pressure at the stagnation point will increase with an increase in the mass density of the target; and for a given target, higher density penetrators would result in smaller values of the pressure at the stagnation point.

Values of R_t and Y_p, computed by using equation (11) and $v_s = 600$ m/s, for different values of ρ_t/ρ_p are listed in Table 2.

We note that Pidsley [4] found for $\rho_t/\rho_p = 0.313$, $R_t = 2.4(\sigma_H)t$ and $Y_p = -0.7(\sigma_H)p$. For many materials the Hugoniot elastic limit equals approximately 1.6 times the yield strength in a quasistatic simple compression test [1].

Results for a fixed value of v_s

The contours of the non-dimensional hydrostatic pressure for $v_s = 600$ m/s are shown in Fig. 5. These values ought to be multipled by 8.02 and 24.57 for the penetrator and target to obtain

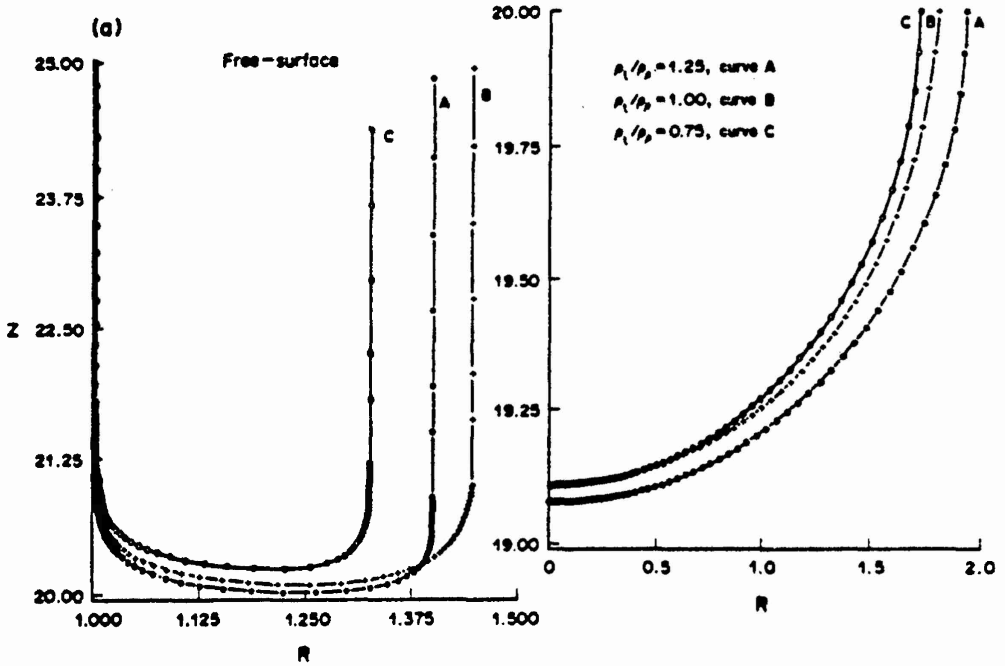

Fig. 4(a). Shapes of the free surfaces of the deformed penetrator and the target/penetrator interface for three different values of ρ_i/ρ_p.

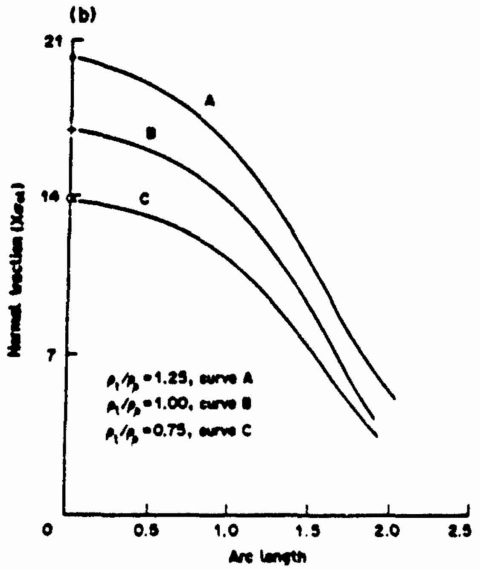

Fig. 4(b). Distribution of mean normal tractions on the target/penetrator interface for three different values of ρ_i/ρ_p. Curve A, $\rho_i/\rho_p = 1.25$; Curve B, $\rho_i/\rho_p = 1.0$; Curve C, $\rho_i/\rho_p = 0.75$.

Table 2

(ρ_i/ρ_p)	R_i $(x\sigma_{0i})$	Y_p $(x\sigma_{0p})$
0.75	7.448	1.963
1.0	8.46	2.293
1.25	9.49	2.63

values of p as a multiple of corresponding σ_0. Thus p_{max} equals $7.3\sigma_{0p}$ in the penetrator and $20.8\sigma_{0t}$ in the target for $\alpha_p = 8.02$ and $\alpha_t = 24.57$. We note that for the hemispherical nosed rigid penetrator and a rigid/perfectly plastic target Batra and Wright [13] computed p_{max} to be $8.0\sigma_{0t}$ for $\alpha_t = 6.15$ and Batra and Lin [19] found $p_{max} = 3\sigma_{0p}$ for $\alpha_p = 5.1$ for a rigid/perfectly plastic cylindrical rod striking a rigid cavity. The variation of the hydrostatic pressure on the axial line, also depicted in Fig. 5, reveals that the pressure decays quickly in the penetrator and rather slowly in the target as we move away from the stagnation point. The distributions of I in the deforming penetrator and target regions are shown in Fig. 6. Also plotted in this figure is the variation of I on the axial line. These plots reveal that significant deformations of the penetrator occur within the hemispherical region of radius nearly 2.0 and centered at the stagnation point. The values of I near the stagnation point are quite high in the penetrator and target regions. As for the values of p, the value of I on the axial line also drops quickly in the penetrator and slowly in the target as we move away from the stagnation point.

In order to see whether or not sharp gradients of I occur across the target/penetrator interface Γ_i, we have plotted in Fig. 7 the variation of I along three arbitrarily selected lines LM, PQ and PS. The abscissa in these figures is the distance from Γ_i of a point along the line

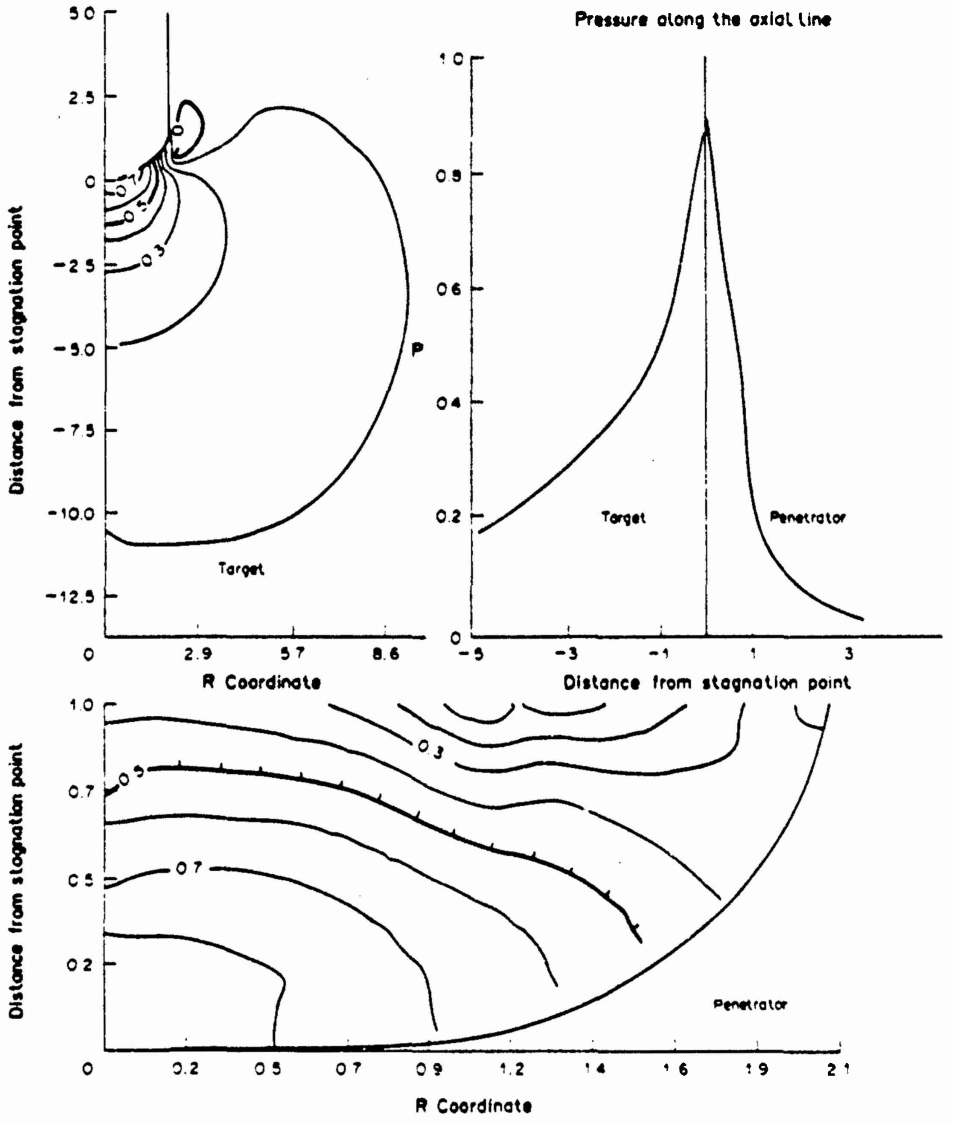

Fig. 5. Contours of non-dimensional hydrostatic pressure for $v_i = 600$ m/s.

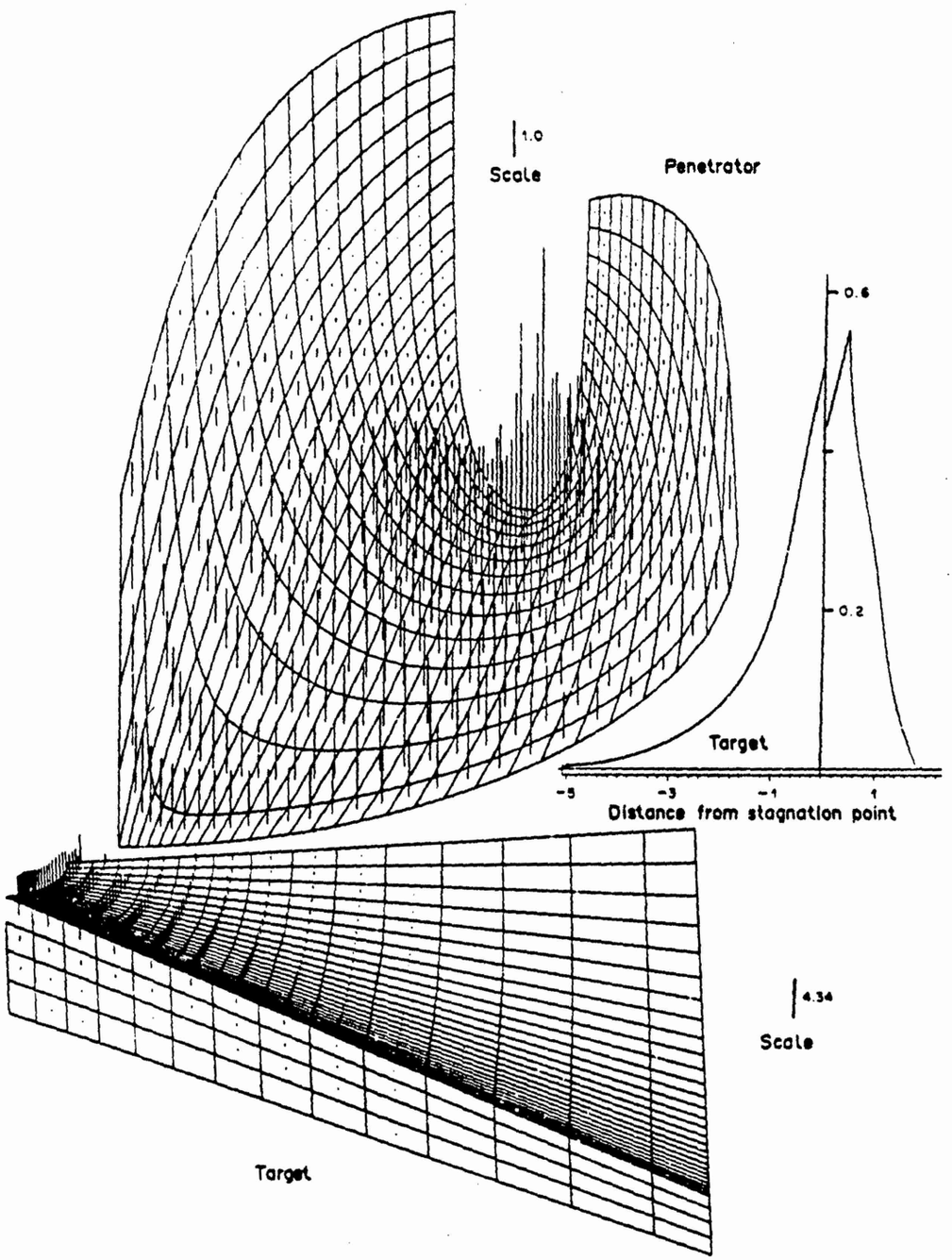

Fig. 6. Distribution of the second-invariant of the strain-rate tensor in the deforming penetrator and target regions and also on the axial line for $v_s = 600$ m/s.

considered. In each case I is discontinuous across Γ_t. On line LM, I for the target particle abutting Γ_t is higher than that for the corresponding penetrator particle but the opposite holds for points on lines PQ and PS. For points on PQ and PS, sharp gradients of I develop in the penetrator region whereas for points on LM, I varies sharply for points on the target side. The value of I at point P where the penetrator particles undergo a change in the flow direction is considerably higher than that for the penetrator particles on line PQ and PS. Since the

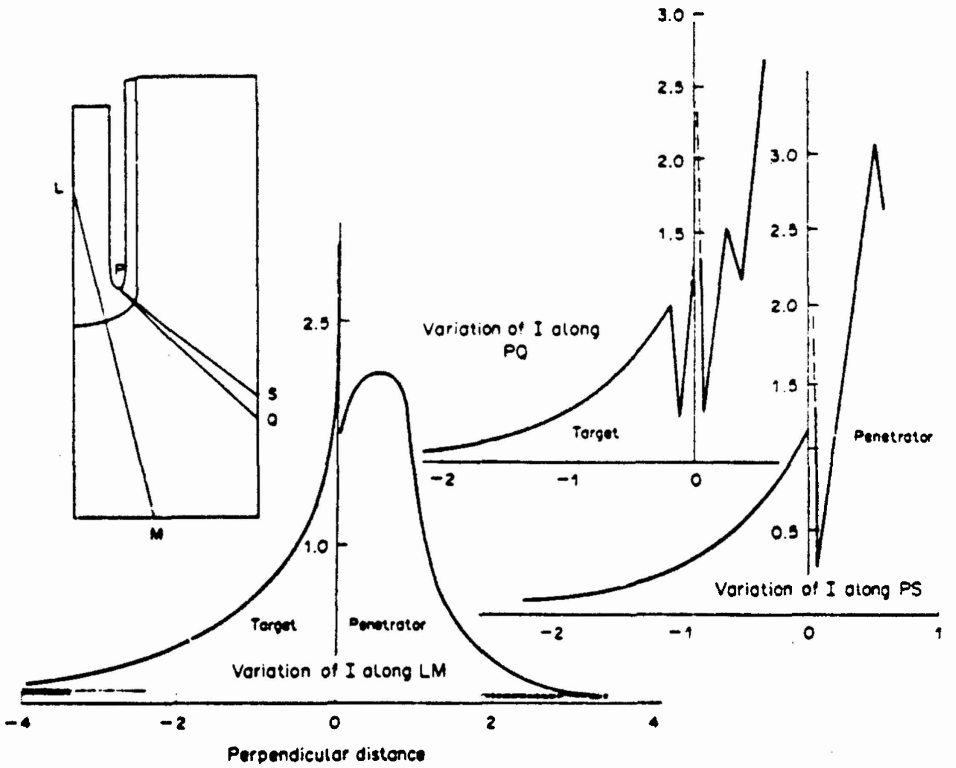

Fig. 7. Variation of the second invariant of the strain-rate tensor on three arbitrary selected lines for $v_s = 500$ m/s.

tangential velocity of target and penetrator particles abutting Γ_i are nearly the same, for normal tractions to be continuous across Γ_i, normal derivatives of $\mathbf{v}$ on Γ_i must be discontinuous if target and penetrator particles are made of different materials. This provides a justification for the jump in the value of I as one crosses Γ_i. Recalling that the hydrostatic pressure contributes significantly to the normal tractions, it is not necessary that I be sharply discontinuous across Γ_i for the normal tractions on the two sides of Γ_i to match with each other.

Histories of field variables

An outstanding problem in mechanics is the choice of the most appropriate constitutive model for the problem at hand. In general, the solution of a boundary-value problem depends strongly upon the constitutive model used. In order to determine which one of the many recently proposed theories [20–23] of large deformation elastoplasticity is suitable for a penetration problem, we compute histories of the hydrostatic pressure, second invariant of the strain-rate tensor and the spin for four penetrator and two target particles. These results should also help identify desirable testing regimes for practical problems.

The first step in finding the histories of a field variable is to plot the streamlines. Streamlines for four penetrator particles that once occupied the places $A(0.10, 5.88)$, $B(0.15, 5.88)$, $C(0.90, 5.88)$ and $D(0.95, 5.88)$, and two target particles sometime situated at $E(0.10, -3.12)$ and $F(0.15, -3.12)$ are shown in Fig. 8. That the streamlines do not intersect or merge together is clear from the blow up of the region enclosed in the box. In the discussion below we refer to the material particle that once occupied the place A as the material particle A.

Histories of field variables for penetrator particles. Figure 9 shows, for $v_s = 500$ m/s, (r, z) coordinates of the four penetrator particles at different non-dimensional times; the time being reckoned from the instant these particles occupied the aforestated places, and the non-dimensional time equals the physical time multiplied by (v_s/r_0). The variation of the radial and axial components of the velocity of these particles is plotted in Fig. 10. Particles A and B, initially near the axial line, arrive in the vicinity of the stagnation point at time $t = 5$ when their

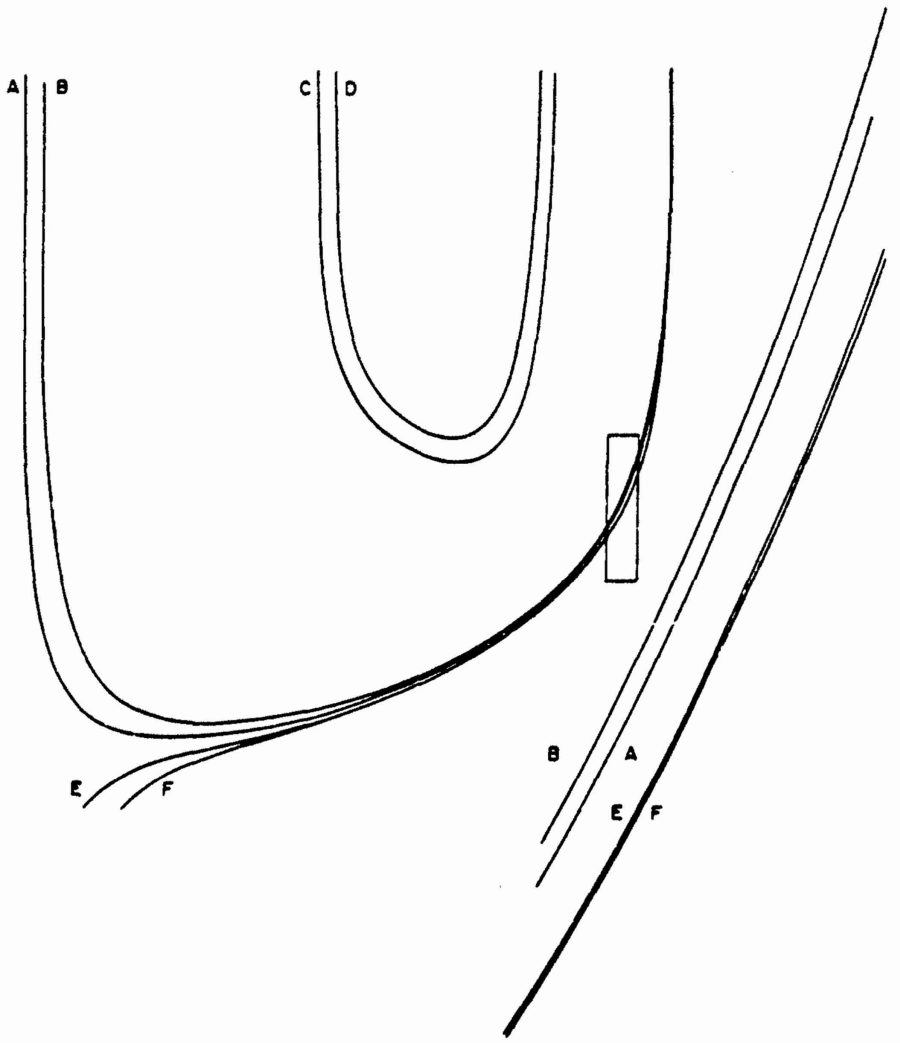

Fig. 8. Streamlines for four penetrator and two target particles for $v_s = 500$ m/s.

axial velocity relative to that of the stagnation point becomes zero. The radial velocity of these particles gradually increases, becomes maximum just before they begin turning upwards at $t \simeq 6.5$ and then decreases to zero quite rapidly. Material particles C and D that were initially close to the free surface of the penetrator approach near their bottom-most positions at $t \simeq 2.6$. Their radial velocity stays zero till they are close to their lowest positions, increases sharply and then decreases to zero equally rapidly too. In Fig. 11, we have plotted histories of the second invariant I of the strain-rate tensor and of the plastic spin. Because the deformations are axisymmetric, there is only one non-zero component of total spin which equals the plastic spin since elastic deformations have been neglected. The peak values of I and the plastic spin for material particles C and D are very large as compared to those for material particles A and B. For particles C and D, the magnitude of the plastic spin is either comparable or slightly larger than the value of I, and the peak values of I and the plastic spin occur at almost the same instant. For these particles, I and the plastic spin increase or decrease in tandem. Peak values of I at particles A and B occur after their axial component of velocity has changed sign, i.e. they are moving upwards as observed from the stagnation point. Whereas I for these particles increases quite rapidly and stays large for an extended period of time, the magnitude of the plastic spin for them increases slowly at first and once these particles are close to the stagnation point, the spin increases rapidly, and subsequently drops to zero at even a faster rate. The histories of the non-dimensional hydrostatic pressure shown in Fig. 12 reveal that for material

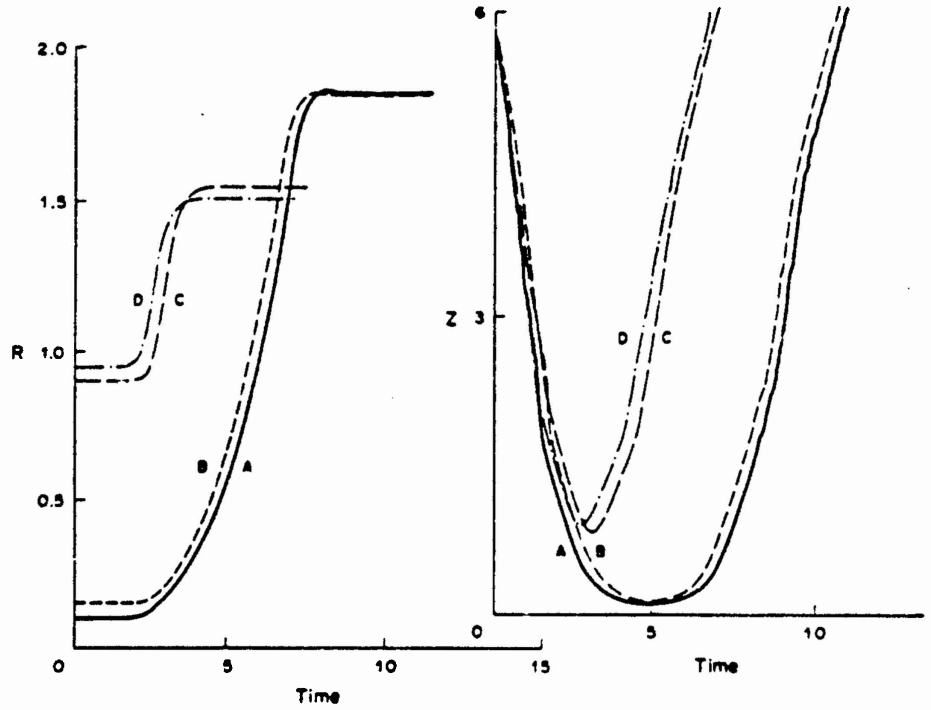

Fig. 9. r and z-coordinates at different times of the four penetrator particles.

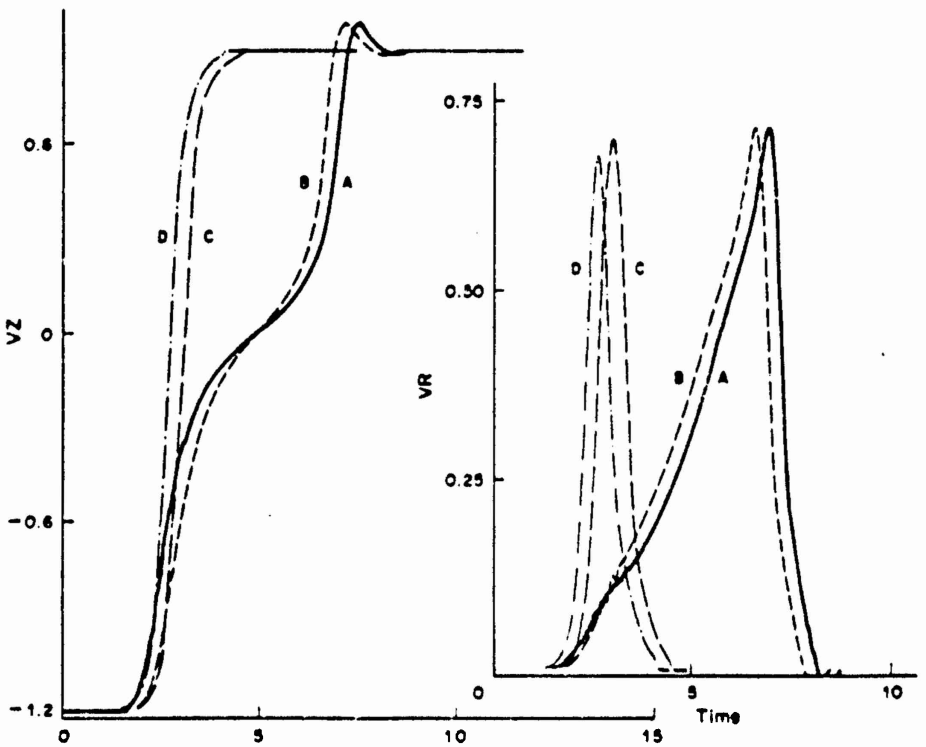

Fig. 10. The variation with time of the axial and radial velocity of the four penetrator particles.

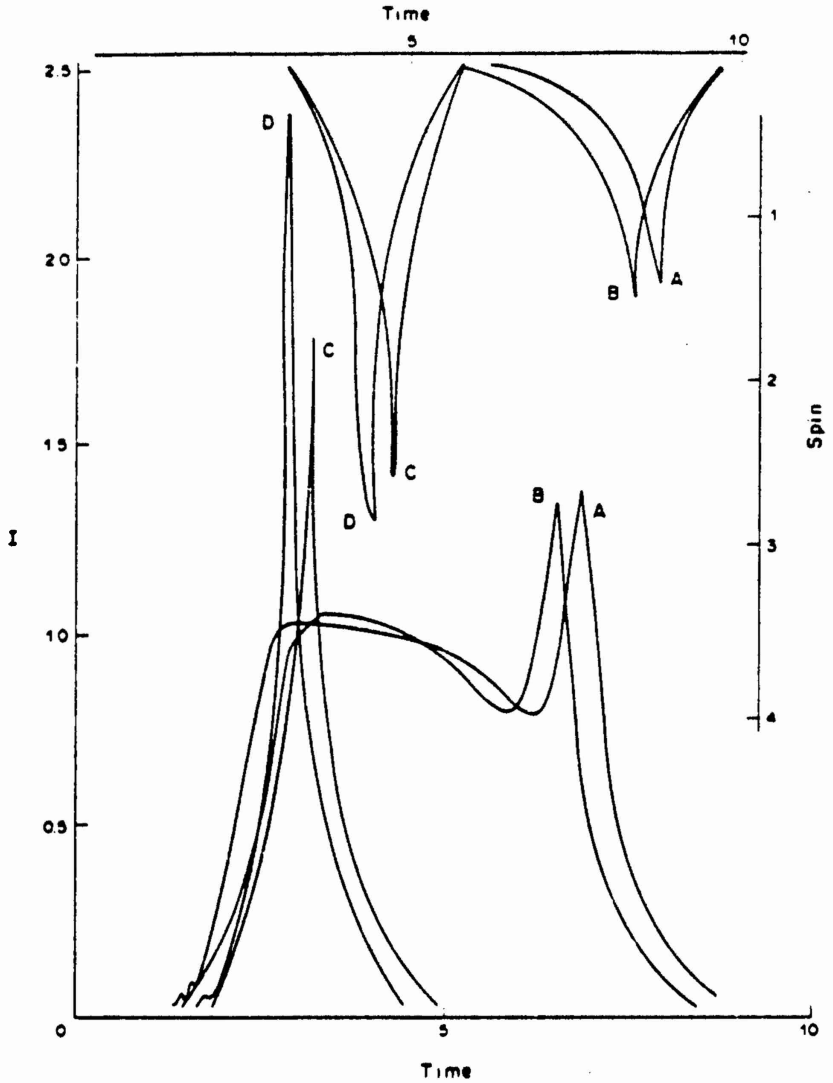

Fig. 11. Histories of the second invariant of the strain-rate tensor and the plastic spin for the four penetrator particles.

particles A and B, p_{max} is very large as compared to that for particles C and D. This is because particles C and D are close to the traction free surface of the penetrator.

Histories of field variables for target particles. Figure 13 depicts the r- and z-coordinates and the radial and axial components of the velocity of the two target particles E and F at different times. As these particles approach the stagnation point $z = 0$ at $t \simeq 7$, their radial velocity begins to increase sharply, becomes maximum at $t = 7.5$ and 6.5, respectively, for E and F, then rapidly decreases to zero. Their axial velocity relative to that of the stagnation point exhibits the reverse trend, i.e. it decreases to zero at $t \simeq 4.5$ and then increases gradually, the rates of decrease and increase of the axial velocity are nearly the same. The histories of the second invariant of the strain-rate tensor and the plastic spin for these two particles are exhibited in Fig. 14. Even though the values of I for these particles gradually increase till $t \simeq 5$, their plastic spin stays zero. At about $t \simeq 5$, both the values of I and of the plastic spin increase rapidly. The peak values of the plastic spin for these particles equal nearly twice the peak values of I for them. The plastic spin decreases to zero much faster than I. The history of the non-dimensional hydrostatic pressure for these particles is shown in Fig. 12. Peak values, equal to $14.2\sigma_{0Y}$, of the hydrostatic pressure at these particles occur when they are close to the stagnation point. Once

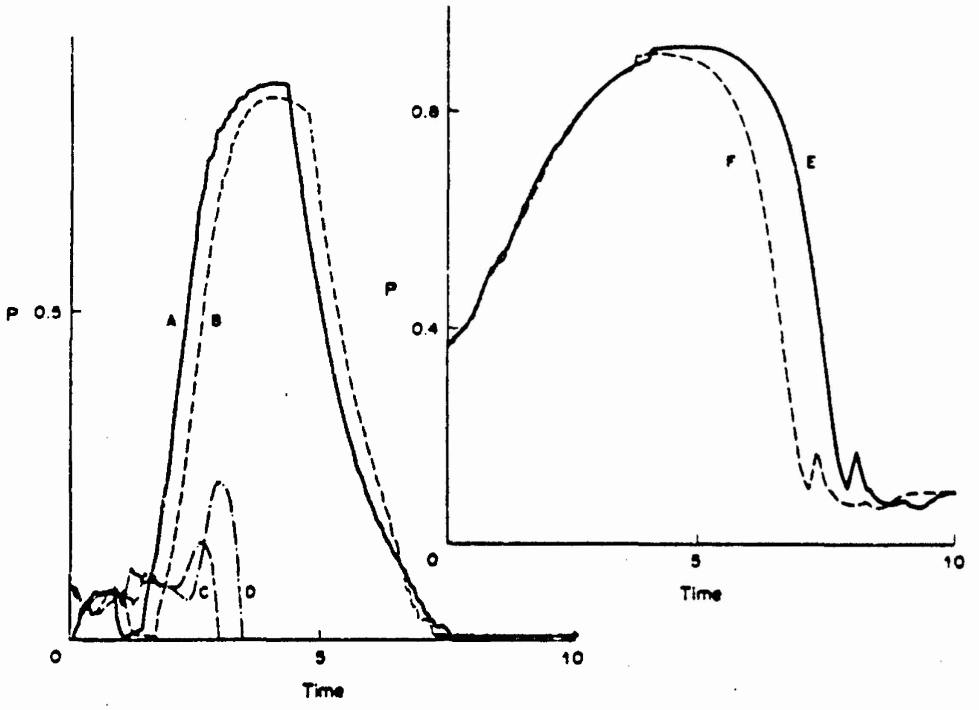

Fig. 12. Histories of the hydrostatic pressure for four penetrator and two target particles.

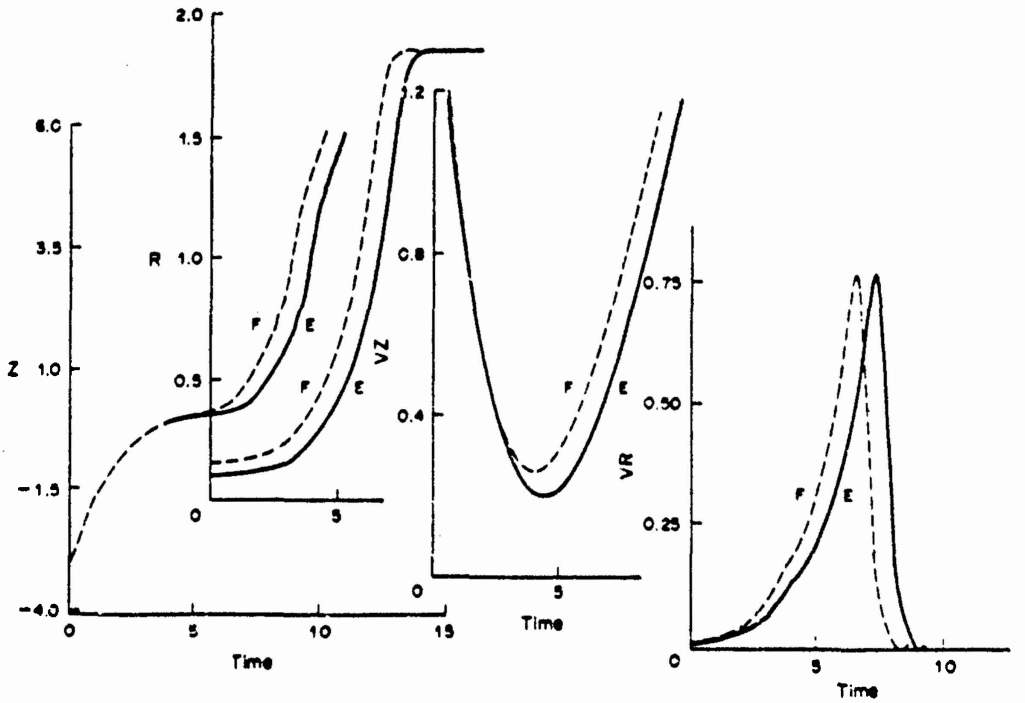

Fig. 13. The variation with time of r and z-coordinates, and the axial and radial velocity of the two target particles.

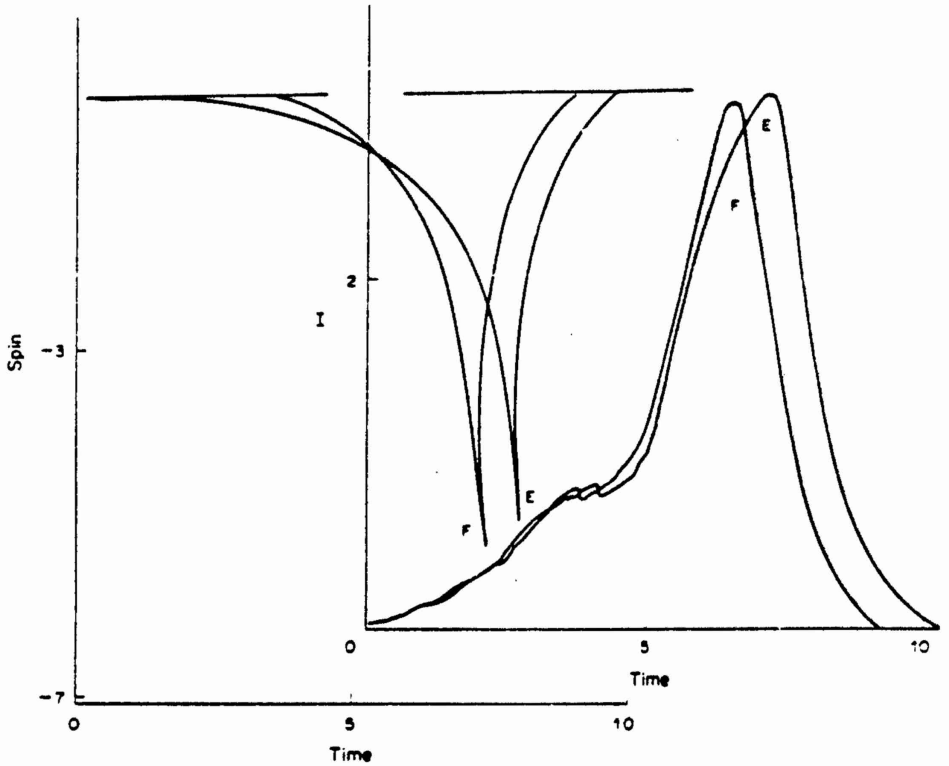

Fig. 14. Histories of the second invariant of the strain-rate tensor and the plastic spin for the two target particles.

these particles leave the area surrounding the stagnation point, the hydrostatic pressure decreases rather rapidly to zero.

CONCLUSIONS

We have studied the penetration of a rigid/perfectly plastic rod penetrating into a thick rigid/perfectly plastic target when the deformations of both as seen by an observer situated at the stagnation point and moving with it are steady. It is found that the shape of the common interface near the stagnation point is ellipsoidal, and significant deformations of the penetrator occur in the hemispherical region of radius $2r_0$ centered at the stagnation point; r_0 being equal to the radius of the undeformed cylindrical portion of the rod. The axial resisting force experienced by the penetrator and the hydrostatic pressure near the stagnation point depend strongly upon the non-dimensional parameter $\alpha = \rho v_s^2/\sigma_0$ where ρ is the mass density, v_s the speed of the stagnation point and σ_0 is the yield stress of the material in a quasistatic simple compression test. For the three speeds considered, the crater radius was found to vary from $1.75r_0$ to $1.92r_0$. The values of the resistive strength parameters introduced by Tate [2] and Alekseevskii [3] depend upon the penetration speed v, and also on ratio ρ_t/ρ_p of the mass densities. The peak values of the plastic spin experienced by a penetrator or a target particle either equal or exceed the peak values of the second invariant I of the strain-rate tensor for it. Thus, plasticity theories which properly account for the evolution of the high plastic spin and deformation induced anisotropy ought to be employed in the study of penetration problems.

Acknowledgements—This work was supported by the U.S. Army Research Office Contract DAAL03-89-K-0050 to the University of Missouri-Rolla. Some of the computations were performed on the NSF sponsored supercomputer center at the University of Illinois-Urbana.

REFERENCES

[1] A. TATE, *J. Mech. Phys. Solids* **15**, 387–399 (1967).
[2] A. TATE, *J. Mech. Phys. Solids* **17**, 141–150 (1969).
[3] V. P. ALEKSEEVSKII, *Comb. Expl Shock Waves* **2**, 63–66 (1966). (Translation from Russian, Faraday Press, New York.)
[4] P. H. PIDSLEY, *J. Mech. Phys. Solids* **32**, 315–333 (1984).
[5] M. E. BACKMAN and W. GOLDSMITH, *Int. J. Engng Sci.* **16**, 1–99 (1978).
[6] M. RAVID and S. R. BODNER, *Int. J. Engng Sci.* **21**, 577–591 (1983).
[7] M. RAVID, S. R. BODNER and I. HOLCMAN, *Int. J. Engng Sci.* **25**, 473–482 (1987).
[8] M. J. FORRESTAL, K. OKAJIMA and V. K. LUK, *J. Appl. Mech.* **55**, 755–760.
[9] J. A. ZUKAS, T. NICHOLAS, H. F. SWIFT, L. B. GRESZCZUK and D. R. CURRAN, *Impact Dynamics*. Wiley-Interscience, New York, (1982).
[10] T. Z. BLAZYNSKI, in *Materials at High Strain Rates* (Edited by T. Z. BLAZYNSKI). Elsevier, New York (1987).
[11] E. W. BILLINGTON and A. TATE, *The Physics of Deformation and Flow*. McGraw-Hill, New York (1981).
[12] M. MACAULEY, *Introduction to Impact Engineering*. Chapman & Hall, London, (1987).
[13] R. C. BATRA and T. W. WRIGHT, *Int. J. Engng Sci.* **24**, 41–54 (1986).
[14] R. C. BATRA, *Int. J. Engng Sci.* **25**, 1131–1141 (1987).
[15] R. C. BATRA, *Comp. Mech.* **3**, 1–12 (1988).
[16] R. C. BATRA and PEI-RONG LIN, *Int. J. Engng Sci.* **26**, 183–192 (1988).
[17] R. C. BATRA and P. R. LIN, *Int. J. Impact Engng* **8**, 99–113 (1989).
[18] R. C. BATRA and P. R. LIN, *Int. J. Engng Sci.* **28**, 93–98 (1990).
[19] P. R. LIN and R. C. BATRA, *Int. J. Engng Sci.* **27**, 1155–1165 (1989).
[20] E. H. LEE, *J. Appl. Mech.* **36**, 1 (1969).
[21] L. ANAND, *J. Appl. Mech.* **47**, 439 (1980).
[22] S. NEMAT-NASSER, Micromechanically based finite plasticity. *Proc. Symp. Plasticity Today* (Edited by A. SAWCZUK). Elsevier, London (1983).
[23] Y. F. DAFALIAS, A simple illustration of the plastic spin concept and its role in finite plastic transformation. *Proc. Current Theories of Plasticity and their Applications*. University of Oklahoma–Norman (1984).
[24] A. TATE, *Int. J. Mech. Sci.* **28**, 599–612 (1986).
[25] R. C. BATRA and XINGJU CHEN, *Int. J. Engng Sci.* **28**, 1347–1358 (1990).
[26] T. GOBINATH and R. C. BATRA, Analysis of a steady state axisymmetric penetration problem. In *Computational Techniques for Contact, Impact, Penetration and Perforation of Solids* (Edited by L. E. SCHWER, N. J. SALAMON and W. K. LIU), ASME AMD, Vol. 103, pp. 235–247 (1989).
[27] A. N. BROOKS and T. J. R. HUGHES, *Comput. Meth. Appl. Mech. Engng* **32**, 199–259 (1982).
[28] A. TATE, *Int. J. Engng Sci.* **16**, 858 (1978).

(Revision received and accepted 29 January 1991)

Computers & Structures Vol. 42, No. 4, pp. 489–495, 1992
Printed in Great Britain

0045-7949/92 $5.00 + 0.00

STEADY-STATE PENETRATION OF TRANSVERSELY ISOTROPIC RIGID/PERFECTLY PLASTIC TARGETS

R. C. BATRA† and A. ADAM

Department of Mechanical and Aerospace Engineering and Engineering Mechanics, University of Missouri-Rolla, Rolla, MO 65401-0249, U.S.A.

(*Received* 11 *December* 1990)

Abstract—Axisymmetric deformations of a transversely isotropic, rigid/perfectly plastic target being penetrated by a long rigid cylindrical rod with an ellipsoidal nose have been analyzed. The deformations of the target appear steady to an observer situated at the penetrator nose tip. The contact between the target and the penetrator is assumed to be smooth. Computed results show that the deformation field adjacent to the penetrator nose surface is significantly influenced by the nose shape, and the ratio of the yield stress in the axial direction to that in the transverse direction. The axial resisting force experienced by the penetrator is found to depend strongly upon the nose shape and the ratio of the yield stress in the axial to that in the transverse direction, but weakly upon the square of the penetration speed.

1. INTRODUCTION

For very thick targets, the steady-state portion of the penetration process constitutes a significant part of the entire penetration event. Accordingly, a considerable amount of work has been done in studying this process. For example, Tate [1, 2] and Alekseevskii [3] have modified models in which the steady deformations of the target and the penetrator are assumed to be governed by purely hydrodynamic incompressible flow processes by incorporating the effects of the material strengths of the target and the penetrator. These strengths were assumed to be some multiple of the yield stress of the respective materials, the multiplying factor has recently been given by Tate [4, 5] by using a solenoidal fluid flow model. Pidsley [6], Batra and Gobinath [7], and Batra and Chen [8] have estimated these multiplying factors from their numerical solutions of the problem.

We refer the reader to the review articles of Backmann and Goldsmith [9], Wright and Frank [10], Anderson and Bodner [11], and books by Zukas *et al.* [12], Blazynski [13], and Macauley [14] for a discussion of various aspects of the penetration problem, and for a list of references on the subject. Ravid and Bodner [15], Ravid *et al.* [16], Forrestal *et al.* [17], and Batra and Chen [8] have proposed engineering models of different complexity.

The works referred to above have assumed the target material to be isotropic. However, manufacturing processes such as rolling induce anisotropy in the material properties. For example, in heavily-rolled brass, the tensile yield stress transverse to the direction of rolling may be as much as ten percent greater than that parallel to the direction of rolling [18]. Greater variations may be obtained by an appropriate combination of mechanical and heat treatments, which produces a final recrystallization texture close to that of a single crystal [19]. Here we assume the target material to be transversely isotropic, and study the effect of varying the yield stress in the axial direction upon the deformation fields during steady-state penetration of the target by a rigid cylindrical penetrator. It is assumed that the degree of anisotropy, defined as the ratio of the yield stress in the axial direction to that in the transverse direction, stays constant during the deformation process. The effect of the speed of penetration as well as the nose shape on the deformations of the target is also investigated.

2. FORMULATION OF THE PROBLEM

We use a cylindrical coordinate system with origin at the center of the penetrator nose and z-axis pointing into the target. We presume that the deformations of the target are axisymmetric and appear steady to an observer situated at the penetrator nose tip and moving with it at a uniform velocity $v_0\mathbf{e}$, $\mathbf{e}$ being a unit vector in the direction of motion of the rigid penetrator, which we take to be the z-axis. Equations governing the target deformations are

$$\operatorname{div}\mathbf{v} = 0, \tag{2.1}$$

$$\rho(\mathbf{v}\cdot\operatorname{grad})\mathbf{v} = \operatorname{div}\boldsymbol{\sigma}. \tag{2.2}$$

Here $\mathbf{v}$ is the velocity of a target particle relative to the observer situated at the penetrator nose tip, ρ is the mass density for the target material, and $\boldsymbol{\sigma}$ is the Cauchy stress tensor. We neglect elastic deformations of the target and have assumed in (2.1) that its deformations are isochoric. Equations (2.1) and (2.2) express, respectively, the balance of mass and the balance of linear momentum.

We assume that the target material obeys Hill's yield criterion [20], which for transversely isotropic

†Also Senior Research Investigator, Intelligent Systems Center.

materials undergoing axisymmetric deformations becomes

$$F[(\sigma_{rr}-\sigma_{\theta\theta})^2+(\sigma_{\theta\theta}-\sigma_{zz})^2] + H(\sigma_{zz}-\sigma_{rr})^2+2M\sigma_{rz}^2=1, \quad (2.3)$$

where

$$2F=1/\delta_{rz}^2,$$
$$2H=2/\delta_{zz}^2-1/\delta_{rr}^2,$$
$$2M=1/\delta_{rz}^2, \quad (2.4)$$

δ_{rr} and δ_{zz} are yield stresses in the r- and z-directions, respectively, and δ_{rz} is the shear yield stress.

The constitutive relation for the target material can be written as

$$\sigma=-p\mathbf{1}+\mathbf{s}, \quad (2.5)$$

$$\begin{Bmatrix} s_{rr} \\ s_{\theta\theta} \\ s_{zz} \end{Bmatrix} = \frac{1}{EI}\begin{bmatrix} 3F+H & H & F \\ H & 3F+H & F \\ F & F & 2(F+H) \end{bmatrix}\begin{Bmatrix} D_{rr} \\ D_{\theta\theta} \\ D_{zz} \end{Bmatrix}, \quad (2.6)$$

$$s_{rz}=D_{rz}/MI, \quad (2.7)$$

$$E=3F(F+2H), \quad (2.8)$$

$$I^2=\frac{F(D_{rr}^2+D_{\theta\theta}^2)+HD_{zz}^2}{F(F+2H)}+\frac{2}{M}D_{rz}^2, \quad (2.9)$$

$$2\mathbf{D}=\operatorname{grad}\mathbf{v}+(\operatorname{grad}\mathbf{v})^T. \quad (2.10)$$

In eqn (2.5), σ is the Cauchy stress tensor, $\mathbf{s}$ the deviatoric stress tensor, and p the hydrostatic pressure not determined by the deformation history. Equations (2.6) and (2.7) relate the components of the deviatoric stress tensor to the components of the strain-rate tensor D. Note that because of the dependence of I upon D_{rr}, $D_{\theta\theta}$, D_{zz}, and D_{rz}, even s_{rz} depends upon all non-zero components of D. Equations (2.6)–(2.9) reduce to those for isotropic rigid/perfectly plastic materials if one takes $F=H=0.5/\sigma_0^2$, $M=1.5/\sigma_0^2$, σ_0 being the yield stress in a quasistatic simple tension or compression test.

Equation (2.1) and the one obtained by substituting from eqns (2.6)–(2.10) into eqn (2.2) are the field equations to be solved for p and $\mathbf{v}$ subject to suitable boundary conditions. Before stating these, we nondimensionalize the variables as follows:

$$\hat{\sigma}=\sigma/\sigma_0, \quad \hat{\mathbf{v}}=\mathbf{v}/v_0,$$
$$\hat{r}=r/r_0, \quad \hat{z}=z/r_0,$$
$$\hat{p}=p/\sigma_0, \quad \hat{\mathbf{s}}=\mathbf{s}/\sigma_0. \quad (2.11)$$

Here r_0 is the radius of the cylindrical portion of the penetrator and σ_0 is a reference stress. Rewriting eqns (2.1) and (2.2) in terms of non-dimensional variables, dropping the superimposed hats, and denoting the gradient and divergence operators in non-dimensional coordinates by grad and div, we obtain the following equations

$$\operatorname{div}\mathbf{v}=0, \quad (2.12)$$

$$\alpha(\mathbf{v}\cdot\operatorname{grad})\mathbf{v}=-\operatorname{grad}p+\operatorname{div}\mathbf{s}, \quad (2.13)$$

where $\alpha=\rho v_0^2/\sigma_0$ is a non-dimensional number and measures the magnitude of inertia forces relative to the flow stress of the material. At the target/penetrator interface we impose

$$\mathbf{t}\cdot(\sigma\mathbf{n})=0, \quad (2.14)$$

$$\mathbf{v}\cdot\mathbf{n}=0, \quad (2.15)$$

where $\mathbf{n}$ and $\mathbf{t}$ are, respectively, the unit outward normal and the unit tangent vectors at a point on the surface. At points far away from the penetrator

$$|\mathbf{v}+\mathbf{e}|\to 0 \quad \text{as} \quad (r^2+z^2)^{1/2}\to\infty, z>-\infty, \quad (2.16)$$

$$|\sigma\mathbf{n}|\to 0 \quad \text{as} \quad z\to-\infty. \quad (2.17)$$

The boundary condition (2.14) states that the target/penetrator interface is smooth, and (2.15) implies that there is no penetration of the target material into the penetrator. Equation (2.16) implies that target particles at a large distance from the penetrator appear to be moving at a uniform speed with respect to it, and eqn (2.17) states that far to the rear the traction field vanishes. Note that the governing eqns (2.13) with $\mathbf{s}$ given by (2.6) and (2.7) are nonlinear in $\mathbf{v}$, and that a solution of the boundary-value problem stated above, if there exists one, will depend on the rate at which quantities in (2.16) and (2.17) tend to zero. Since the problem is difficult to solve analytically, we seek an approximate solution of the problem by the finite element method.

3. FINITE ELEMENT SOLUTION OF THE PROBLEM

3.1. *Computational considerations*

Recalling that the target deformations are assumed to be axisymmetric, only the finite region R shown in Fig. 1 is studied, and the boundary conditions (2.16) and (2.17) are replaced by the following

$$v_r=-1.0, \quad v_z=0, \quad \text{on the boundary surface EFA,} \quad (3.1)$$

$$\sigma_{zz}=1, \quad v_r=0, \quad \text{on the bottom surface AB.} \quad (3.2)$$

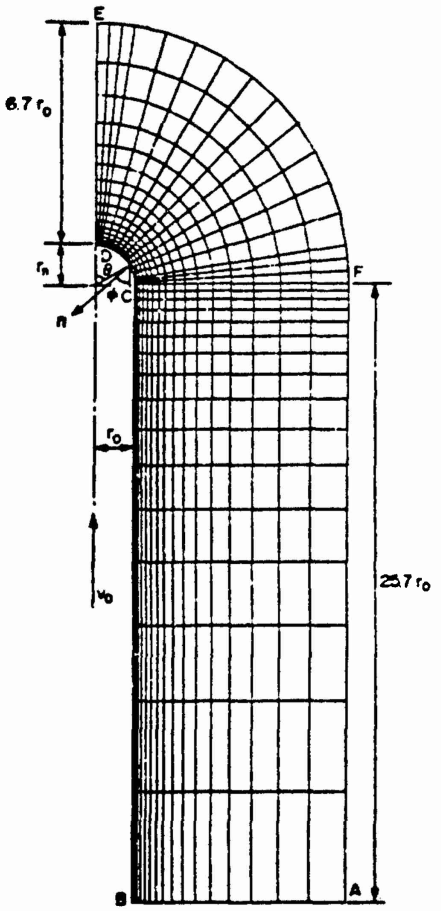

Fig. 1. The finite region analyzed and its discretization.

On the axis of symmetry DE, we impose

$$\sigma_{rr} = 0, \qquad v_r = 0. \tag{3.3}$$

A finite element solution of the problem defined by eqns (2.12) and (2.13) with s given by non-dimensionalized versions of (2.6)–(2.10), and boundary conditions (2.14), (2.15), and (3.1)–(3.3) has been found for several values of α, δ_{zz}/δ_{xx}, and penetrator nose shapes. The finite element code developed by Batra [21] was modified to solve the present problem. The changes made were checked by solving the same penetration problem for an isotropic target with the modified code by setting $F = H = 0.5$, and $M = 1.5$, and with the original code. Since in the numerical solution of the problem, eqn (2.12) is only approximately satisfied, the two sets of results for the same problem computed with the original code and the modified code, as shown in Fig. 2, agree qualitatively, but differ quantitatively by about ten percent. We have used the method of Lagrange multipliers to satisfy the incompressibility constraint (2.12), and the boundary condition (2.15).

3.2. *Results for the transversely isotropic target*

We have assigned the following values to various variables when computing numerical results that are presented below

$$\sigma_0 = \delta_{xx} = \delta_{yy} = 498 \text{ MPa},$$

$$\rho = 7860 \text{ kg/m}^3, \quad r_0 = 2.54 \text{ mm}. \tag{3.4}$$

The effect of varying δ_{zz}, v_0, and the penetrator nose shape is analyzed. The value of δ_{zz} is computed from

$$\frac{1}{\delta_{zz}^2} = \frac{1}{\delta_{xx}^2} + \frac{2}{\delta_{zz}^2}. \tag{3.5}$$

Except when discussing the effect of the nose shape

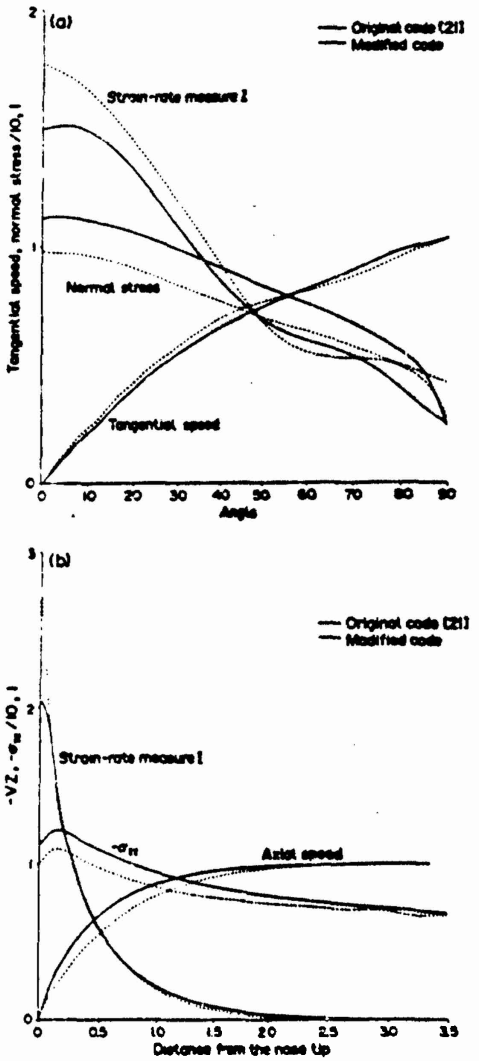

Fig. 2. Comparison of results for an isotropic target computed with the two codes.

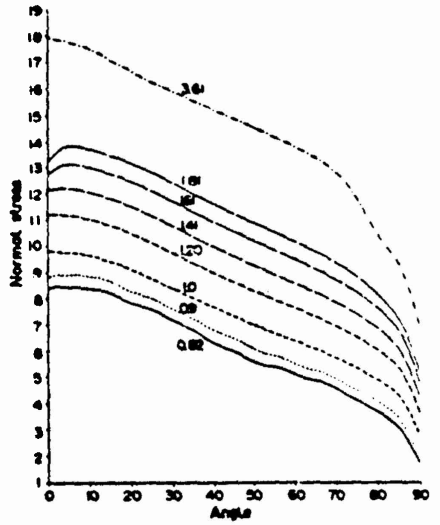

Fig. 3. Effect of the yield stress in the axial direction on the distribution of the normal stress at target particles on the penetrator nose surface. $\alpha = 6.25$.

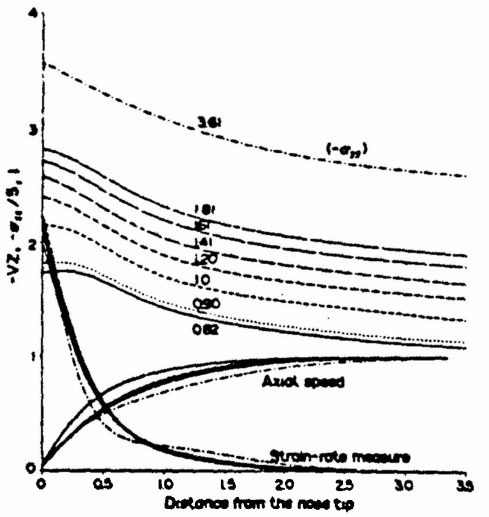

Fig. 5. Effect of the yield stress in the axial direction on I, σ_{zz}, and v_z at target particles on the axial line. $\alpha = 6.25$.

on the deformations of the target, the penetrator nose is taken to be hemispherical.

Figure 3 shows the effect of the yield stress in the axial direction on the distribution of the normal stress at target particles situated on the penetrator/target interface when $\alpha = 6.25$. As expected, the magnitude of the normal stress increases with an increase in the value of δ_{zz}. The range of values of δ_{zz} considered is considerably more than that likely to occur in a practical situation. In Figure 4, we have plotted the variation with δ_{zz} of the strain-rate measure I and the tangential speed at target particles abutting the

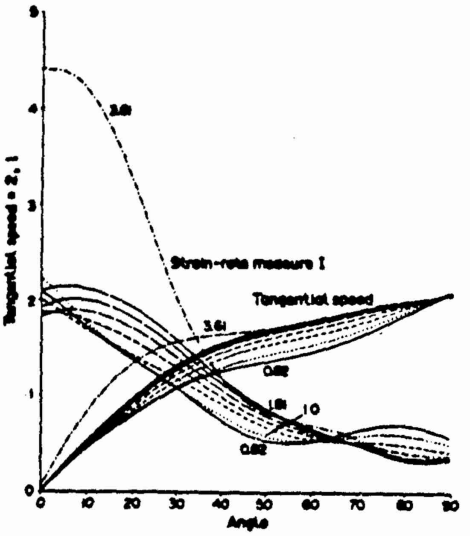

Fig. 4. Effect of the yield stress in the axial direction on the strain-rate measure I and the tangential speed at target particles on the penetrator nose surface. $\alpha = 6.25$.

penetrator nose surface for a hemispherical nosed penetrator and $\alpha = 6.25$. At every target particle on the penetrator nose surface, both the tangential speed and the strain-rate measure I increase with δ_{zz}. The tangential speed varies slowly with the value of δ_{zz} at a target particle on the penetrator nose periphery. The dependence of $(-\sigma_{zz})$, I, and the axial velocity at target particles on the axial line upon the yield stress δ_{zz} is depicted in Fig. 5. The rate of decay of the axial velocity as seen by an observer moving with the penetrator nose tip decreases with an increase in the value of δ_{zz}. We note that the values of I and the absolute axial velocity become zero at target particles on the axial line whose distance from the penetrator nose tip exceeds $3r_0$. Thus, the region studied is adequate. The values of σ_{zz} do not decay to zero, but approach the value of p as we move away from the penetrator nose surface. We recall that we have neglected elastic deformations of the target, and the hydrostatic pressure does not influence the yielding of the material. The consideration of elastic deformations should give a better estimate of the hydrostatic pressure at a point.

The distributions of the normal stress and the strain-rate measure I at target particles adjoining the target/penetrator interface for four different nose shapes, i.e. $r_n/r_0 = 0.2$, 0.5, 1.0, and 2.0, are shown in Fig. 6. Here $2r_0$ and $2r_n$ equal the length of the principal axes in the r and z directions, respectively, of the penetrator nose. The normal stress at the stagnation point appears to be the same for all four different nose shapes. The normal stress decreases rapidly with the angular position θ for a long narrow nose. For the essentially blunt nose, the normal stress stays virtually constant on the entire nose surface, and rapidly drops to zero near the nose periphery. A similar behavior was found by Batra for an isotropic

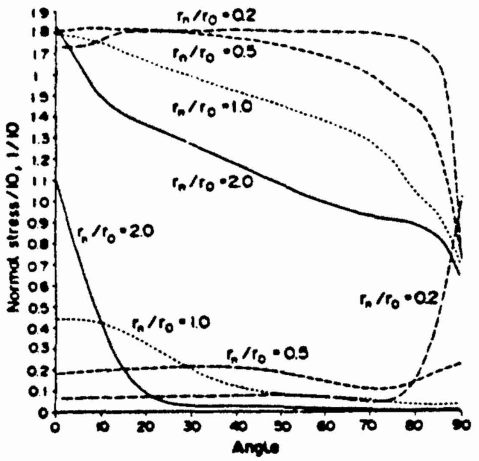

Fig. 6. Distribution of the normal stress and the strain-rate measure I at target particles on the penetrator nose surface for four different shapes of the penetrator nose.

viscoplastic [21] and an isotropic thermoviscoplastic target [22]. For a cylindrical penetrator with a long pointed nose, the strain-rate measure I assumes highest values at the stagnation point, and the values of I drop off sharply with the angular position θ. However, for a blunt nose, I stays essentially constant at a relatively low value on the entire surface and suddenly shoots up near the nose periphery. Thus, very severe deformations of the target occur at points surrounding the stagnation point for a long tapered nosed penetrator, and near the nose periphery for a blunt nosed penetrator. The variation of I, $(-v_z)$, and $(-\sigma_{zz})$ at target particles on the axial line for four different nose shapes is depicted in Fig. 7. The value of the axial velocity changes rather slowly for a blunt nosed penetrator, but quite rapidly for a long tapered nosed penetrator. The difference in the values of $(-\sigma_{zz})$ at a point on the axial line distant $4r_0$ from the penetrator nose tip is mainly due to the different limiting values of the hydrostatic pressure for the four nose shapes. Ideally, the pressure should decay to zero at target points far away from the penentrator nose. However, the assumption that the target material is rigid/perfectly plastic and the observation that the strain-rates are extremely small at target points whose distance from the penetrator nose tip exceeds $4r_0$ suggest that the computed values of p at target particles far away from the penetrator nose surface are not very reliable.

In Fig. 8, we have plotted for a hemispherical nosed penetrator and $\delta_{zz}/\sigma_0 = 1.8$ the distribution of the normal stress, I, and the tangential speed for different values of α. As for an isotropic target [21], the normal stress at target particles near the nose periphery decreases with α. The tangential speed and the values of I seem to be affected very little by the value of α. At target particles situated on the axial line, the values of σ_{zz}, I, and v_r do not change much when α is increased from 3.0 to 6.25. Their plots and those for $\delta_{zz}/\sigma_0 = 3.6$ are not included in the paper. We note that results for $\delta_{zz}/\sigma_0 = 3.6$ are qualitatively similar to those for $\delta_{zz}/\sigma_0 = 1.8$.

Figure 9 shows the variation of the axial speed v_r with r on the planes $z = 0$ and $z = -1.0$ for the four different nose shapes. These results indicate that the target material adjacent to the sides of the penetrator appears to extrude rearward as a uniform block that is separated from the bulk of the stationary target material by a narrow region with a sharp velocity gradient. This observation provides a partial justification for the velocity field assumed by Ravid and

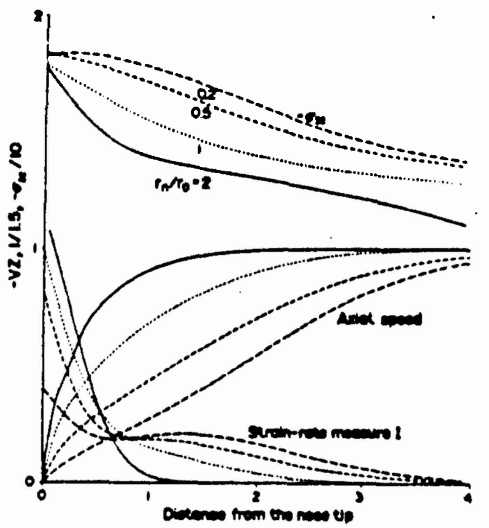

Fig. 7. Distribution of I, v_r, and σ_{zz} at target particles on the axial line for four different shapes of the penetrator nose.

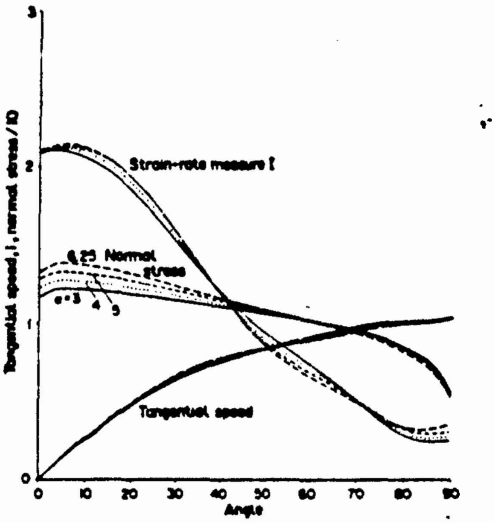

Fig. 8. Distribution of the normal stress, I, and the tangential speed on the penetrator nose surface for different values of α.

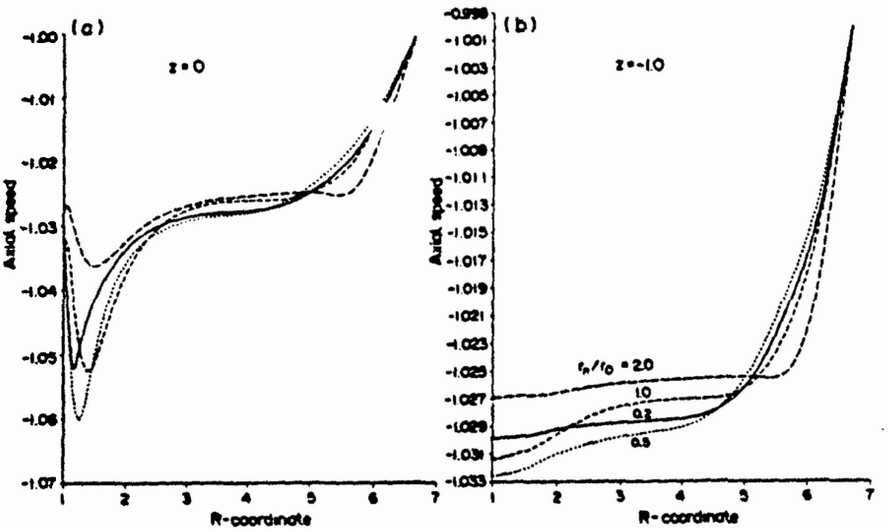

Fig. 9. Variation of the axial speed with r on the surfaces $z = 0$ and $z = -1.0$.

Bodner [15] in their work involving targets of finite thickness. We add that Batra and Wright [23] found a similar result for the steady state penetration of isotropic rigid/perfectly plastic targets.

The axial resisting force F experienced by the penetrator is given by

$$F = 2\int_0^{\pi/2} (\mathbf{n}\cdot\boldsymbol{\sigma}\mathbf{n}) \times \frac{\cos\phi \sin\theta[\sin^2\theta + (r_0/r_n)^4\cos^2\theta]^{1/2}}{[\sin^2\theta + (r_0/r_n)^2\cos^2\theta]^2}\,d\theta, \quad (3.6)$$

$$\cos\phi = \frac{z/r_n^2}{[(r/r_0^2)^2 + (z/r_n^2)^2]^{1/2}}, \quad (3.7)$$

where the angle θ is defined in Fig. 1, and (r, z) are the coordinates of a point on the penetrator/target interface. The corresponding axial force in physical units is given by $(\pi r_0^2\sigma_0)F$. We note that the expression given by Batra [21] for the axial force, except for the hemispherical nose shape, is in error. The dependence of the axial force upon α, r_n/r_0, and δ_m/σ_0 is exhibited in Fig. 10. For each one of the two values of δ_m/σ_0 considered herein, F depends upon α very weakly. However, F depends strongly upon r_n/r_0 and δ_m/σ_0; the resisting force is maximum for a blunt nosed and least for a tapered nosed penetrator. F increases rapidly with δ_m first, but slowly after δ_m/σ_0 exceeds approximately 1.9.

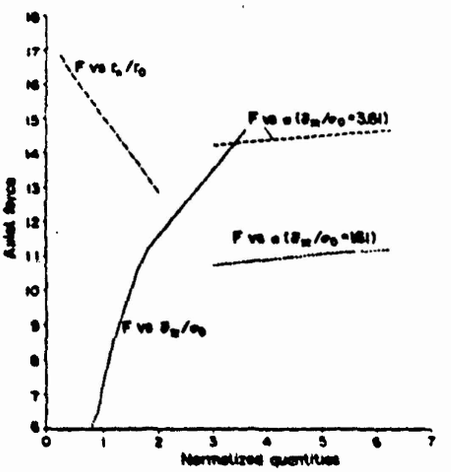

Fig. 10. Dependence of the axial resisting force upon various parameters.

4. CONCLUSIONS

We have studied the steady state penetration of a rigid/perfectly plastic and transversely isotropic target being penetrated by a rigid cylindrical penetrator having an ellipsoidal nose. It is found that the axial resisting force experienced by the penetrator depends strongly upon the penetrator nose shape, and also upon the ratio of the yield stress in the axial direction to that in a transverse direction. The axial resisting force depends rather weakly upon the square of the penetration speed. Peak values of the strain-rate measure I occur near the stagnation point for a long tapered nosed penetrator, but near the nose periphery for a blunt nosed penetrator.

Acknowledgements—This work was supported by the U.S. Army Research Office Contract DAAL03-89-K-0050 to the University of Missouri-Rolla. Some of the computations were performed on the NSF Supercomputer Center in Urbana, Illinois.

REFERENCES

1. A. Tate, A theory for the deceleration of long rods after impact. *J. Mech. Phys. Solids* **15**, 387–399 (1967).
2. A. Tate, Further results in the theory of long rod penetration. *J. Mech. Phys. Solids* **17**, 141–150 (1969).
3. V. P. Alekseevskii, Penetration of a rod into a target at high velocity. *Comb. Expl. and Shock Waves* **2**, 63–66 (1966). (Translation from Russian, Faraday Press, New York.)
4. A. Tate, Long rod penetration models—part II. Extensions to the hydrodynamic theory of penetration. *Int. J. Mech. Sci.* **28**, 599–612 (1986).
5. A. Tate, A simple hydrodynamic model for the strain field in a target by the penetration of a high speed long rod projectile. *Int. J. Engng Sci.* **16**, 858 (1978).
6. P. H. Pidsley, A numerical study of long rod impact onto a large target, *J. Mech. Phys. Solids* **32**, 315–333 (1984).
7. R. C. Batra and T. Gobinath, Steady state axisymmetric deformations of a thermoviscoplastic rod penetrating a thick thermoviscoplastic target. *Int. J. Impact Engng* **11**, 1–31 (1991).
8. R. C. Batra and Xingju Chen, An approximate analysis of steady state axisymmetric deformations of viscoplastic targets. *Int. J. Engng. Sci.* **29**, 1347–1358 (1990).
9. M. E. Backmann and W. Goldsmith, The mechanics of penetration of projectiles into targets. *Int. J. Engng Sci.* **16**, 1–99 (1978).
10. T. W. Wright and K. Frank, *Approaches to Penetration Problems*. SMIRT Symposium, No. 14, Impact, Lausanne, Switzerland (1987).
11. C. E. Anderson and S. R. Bodner, The status of ballistic impact modeling. *Int. J. Impact Engng* **7**, 9–35 (1988).
12. J. A. Zukas *et al.*, *Impact Dynamics*. Wiley–Interscience, New York (1982).
13. T. Z. Blazynski, in *Materials at High Strain Rates*, (Edited by T. Z. Blazynski). Elsevier Applied Science, London (1987).
14. M. Macauley, *Introduction to Impact Engineering*. Chapman & Hall, London (1987).
15. M. Ravid and S. R. Bodner, Dynamic perforation of viscoplastic plates by rigid projectiles. *Int. J. Engng Sci.* **21**, 577–591 (1983).
16. M. Ravid S. R. Bodner and I. Holcman, Analysis of very high speed impact. *Int. J. Engng Sci.* **25**, 473–482 (1987).
17. M. J. Forrestal, K. Okajima and V. K. Luk, Penetration of 6061-T651 aluminum targets with rigid long rods. *J. Appl. Mech.* **55**, 755–760 (1988).
18. M. Cook, *J. Inst. Metals* **60**, 159 (1937).
19. W. M. Baldwin, Jr, *Trans. Am. Inst. Min. Met. Engng* **166**, 591 (1946).
20. R. Hill, *The Mathematical Theory of Plasticity*. Oxford University Press (1960).
21. R. C. Batra, Steady state penetration of viscoplastic targets. *Int. J. Engng Sci.* **25**, 1131–1141 (1987).
22. R. C. Batra, Steady state penetration of thermoviscoplastic targets. *Comp. Mech.* **3**, 1–12 (1988).
23. R. C. Batra and T. W. Wright, Steady state penetration of rigid perfectly plastic targets. *Int. J. Engng Sci.* **24**, 41–54 (1986).

Acta Mechanica 92, 9–27 (1992)

ACTA MECHANICA
© Springer-Verlag 1992

Steady state penetration of elastic perfectly plastic targets

R. Jayachandran and **R. C. Batra**, Rolla, Missouri

(Received March 5, 1991; revised May 7, 1991)

Summary. Steady state axisymmetric deformations of an elastic perfectly plastic target being penetrated by a fast moving rigid cylindrical rod have been analyzed by the finite element method. The target is assumed to obey the von Mises yield criterion and the associated flow rule. Contact between target and penetrator has been assumed to be smooth. A mixed formulation, in which two components of the velocity and four components of the deviatoric stress tensor at each node point, and the hydrostatic pressure at the centroid of an element are taken as unknowns, is employed. This should give a better estimate of tractions acting on the penetrator nose, and hence of the axial resisting force experienced by the penetrator. The effect of the penetrator speed, its nose shape and the elasticity of the target material on the target deformations, and the axial force experienced by the penetrator has been studied. The consideration of elastic effects helps delineate the elastic-plastic boundary in the target.

1 Introduction

An outstanding problem in penetration mechanics is to find, within reasonable resources, whether or not for the given penetrator and target geometries, materials, target support conditions, penetrator speed, and the angle of attack, the target will be perforated or not. If the target is perforated, the speed of the penetrator when it ejects out of the target is of interest. And if the target is not perforated, one will like to know the shape and size of the hole made in the target. This problem has defied a complete solution for many years. We refer the reader to review articles by Backman and Goldsmith [1], Wright and Frank [2], Anderson and Bodner [3], and the books by Zukas et al. [4], Blazynski [5], and MaCauley [6] for a summary of the available literature on ballistic penetration. Awerbuch [7], Awerbuch and Bodner [8], Ravid and Bodner [9], Ravid et al. [10], Forrestal et al. [11], and Batra and Chen [12] have proposed engineering models of different complexity.

In recent years, emphasis has been placed on kinetic energy penetrators, which for terminal ballistic purposes may be regarded as long metal rods travelling at high speeds. For impact velocities in the range of 2 – 10 km s, incompressible hydrodynamic flow equations can be used to describe adequately the impact and penetration phenomena, because large stresses occurring in hypervelocity impact permit one to neglect the rigidity and compressibility of the striking bodies. Birkhoff et al. [13] and Pack and Evans [14] have proposed models which require the use of the Bernoulli equation or its modification to describe the hypervelocity impact. At ordnance velocities (0.5 – 2 km s), the material strength becomes an important parameter. Allen and Rogers [15] represented the material strength as a resistive pressure. Alekseevskii [16] and Tate [17], [18] have considered separate resistive pressures for the penetrator and the target and proposed that these equal some multiple of the uniaxial yield stress of the material. However, the

multiplying factor was not specified. Tate [19], [20], Pidsley [21], Batra and Gobinath [22], Gobinath and Batra [23], and Batra and Chen [12] have estimated these multiplying factors. Whereas Tate used a solenoid fluid flow model to simulate the steady state penetration process, other investigations relied on a numerical solution of the problem.

We recall that the one-dimensional penetration theories [15]–[18] ignore the lateral motion, plastic flow and the detailed dynamic effects. In an attempt to understand better these approximations, Batra and Wright [24] studied the problem of a rigid cylindrical rod with a hemispherical nose penetrating into a rigid perfectly plastic target. The target deformations as seen by an observer moving with the penetrator nose tip, were presumed to be steady. Subsequently, Batra and his co-workers [25]–[30] studied the effect of nose shape, strain hardening, strain-rate hardening and thermal softening characteristics of the target material. Batra and Gobinath [22]–[23] have analyzed the steady state penetration problem in which both the target and the penetrator deform.

When the target material is modeled as rigid perfectly plastic it is likely that the hydrostatic pressure at target points adjoining the penetrator target interface is increased because of the rigidity of the surrounding target material. Also, computations of stresses and hence tractions on the target, penetrator interface from the finite element solution in which velocities at nodal points are taken as unknowns is less accurate as compared to the nodal velocities. We alleviate these concerns here by including the effect of material elasticity in the problem formulation, and using a mixed finite element formulation in which both the nodal velocities and nodal stresses are taken as unknowns.

2 Formulation of the problem

We use a cylindrical coordinate system with origin attached to the center of the penetrator nose, moving with it at a uniform speed v_0, and positive z-axis pointing into the target, to describe the deformations of the target. These deformations appear to be steady to an observer situated at the origin of this coordinate system, and are governed by the following equations:

Balance of mass: $$\operatorname{div} \boldsymbol{v} = 0. \tag{1}$$

Balance of linear momentum: $$\operatorname{div} \boldsymbol{\sigma} = \varrho(\boldsymbol{v} \cdot \operatorname{grad})\, \boldsymbol{v}. \tag{2}$$

Constitutive relations: $$\boldsymbol{\sigma} = -p\boldsymbol{I} + \boldsymbol{s}, \tag{3}$$

$$\overset{\nabla}{\boldsymbol{s}} = 2G(\boldsymbol{D} - \boldsymbol{D}^p), \tag{4}$$

$$\boldsymbol{s} = 2\mu(I)\, \boldsymbol{D}^p, \tag{5}$$

where

$$2\mu = \frac{\sigma_0}{\sqrt{3}\, I}, \quad 2I^2 = \operatorname{tr}(\boldsymbol{D}^{p2}), \tag{6.1, 2}$$

$$\overset{\nabla}{\boldsymbol{s}} = (\boldsymbol{v} \cdot \operatorname{grad})\, \boldsymbol{s} + \boldsymbol{s}\boldsymbol{W} - \boldsymbol{W}\boldsymbol{s}. \tag{7}$$

$$2\boldsymbol{D} = \operatorname{grad} \boldsymbol{v} + (\operatorname{grad} \boldsymbol{v})^T, \quad 2\boldsymbol{W} = \operatorname{grad} \boldsymbol{v} - (\operatorname{grad} \boldsymbol{v})^T. \tag{8}$$

Equations (1) and (2) are written in the Eulerian description of motion. The operators grad and div denote the gradient and divergence operators on fields defined in the present configuration. In Eqs. (1)–(8), $\boldsymbol{v}$ is the velocity of a target particle relative to the penetrator, $\boldsymbol{\sigma}$ the Cauchy stress

tensor, s its deviatoric part, p the hydrostatic pressure not determined by the deformation history, and an open circle on s indicates the Jaumann derivative defined by Eq. (7) for the steady stress field. Furthermore, G is the shear modulus, D^p the plastic strain-rate, μ defined by Eq. (6.1) may be interpreted as the shear viscosity of the target material, σ_0 is the yield stress in a quasistatic simple compression test, D the strain-rate tensor and W is the spin tensor. Equation (4) expresses Hooke's law written in the rate form and is based on the tacit assumption that the strain-rate has additive decomposition into elastic and plastic parts. We note that Pidsley [21] used the ordinary time derivative rather than the Jaumann rate in Eq. (4). Equation (5) follows from the assumption that the target material obeys von Mises yield criterion and the associated flow rule. However, in Eqs. (3)–(5) we have assumed that a material particle is undergoing elastic and plastic deformations simultaneously. Substitution from Eqs. (5) and (7) into Eq. (4) gives the following differential equation for s:

$$(v\cdot\operatorname{grad})\, s + sW - Ws + (G/\mu)\, s = 2GD. \tag{9}$$

We non-dimensionalize variables as follows:

$$\bar{\sigma} = \sigma/\sigma_0, \quad \bar{s} = s/\sigma_0, \quad \bar{p} = p/\sigma_0, \quad \bar{v} = v/v_0, \quad \bar{r} = r/r_0,$$
$$\bar{z} = z/r_0, \quad \bar{r}_n = r_n/r_0, \quad \bar{I} = I\,\frac{r_0}{v_0}, \tag{10}$$

where the superimposed bar indicates the non-dimensional variable, the pair (r, z) the cylindrical coordinates of a point, v_0 the uniform penetrator speed, r_0 the radius of the cylindrical part of the penetrator, and $2r_0$ and $2r_n$ equal the length of the principal axes of the ellipsoidal nose in the r and z directions, respectively. Equations (1), (2), and (9), when written in terms of non-dimensional variables become

$$\operatorname{div} v = 0, \tag{11}$$

$$-\operatorname{grad} p + \operatorname{div} s = \alpha(v\cdot\operatorname{grad})\, v, \tag{12}$$

$$s + \beta\gamma\big((v\cdot\operatorname{grad})\, s + sW - Ws\big) = \beta D, \tag{13}$$

where

$$\alpha = \frac{\varrho v_0^{\,2}}{\sigma_0}, \quad \gamma = \frac{\sigma_0}{G}, \quad \text{and} \quad \beta = \frac{1}{2\sqrt{3}\, I} \tag{14}$$

are non-dimensional numbers, and we have dropped the superimposed bars. Henceforth, we will use only non-dimensional variables. Note that α and γ are constants for the given problem, but β varies from point to point in the deforming region. The value of α signifies the importance of inertia forces relative to the flow stress of the material, and that of γ gives the effect of material elasticity. For most metals γ is of the order of 10^{-3}. For a rigid perfectly plastic material γ equals zero. The value of the Weissenberg number $(\beta\gamma)$ varies from 10^{-3} to 10^{4} in the deforming region.

We assume that the target/penetrator interface is smooth, and impose on it the following boundary conditions:

$$t\cdot(\sigma n) = 0, \tag{15}$$

$$v\cdot n = 0. \tag{16}$$

Here n and t are, respectively, a unit normal and a unit tangent vector to the surface. Equation (15) implies that there is no frictional force acting at the contact surface, and the boundary condition (16) ensures that there is no interpenetration of the target material into the penetrator and vice-versa. A partial justification for boundary condition (15) is that a thin layer of material at the interface either melts or is severely degraded by adiabatic shear. At points far away from the penetrator, we impose

$$|v + e| \to 0, \quad \text{as} \quad (r^2 + z^2)^{1/2} \to \infty, \quad z > -\infty, \tag{17}$$

$$|\sigma n| \to 0, \quad \text{as} \quad z \to -\infty, \quad r \geqq 1, \tag{18}$$

where e is a unit vector in the positive z-direction. The boundary condition (17) embodies the assumption that target particles far from the penetrator and not on the bounding back surface appear to be moving at a uniform velocity with respect to it. Equation (18) implies that when a target particle has moved far to the rear of the penetrator, the surface tractions on it vanish.

The problem formulation outlined above differs from that studied earlier by Batra and co-workers [25]—[30] because of the consideration of elastic deformations here. In earlier work substitution for s in Eq. (12) resulted in non-linear field equations for v. Here, Eq. (13) can not be solved easily for s; accordingly we solve Eqs. (11)—(13) for p, v and s. This necessitates that the boundary conditions for stress components be prescribed at the entrance region. Shimazaki and Thompson [31] have studied a simple problem whose governing equations are similar to Eqs. (11)—(13), and have justified prescribing p and s at the entrance region.

3 Finite element formulation of the problem

Unless we use special infinite elements, a numerical solution of the problem requires that we consider a finite region. Accordingly, we study deformations of the region R shown in Fig. 1, and replace boundary conditions (17) and (18) at the far surfaces by the following conditions (19) and (21) on the boundary surfaces of the finite region being analyzed:

$$v_r = 0, \quad v_z = -1.0 \quad \text{on the bounding surface } EFA, \tag{19}$$

$$\sigma_{rz} = 0, \quad v_r = 0 \quad \text{on the axis of symmetry } DE, \tag{20}$$

$$\sigma_{zz} = 0, \quad v_r = 0 \quad \text{on the surface } AB. \tag{21}$$

Conditions (20) follow from the assumed axisymmetric nature of deformations. The validity of replacing (17) by (19), (18) by (21), and the accuracy of the computed results depend upon the size of the region R. Since Eq. (13) can not be solved explicitly for s, but is to be solved simultaneously with Eqs. (11) and (12), we need to specify the state of stress of the material entering the control volume (e.g. see Shimazaki and Thompson [31]). Accordingly we set

$$p = 0, \quad s_{rr} = 0, \quad s_{\theta\theta} = 0, \quad s_{zz} = 0 \quad \text{and } s_{rz} = 0 \quad \text{on the boundary surface } EFA. \tag{22}$$

The first step in analyzing the problem numerically is to obtain a weak formulation of the problem. Let ϕ and ψ be smooth and bounded vector and tensor-valued functions defined on the region R that vanish on the surface EFA, and $\phi_r = 0$ on AB and DE, $\phi \cdot n = 0$ on the target/penetrator interface BCD. Also, let η be a bounded, scalar valued function defined on R. Taking the inner product of both sides of Eqs. (11), (12), and (13) with η, ϕ and ψ, integrating the

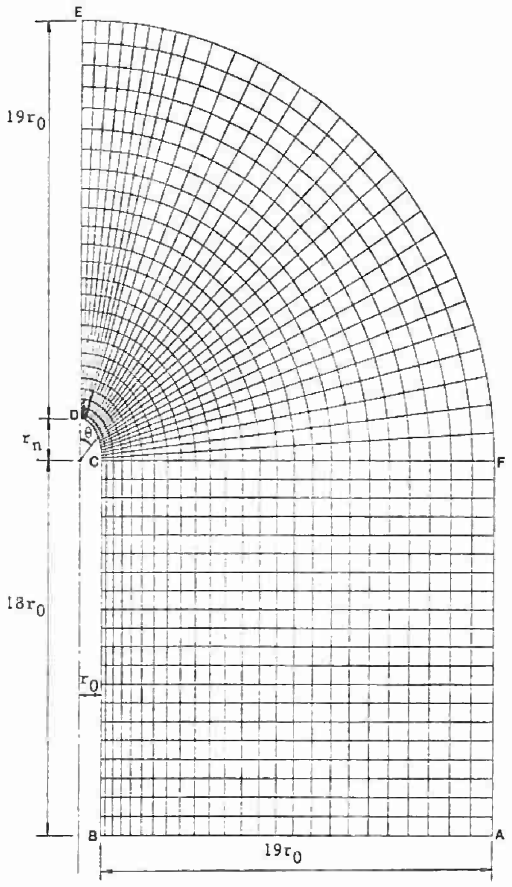

Fig. 1. The finite region studied and its discretization

resulting equations over R, using the divergence theorem, the traction boundary conditions (15), (19) and (20), and the aforestated boundary conditions on ϕ and ψ, we arrive at the following equations:

$$\int \eta(\operatorname{div} v)\, dV = 0, \tag{23}$$

$$\int p(\operatorname{div}\phi)\, dV - \int s:\left(\operatorname{grad}\phi + (\operatorname{grad}\phi)^T\right) dV = \alpha \int [(v\cdot\operatorname{grad})\, v]\cdot\phi\, dV, \tag{24}$$

$$\int \psi:\bar{s}\, dV = \frac{1}{2}\int \beta(I)\, \psi:[\operatorname{grad} v + (\operatorname{grad} v)^T]\, dV, \tag{25}$$

$$\bar{s} = s + \beta\gamma\left((v\cdot\operatorname{grad})\, s + sW - Ws\right). \tag{26}$$

Here and below the integrations are over the region R. The boundary value problem defined by Eqs. (11)–(13), (15), (16), and (19)–(22) is equivalent to the statement that v and s satisfy the prescribed essential boundary conditions and Eqs. (23)–(25) hold for every ϕ, ψ and η such that grad ϕ, grad ψ, and η are square integrable over R, and ϕ and ψ satisfy the stated homogeneous essential boundary conditions.

An approximate solution of Eqs. (23)–(25) has been obtained by using the finite element method (e.g. see Hughes [32]). In order to preclude spurious oscillations in the stress deviator s and also to improve upon the rate of convergence, we employed the Petrov-Galerkin approximation of Eq. (25) but Galerkin approximation of Eqs. (23) and (24) (see Hughes [32]). The region R is divided into quadrilateral subregions, called finite elements, over each of which

v and s are approximated by simple polynomials defined in terms of their values at the four corner nodes. The pressure p is assumed to be uniform over each element; this value is assigned to the centroid of the element. The basis functions used in the Petrov-Galerkin approximation are those given by Brooks and Hughes [33]. The boundary condition (16) on target/penetrator interface BCD is enforced by using the method of Lagrange multipliers.

We note that Eqs. (23)–(25) are coupled and are nonlinear in v. The following iterative technique was used to linearize them:

$$\int \eta(\operatorname{div} v^m)\, dV = 0, \tag{27}$$

$$\int p^m(\operatorname{div} \phi)\, dV - \int s(v^{m-1}) : (\operatorname{grad} \phi + (\operatorname{grad} \phi)^T)\, dV = \alpha \int ((v^{m-1} \cdot \operatorname{grad})\, v^m) \cdot \phi\, dV, \tag{28}$$

$$\int \psi : s\, dV + \int \psi : \bar{s}(v^{m-1})\, dV = \int \beta(I^{m-1})\, \psi : [\operatorname{grad} v^{m-1} + (\operatorname{grad} v^{m-1})^T]\, dV, \tag{29}$$

where m is the iteration number. The iterative process was stopped when

$$\left(\sum \|v^m - v^{m-1}\|^2\right)^{1/2} \leqq 0.01 \left(\sum \|v^{m-1}\|^2\right)^{1/2}, \tag{30.1}$$

$$\left(\sum |p^m - p^{m-1}|^2\right)^{1/2} \leqq 0.01 \left(\sum |p^{m-1}|^2\right)^{1/2}, \tag{30.2}$$

$$\left(\sum \|s^m - s^{m-1}\|^2\right)^{1/2} \leqq 0.01 \left(\sum \|s^{m-1}\|^2\right)^{1/2}, \tag{30.3}$$

where $\|v\|^2 = v_r^2 + v_z^2$, and $\|s\|^2 = \operatorname{tr}(ss^T)$. The summation sign refers to the sum of the indicated quantity evaluated at all nodes in the finite element mesh. This convergence criterion is weaker than the local norm used by Batra and his co-workers [25]–[30].

Having determined pressure $\bar{p}$ at the centroids of elements, the pressure at node points is computed from

$$\sum_{j=1}^{M} \left(\int N_i N_j\, dV\right) p_j\, dV = \int N_i \bar{p}\, dV, \qquad i = 1, 2, \ldots, M \tag{31}$$

where M is the number of nodes, and $N_1, N_2, \ldots$ are the piecewise bilinear finite element basis functions. We note that Eq. (31) also serves to smooth out the pressure field.

4 Computation and discussion of results

A computer code based on Eqs. (27)–(29) and employing 4-noded quadrilateral elements has been developed. The two components (v_r, v_z) of the velocity and four components (s_{rr}, s_{00}, s_{rz}, and s_{zz}) of the deviatoric stress tensor are taken as unknowns at each node, and the hydrostatic pressure p is assumed to be constant within an element. The validity of the computer code was established by solving the radial flow problem discussed by Shimazaki and Thompson [31]. For the same finite element grid and numerical values of parameters as those used by Shimazaki and Thompson [31], the two sets of computed results plotted in Fig. 2 agree well with each other. Another test problem studied was a hypothetical one involving the flow of a Navier-Stokes fluid in a circular pipe and achieving a favorable comparison between the computed and analytical results; this problem is discussed in the Appendix.

In the results presented below, the target material was assumed to be an aluminium-alloy for which we took $\sigma_0 = 340$ MPa, $G = 27$ GPa, and $\varrho = 2\,890$ kg/m^3. However, the results are presented below in terms of non-dimensional numbers and are therefore valid for other

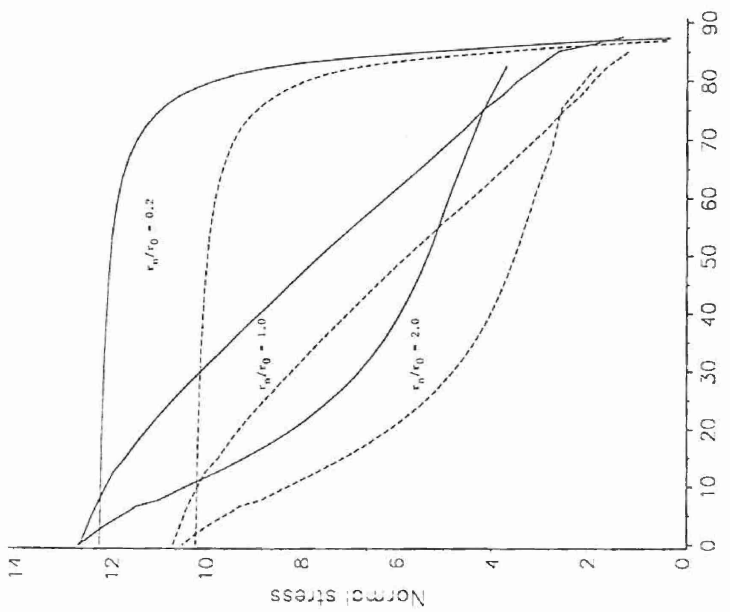

Fig. 3. Distribution of the compressive normal stress on the penetrator nose surface for three different nose shapes and when the target material is modeled as elastic perfectly plastic and as rigid perfectly plastic. $\alpha = 10$

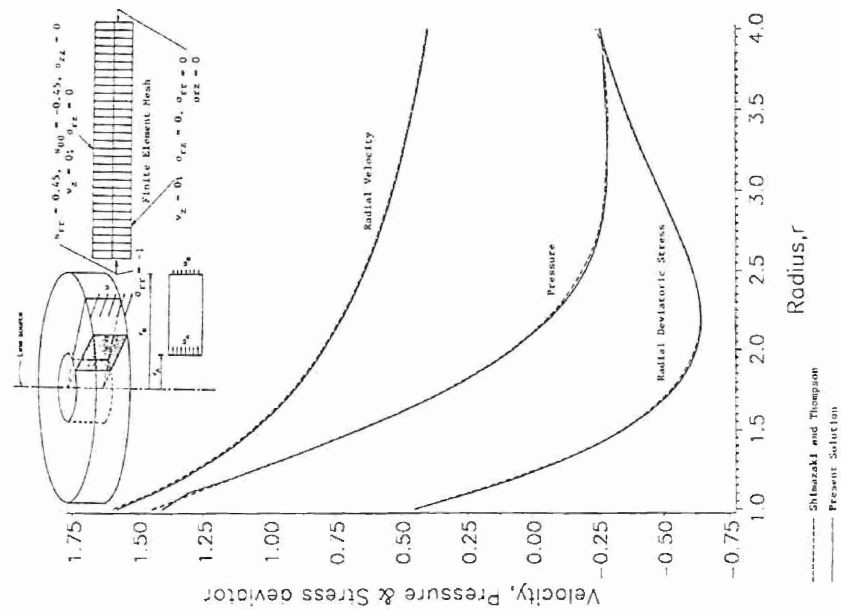

Fig. 2. Comparison of the presently computed solution with that of Shimazaki and Thompson for the radial flow problem

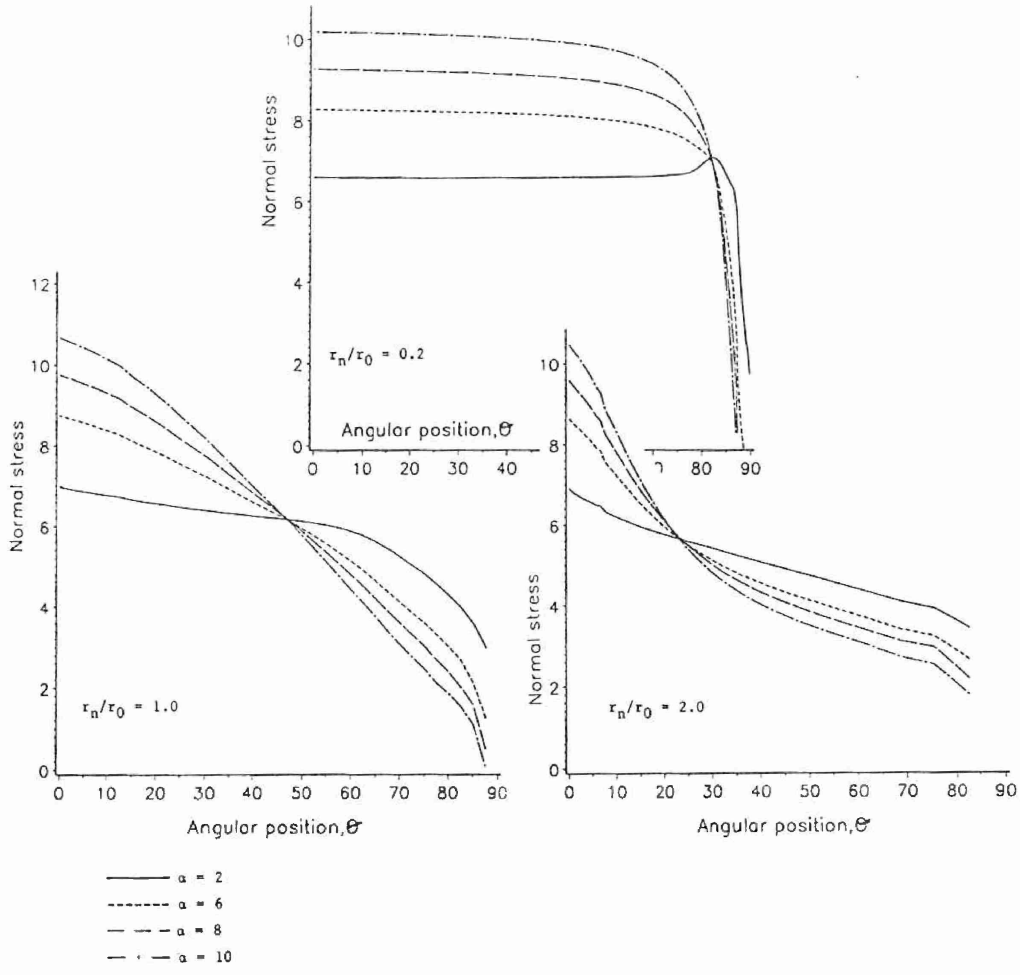

Fig. 4. Distribution of the compressive normal stress on the penetrator nose surface for the three different nose shapes and for $\alpha = 2, 6, 8$, and 10 when the target material is modeled as elastic perfectly plastic

combinations of target material and penetration speed. The finite element subdivision of the target region when the penetrator has an ellipsoidal nose with $r_n/r_0 = 2.0$ is shown in Fig. 1. The components of the deviatoric stress tensor and the hydrostatic pressure were assigned to be zero at the entrance region EFA.

Figure 3 depicts the effect of material elasticity ($\gamma = 1.26 \times 10^{-2}$) on the pressure distribution at the nose surface for three different nose shapes with $r_n/r_0 = 0.2$, 1.0, and 2.0, and when α was set equal to 10.0. For each nose shape the normal pressure on the nose surface was lower when material elasticity was accounted for than that for the rigid perfectly plastic case ($\gamma = 0$). However, the general shapes of the curves are unaffected by the consideration of elastic effects. The normal stress at the stagnation point is nearly the same for the three nose shapes, but the shape of the normal stress versus angular position θ curve depends strongly upon the nose shape. As expected, for the blunt nose, the normal stress stays constant over most of the nose surface, and drops off rapidly to zero near the nose periphery. For the hemispherical nosed penetrator, the normal stress drops off nearly evenly as one moves away from the center to the

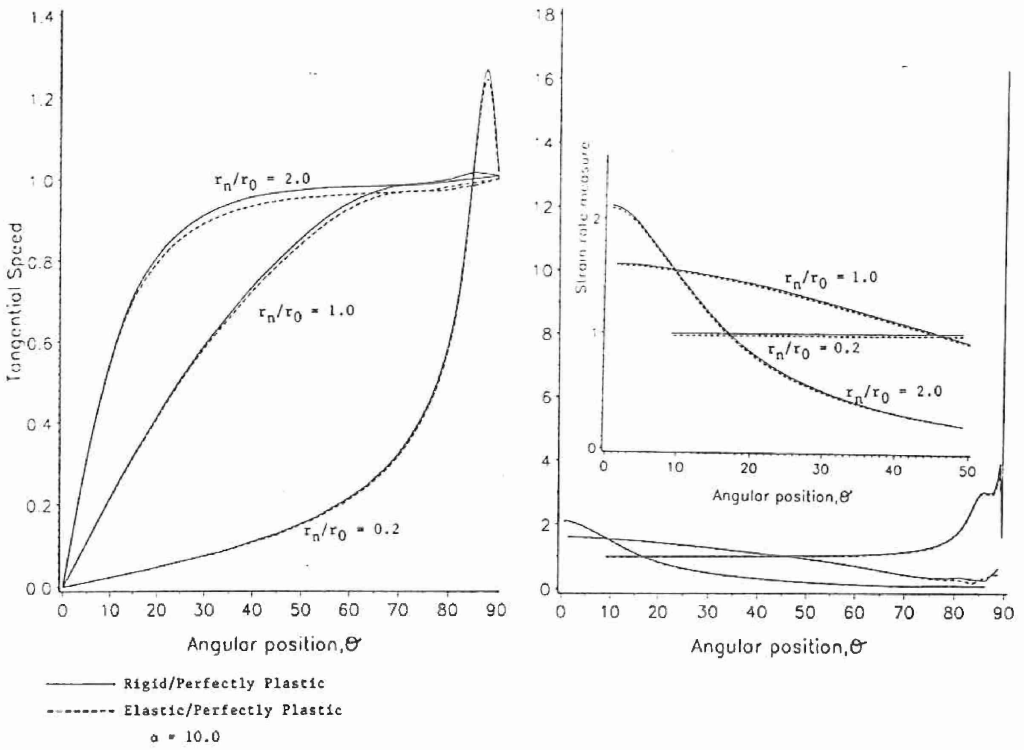

Fig. 5. Distribution of the tangential speed and the strain-rate measure I upon the penetrator nose surface for three different nose shapes; $\alpha = 10$

nose periphery. For the ellipsoidal nosed penetrator the normal stress drops off quite rapidly for $0° \leqq \theta \leqq 30°$, and rather slowly for $\theta > 30°$. The curvature of the curve for $r_n/r_0 = 2.0$ is opposite to that of the curve for $r_n/r_0 = 1.0$ or 0.2.

The distribution of the compressive normal stress on the nose surface for $\alpha = 2$, 6, 8, and 10 and when the target material is modeled as elastic perfectly plastic is plotted in Fig. 4. For each of the three nose shapes considered the normal stress at points on the nose surface for which $0 \leqq \theta \leqq \theta_c$ increases with α, that at points with $\theta > \theta_c$ decreases with α. The value of θ_c equals approximately 22°, 45°, and 82°, for the long tapered ellipsoidal nosed, hemispherical nosed and the blunt nosed penetrators, respectively. The normal stress at points near the nose periphery was found to be positive for $\alpha > 15$ implying thereby that the target particles tended to separate away from the penetrator. However, for the blunt nosed penetrator this tendency of the target particles to separate away from the penetrator adjacent to the nose periphery was also observed at lower values of α.

The distribution of the tangential speed on the penetrator nose surface and the strain-rate measure I at the centroids of elements abutting the penetrator nose surface for the three different nose shapes and $\alpha = 10.0$ is shown in Fig. 5. It is apparent that the material elasticity has negligible effect on the tangential speed and the strain-rate measure I. For the long tapered nosed penetrator, the tangential speed increases very rapidly for $0 \leqq \theta \leqq 20°$, attains the value of 1.0 at $\theta \approx 30°$, and then stays close to 1.0 for $30° \leqq \theta \leqq 90°$. For the hemispherical nosed penetrator the tangential speed increases gradually from 0 at $\theta = 0°$ to 1.0 at $\theta \approx 60°$ and does not vary much for $60° < \theta \leqq 90°$. The trend is quite different for the blunt nosed penetrator. In this case the

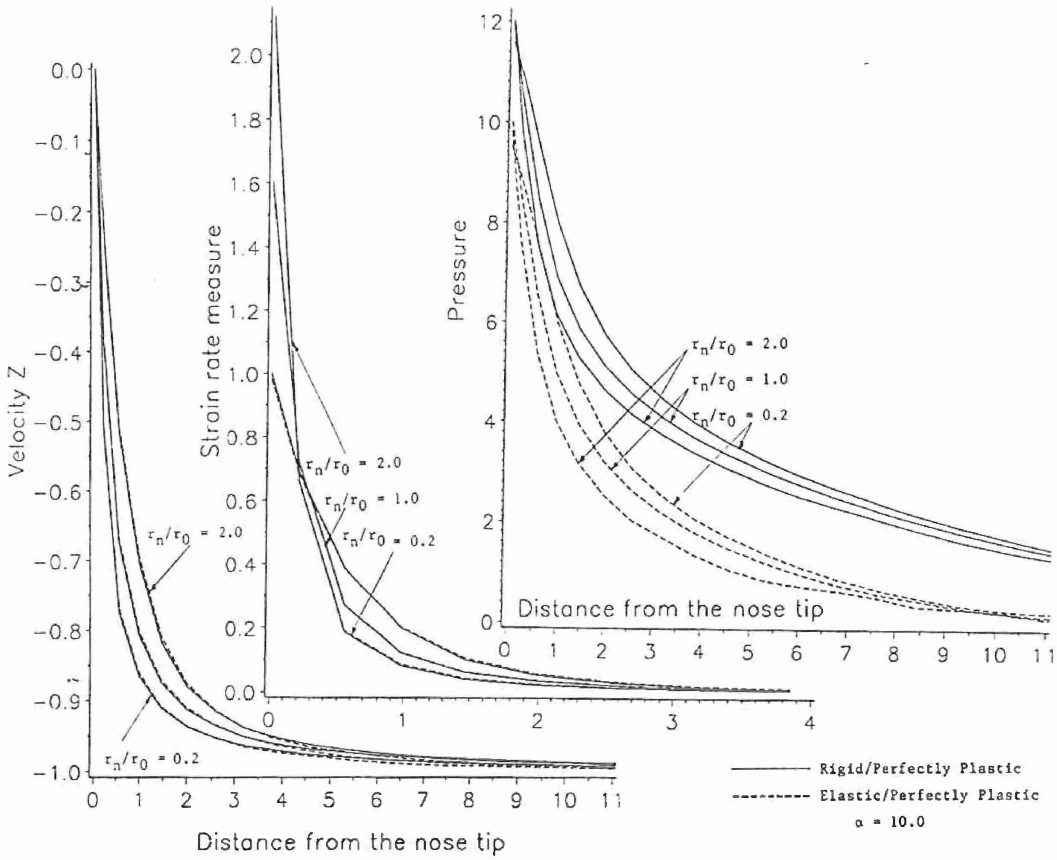

Fig. 6. Variation of the pressure, strain-rate measure I and the z-velocity on the axial line with the distance from the penetrator nose tip

tangential speed increases slowly for $\theta \leqq 50^\circ$, and then very rapidly. The maximum value of the tangential speed computed for the blunt nosed penetrator is more than that for the other two nose shapes. For the blunt nosed penetrator the peak values of the strain-rate measure I are an order of magnitude higher than that for the long tapered nosed penetrator. Whereas I_{max} occurs near the nose periphery for the blunt nosed penetrator, peak values of I for the other two nose shapes are realized at the stagnation point. Both for the hemispherical and the elliptical nosed penetrator, I decreases slowly from its maximum value at the nose center to nearly zero at the nose periphery.

We have plotted the variation of the hydrostatic pressure, strain-rate measure I and the axial velocity along the axis of symmetry in Fig. 6. The consideration of material elasticity has very little effect on the distribution of I and the axial velocity but reduces noticeably the value of the hydrostatic pressure. The value of I at the stagnation point is maximum for the ellipsoidal nosed penetrator and least for the blunt nosed penetrator; the former equals nearly twice the latter. It is clear that severe deformations of the target occur at points situated at most $3r_0$ from the penetrator nose surface. Thus the target region studied is adequate. The pressure drops off more slowly when the target material is modeled as rigid perfectly plastic as compared to the case when it is modeled as elastic perfectly plastic. The general shapes of the curves I, v_z or p versus the distance from the nose tip are unaffected by the penetrator nose shape and by the consideration of material elasticity.

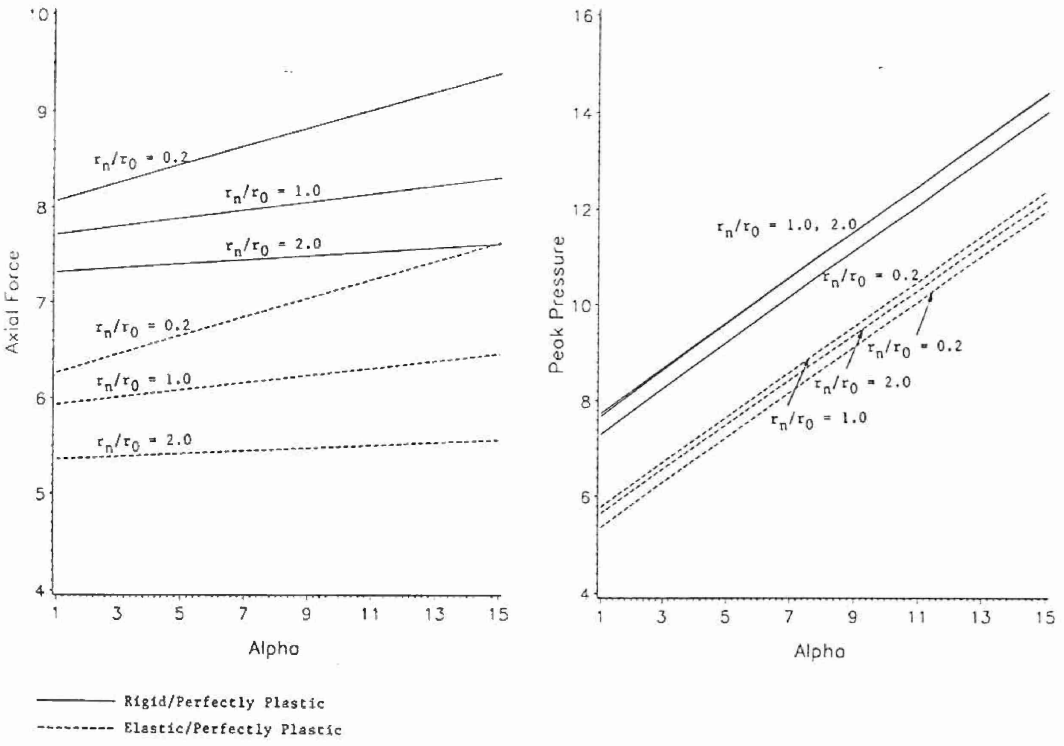

Fig. 7. Dependence of the peak pressure at the stagnation point and the axial resisting force experienced by the penetrator upon α

The dependence of the peak pressure that occurs at the stagnation point, and of the axial resisting force F experienced by the penetrator upon α is depicted in Fig. 7. The axial resisting force F is given by

$$F = 2\int_0^{\pi/2} (n\cdot\sigma n)\,\frac{\cos\phi\ \sin\theta\ [\sin^2\theta + (1/r_n)^4\ \cos^2\theta]^{1/2}}{[\sin^2\theta + (1/r_n)^2\ \cos^2\theta]^2}\,d\theta, \tag{32.1}$$

$$\cos\phi = \frac{z/r_n^{\,2}}{[r^2 + (z/r_n^{\,2})^2]^{1/2}}, \tag{32.2}$$

where the angle θ is defined in Fig. 1 and (r, z) are the coordinates of a point on the penetrator/target interface. The corresponding axial force in physical units is given by $(\pi r_0^{\,2}\sigma_0)\,F$. For each nose shape, the relationships between p_{max} and α, and F and α are nearly affine, and the consideration of elastic effects lowers the value of p_{max} by about 2, and of F by 1.8. The least squares fit to the computed data gives

$$p_{max} = 6.82 + 0.48\alpha, \quad F = 7.97 + 0.094\alpha, \quad r_n/r_0 = 0.2, \tag{33.1}$$

$$p_{max} = 7.20 + 0.48\alpha, \quad F = 7.67 + 0.042\alpha, \quad r_n/r_0 = 1.0, \tag{33.2}$$

$$p_{max} = 7.26 + 0.48\alpha, \quad F = 7.29 + 0.021\alpha, \quad r_n/r_0 = 2.0, \tag{33.3}$$

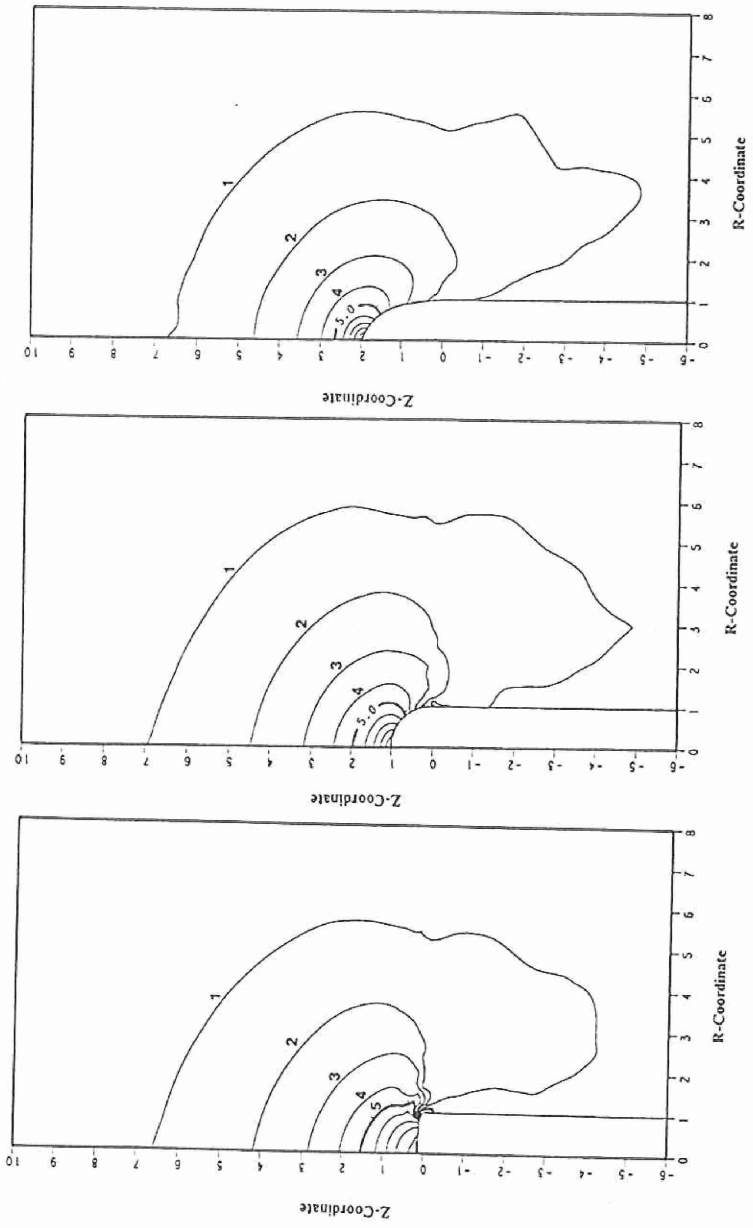

Fig. 8. Contours of the hydrostatic pressure in the deforming target region for three different nose shapes, $\alpha = 10$

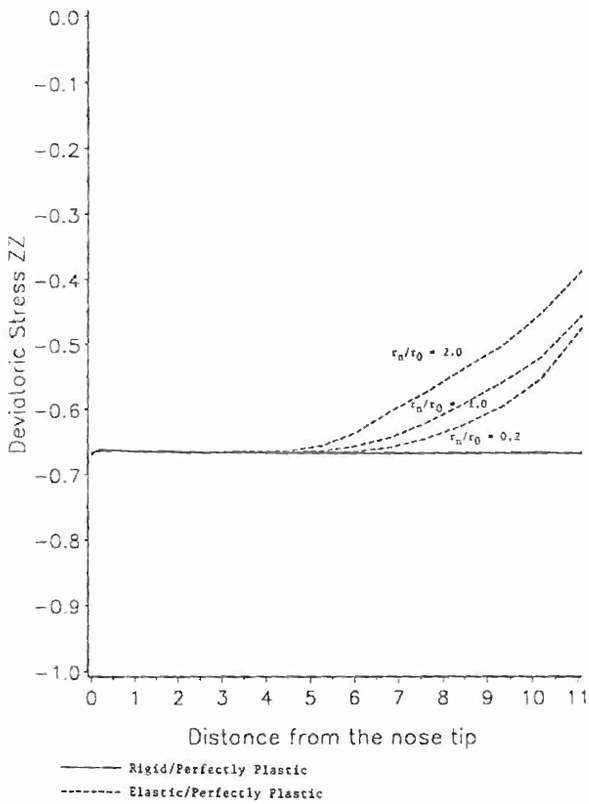

Fig. 9. Variation of the deviatoric stress s_{zz} on the axial line

when the target material is modeled as rigid perfectly plastic, and

$$p_{max} = 4.87 + 0.47\alpha, \quad F = 6.17 + 0.096\alpha, \quad r_n/r_0 = 0.2, \tag{34.1}$$

$$p_{max} = 5.29 + 0.47\alpha, \quad F = 5.90 + 0.038\alpha, \quad r_n/r_0 = 1.0, \tag{34.2}$$

$$p_{max} = 5.16 + 0.47\alpha, \quad F = 5.32 + 0.019\alpha, \quad r_n/r_0 = 2.0, \tag{34.3}$$

when it is taken to be elastic perfectly plastic. We note that the dependence of F upon α is quite weak.

The contours of the hydrostatic pressure in the deforming target region for the three different nose shapes and $\alpha = 10$ are depicted in Fig. 8. These show that the pressure falls off to zero, not only on the axial line, but also along other radial lines as one moves away from the penetrator nose surface. The contour of the zero hydrostatic pressure near the bounding surface is not plotted in order to focus on the narrow region surrounding the penetrator/target interface. For each one of the three nose shapes examined, the pressure near the nose periphery drops off to a very small value. The pressure gradient at points near the nose tip is steepest for the ellipsoidal nosed penetrator.

On the axial line uniaxial strain conditions prevail approximately. Thus the magnitude of the deviatoric stress s_{zz} at a point on the axial line should equal $(2/3\sigma_0)$ whenever the material point is deforming plastically. For a rigid perfectly plastic target material and for each nose shape considered, the computed value of $|s_{zz}|$ came out to be $2/3\sigma_0$ as shown in Fig. 9. Near the boundary point F of the target region studied, $|s_{zz}|$ rapidly dropped to the prescribed zero value. This rapid drop is not shown in the figure. However, when the target material is modeled as

elastic perfectly plastic, $|s_{zz}|$ equals $(2/3\sigma_0)$ for a distance of $3r_0$ to $4r_0$ from the nose tip and then gradually decreases to the assigned value of zero at the outer boundary. The penetrator nose shape influences the rate of decay of $|s_{zz}|$: the plastic deformation progresses farther for the blunt nosed penetrator and $|s_{zz}|$ decays slowly for it as compared to the ellipsoidal nosed penetrator. On the axial line, the Bernoulli equation in terms of non-dimensional variables and as modified by Tate [17], [18] is

$$\frac{1}{2}\alpha + R_t = -\sigma_{zz}^s = p^s + \frac{2}{3} \tag{35}$$

where R_t accounts for the strength of the target material, and σ_{zz}^s and p^s are the values of σ_{zz} and p at the stagnation point. Having computed σ_{zz} and knowing α, we can find R_t. For the three nose shapes considered, the least squares fit to the computed values of R_t for different values of α gives the following:

$$R_t = 7.48 - 0.020\alpha, \quad (r_n/r_0) = 0.2, \tag{36.1}$$

$$R_t = 7.86 - 0.018\alpha, \quad (r_n/r_0) = 1.0, \tag{36.2}$$

$$R_t = 7.92 - 0.024\alpha, \quad (r_n/r_0) = 2.0, \tag{36.3}$$

for a rigid perfectly plastic target, and

$$R_t = 5.53 - 0.027\alpha, \quad (r_n/r_0) = 0.2, \tag{37.1}$$

$$R_t = 5.96 - 0.027\alpha, \quad (r_n/r_0) = 1.0, \tag{37.2}$$

$$R_t = 5.83 - 0.032\alpha, \quad (r_n/r_0) = 2.0, \tag{37.3}$$

for an elastic perfectly plastic target. In either case the dependence of R_t upon α is very weak and this explains why the assumption of constant R_t in simpler theories of penetration gives good results. Tate [19] has proposed that

$$R_t = \frac{2}{3} + \ln\left(\frac{2E_t}{3\sigma_0}\right), \tag{38}$$

where E_t is Young's modulus of the target material. Thus for values of G and σ_0 taken herein,

$$R_t = \frac{2}{3} + \ln\left(\frac{2}{3}\left(\frac{3 \times 27 \times 10^9}{0.34 \times 10^9}\right)\right) = 5.734 \tag{39}$$

which is close to the values computed for the elastic perfectly plastic target. Recalling that $p^s = p_{max}$, it is interesting to note that the slope of the least squares fit to the p_{max} vs. α data is close to 0.5 as it should be if Eq. (35) were to hold.

As is transparent from Fig. 9 the stress state at target particles far away from the target/penetrator interface lies inside the surface defined by

$$\text{tr}\,(s^2) = \frac{2}{3}. \tag{40}$$

This is certainly true of points on the boundary surface EFA where $s = 0$ is prescribed. The constitutive assumptions (4)–(6) tacitly assume that each target particle is deforming elastically and plastically. However, points where $\|s\|$ is small are undergoing negligible plastic deforma-

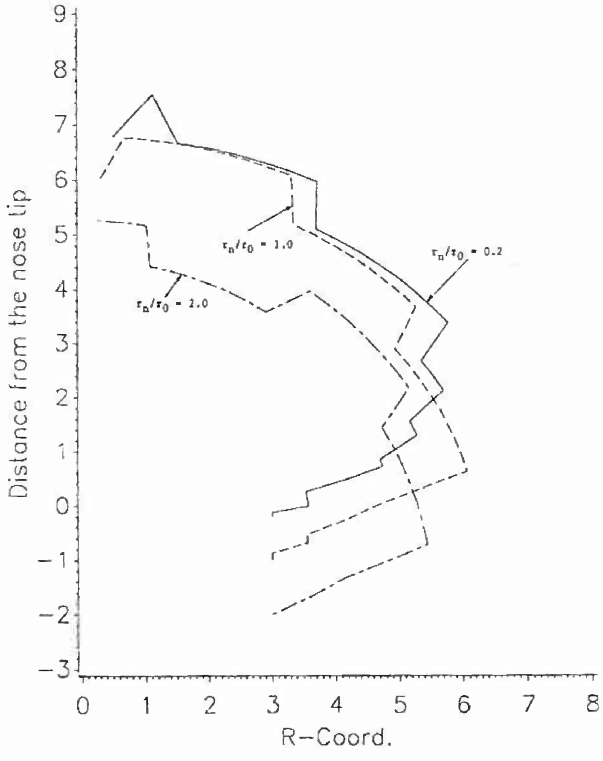

Fig. 10. Elastic-plastic boundary for three different nose shapes, and $\alpha = 10$

tions. Here we classify points for which the stress state satisfies the condition (40) as deforming plastically and those for which the stress state lies inside the surface (40) as deforming elastically. The elastic plastic boundary computed by using this criterion and obtained by joining points that are deforming plastically by straight line segments is depicted in Fig. 10.These curves suggest that less of the material ahead of the penetrator nose tip and to the sides of the rigid rod is deformed plastically for the ellipsoidal nosed penetrator as compared to the other two nose shapes considered. The distance of the elastic-plastic boundary from the penetrator nose tip is found to be 5.4, 6.8, and 7.7, respectively, according as the penetrator nose shape is ellipsoidal, hemispherical or blunt. Tate [19] presumed that a material particle was deforming either elastically or plastically and based on his solenoid flow model he found the axial distance of the elastic-plastic boundary from the stagnation point to be 6.71, which compares well with our computed values. The computed results, not plotted herein, show that ahead of the penetrator the elastic-plastic boundary does not advance much when α is increased from 6 to 10 for the hemispherical and blunt nosed penetrator but does move appreciably for the ellipsoidal nosed penetrator. As soon as a material particle goes past the nose periphery, stresses on it are relieved and the stress state for it lies inside the surface defined by (40).

A measure of the deformation of a material particle is the value of the effective strain ε, defined as

$$\dot{\varepsilon} = \left(\frac{1}{2}\,\mathrm{tr}\,D^2\right)^{1/2} = I \tag{41}$$

at that point. For a steady state penetration problem Tate [20] has described a method to compute different components of the finite strain tensor from a knowledge of the velocity field. He showed that contours of the circumferential strain are approximately parallel to the crater

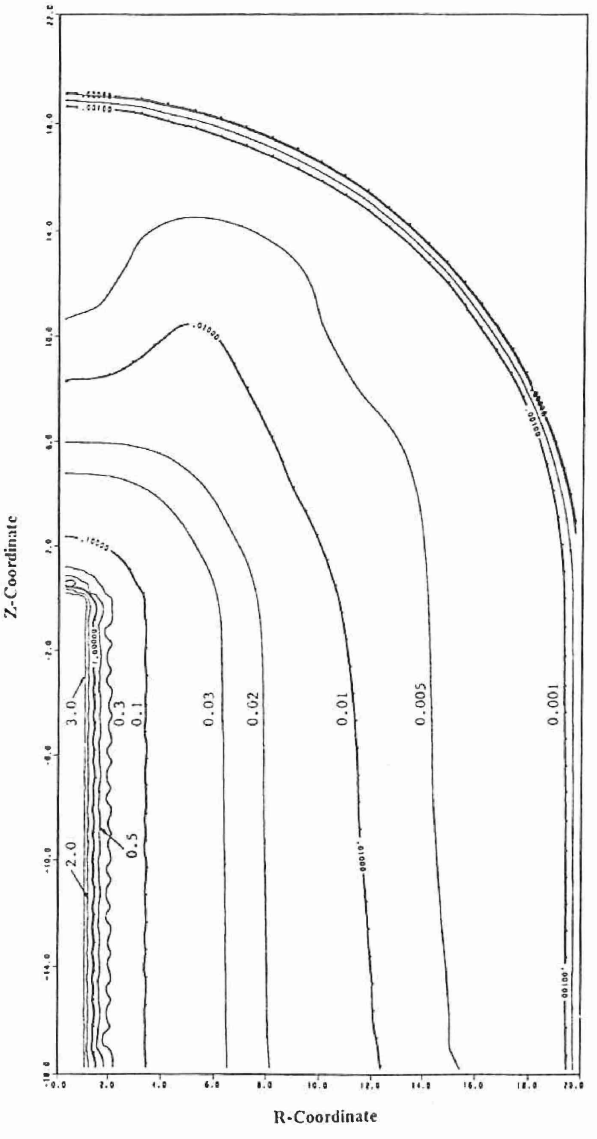

Fig. 11. Contours of the effective strain in the deforming target region for a blunt nosed penetrator, and $\alpha = 10$

surface and that the circumferential strain at a point distance a little more than one radius from the crater tip equals 5%. Because of the steady state deformations, we write Eq. (41) as

$$(v \cdot \text{grad})\, \varepsilon = I \tag{42}$$

and first compute I from the velocity field, and then find ε as a solution of Eq. (42) with the boundary condition $\varepsilon = 0$ on EFA. These contours basically look alike for the three nose shapes, and are shown in Fig. 11 only for the blunt nosed penetrator. The contours of ε suggest that severe deformations propagate farther to the side than ahead of the penetrator nose. The peak values of ε occur at target particles near the target penetrator interface and equal 100%. We recall that no failure or fracture criterion is included in our work. Thus a material point can undergo an unlimited amount of deformation. As expected, the strain gradients are high at points near the target/penetrator interface and rapidly decay as one moves away from this interface.

5 Conclusions

We have analyzed the steady state axisymmetric deformations of an elastic perfectly plastic target being penetrated by a fast moving rigid cylindrical rod. Three different nose shapes, i.e., ellipsoidal, hemispherical, and blunt are considered. For each nose shape the effect of the penetration speed upon the deformations of the target is investigated. The consideration of elastic effects necessitates that the problem be analyzed by using a mixed formulation in which both velocities and stresses at a node point are taken as unknowns.

The peak hydrostatic pressure at the stagnation point is lower when elastic effects are included than when they are not. Also, the axial resisting force experienced by the penetrator is found to be lower when the target material is modeled as elastic perfectly plastic than when it is modeled as rigid perfectly plastic. In either case, the axial force depends upon the non-dimensional parameter α very weakly. Similarly the strength parameter appearing in the modified Bernoulli equation is found to be essentially independent of α, and the computed value is close to that given by Tate. For the blunt nosed penetrator, plastic deformations spread farther ahead of the penetrator nose as well as to its sides as compared to those when the penetrator nose is ellipsoidal or hemispherical. The distance of the elastic-plastic boundary from the penetrator nose tip along the axis of symmetry is found to compare well with that estimated by Tate.

Appendix

One of the problems analyzed in order to establish the validity of the finite element code developed is the following hypothetical problem. Consider the flow of a homogeneous and incompressible Navier-Stokes fluid of unit mass density and unit viscosity. The flow is governed by equations obtained from Eqs. (1) through (8) when $\varrho = 1$, $\sigma_0 \sqrt{3}I = 2$, omitting Eq. (4) and adding the body force vector to the left-hand side of Eq. (2). These equations have the solution

$$v_r = r(1 - r), \quad v_z = -z(2 - 3r), \quad p = z. \tag{A1}$$

$$g_r = 3 + r(1 - r)(1 - 2r), \quad g_z = 1 - 3z\,r + 3zr(1 - r) + z(2 - 3r)^2. \tag{A2}$$

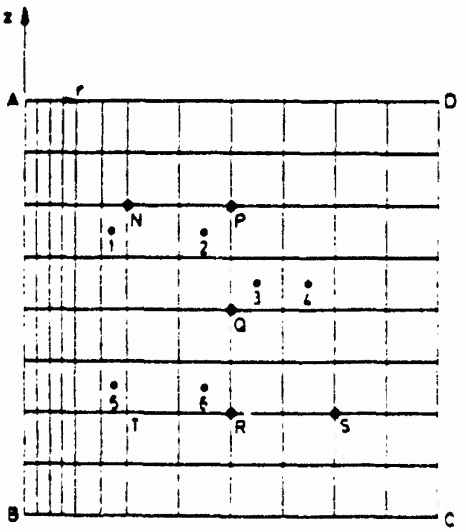

Fig. A1. The finite element mesh used for the test problem

Table A 1. Comparison of analytical and numerical solution. The good agreement between the computed and analytical values of v_r, v_z, and p establishes the validity of the code

Point	Analytical values		Computed values		Point	Analytical value	Computed value
	v_r	v_z	v_r	v_z		$-p$	$-p$
N	0.1875	0.3125	0.1890	0.3116	1	0.3125	0.3311
P	0.2500	0.1250	0.2504	0.1250	2	0.3125	0.3115
Q	0.2500	0.2500	0.2502	0.2500	3	0.4375	0.4329
R	0.2500	0.3750	0.2501	0.3750	4	0.4375	0.4318
S	0.1875	−0.1875	0.1875	−0.1875	5	0.6875	0.7032
T	0.1875	0.9375	0.1876	0.9374	6	0.6875	0.6819

where v_r and v_z are, respectively, the radial and axial components of the velocity, and g_r and g_z equal the radial and axial components of the body force per unit mass.

The finite element mesh used to compute the solution is shown in Fig. A 1. On surfaces *AB*, *BC*, and *CD*, both v_r and v_z as given by Eq. (A 1) were prescribed, on the surface *AD*, v_r and the normal traction, equal to σ_{zz}, were specified. In this case, the specification of the state of stress at the entrance region was not needed. In Table A 1, we have listed the converged computed results and the values from the analytical solution (A 1) at various points in the domain. Recall that the pressure field is assumed to be constant within an element; this value is assigned to the centroid of the element. The pressure field at other points is interpolated from its values at the centroids of the elements.

Acknowledgements

This work was supported by the U.S. Army Research Office Contract DAAL-89-K-0050 to the University of Missouri-Rolla. Some of the computations were performed on the NSF sponsored supercomputer center at the University of Illinois at Urbana-Champaign.

References

[1] Backman, M. E., Goldsmith, W.: The mechanics of penetration of projectiles into targets. Int. J. Engng Sci. **16**, 1–99 (1978).
[2] Wright, T. W., Frank, K.: Approaches to penetration problems. SMIRT Symposium, No. 14, Impact. Lausanne, Switzerland 1987.
[3] Anderson, C. E., Bodner, S. R.: The status of ballistic impact modelling. Int. J. Impact Engng. **7**, 9–35 (1985).
[4] Zukas, J. A. et al.: Impact dynamics. New York: Wiley-Interscience 1982.
[5] Blazynski, T. Z.: In: Materials at high strain rates (Blazynski, T. Z., ed.) London, New York: Elsevier 1987.
[6] MaCauley, M.: Introduction to impact engineering. London, New York: Chapman and Hall 1987.
[7] Awerbuch, J.: Technion-Israel Institute of Technology, MED Report No. 28 (1970).
[8] Awerbuch, J., Bodner, S. R.: Analysis of the mechanics of perforation of projectiles in metallic plates. Int. J. Solids Struct. **10**, 671–684 (1974).
[9] Ravid, M., Bodner, S. R.: Dynamic perforation of viscoplastic plates by rigid projectiles. Int. J. Engng Sci. **21**, 577–591 (1983).
[10] Ravid, M., Bodner, S. R., Holeman, I.: Analysis of very high speed impact. Int. J. Engng. Sci. **25**, 473–482 (1987).
[11] Forrestal, M. J., Okajima, K., Luk, V. K.: Penetration of 6061-T651 Aluminum targets with rigid long rods. J. Appl. Mech. **55**, 755–760 (1988).

[12] Batra, R. C., Chen, X.: An approximate analysis of steady state axisymmetric deformations of viscoplastic targets. Int. J. Engng. Sci. **28**. 1347 – 1358 (1990).
[13] Birkhoff, G., MacDougall, D. P., Pugh, E. M., Taylor, G.: Explosives with lined cavities. J. Appl. Phys. **19**. 563 – 582 (1948).
[14] Pack, D. C., Evans, W. M.: Penetration by high-velocity jets. Proc. Phys. Soc. Lond. B **64**. 298 – 310 (1951).
[15] Allen, W. A., Rogers, J. W.: Penetration of a rod into a semi-infinite target. J. Franklin Inst. **272**. 275 – 284 (1961).
[16] Alekseevskii, V. P.: Penetration of a rod into a target at high velocity. Comb. Expl. and Shock Waves **2**. 63 – 66 (1966). (Translation from Russian, Faraday Press, New York)
[17] Tate, A.: A theory for the deceleration of long rods after impact. J. Mech. Phys. Solids **15**. 387 – 399 (1967).
[18] Tate, A.: Further results in the theory of long rod penetration. J. Mech. Phys. Solids **17**. 141 – 150 (1969).
[19a] Tate, A.: Long rod penetration models. Part I. A flow field model for high speed long rod penetration. Int. J. Mech. Sci. **28**. 535 – 548 (1986).
[19b] Tate, A.: Long rod penetration models. Part II. Extensions to the hydrodynamic theory of penetration. Int. J. Mech. Sci. **28**. 599 – 612 (1986).
[20] Tate, A.: A simple hydrodynamic model for the strain field in a target by the penetration of a high speed long rod projectile. Int. J. Engng. Sci. **16**. 845 – 858 (1978).
[21] Pidsley, P. H.: A numerical study of long rod impact onto a large target. J. Mech. Phys. Solids **32**. 315 – 333 (1984).
[22] Batra, R. C., Gobinath, T.: Steady state axisymmetric deformations of a thermoviscoplastic rod penetrating a thick thermoviscoplastic target. Int. J. Impact Engng. **11**. 1 – 31 (1991).
[23] Gobinath, T., Batra, R. C.: A steady state axisymmetric penetration problem for rigid perfectly plastic materials. Int. J. Engng. Sci. **29**. 1315 – 1331 (1991).
[24] Batra, R. C., Wright, T. W.: Steady state penetration of rigid perfectly plastic targets. Int. J. Engng. Sci. **24**. 41 – 54 (1986).
[25] Batra, R. C.: Steady state penetration of viscoplastic targets. Int. J. Engng. Sci. **25**. 1131 – 1411 (1987).
[26] Batra, R. C.: Steady state penetration of thermoviscoplastic targets. Comp. Mech. **3**. 1 – 12 (1988).
[27] Batra, R. C., Lin, P. R.: Steady state deformations of a rigid perfectly plastic rod striking a rigid cavity. Int. J. Engng. Sci. **26**. 183 – 192 (1988).
[28] Batra, R. C., Lin, P. R.: Steady state axisymmetric deformations of a thermoviscoplastic rod striking a hemispherical rigid cavity. Int. J. Impact Engng. **8**. 99 – 113 (1989).
[29] Batra, R. C., Lin, P. R.: Histories of stress, temperature and spin in steady state deformations of a thermoviscoplastic rod striking a hemispherical rigid cavity. Int. J. Engng. Sci. **28**. 93 – 98 (1990).
[30] Lin, P. R., Batra, R. C.: Histories of stress, strain-rate, temperature, and spin in steady state penetration problems. Int. J. Engng. Sci. **27**. 1155 – 1165 (1989).
[31] Shimazaki, Y., Thompson, E. G.: Elasto visco-plastic flow with special attention to boundary conditions. Int. J. Num. Meth. Engng **17**. 97 – 112 (1981).
[32] Hughes, T. J. R.: The finite element method. Linear static and dynamic problems. Englewood Cliffs: Prentice-Hall 1987.

Authors' address: R. Jayachandran and R. C. Batra, Department of Mechanical and Aerospace Engineering and Engineering Mechanics, University of Missouri-Rolla, Rolla, MO 65401, U.S.A.

Int. J. Engng Sci. Vol. 30, No. 8, pp. 1009–1026, 1992
Printed in Great Britain.

0020-7225/92 $5.00 + 0.00

STEADY STATE AXISYMMETRIC DEFORMATIONS OF A THICK ELASTIC–THERMOVISCOPLASTIC TARGET

R. JAYACHANDRAN and R. C. BATRA
Department of Mechanical and Aerospace Engineering and Engineering Mechanics, University of Missouri-Rolla, Rolla, MO 65401-0249, U.S.A.

Abstract—We study thermomechanical deformations of a thick elastic–viscoplastic target being penetrated by a rigid long cylindrical rod, and assume that target deformations as seen by an observer situated at the penetrator nose tip are steady. We presume that the target response can be adequately modeled by the Brown–Kim–Anand flow rule. We analyze the effect of different material parameters on the deformations of the target in order to elucidate their relative importance, and hence enumerate more critical ones. We also study the effect of the penetrator nose shape and the penetrator speed on the deformations of the target.

INTRODUCTION

One of the unresolved issues in penetration mechanics as well as in large deformation elastoplasticity is the choice of an appropriate constitutive relation used to model the finite plastic deformations of a material. Many of the recently proposed theories (e.g. [1–4]) of large deformation elastoplasticity are based on different kinematic assumptions and necessitate the hypothesizing of constitutive relations for variables that are not simply related to each other. Here we use one such theory, namely that due to Brown–Kim–Anand (hereafter referred to as BKA) [4], and study in detail the effect of varying the material parameters in it on the deformations of the target. This should help identify the critical parameters in the constitutive relation, at least for the penetration problem. A similar study was conducted earlier [5, 6] for the Litonski–Batra and the Bodner–Partom flow rules.

We refer the reader to review articles by Backman and Goldsmith [7], Wright and Frank [8], Wright [9], and Anderson and Bodner [10] for a review and discussion of most of the work done on ballistic penetration. Different engineering models have been proposed by Awerbuch [11], Awerbuch and Bodner [12], Ravid and Bodner [13], Ravid *et al.* [14], Forrestal *et al.* [15], and Batra and Chen [16]. For impact velocities in the range of 0.5–10 km/s, Birkhoff *et al.* [17], Pack and Evans [18], Allen and Rogers [19], Alekseevskii [20], and Tate [21] have proposed using the Bernoulli equation or its modification to analyze the impact phenomenon. The last three references introduced a resistive pressure, dependent upon the material strength, in the Bernoulli equation. Tate [22–24], Pidsley [25], Batra and Gobinath [26], Batra and Chen [16], and Jayachandran and Batra [27] have estimated the value of the resistive pressure. Whereas Tate used a solenoid fluid flow model of the steady state penetration process, other investigations used a numerical solution of the problem. Both Pidsley [25] and Wright [9] have pointed out that the transverse gradients of the shear stress evaluated on the axial line make noticeable contributions to the resistive pressure terms in the modified Bernoulli equation. The books by Zukas *et al.* [28], Blazynski [29], and Macauley [30] may be consulted for the available literature on ballistic penetration.

FORMULATION OF THE PROBLEM

With respect to a cylindrical coordinate system with origin at the center of the penetrator nose and positive z-axis pointing into the target, equations governing the target deformations are:

Balance of mass:

$$\operatorname{div} \mathbf{v} = 0, \tag{1}$$

Balance of linear momentum:

$$\operatorname{div}\boldsymbol{\sigma} = \rho(\mathbf{v}\cdot\operatorname{grad})\mathbf{v}, \tag{2}$$

Balance of internal energy:

$$-\operatorname{div}\mathbf{q} + \operatorname{tr}(\boldsymbol{\sigma}\mathbf{D}^p) = \rho\dot{U}, \tag{3}$$

Constitutive relations:

$$\boldsymbol{\sigma} = -p\mathbf{1} + \mathbf{s}, \tag{4.1}$$

$$\overset{\circ}{\mathbf{s}} = 2G(\mathbf{D} - \mathbf{D}^p), \tag{4.2}$$

$$\mathbf{D}^p = \mathbf{s}/2\mu(I, \theta, g), \tag{4.3}$$

$$\mu(I, \theta, g) = \frac{1}{3}\frac{g}{\xi I}\sinh^{-1}(\phi^m), \tag{4.4}$$

$$\dot{g} = h_0 I\left(\max\left(0, \left(1 - \frac{g}{g^*}\right)\right)\right)^a, \tag{4.5}$$

$$g^* = \bar{g}\phi^n, \tag{4.6}$$

$$\phi = \frac{I}{A}\exp\left(\frac{Q}{RT}\right), \tag{4.7}$$

$$q = -k\operatorname{grad}\theta, \qquad \theta = T - T_0, \tag{5}$$

$$U = c\theta, \tag{6}$$

where

$$2I^2 = \operatorname{tr}(\mathbf{D}^p)^2, \tag{7.1}$$

$$\overset{\circ}{\mathbf{s}} = (\mathbf{v}\cdot\operatorname{grad})\mathbf{s} + \mathbf{s}\mathbf{W} - \mathbf{W}\mathbf{s}, \tag{7.2}$$

$$2\mathbf{D} = \operatorname{grad}\mathbf{v} + (\operatorname{grad}\mathbf{v})^T, \tag{7.3}$$

$$2\mathbf{W} = \operatorname{grad}\mathbf{v} - (\operatorname{grad}\mathbf{v})^T. \tag{7.4}$$

Equations (1), (2), and (3) are written in the Eulerian description of motion. The operators grad and div denote the gradient and divergence operators on fields defined in the present configuration. In equations (1)–(7), $\mathbf{v}$ is the velocity of a target particle relative to the penetrator, $\boldsymbol{\sigma}$ the Cauchy stress tensor, $\mathbf{s}$ its deviatoric part, p the hydrostatic pressure not determined by the deformation history, an open circle on $\mathbf{s}$ indicates its Jaumann derivative defined by equation (7.2) for the steady stress field, $\mathbf{q}$ is the heat flux vector, and U is the specific internal energy. Furthermore, G is the shear modulus, $\mathbf{D}^p$ the plastic strain-rate, μ defined by equation (4.4) may be interpreted as the shear viscosity of the target material, g is an internal variable whose evolution rate is postulated to be given by equation (4.5), Q the activation energy, R the gas constant, T the absolute temperature, T_0 the ambient absolute temperature, m the strain-rate sensitivity, h_0 a constant rate of athermal hardening, and the quantity g^* represents a saturation value of g associated with given values of the temperature and strain-rate. In order to characterize the viscoplastic response of a material, one needs to assign values to ξ, m, h_0, a, $\bar{g}$, n, A, Q, and R. Equation (4.2) is Hooke's law in the rate form when the dependence of the shear modulus upon the mass density or the hydrostatic pressure is neglected, equation (5) is the Fourier law of heat conduction, and equation (6) is a constitutive relation for the specific internal energy. The thermal conductivity k and the specific heat c are taken to be constants. The strain-rate tensor $\mathbf{D}$ defined by equation (7.3) is assumed to have additive decomposition into elastic and plastic $\mathbf{D}^p$ parts, and $\mathbf{W}$ defined by equation (7.4) is the spin tensor.

As has been pointed out by Batra and Gobinath [26], the problem formulation does include thermal stresses caused by the uneven temperature rise at different material particles. However, the change in the mass density due to temperature rise of a material particle is not considered.

Henceforth, we use non-dimensional variables defined below and indicated by an overbar.

$$\bar{\sigma}=\frac{\sigma}{\sigma_0},\quad \bar{\mathbf{s}}=\frac{\mathbf{s}}{\sigma_0},\quad \bar{p}=\frac{p}{\sigma_0},\quad \bar{\mathbf{v}}=\frac{\mathbf{v}}{v_0},\quad \bar{r}=\frac{r}{r_0},\quad \bar{z}=\frac{z}{r_0},$$

$$\bar{I}=I\frac{r_0}{v_0},\quad \bar{b}=b\frac{v_0}{r_0},\quad \bar{\mathbf{D}}=\mathbf{D}\frac{r_0}{v_0},\quad \bar{A}=A\frac{r_0}{v_0},\quad \bar{\theta}=\frac{\theta}{\theta_0},$$

$$\theta_0=\frac{\sigma_0}{\rho c},\quad \bar{h}_c=\frac{h_c}{\rho c v_0},\quad \bar{g}=\frac{g}{\sigma_0},\quad \bar{\tilde{g}}=\frac{\tilde{g}}{\sigma_0},\quad \bar{h}_0=\frac{h_0}{\sigma_0},\quad \bar{g}^*=\frac{g^*}{\sigma_0}. \tag{8}$$

Here σ_0 is the yield stress of the target material in a quasistatic simple compression test, r_0 is the radius of the cylindrical part of the penetrator, v_0 is the steady speed of penetration, and h_c is the coefficient of heat transfer between the target and the penetrator.

The governing equations, when written in terms of nondimensional variables, become

$$\operatorname{div}\mathbf{v}=0, \tag{9.1}$$

$$-\operatorname{grad}p+\operatorname{div}\mathbf{s}=\alpha(\mathbf{v}\cdot\operatorname{grad})\mathbf{v}, \tag{9.2}$$

$$\mathbf{s}+\beta\gamma[(\mathbf{v}\cdot\operatorname{grad})\mathbf{s}+\mathbf{s}\mathbf{W}-\mathbf{W}\mathbf{s}]=2\beta\mathbf{D}, \tag{9.3}$$

$$\operatorname{tr}(\boldsymbol{\sigma}\mathbf{D}^p)+\delta\operatorname{div}(\operatorname{grad}\theta)=(\mathbf{v}\cdot\operatorname{grad})\theta, \tag{9.4}$$

where

$$\alpha=\frac{\rho v_0^2}{\sigma_0},\quad \beta=\frac{\mu v_0}{\sigma_0 r_0},\quad \gamma=\frac{\sigma_0}{G},\quad \delta=\frac{k}{\rho c v_0 r_0}, \tag{10}$$

are non-dimensional numbers, and we have dropped the overbars. Henceforth, we work in terms of nondimensional variables. The values of α, γ, and δ signity, respectively, the importance of inertia force relative to the flow stress of the material, material elasticity, and the heat transfer due to conduction.

We note that the governing equations are highly nonlinear, and we seek their approximate solution by the finite element method, which necessitates that we consider a finite region. The bounded region R of the target whose deformations are analyzed is depicted in Fig. 1, which also shows the discretization of the domain into finite elements. The boundary conditions imposed on this finite region are

$$v_r=0,\quad v_z=-1.0,\quad p=0,\quad s_{rr}=0,\quad s_{\theta\theta}=0,\quad s_{zz}=0,\quad s_{rz}=0,\quad \theta=\theta_0,$$

on the boundary surface EFA, (11.1)

$$\sigma_{rz}=0,\quad v_r=0,\quad \frac{\partial\theta}{\partial r}=0,\quad \text{on the axis of symmetry DE,} \tag{11.2}$$

$$\mathbf{v}\cdot\mathbf{n}=0,\quad \mathbf{t}\cdot(\boldsymbol{\sigma}\mathbf{n})=0,\quad \mathbf{q}\cdot\mathbf{n}=h_c(\theta-\theta_a),$$

on the target/penetrator interface DCB, (11.3)

$$\sigma_{zz}=0,\quad v_r=0,\quad \frac{\partial\theta}{\partial z}=0,\quad \text{on the bounding surface BA.} \tag{11.4}$$

The validity of replacing boundary conditions at the boundaries of the semi-infinite target region by conditions (11.1) and (11.4) on the bounding surfaces EFA and BA of the finite target region studied was established by analyzing the problem over successively larger regions

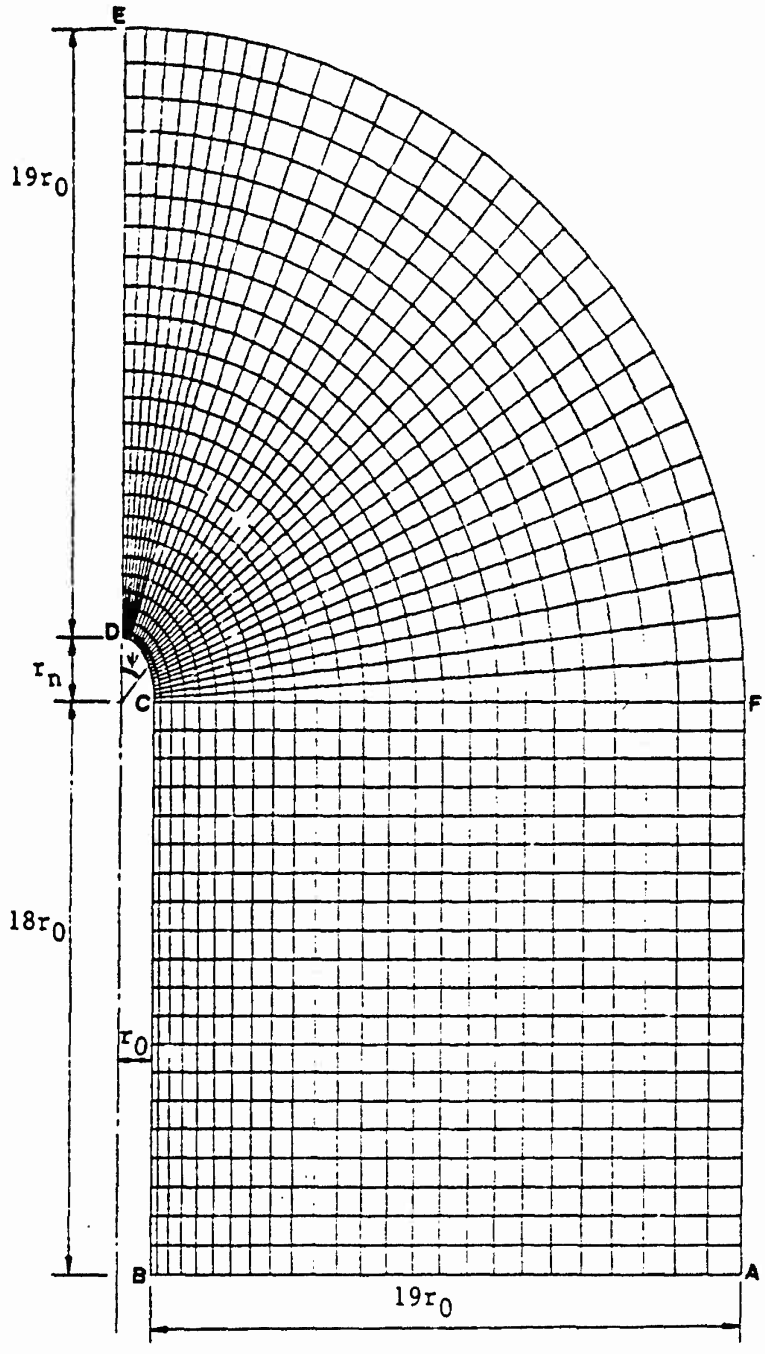

Fig. 1. Finite target region studied and its discretization.

each new region containing the previous one, until the solution variables at points on the target/penetrator interface DC changed by less than 4.7%. Of the variables p, $\mathbf{v}$, θ, $\mathbf{s}$, and g of interest, the variation in $\mathbf{s}$ was the largest and it occurred at points near the nose periphery. The boundary conditions on p and components of $\mathbf{s}$ on the surface EFA are needed, since here we need to solve equation (9.3) for $\mathbf{s}$, along with equations (9.1), (9.2), and (9.4) for p, $\mathbf{v}$ and θ; e.g. see Shimazaki and Thompson [31]. Conditions (11.2) follow from the assumed axisymmetric nature of deformations. The imposed boundary conditions (11.3) on the target/penetrator interface DCB imply that there is no interpenetration of the target material

into the penetrator, the contact surface is smooth, and the heat flux between the target and the penetrator is proportional to the temperature difference between the two; θ_a being the average temperature of the penetrator. The boundary conditions (11.4) on BA are a good approximation, provided that the surface BA is far removed from DC, as is the case here.

COMPUTATIONAL CONSIDERATIONS

As shown in Fig. 1, the region R is divided into quadrilateral elements, the elements being smaller near the target/penetrator interface DC and gradually becoming larger as we move away from this surface. There was no attempt made to optimize the mesh for a given number of nodes. However, keeping R fixed, results were computed with three successively finer meshes containing 700, 900, and 1250 elements. The peak values of p, θ, and I for these three meshes were found to be (12.07, 3.42, 1.38), (12.17, 3.69, 1.52), and (12.10, 3.67, 1.53), respectively. Henceforth, we employ the mesh with 1250 elements.

Within each element the values of v_r, v_z, s_{rr}, s_{rz}, s_{zz}, $s_{\theta\theta}$, θ, and g are approximated by bilinear polynomials expressed in terms of their values at the four corner nodes, and the hydrostatic pressure p is assumed to be constant. The discontinuous pressure field $\bar{p}$ thus computed is smoothened *a posteriori* by using

$$\sum_{j=1}^{M}\left(\int_R N_i N_j \, dV\right)p_j = \int_R N_i \bar{p} \, dV, \qquad i = 1, 2, \ldots, M \tag{12}$$

where M equals the number of nodes, and $N_1, N_2, \ldots, N_M$ are the piecewise bilinear finite element basis functions.

We used the Petrov–Galerkin formulation [32] of equations (9.3) and (9.4), and the Galerkin approximation [32] of equations (9.1) and (9.2). The iterative process used to solve the resulting nonlinear algebraic equations was stopped when

$$\left(\sum \|\phi^m - \phi^{m-1}\|^2\right)^{1/2} \leq 0.01\left(\sum \|\phi^m\|^2\right)^{1/2} \tag{13}$$

where the summation sign implies the sum of the value of the indicated quantity at all nodes, $\|\phi\|^2 = \mathrm{tr}(\phi\phi^T)$ when ϕ is a second order tensor, $\|\phi\|^2 = \phi_r^2 + \phi_z^2$ when ϕ is a vector, and $\|\phi\| = |\phi|$ when ϕ is a scalar. The convergence criterion (13) is applied to v's, θ, p, and g. This convergence criterion is weaker than that used by Batra [5], who checked for the convergence of the solution variables at each node. Batra used 6-noded triangular elements and approximated the solution variables, except for p, by piecewise quadratic polynomials, and p by piecewise linear polynomials defined in terms of their values at the three corner nodes.

The code developed by Jayachandran and Batra [27] was modified to solve the present problem. The boundary condition $(11.3)_1$ on the target/penetrator interface is satisfied by using the method of Lagrange multipliers.

RESULTS AND DISCUSSION

When computing results, we assigned the following values to various material and geometric parameters.

$$\rho = 7860\ \mathrm{kg/m^3}, \quad \sigma_0 = 405\ \mathrm{MPa}, \quad G = 80\ \mathrm{GPa}, \quad c = 473\ \mathrm{J/kg\,^\circ C},$$
$$k = 50\ \mathrm{W/m\,^\circ C}, \quad h_c = 20\ \mathrm{W/m^2\,^\circ C}, \quad \theta_a = 0^\circ\mathrm{C}, \quad r_0 = 10\ \mathrm{mm},$$
$$A = 6.346 \times 10^{15}\ \mathrm{s^{-1}}, \quad Q = 275\ \mathrm{kJ/mol}, \quad \bar{g} = 405\ \mathrm{MPa}, \quad h_0 = 5000\ \mathrm{MPa},$$
$$\xi = 3.25, \quad m = 0.1, \quad n = 0.002, \quad a = 1.5, \quad \alpha = 10, \quad r_n = 1.0. \tag{14}$$

Here $2r_n$ equals the length of the principal axis of the elliptical penetrator nose in the z-direction. For the values of ρ, σ_0, and c given above, the reference temperature θ_0 used to nondimensionalize the temperature rise equals 108.9°C. Since we are interested in delineating the effect of different values of material and geometric parameters in the BKA flow rule on the deformations of the target, the base values assigned as in (14) to different parameters are of less significance. The present study should enumerate the relative importance of various material parameters and hence help design experiments for the precise determination of more critical ones. The range of values of material parameters considered herein is probably more than that likely to occur for any real material. The variables that are assigned values different from those given above are so indicated in the figures along with their new values.

All of the results presented below and values of variables indicated in figures, unless stated otherwise, are non-dimensional.

(a) Effect of penetration speed

Figure 2 depicts, for $\alpha = 2, 6, 8$, and 10, the variation of the normal stress, strain-rate measure I, tangential speed, and the temperature rise at target particles abutting the hemispherical penetrator nose surface. The angular position ψ, indicated in Fig. 1, is measured from the centroidal axis. In this and other figures, various quantities have been scaled appropriately so as to fit on the same plot. The normal stress on the penetrator nose surface is independent of α for $\psi \approx 45°$, and the normal stress at a point on the penetrator nose surface increases with α for $\psi < 45°$ and the reverse happens for $\psi > 45°$. Such a behavior was also observed by Batra and Wright [33] for a rigid plastic target, by Jayachandran and Batra [27] for

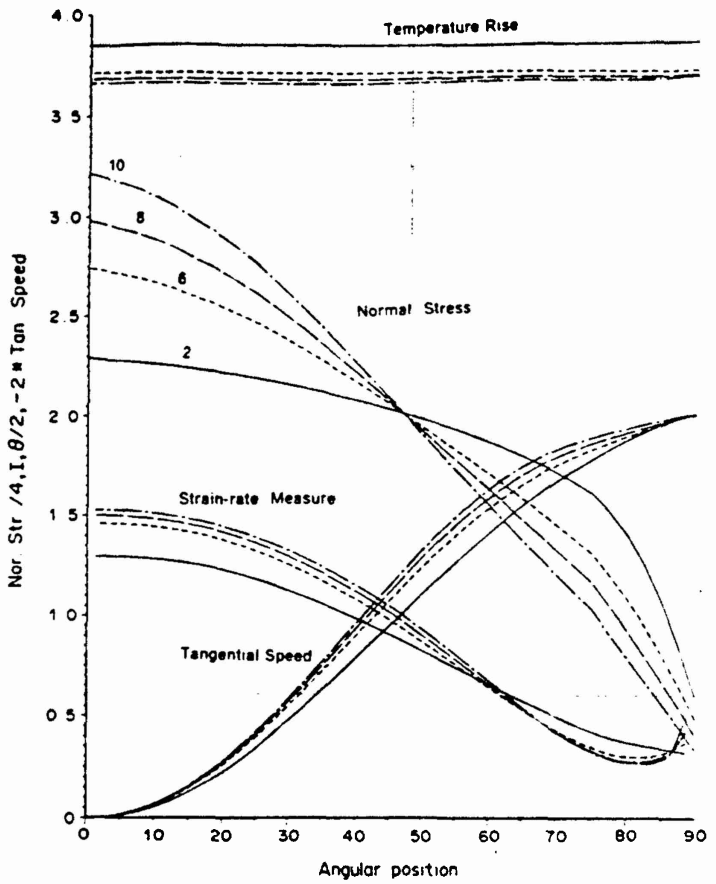

Fig. 2. Distribution of the tangential speed, strain-rate measure, normal stress, and the temperature rise at target particles on the penetrator nose surface for $\alpha = 2, 6, 8$, and 10.

an elastic–plastic target, by Batra [5] for a viscoplastic target obeying the Litonski–Batra flow rule, and by Batra and Adam [6] for a viscoplastic target following the Bodner–Partom flow law. The values of the nondimensional strain-rate measure I at and near the penetrator nose tip decrease with an increase in the value of α. We note that the change in the dimensional values of I is more than that in the nondimensional values since the former are obtained by multiplying the latter by v_0/r_0. However, the temperature rise is nearly uniform over the penetrator nose surface, and its value decreases with an increase in the value of α, mainly because more heat is transferred due to convection at higher speeds. We note that Batra [5], and Batra and Adam [6] observed similar behavior for the Litonski–Batra and Bodner–Partom flow rules, respectively.

In Fig. 3 we have plotted the variation of the strain-rate measure I, temperature rise θ, $(-\sigma_{zz})$, and the axial velocity for $\alpha = 2, 6, 8$, and 10. Whereas the strain-rate measure I and the temperature rise drop sharply as one moves away from the nose tip, the value of $(-\sigma_{zz})$ decreases slowly to zero mainly because the hydrostatic pressure p drops off slowly with the axial distance from the nose surface. For $\alpha = 10$, $v_0 = 771$ m/s, and the peak values of I and the temperature rise equal, respectively, $3.55 \times 10^5\ s^{-1}$ and 408°C. It seems that there is a thin layer of material, of thickness nearly $0.2r_0$, around the penetrator nose surface in which the temperature rise is quite high. Severe deformations of the target material occur at particles situated within a distance of $3r_0$ from the penetrator nose surface. Thus, the target region studied is quite adequate.

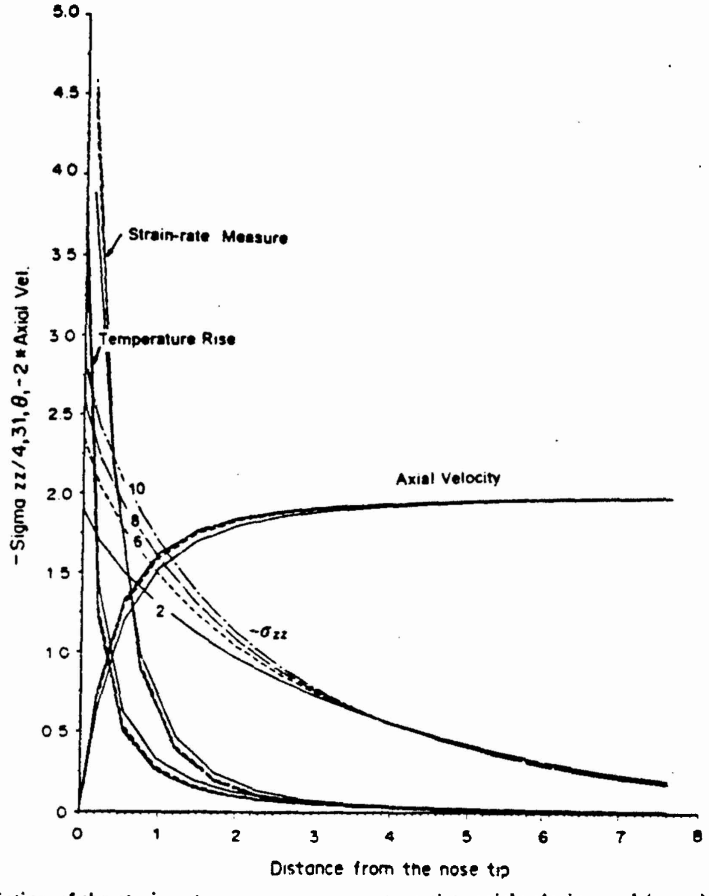

Fig. 3. Variation of the strain-rate measure, temperature rise, axial velocity, and $(-\sigma_{zz})$ at points on the axial line for $\alpha = 2, 6, 8$, and 10.

by the value of n. The dependence of the tangential speed upon n is rather weak, as is the dependence of all quantities upon n at points situated more than $2r_0$ from the penetrator nose tip. For each value of n considered herein, the axial stress decays slowly with the distance from the nose tip.

In Fig. 10 we have plotted the variation, on the penetrator nose surface, of the tangential speed, strain-rate measure I, normal stress and the temperature rise for strain-rate hardening parameter $m = 0.01$, 0.02, 0.05, 0.1, 1.0, and 10.0. The curves for $m \geq 0.1$ overlap each other, indicating the saturation of the strain-rate hardening effects. Whereas the values of I and the tangential speed decrease those of the normal stress and the temperature rise increase with an increase in the value of m. For $m = 0$, the target particles tended to separate away from the penetrator nose surface near the nose periphery. Hence, results for this case are not included herein. For the aforestated values of m, the hydrostatic pressure p at the stagnation point equals 8.87, 10.63, 12.04, 12.10, 12.10, and 12.10, respectively. Thus, an increase in the value of the normal stress is due to both an increase in the value of p and the enhanced hardening of the material for higher values of m in the range $0.01 \leq m \leq 0.1$. In this case the temperature rise is almost evenly distributed on the target/penetrator interface. On the axial line (cf. Fig. 11), the values of I and the tangential speed seem not to depend upon m. However, the values of the temperature rise and the axial stress $(-\sigma_{zz})$ are influenced by the value of m considered. The curves depicting the variation of the axial stress and the temperature rise with z, the distance from the nose tip, for $m = 0.05$, 0.1, and 10.0 essentially coincide with each other.

The axial resisting force F (cf. Fig. 4) experienced by the penetrator increases sharply when

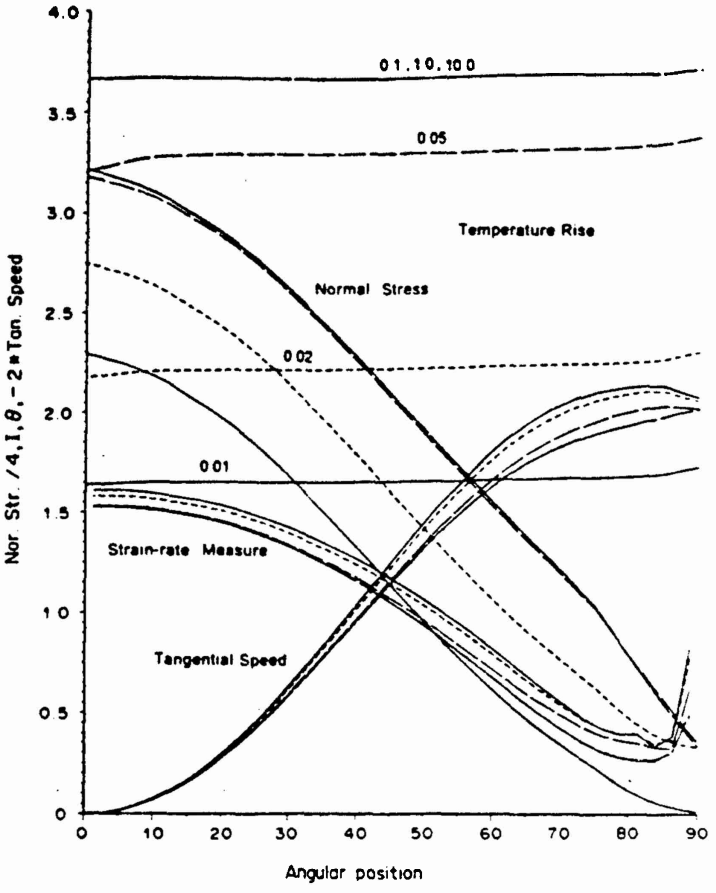

Fig. 10. Effect of different values of the strain-rate hardening parameter m on the distribution of the normal stress, tangential speed, temperature rise, and the strain-rate measure on the penetrator nose surface.

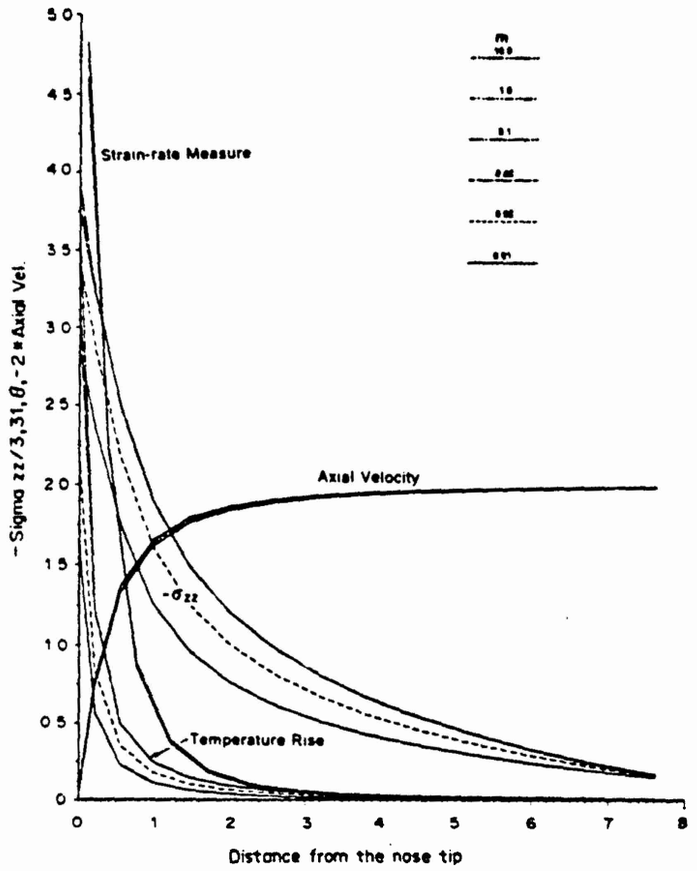

Fig. 11. Effect of m on the variation of the normal stress, axial velocity, temperature rise, and the strain-rate measure on the axial line.

the value of m is increased from 0.01 to 0.1, but levels off subsequently. Out of the other parameters, h_0, $\bar{g}$, and Q that increase the hardening of the material, F depends strongly upon $\bar{g}$ and rather weakly upon h_0. The values of F increase rapidly with an increase in the value of Q for $Q \leq 150$ kJ/mol, and then quite slowly.

Figure 12 depicts the distribution of the strain-rate measure I, tangential speed, normal stress, and the temperature rise on the penetrator nose surface for $a = 0.01$, 0.1, 1.5, 3, 10, and 100. The values of I and the tangential speed are affected very little by the value of a. Also, the values of $a \leq 0.1$ and $a \geq 3.0$ have negligible effect on target deformations. The normal stress and the temperature rise decrease with an increase in the value of a from 0.1 to 3.0. We note that the value of a is usually selected to represent best the experimental hardening curves. The axial resisting force F experienced by the penetrator decreases when a is increased from 0.1 to 3.0, and stays constant subsequently. As evidenced by the results plotted in Fig. 13, the values, at points on the axial line, of the temperature rise, strain-rate measure, axial speed, and the axial stress are affected very little by the value of a. The effect of changing the value of the pre-exponential factor A on the distribution of the aforementioned four variables is shown in Fig. 14. The values of the temperature rise and the normal stress decrease, and those of the tangential speed and the strain-rate measure I increase with an increase in the value of A. Equations (4.6) and (4.7) suggest that an increase in the value of A reduces the saturation value g^* of g. When g equals g^*, further resistance to flow does not develop. The results plotted in Fig. 4 indicate that the axial resisting force experienced by the penetrator decreases noticeably with an increase in the value of A.

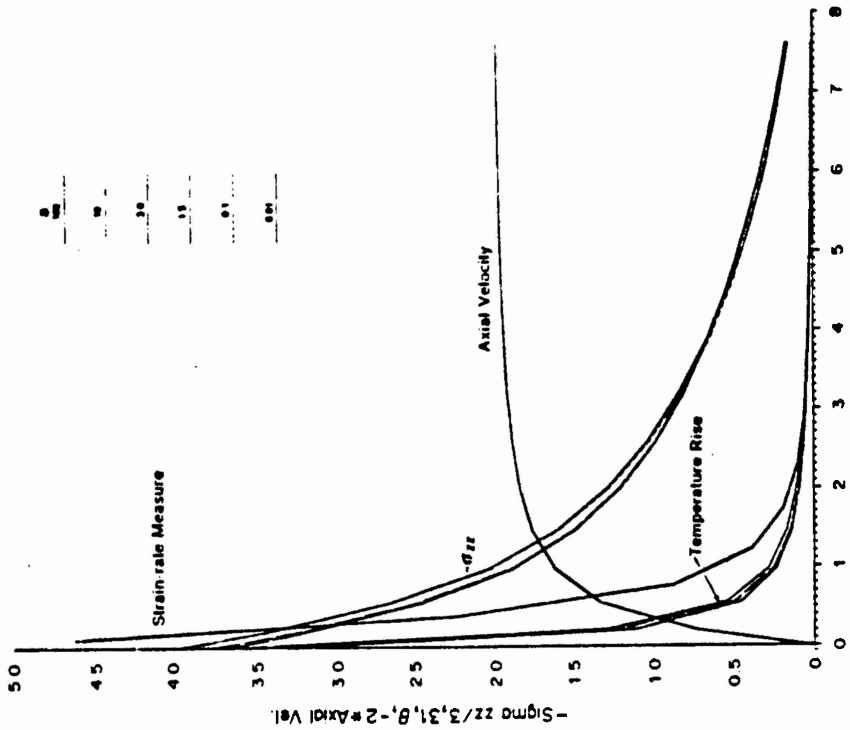

Fig. 13. Effect of a on the variation of the normal stress, axial velocity, temperature rise, and the strain-rate measure on the axial line.

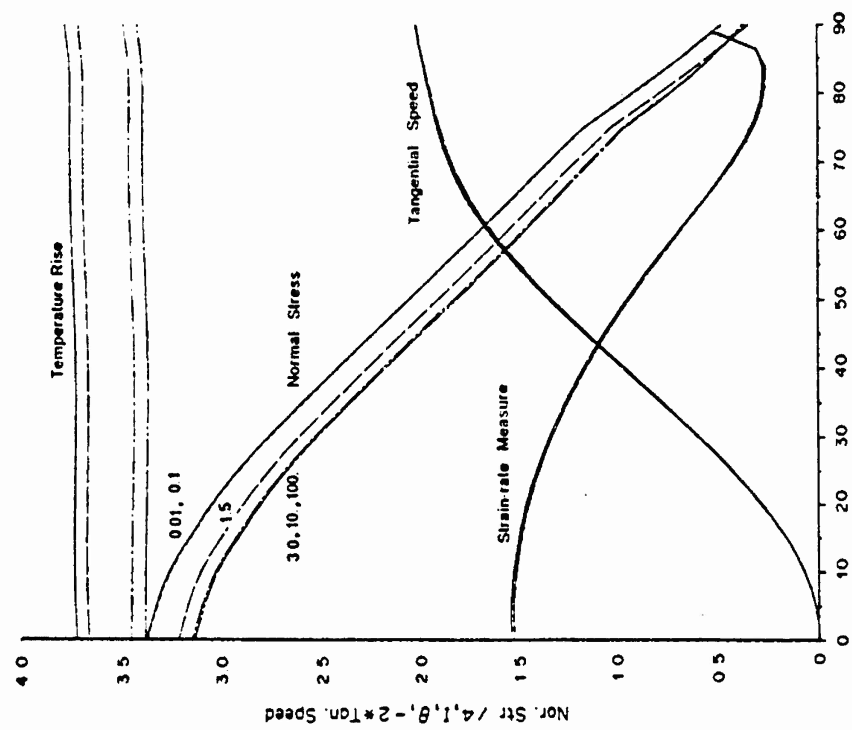

Fig. 12. Distribution of the temperature rise, normal stress, strain-rate measure, and the tangential speed on the penetrator nose surface for different values of a.

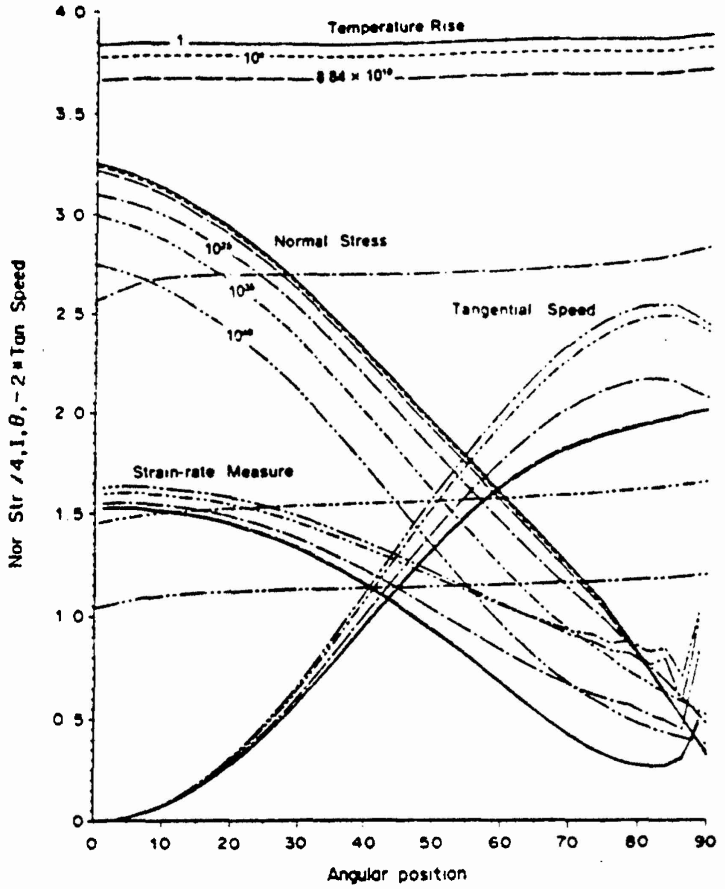

Fig 14. Effect of different values of A on the distribution of the temperature rise, normal stress, strain-rate measure, and the tangential speed on the penetrator nose surface.

CONCLUSIONS

We have studied the steady state axisymmetric deformations of a thermoelastic–viscoplastic target being penetrated by a long rigid cylindrical rod by the finite element method, using bilinear quadrilateral elements. The target material is modeled by a viscoplastic flow rule proposed recently by BKA. Within each element, the fields of the velocity, deviatoric stress tensor, temperature, and an internal variable are approximated by bilinear polynomials, and the hydrostatic pressure is assumed to be constant. It is found that the axial resisting force experienced by the penetrator depends weakly upon the penetration speed. The material strength parameter, introduced by Tate, in the modified Bernoulli equation, is found not to depend upon the penetrator nose shape. The material parameters that enhance the hardening of the material in plane strain compression of a block made of the target material increase the axial resisting force acting on the penetrator. The severe deformations of the target are confined to material particles situated at most one penetrator diameter away from the target/penetrator interface. Thus, the target region analyzed herein is adequate, and the computed results do not depend upon the extent of the domain analyzed.

Acknowledgements—This work was supported by the U.S. Army Research Office Contract DAAL89-K-0050 to the University of Missouri-Rolla. Some of the computations were performed on the NSF sponsored supercomputer center at the University of Illinois at Urbana–Champaign.

REFERENCES

[1] E. H. LEE, *J. Appl. Mech.* **36**, 1 (1969).
[2] S. NEMAT-NASSER, in *Proc. Symp. Plasticity Today* (Edited by A. SAWCZUK), Elsevier, London (1983).
[3] Y. F. DAFALIAS, *Proc. Current Theories of Plasticity and Their Applications*. Univ. of Oklahoma-Norman, Okla (1984).
[4] S. B. BROWN, K. H. KIM and L. ANAND, *Int. J. Plasticity* **5**, 95 (1989).
[5] R. C. BATRA, *Comp. Mech.* **3**, 1 (1988).
[6] R. C. BATRA and A. ADAM, *Int. J. Engng Sci.* **29**, 1391 (1991).
[7] M. E. BACKMAN and W. GOLDSMITH, *Int. J. Engng Sci.* **16**, 1 (1978).
[8] T. W. WRIGHT and K. FRANK, Approaches to Penetration Problems, *SMIRT Symposium*, No. 14, Impact. Lausanne, Switzerland (1987).
[9] T. W. WRIGHT, in *Lecture Notes in Engineering*, Vol. 3, Computational Aspects of Penetration Mechanics (Edited by J. CHANDRA and J. FLAHERTY). Springer, New York (1983).
[10] C. E. ANDERSON and S. R. BODNER, *Int. J. Impact Engng* **7**, 9 (1988).
[11] J. AWERBUCH, Technion-Israel Institute of Technology, MED Report No. 28 (1970).
[12] J. AWERBUCH and S. R. BODNER, *Int. J. Solids and Structures* **10**, 671 (1974).
[13] M. RAVID and S. R. BODNER, *Int. J. Engng Sci.* **21**, 577 (1983).
[14] M. RAVID, S. R. BODNER and I. HOLCMAN, *Int. J. Engng Sci.* **25**, 473 (1987).
[15] M. J. FORRESTAL, K. OKAJIMA and V. K. LUK, *J. Appl. Mech.* **55**, 755 (1988).
[16] R. C. BATRA and XINGJU CHEN, *Int. J. Engng Sci.* **28**, 1347 (1990).
[17] G. BIRCKOFF, D. P. MCDOUGALL, E. M. PUGH and G. TAYLOR, *Proc. Phys. Soc. Lond.* **57**, 147 (1945).
[18] D. C. PACK and W. M. EVANS, *Proc. Phys. Soc. Lond.* **B64**, 298 (1951).
[19] W. A. ALLEN and J. W. ROGERS, *J. Franklin Inst.* **272**, 275 (1961).
[20] V. P. ALEKSEEVSKII, *Comb. Expl. Shock waves* **2**, 63 (1966). (Translation from Russian, Faraday Press, New York.)
[21] A. TATE, *J. Mech. Phys. Solids* **15**, 387 (1967).
[22] A. TATE, *J. Mech. Phys. Solids* **17**, 141 (1969).
[23] A. TATE, *Int. J. Mech. Sci.* **28**, 535 (1986).
[24] A. TATE, *Int. J. Mech. Sci.* **28**, 599 (1986).
[25] P. H. PIDSLEY, *J. Mech. Phys. Solids* **32**, 315 (1984).
[26] R. C. BATRA and T. GOBINATH, *Int. J. Impact Engng* **11**, 1 (1991).
[27] R. JAYACHANDRAN and R. C. BATRA, *Acta Mech.* In press (1992).
[28] J. A. ZUKAS *et al.*, *Impact Dynamics*. Wiley-Interscience, New York (1982).
[29] T. Z. BLAZYNSKI, in *Materials at High Strain Rates* (Edited by T. Z. BLAZYNSKI). Elsevier, London (1987).
[30] M. MACAULEY, *Introduction to Impact Engineering*. Chapman & Hall, London (1987).
[31] Y. SHIMAZAKI and E. G. THOMPSON, *Int. J. Num. Meth. Engng* **17**, 97 (1981).
[32] T. J. R. HUGHES, *The Finite Element Method. Linear Static and Dynamic Problems*. Prentice-Hall, Englewood Cliffs, New York (1987).
[33] R. C. BATRA and T. W. WRIGHT, *Int. J. Engng Sci.* **24**, 41 (1986).

(Revision received 21 November 1991; accepted 16 December 1991)

Int. J. Engng Sci. Vol. 29, No. 11, pp. 1391–1408, 1991
Printed in Great Britain.

0020–7225/91 $3.00 + 0.00

EFFECT OF VISCOPLASTIC FLOW RULES ON STEADY STATE PENETRATION OF THERMOVISCOPLASTIC TARGETS

R. C. BATRA and ASLAM ADAM

Department of Mechanical and Aerospace Engineering and Engineering Mechanics, University of Missouri–Rolla, Rolla, MO 65401-0249, U.S.A.

Abstract—Steady state thermomechanical deformations of a thick viscoplastic target being penetrated by a fast moving long rigid cylindrical penetrator are analysed by the finite element method. Two different constitutive relations, the Bodner–Partom flow rule, and the Litonski–Batra flow rule, are used to model the viscoplastic response of the material. The two flow rules are adjusted to give essentially similar shear stress–shear strain curves during the overall adiabatic simple shearing deformations of a block deformed at an average strain-rate of 3300 s^{-1}. For the Bodner–Partom flow rule, the effect on target deformations of the penetrator nose shape, penetrator speed, and the variation in the values of material parameters of the target is also studied.

1. INTRODUCTION

Given the penetrator and target geometries, materials, target support conditions, penetrator speed, and the angle of attack, one would like to find out whether or not the target will be perforated, and if yes, the speed of the penetrator when it comes out of the target. If not, the shape and size of the hole made in the target is of interest. A complete analysis of this problem within reasonable resources is still not possible. There have been numerous attempts made to analyze simplified versions of the problem. Backman and Goldsmith [1] have reviewed the open literature on ballistic penetration till 1977. It describes various physical mechanisms involved in the penetration and perforation processes, and also discusses many engineering models. Other review articles and books include those by Wright and Frank [2], Anderson and Bodner [3], Zukas *et al.* [4], Blazynski [5], and Macauley [6]. Ravid and Bodner [7], Ravid *et al.* [8], and Forrestal *et al.* [9] have proposed engineering models of varying complexity.

When a fast moving long rod strikes a very thick target, the deformations of the two appear to be steady to an observer situated at the stagnation point and moving with it after the rod has penetrated into the target a few rod diameters. This steady state lasts until the stagnation point reaches close to the other end of the target. For very high striking speeds, the steady deformations of the target and the penetrator can be assumed to be governed by purely hydrodynamic incompressible flow processes. Tate [10, 11] and Alekseevskii [12] modified this model by incorporating the effects of material strengths of the target and the projectile. These were assumed to equal some multiple of the uniaxial yield stress of the respective materials, but the multiplying factor was unspecified. Tate [13, 14], Pidsley [15], Batra and Gobinath [16], and Batra and Chen [17] have estimated these multiplying factors. Whereas Tate used a solenoidal fluid flow model to simulate the steady state penetration process, the other investigations relied on a numerical solution of the problem.

One of the unresolved issues in penetration mechanics is the choice of the most appropriate constitutive relation for the penetrator and target materials. In order to assess the effect of the constitutive models used for the target material, we presume herein that the penetrator is rigid and use two different constitutive relations for the target material. The two constitutive relations give virtually the same shear stress–shear strain curves during the numerical simulation of overall adiabatic simple shearing of a viscoplastic block deformed at an average strain-rate of 3300 s^{-1}. For the Bodner–Partom flow rule [18], the effect of varying the penetrator nose shape, the penetration speed, and the values of material parameters on the deformations of the target has also been explored. A similar study for the Litonski–Batra flow rule has already been conducted by Batra [19].

2. FORMULATION OF THE PROBLEM

We use a cylindrical coordinate system, with origin at the center of the penetrator nose and moving with it at a uniform speed v_0 and positive z-axis pointing into the target. Equations governing the thermomechanical deformations of the target are:

$$\operatorname{div}\mathbf{v} = 0, \tag{2.1}$$

$$\operatorname{div}\boldsymbol{\sigma} = \rho(\mathbf{v}\cdot\operatorname{grad})\mathbf{v}, \tag{2.2}$$

$$-\operatorname{div}\mathbf{q} + \operatorname{tr}(\boldsymbol{\sigma}\mathbf{D}) = \rho(\mathbf{v}\cdot\operatorname{grad})U, \tag{2.3}$$

$$\mathbf{D} = (\operatorname{grad}\mathbf{v} + (\operatorname{grad}\mathbf{v})^T)/2. \tag{2.4}$$

Equations (2.1)–(2.3), written in the Eulerian description of motion, express, respectively, the balance of mass, balance of linear momentum, and the balance of internal energy. Here we have neglected elastic deformations of the target, and assumed that plastic deformations are isochoric and all of the plastic working, rather than 90–95% of it as asserted by Farren and Taylor [20] is converted into heating. The operators grad and div denote the gradient and divergence operators on fields defined in the present configuration. Furthermore, $\boldsymbol{\sigma}$ is the Cauchy stress tensor, ρ the mass density of the target material, $\mathbf{v}$ the velocity of the target particle relative to the penetrator, $\mathbf{q}$ the heat flux per unit present area, $\mathbf{D}$ the strain-rate tensor, and U the specific internal energy. We need to specify constitutive relations and boundary conditions in order to complete the formulation of the problem.

For the target material, we assume that

$$\mathbf{q} = -k\operatorname{grad}\theta, \tag{2.5}$$

$$U = c\theta \tag{2.6}$$

and either the Litonski–Batra flow rule [19]

$$\boldsymbol{\sigma} = -p\mathbf{1} + 2\mu(I, \theta, \psi)\mathbf{D}, \tag{2.7}$$

$$2\mu(I, \theta, \psi) = \frac{\sigma_0}{\sqrt{3}\,I}(1 + bI)^e(1 - \nu\theta)(1 + \psi/\psi_0)^q, \tag{2.8}$$

$$\operatorname{tr}(\boldsymbol{\sigma}\mathbf{D}) = \sigma_0\dot{\psi}(1 + \psi/\psi_0)^q, \tag{2.9}$$

$$I^2 = \frac{1}{2}\operatorname{tr}(\mathbf{D}^2), \tag{2.10}$$

or the Bodner–Partom flow rule [18]

$$\mathbf{s} = \left(z_2\Big/\left(\sqrt{3}\,I\left[\frac{2n}{n+1}\ln(D_0/I)\right]^{1/2n}\right)\right)\mathbf{D}, \qquad \mathbf{s} = \boldsymbol{\sigma} + p\mathbf{1} \tag{2.11}$$

$$n = \frac{a}{T}, \qquad z_2 = z_1 + (z_3 - z_1)\exp(-mW/z_3), \tag{2.12}$$

$$\dot{W} = \operatorname{tr}(\boldsymbol{\sigma}\mathbf{D}) = \operatorname{tr}(\mathbf{s}\mathbf{D}). \tag{2.13}$$

Equation (2.5) is the Fourier law of heat conduction, k the constant thermal conductivity, θ is the change in the temperature of a material particle from that in the undeformed configuration, c the constant specific heat, p the hydrostatic pressure not determined by the deformation history, and σ_0 is the yield stress in a quasistatic simple tension or compression test. The constitutive relation (2.7) was proposed by Batra [19]. It incorporates and generalizes that suggested by Litonski [21] for simple shearing deformations. Batra and his coworkers [19, 22–24] have used it to study thermomechanical penetration problems, and the initiation and growth of shear bands in viscoplastic materials. In equations (2.7) and (2.8), the material parameters b and e characterize the strain-rate sensitivity of the material, ν describes its thermal softening, and ψ_0 and q the strain hardening of the material. Equation (2.9) states that

the rate of increase of ψ at a material point is proportional to the plastic working there. Thus, the present value of ψ depends upon the history of the deformation. The linear dependence of the flow stress upon the temperature rise has been used by Tate [25] in the analysis of a penetration problem, and has been observed by Bell [26], Lin and Wagoner [27], and Lindholm and Johnson [28]. I^2 defined by equation (2.10) equals the second-invariant of the strain-rate tensor, since the deformations are taken to be isochoric. Should the temperature rise at a material point exceed $1/\nu$ so as to make μ negative, we set $\mu = 0$. Thus, the material point will behave like an incompressible fluid. However, no account is taken of the latent heat needed for the phase transformation to occur.

In equations (2.11)–(2.13), $\mathbf{s}$ is the deviatoric stress tensor, T the absolute temperature of a material particle, W the plastic work done, and z_2 may be considered as an internal variable whose present value at a material point depends upon the density of the plastic work done at that point. D_0 is the limiting value of the plastic strain-rate, and is usually assigned a large value. Besides D_0, we need to specify a, z_1, z_3, and m to characterize the material. We identify the parameter a with the melting temperature of the material, and once T equals a, we set $\mathbf{s} = \mathbf{0}$, analogous to what we did for the Litonski–Batra flow rule.

We note that there is no loading or explicit yield surface assumed with either (2,7) or (2.11). The limiting value of $s_e = (1/2 \operatorname{tr} \mathbf{s}^2)^{1/2}$ as I approaches zero is $\sigma_0/\sqrt{3}$ for the Litonski–Batra law, and is zero for the Bodner–Partom law.

Rewriting equation (2.7) as

$$\boldsymbol{\sigma} = -(\bar{p} + \beta K\theta)\mathbf{1} + 2\mu(I, \theta, \psi)\mathbf{D}, \tag{2.14}$$

where β and K equal, respectively, the coefficient of thermal expansion and the bulk modulus of the material, we see that equation (2.7) embodies implicitly thermal stresses caused by the nonuniform temperature rise at different material particles. However, the change in the mass density due to temperature rise of a material particle is not considered. In equation (2.14), $\bar{p}$ is not determined by the deformation history of a material particle, and the addition of a determinate term to it gives rise to p in equation (2.7), which is taken to be an independent variable throughout this work.

We introduce non-dimensional variables, indicated below by a superimposed bar, as follows:

$$\begin{gathered}
\bar{\boldsymbol{\sigma}} = \boldsymbol{\sigma}/\sigma_0, \quad \bar{p} = p/\sigma_0, \quad \bar{\mathbf{v}} = \mathbf{v}/v_0, \quad \bar{r} = r/r_0, \\
\bar{z} = z/r_0, \quad \bar{\theta} = \theta/\theta_0, \quad \bar{T} = T/T_0, \quad \bar{b} = bv_0/r_0, \\
\bar{\nu} = \nu\theta_0, \quad \alpha = \rho v_0^2/\sigma_0, \quad \bar{k} = k/(\rho c v_0 r_0), \quad T_0 = \theta_0 + 273, \\
\theta_0 = \sigma_0/(\rho c), \quad \bar{\mathbf{s}} = \mathbf{s}/\sigma_0, \quad \bar{z}_2 = z_2/\sigma_0, \quad \bar{z}_1 = z_1/\sigma_0, \\
\bar{z}_3 = z_3/\sigma_0, \quad \bar{W} = W/\sigma_0, \quad \bar{D}_0 = D_0 v_0/r_0, \quad \bar{a} = a/\theta_0, \\
\bar{h} = h/(v_0\rho c).
\end{gathered} \tag{2.15}$$

Here r_0 is the radius of the cylindrical part of the penetrator and the heat transfer coefficient h appears in the boundary condition (2.25) below. Substituting from equations (2.5) and (2.6) into equation (2.3), rewriting it and equations (2.1), (2.2), (2.4), and the constitutive relations (2.7) and (2.11) in terms of non-dimensional variables, and dropping the superimposed bars, we arrive at the following set of equations.

$$\operatorname{div} \mathbf{v} = 0, \tag{2.16}$$

$$\operatorname{div} \mathbf{v} = \alpha(\mathbf{v} \cdot \operatorname{grad})\mathbf{v}, \tag{2.17}$$

$$\operatorname{tr}(\boldsymbol{\sigma}\mathbf{D}) + k \operatorname{div}(\operatorname{grad} \theta) = (\mathbf{v} \cdot \operatorname{grad})\theta, \tag{2.18}$$

where either

$$\boldsymbol{\sigma} = -p\mathbf{1} + \frac{1}{\sqrt{3}\, I}(1 + bI)^r(1 - \nu\theta)(1 + \psi/\psi_0)^q\mathbf{D}, \tag{2.19}$$

$$\frac{\operatorname{tr}(\boldsymbol{\sigma}\mathbf{D})}{(1 + \psi/\psi_0)^q} = (\mathbf{v} \cdot \operatorname{grad})\psi, \tag{2.20}$$

or

$$\boldsymbol{\sigma} = -p\mathbf{1} + \left(z_2 \Big/ \left(\sqrt{3}\, I \left[\frac{2n}{n+1} \ln(D_0/I)\right]^{1/2n}\right)\right)\mathbf{D}, \tag{2.21}$$

$$\mathrm{tr}\,(\boldsymbol{\sigma}\mathbf{D}) = (\mathbf{v} \cdot \mathrm{grad})W, \tag{2.22}$$

and n, and z_2 are given by expressions (2.12).

We assume that the target/penetrator interface is smooth, and impose on it the following boundary conditions.

$$\mathbf{t} \cdot (\boldsymbol{\sigma}\mathbf{n}) = 0, \tag{2.23}$$

$$\mathbf{v} \cdot \mathbf{n} = 0, \tag{2.24}$$

$$\mathbf{q} \cdot \mathbf{n} = h(\theta - \theta_a), \tag{2.25}$$

where h is the heat transfer coefficient between the penetrator and the target, θ_a is an average temperature of the penetrator, and $\mathbf{n}$ and $\mathbf{t}$ are, respectively, a unit normal and a unit tangent vector to the surface. Equation (2.25) accounts approximately for the heat exchange between the penetrator and the target. At points far away from the penetrator

$$|\mathbf{v} + \mathbf{e}| \to 0, \quad \theta \to 0, \quad \psi \to 0, \quad W \to 0 \text{ as } (r^2 + z^2)^{1/2} \to \infty, \quad z > -\infty, \tag{2.26}$$

$$|\boldsymbol{\sigma}\mathbf{n}| \to 0, \quad |\mathbf{q} \cdot \mathbf{n}| \to 0, \quad \psi \to 0, \quad W \to 0 \text{ as } z \to -\infty, \quad r \geq r_0, \tag{2.27}$$

where $\mathbf{e}$ is a unit vector along the positive z-axis. The boundary condition (2.26) implies that target particles at a large distance from the penetrator appear to be moving at a uniform velocity with respect to it, and experience no change in their temperature. Equation (2.27) states that when target particles have moved far to the rear of the penetrator, the surface tractions and heat flux on them vanish. Recalling the constitutive relations (2.7) and (2.11), we see that the vanishing of surface tractions at far away points does not imply that the pressure there vanishes. Ideally, one should specify the rate of decay of quantities in equations (2.26) and (2.27). However, at this time, there is no hope of proving an existence or uniqueness theorem for an analytical solution of the stated problem. We, therefore, gloss over this rather difficult issue. Herein we assume that the aforestated problem has a solution and seek its approximation by the finite element method.

3. COMPUTATIONAL CONSIDERATIONS

Unless one uses special infinite elements, a numerical solution of the problem necessitates that we consider a finite region. Since the target deformations are assumed to be axisymmetric, only the deformations of the target region R shown in Fig. 1 are studied, and the boundary conditions (2.26) and (2.27) at the far surfaces are replaced by the following conditions (3.1) and (3.3) on the boundary surfaces of the finite region being analyzed.

$$\sigma_{zz} = 0, \quad v_r = 0, \quad \frac{\partial \theta}{\partial z} = 0 \quad \text{on the surface } AB, \tag{3.1}$$

$$\sigma_{rz} = 0, \quad v_r = 0, \quad \frac{\partial \theta}{\partial r} = 0 \quad \text{on the axis of symmetry } DE, \tag{3.2}$$

$$v_r = 0, \quad v_z = -1.0, \quad \theta = 0, \quad \psi = 0, \quad W = 0 \quad \text{on the boundary surface } EFA. \tag{3.3}$$

Conditions (3.2) follow from the assumed symmetry of deformations. The validity of replacing (2.26) by (3.3), and (2.27) by (3.1), and the accuracy of the computed results depend upon the size of the region R. Keeping DE fixed, we increased the distance BC until the change in the values of solution variables such as the pressure p, velocity $\mathbf{v}$, and tempeature θ at points in the vicinity of the target/penetrator interface was less than 0.1%. Then, BC was kept fixed and the size of DE was increased to attain convergence of the solution variables at points adjoining the target-penetrator interface. The region so obtained and its finite element discretization depicted in Fig. 1 were used to compute all of the results presented and discussed below. The

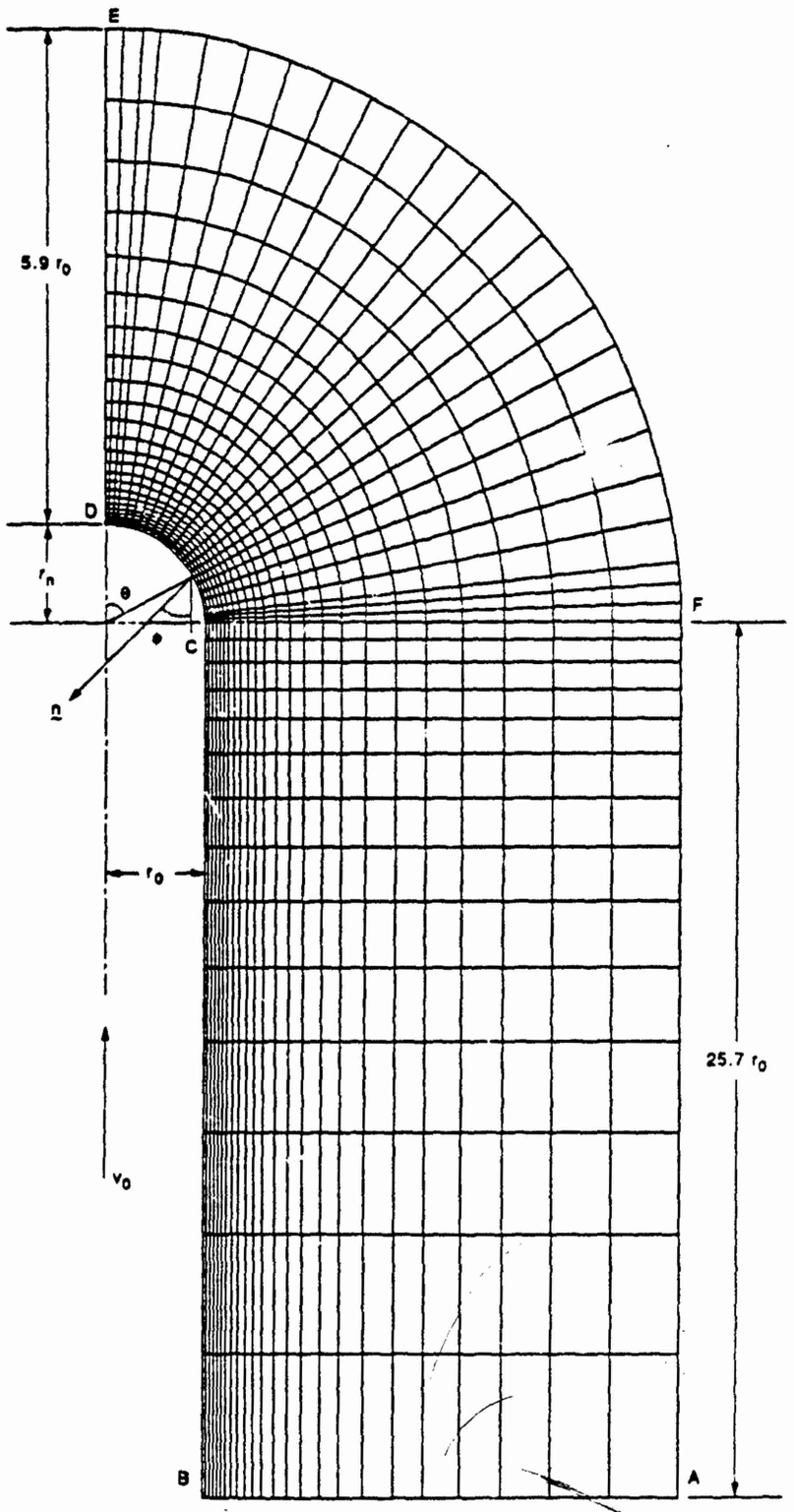

Fig. 1. The finite region studied and its discretization.

finite element mesh is very fine in darker regions. The size of the region considered herein is considerably more than that studied by Batra [19]. An increase in the distance DE resulted in a decrease in the axial resisting force experienced by the penetrator, but an increase in the distance BE increased the axial resisting force acting on the penetrator.

The finite element code developed by Batra [19] to solve for target deformations when its material is modeled by constitutive relation (2.19) was modified to include the Bodner–Partom flow rule (2.21). A weak formulation of the problem and an iterative technique to solve the nonlinear system of equations is also given in [19]. Whereas Batra [19] used six-noded triangular elements, here we use 9-noded quadrilateral elements to approximate the fields of $\mathbf{v}$, θ, and ψ within an element. The hydrostatic pressure p is assumed to be bilinear on each quadrilateral element, and is defined in terms of its values at the four corner nodes. Batra [29] has shown that when a problem similar to the one being studied here is analyzed by using identical nodal locations but either 6-noded triangular or 9-noded quadrilateral elements, the two sets of results are identical, except that the quadrilateral elements give smoother fields. In either case, *no posteriori* smoothing technique was applied to the computed values of the nodal pressures. In the results presented below, as well as in [19], the solution of the nonlinear system of equations was assumed to have converged, if at each nodal point the norm of the increments in v_r, v_z, and θ differed by less than 2% of the norm of v_r, v_z, and θ. Here v_r and v_z equal, respectively, the r- and z-components of the velocity of a point relative to an observer situated at the stagnation point and moving with it.

4. NUMERICAL RESULTS

4.1 Comparison of predictions from the two constitutive relations

We note that experimental data for the range of deformations expected to occur in the penetration problem under study is not available in the open literature. Batra and Kim [30] determined values of material parameters appearing in the two constitutive relations by ensuring that the computed shear stress–shear strain curve during overall adiabatic simple shearing deformations of a viscoplastic block deformed at an average strain-rate of $3300\,s^{-1}$ matched well with the experimental curve of Marchand and Duffy [31] for a HY-100 structural steel. We use those values, and list them below.

(a) Values same for both constitutive laws

$$\rho = 7860\,kg/m^3, \quad \sigma_0 = 405\,MPa, \quad c = 473\,J/kg\,°C,$$
$$K = 50\,W/m\,°C, \quad h = 20\,W/m^2\,°C, \quad \theta_a = 0, \quad r_0 = 2.54\,mm.$$

(b) Litonski–Batra flow rule

$$\nu = 6.55 \times 10^{-4}/°C, \quad \psi_0 = 0.012, \quad q = 0.054, \quad e = 0.01872,$$
$$b = 10^4\,s.$$

(c) Bodner–Partom flow rule

$$a = 1800°K, \quad z_1 = 3.778, \quad z_3 = 3.185, \quad m = 2.5,$$
$$D_0 = 3.3 \times 10^6\,s^{-1}.$$

Thus, the reference temperature θ_0 used to non-dimensionalize the temperature rise equals 108.9°C.

Figure 2 depicts the distribution of the normal stress, temperature rise, tangential speed, and I on the nose surface when the penetrator nose is hemispherical and $\alpha = 4.5$. In these plots, the values of the normal stress and the temperature rise have been divided by ten, in order for the curves to fit on the same graph. The values of the tangential speed and the strain-rate measure I as computed with the two constitutive relations come out to be very close to each other. The two temperature distributions agree qualitatively, and seem to differ by essentially a constant value. At first glance it seems that this difference is due to the different scales of temperature in

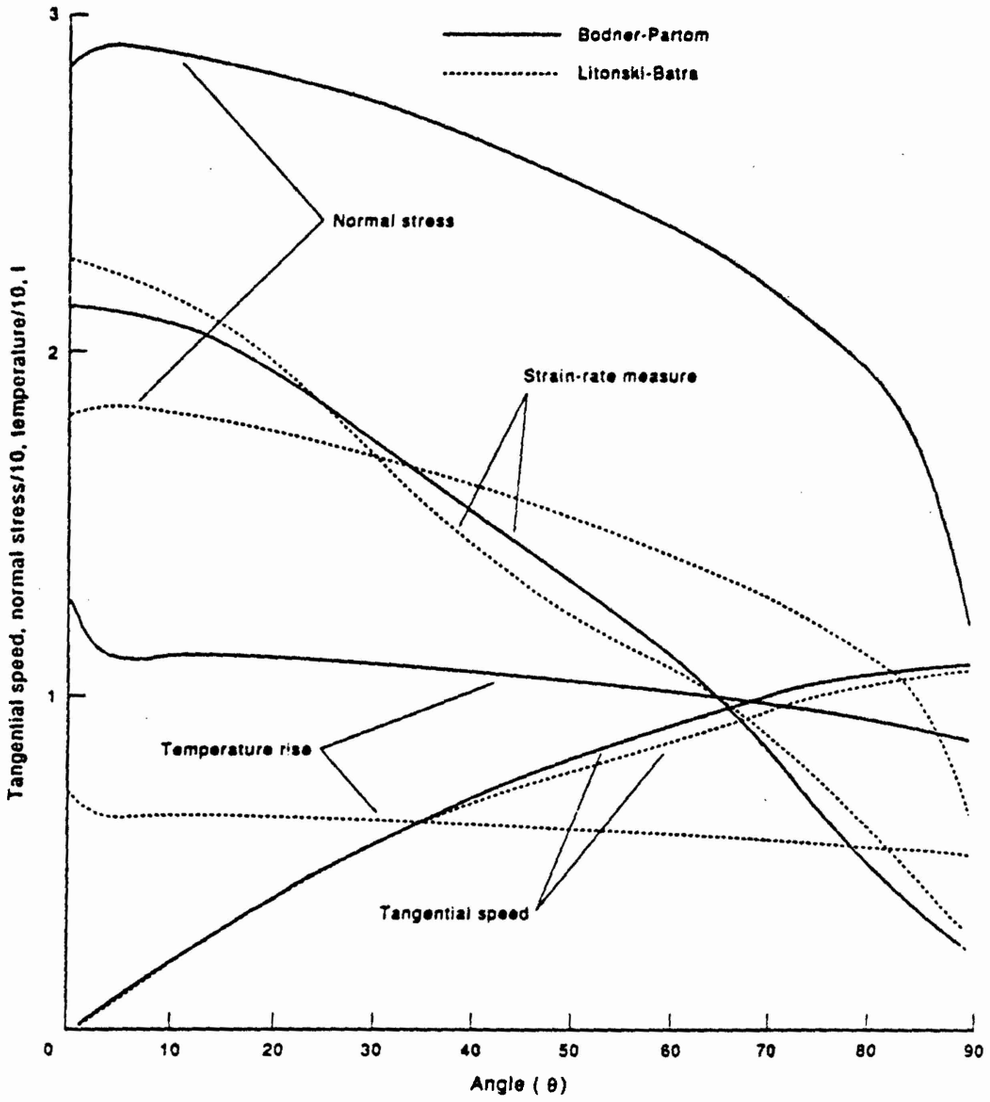

Fig. 2. Comparison of the variation of I, normal stress, tangential speed, and the temperature rise at target particles abutting the penetrator nose surface for the two constitutive relations.

the two constitutive relations. However, this was not found to be the case. Both constitutive relations predict sharply higher values of the temperature rise at target particles near the stagnation point. A possible explanation for this is that, at the stagnation point a considerable amount of heat is generated, but little is conducted away due to the low value of the thermal conductivity, and the heat loss due to convection is also very small because of the relatively small values of the speed of the particles surrounding the stagnation point. As one moves away from the stagnation point, heat loss due to convection increases because of the increased speed of target particles. The distribution of the normal stress on the penetrator/target interface as computed by the two constitutive relations also agrees qualitatively. However, the two normal stress distributions differ quantitatively, mainly because of the difference in the values of the hydrostatic pressure as computed by the two constitutive relations. For example, the peak pressure at or near the stagnation point equalled 18.71 and 30.16, respectively, for the Litonski–Batra and the Bodner–Partom flow rules. Because of the differences in the values of the deviatoric stress tensor $\mathbf{s}$ and the strain-rate measure I as computed by the two constitutive relations, the rate of energy dissipated due to plastic working and hence, the resulting

temperature distribution is different in the two cases. We note that the two constitutive relations are calibrated to give identical response in overall adiabatic simple shearing deformations of a viscoplastic block deformed at an average strain-rate of 3300 s^{-1}. The state of deformations at a target particle need not correspond to that of simple shearing. Also, the calibration procedure involves solving a nonlinear initial-boundary-value problem whose solution may be non-unique. Thus, two different sets of values of material parameters may give the same shear stress–shear strain curve. The axial resisting force equalled 15.24 and 25.19, respectively, for the Litonski–Batra flow rule and the Bodner–Partom flow rule.

Figure 3 shows the distribution of $(-\sigma_{zz})$, I, θ, and $(-v_z)$ on the axial line as computed by using the two constitutive relations. Whereas the two sets of values of I and v_z are very close to each other, those of θ and σ_{zz} agree qualitatively. These do indicate that significant deformations occur at target points whose distance from the target/penetrator interface is less than one penetrator diameter. The values of (I, θ) at the stagnation point are found to be (2.09, 7.35) and (2.14, 13.58) for the Litonski–Batra and Bodner–Partom flow rules, respectively. Thus, for the Bodner–Partom law, the temperature at the stagnation point almost equalled the presumed melting temperature of 1800°K.

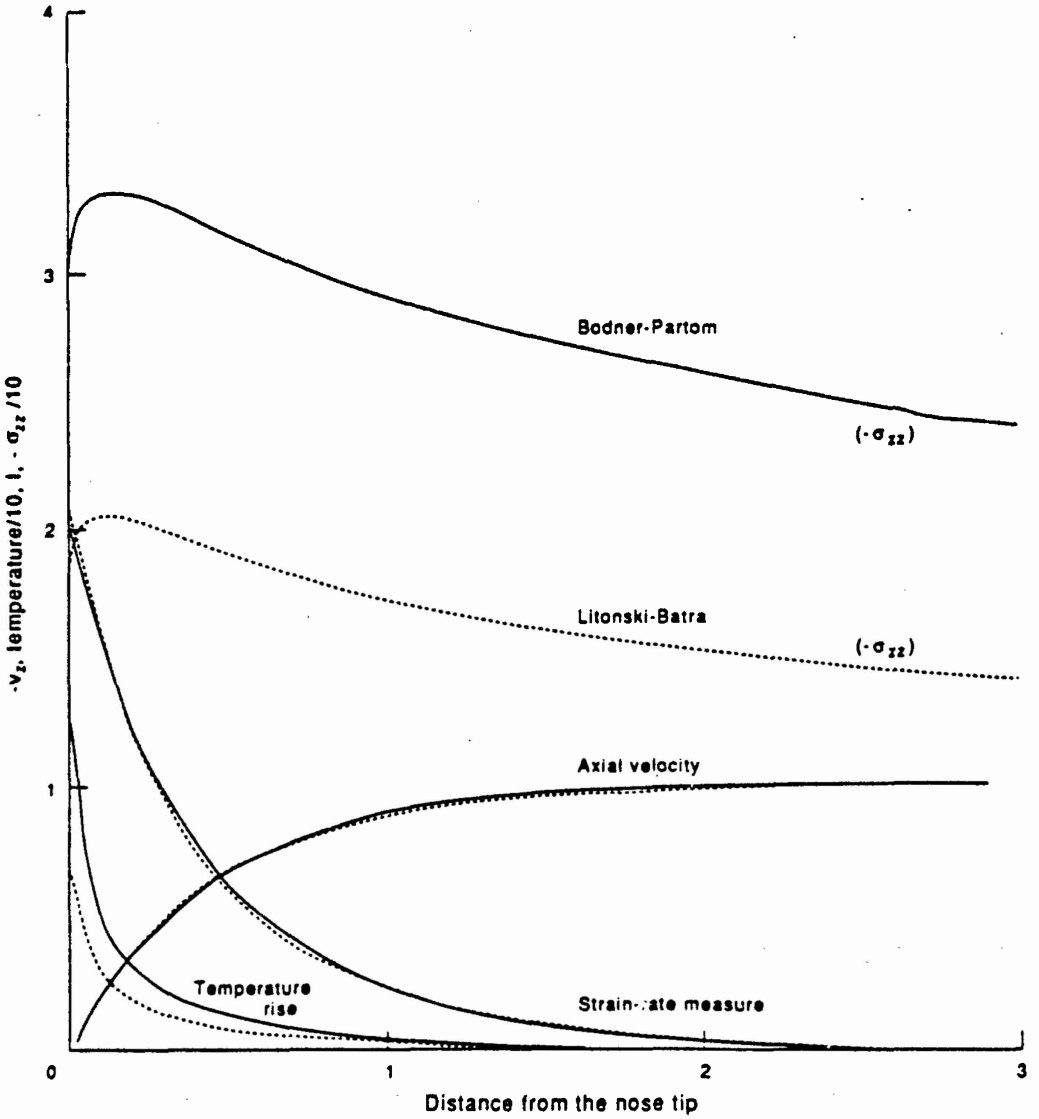

Fig. 3. Comparison of the variation of $(-\sigma_{zz})$, I, θ, and $(-v_z)$ on the axial line for the two constitutive relations.

4.2 Results for the Bodner–Partom flow rule

We now study the effect of different material parameters in the Bodner–Partom law on the deformations of the target. This will elucidate the relative importance of various material parameters and hence help design experiments for the precise determination of more critical ones. Since we are interested in the parameteric study, the values of different parameters used is of less significance. The range of values of material parameters considered herein is probably more than that likely to be encountered for any real material. We have assigned the following values to various non-dimensional material and geometric parameters.

$$D_0 = 6, \qquad z_1 = 1.505, \qquad z_3 = 1.236, \qquad m = 5, \qquad r_n = 1.0, \qquad \alpha = 2.1 \tag{4.1}$$

Except when studying the effect of changes in the melting temperature a of the material, it was set equal to 1200°K. The variables that are assigned values different from those given above are so indicated in the figures, along with their new values. In (4.1), $2r_n$ equals the length of the principal axis of the ellipsoidal nose in the z-direction.

In Fig. 4, we have plotted the variation of the normal stress, strain rate measure I, the

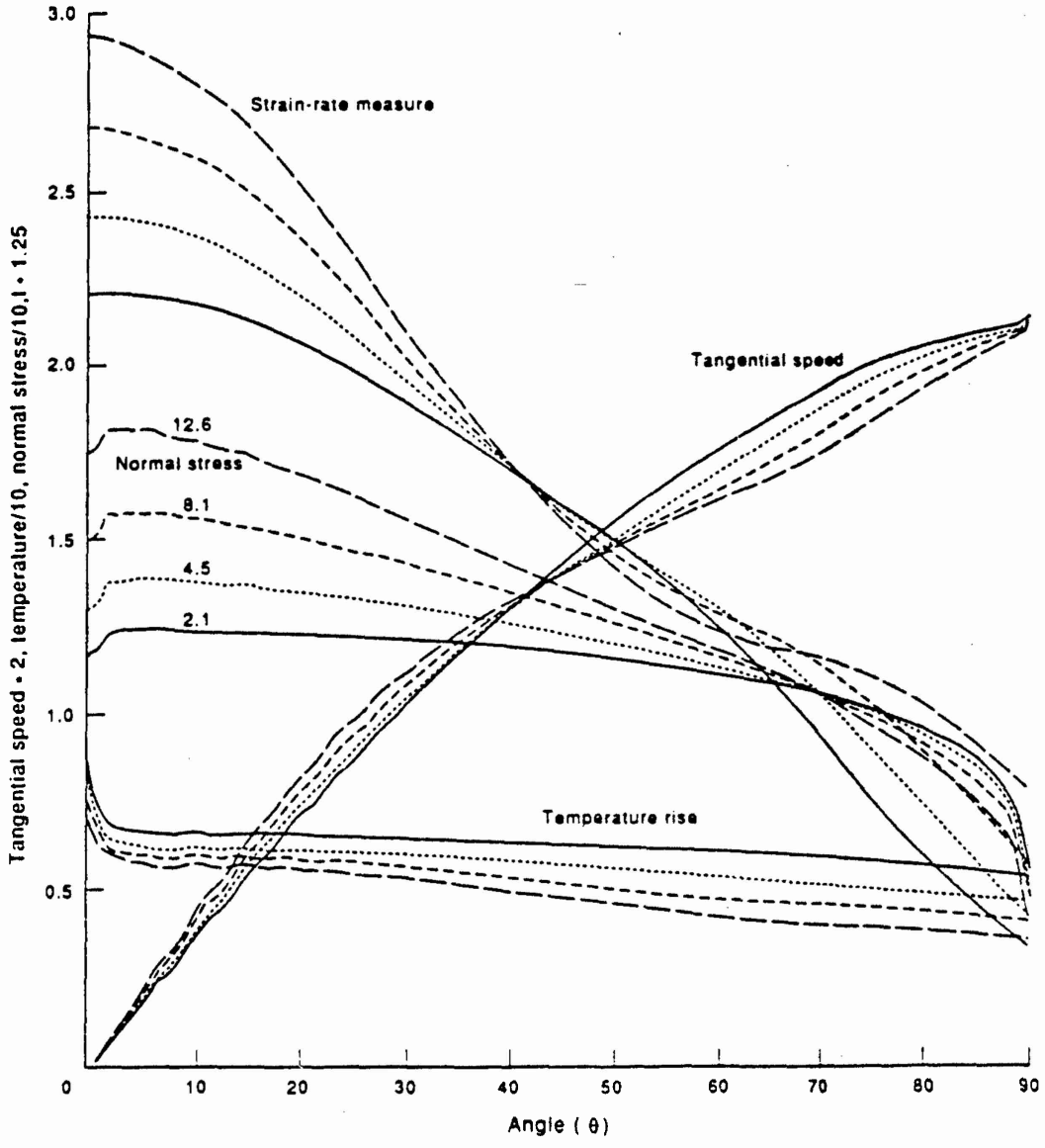

Fig. 4. Variation of I, normal stress, the tangential speed, and the temperature rise at target particles adjoining the penetrator nose surface for different values of α.

tangential speed, and the temperature rise on the penetrator/target interface for four different values of α. Note that these variables are multipled by different numbers so that the same vertical scale could be used. As expected, the normal stress on the target/penetrator interface increases with an increase in the value of α. However, for every value of α considered, it does drop off quite rapidly near the periphery of the penetrator nose, and seems to be independent of α at the point for which the angle $\theta \simeq 70°$. A similar behavior at $\theta \simeq 45°$ was observed by Batra [19] for the Litonski–Batra flow rule. The values of I for $\theta \leq 40°$ and $\theta \geq 70°$ increase with an increase in the value of α, but at many points for which $40° < \theta < 70°$, they exhibit the opposite trend. As the penetration speed v_0 is varied, the dimensional values of I change more than the non-dimensional ones, since the latter need to be multipled by v_0/r_0 to obtain the former. The same is true about the tangential speed on the target/penetrator interface. However, with an increase in the value of α, the tangential speed increases at points on the target/penetrator interface that are near the axial line, but decreases at points near the nose periphery. It would appear from the distributions of the normal stress and I on the penetrator/target interface that the temperature rise at target particles abutting the penetrator nose should increase with an increase in the value of α. However, the temperature rise at the nose surface decreases with an increase in the penetration speed, because at higher speeds, the

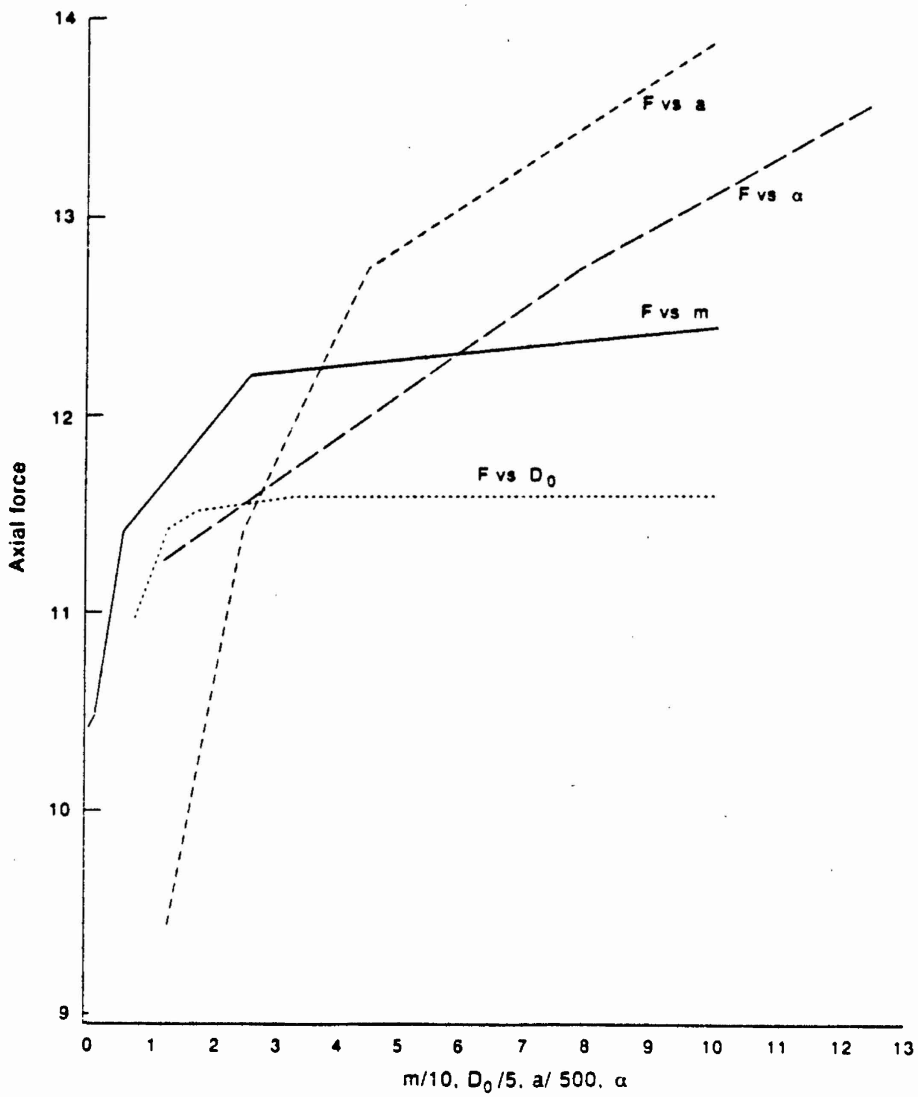

Fig. 5. Dependence of the axial resisting force upon various parameters.

heat loss due to convection increases significantly. A similar trend in the temperature distribution was computed by Batra [19] with the Litonski–Batra flow rule.

The axial resisting force F is given by

$$F = 2\int_0^{\pi/2} (\mathbf{n}\cdot\boldsymbol{\sigma}\mathbf{n}) \frac{\cos\phi \sin\theta[\sin^2\theta + (1/r_n)^4\cos^2\theta]^{1/2}}{[\sin^2\theta + (1/r_n)^2\cos^2\theta]^2} d\theta, \tag{4.2}$$

$$\cos\phi = \frac{z/r_n^2}{[r^2 + (z/r_n^2)^2]^{1/2}}, \tag{4.3}$$

where the angle θ is defined in Fig. 1, and (r, z) are the coordinates of a point on the penetrator/target interface. The corresponding axial force in physical units is given by $(\pi r_0^2\sigma_0)F$. We note that the expression given by Batra [19] for the axial force, except for the hemispherical nose shape, is in error. The dependence of the axial force upon α is exhibted in Fig. 5; the axial force depends upon α rather weakly, and the relation between the two is

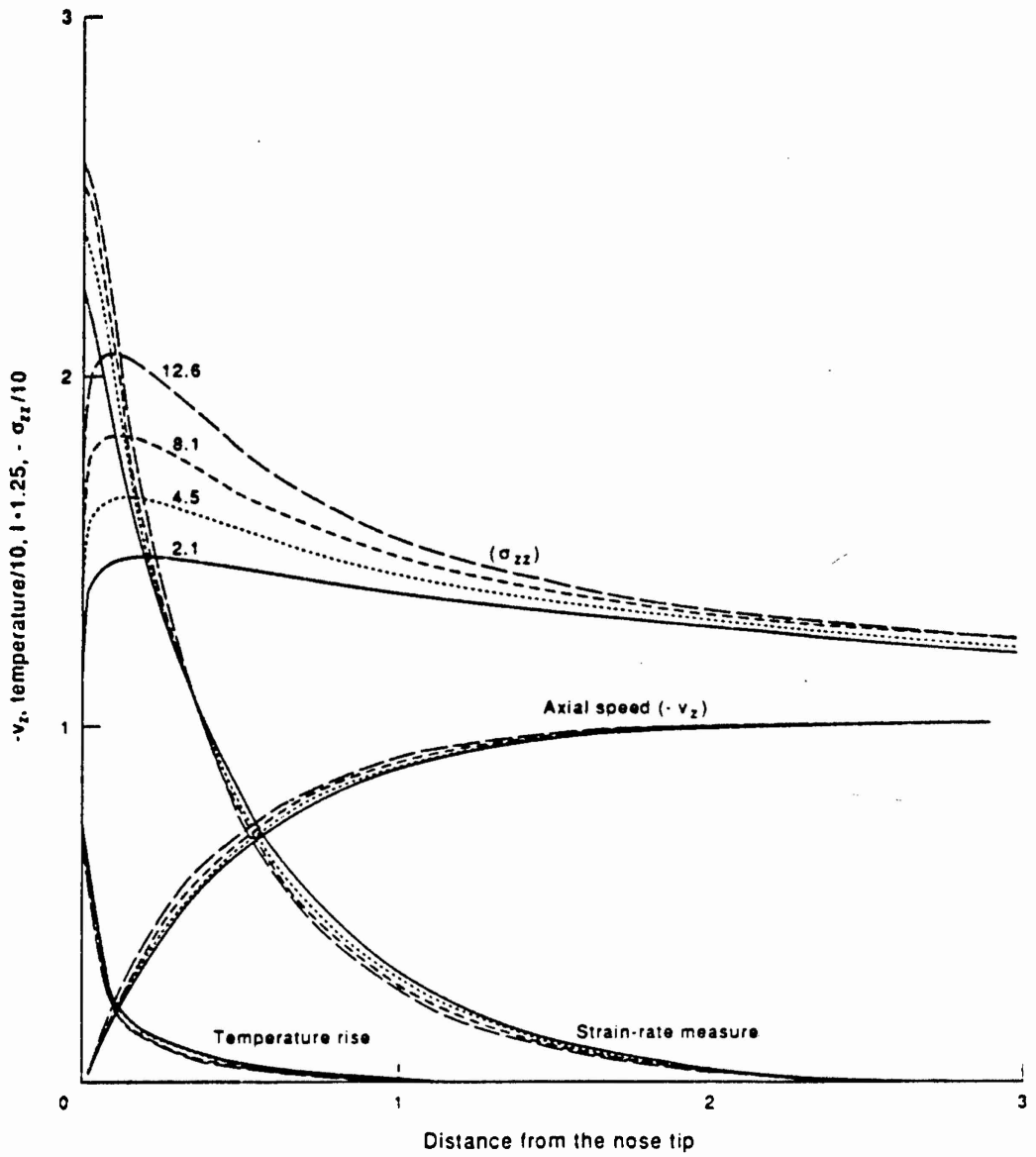

Fig. 6. Dependence of the temperature rise, I, σ_{zz}, and v_z at target particles on the axial line upon α.

nearly affine. Because of the increase in F with α, for the same initial kinetic energies of penetrators, those moving at higher speeds will give lower values of the penetration depth.

The variation of the temperature rise θ, I, σ_{zz}, and v_z along the axial line for the four different values of α considered is shown in Fig. 6. These plots vividly reveal that severe deformations of the target occur in the vicinity of the target/penetrator interface. The values of I and θ drop to zero rather quickly, and stay at zero for $z \geq 2.0$. This ensures the adequacy of the region considered. The values of σ_{zz} decay slowly, mainly because the hydrostatic pressure which contributes noticeably to σ_{zz} drops off slowly.

Figure 7 depicts the distribution of the tangential speed, normal stress, temperature rise, and I on the target/penetrator interface for several values of m. For larger values of m, the value of z_2 appraches the saturation value z_1 for smaller values of the plastic work density W. At a target particle abutting the penetrator nose, the values of the normal stress and the temperature rise increase monotonically with an increase in the value of m, those of I do not show any definite trend. The values of the tangential speed do not change that much when m is varied. The

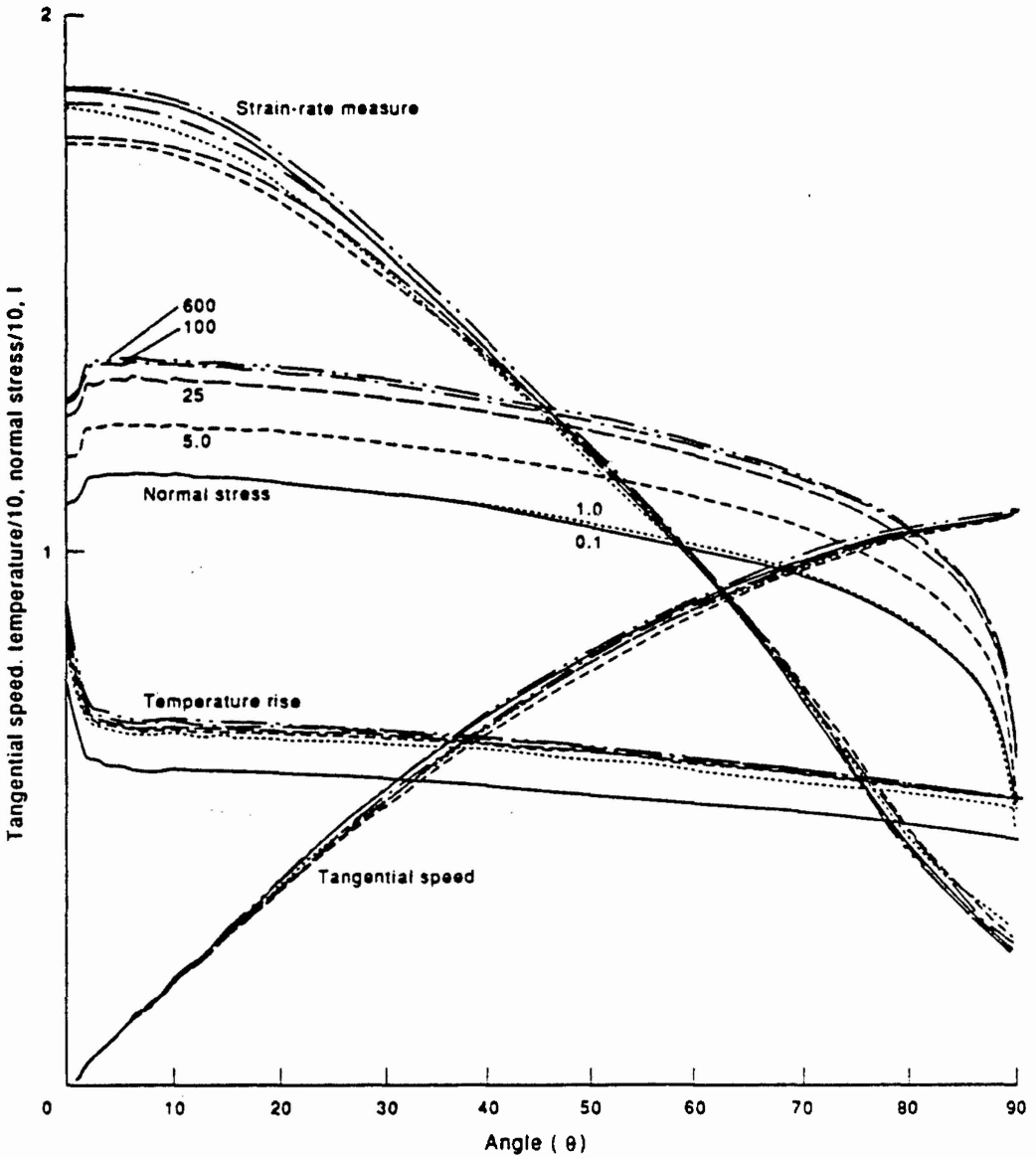

Fig. 7. Effect of m on the normal stress, tempeature rise, and I at target particles on the penetrator nose surface.

distributions of the normal stress and the temperature rise are affected very little when m is increased from 100 to 600.

The effect of changing the non-dimensional value of D_0 on the distribution of the normal stress, temperature rise θ, the tangential speed, and I on target particles adjoining the hemispherical penetrator nose is shown in Fig. 8. The values of the normal stress and I increase with an increase in the value of D_0. Recall that D_0 defines the limiting value of I. The peak values of I at a target particle located near the stagnation point keep on increasing with D_0, albeit slowly; those of the normal stress increase even more slowly. For none of the values of D_0 considered, does the computed peak value of I equal D_0. The values of θ decrease with an increase in D_0, possibly because of the increase in the rate of heat loss due to convection. The values of the tangential speed change very little with D_0. The axial resisting force experienced by the penetrator, plotted in Fig. 5, first increases with D_0, and then levels off.

Figure 9 depicts the effect of varying the value of a upon the distribution of the normal stress, strain rate measure I, temperature rise θ, and the tangential speed at target particles

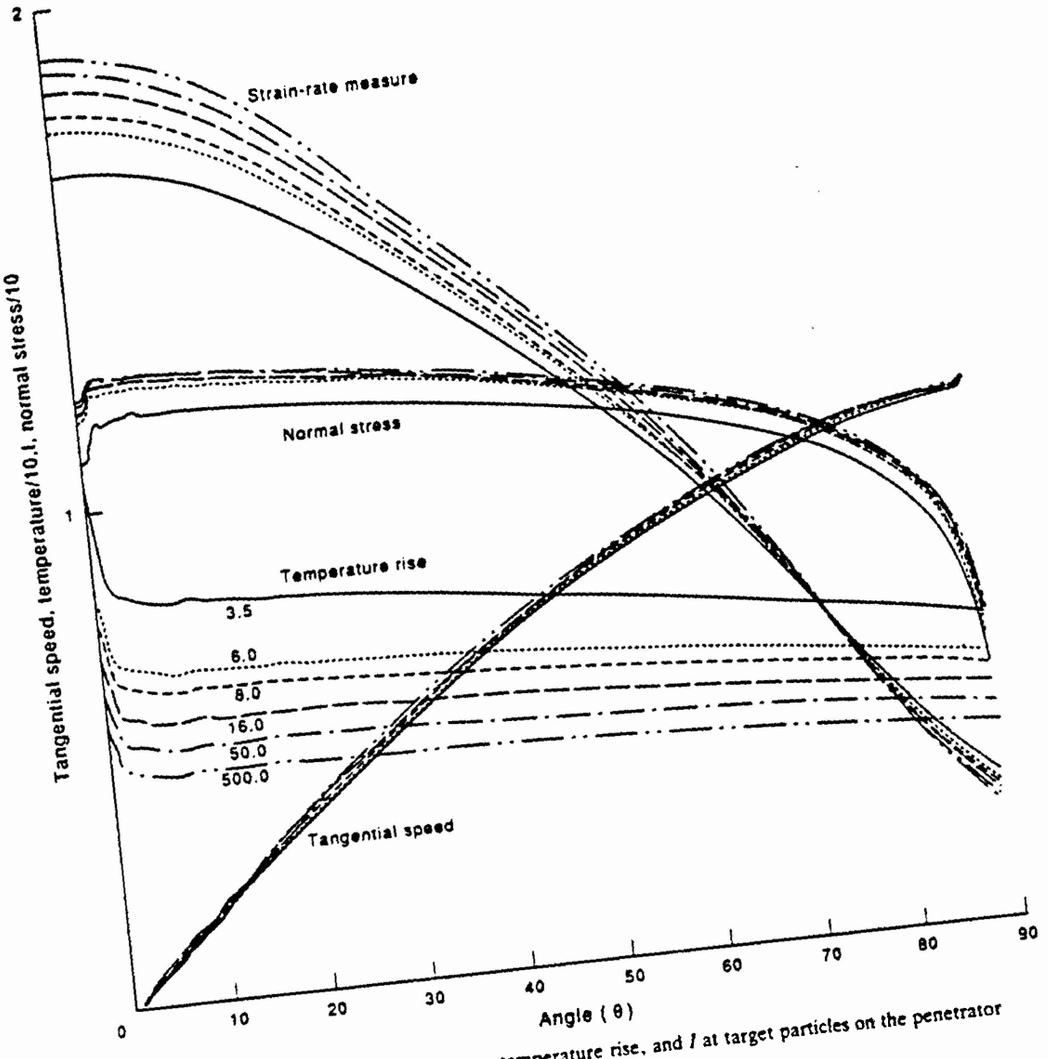

Fig. 8. Effect of D_0 on the normal stress, temperature rise, and I at target particles on the penetrator nose surface.

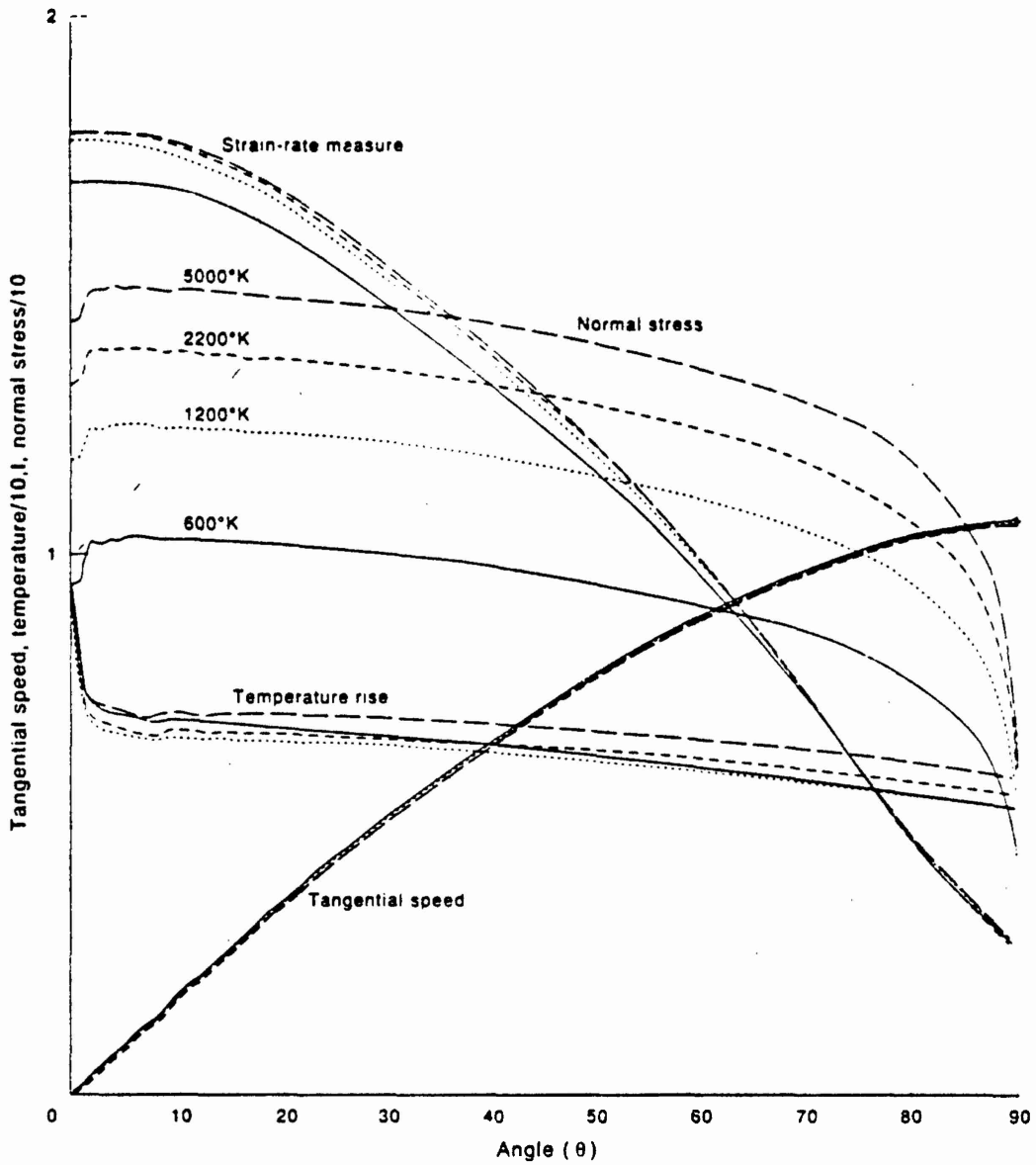

Fig. 9. Effect of a on the normal stress, temperature rise, and I at target particles on the penetrator nose surface.

adjacent to the penetrator nose surface. Whereas both the normal stress and I increase with an increase in the value of a, the temperature rise at a point does not show any clear trend. The values of the tangential speed seem to be unaffected by the value of a. Higher values of a imply that the material will thermally soften less for the same temperature rise. Consequently, it will offer more resistance to penetration as suggested by the larger values of the normal force acting on the target/penetrator interface. The axial resisting force experienced by the penetrator keeps on increasing with a, but the rate of increase drops off at larger values of a.

The distribution of the normal stress, strain-rate measure I, and the tangential speed at target particles abutting the penetrator nose surface for three different nose shapes, i.e. $r_n/r_0 = 2.0$, 1.0, and 0.5, is plotted in Fig. 10. The curves representing the normal stress distribution when $r_n/r_0 = 2.0$ and 1.0 have curvature of opposite signs. For the penetrator nose shape with $r_n/r_0 = 0.5$, the normal stress changes very little over the region $10° \leq \theta \leq 45°$. At any particular location on the penetrator nose surface, the tangential speed decreases with a decrease in the value of r_n/r_0. For the long tapered nosed penetrator, the strain-rate measure I

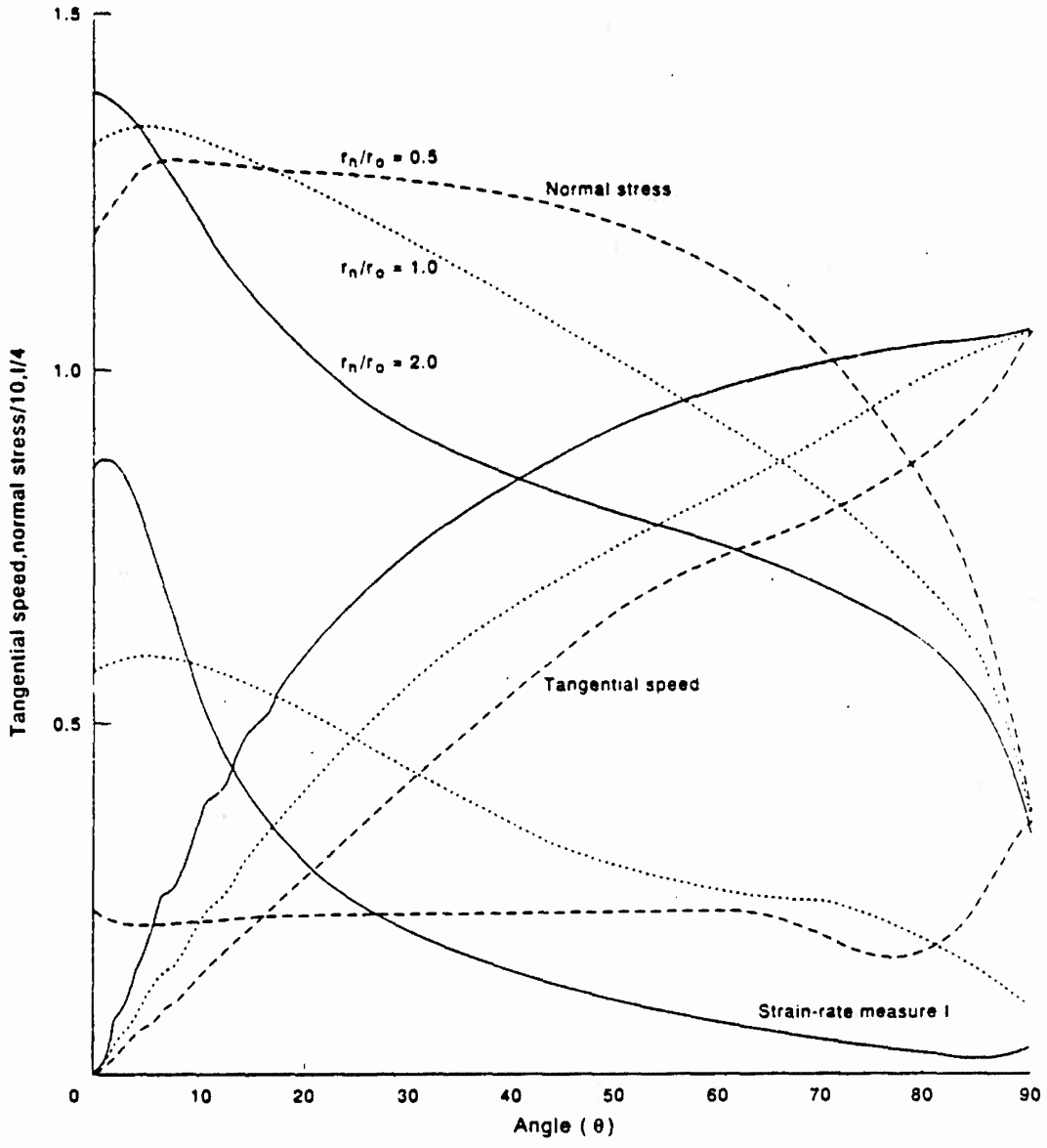

Fig. 10. Effect of nose shape on the normal stress, strain-rate measure I, and the tangential speed at target particles on the penetrator nose surface.

assumes its peak value at a target particle near the stagnation point. For a somewhat blunt nosed penetrator, the strain-rate measure I stays constant over most of the penetrator nose surface, and increases near the nose periphery. We recall that the results [19] computed with the Litonski–Batra flow rule agree qualitatively with the ones given in Fig. 10. For the Bodner–Partom flow rule, the convergence of the solution for the case when $r_n/r_0 = 0.2$ necessitated an increase in the value of D_0, presumably because the peak value of I near the nose periphery approached D_0 and the term $\ln(D_0/I)$ in the denominator of the right-hand side of equation (2.21) became negative, and the denominator in equation (2.21) could not be evaluated. Thus, results for this case are not included herein. One way to get around this problem is to increase D_0. Results plotted in Fig. 11 reveal that at target particles on the axial line, the rate of decrease of $(-\sigma_{zz})$ and I with the distance from the penetrator nose tip becomes less as the value of r_n/r_0 is decreased. For the somewhat blunt nosed penetrator $(r_n/r_0 = 0.5)$, the target particles deform less severely, but more of the target material is deformed as compared to that for the long tapered nosed penetrator.

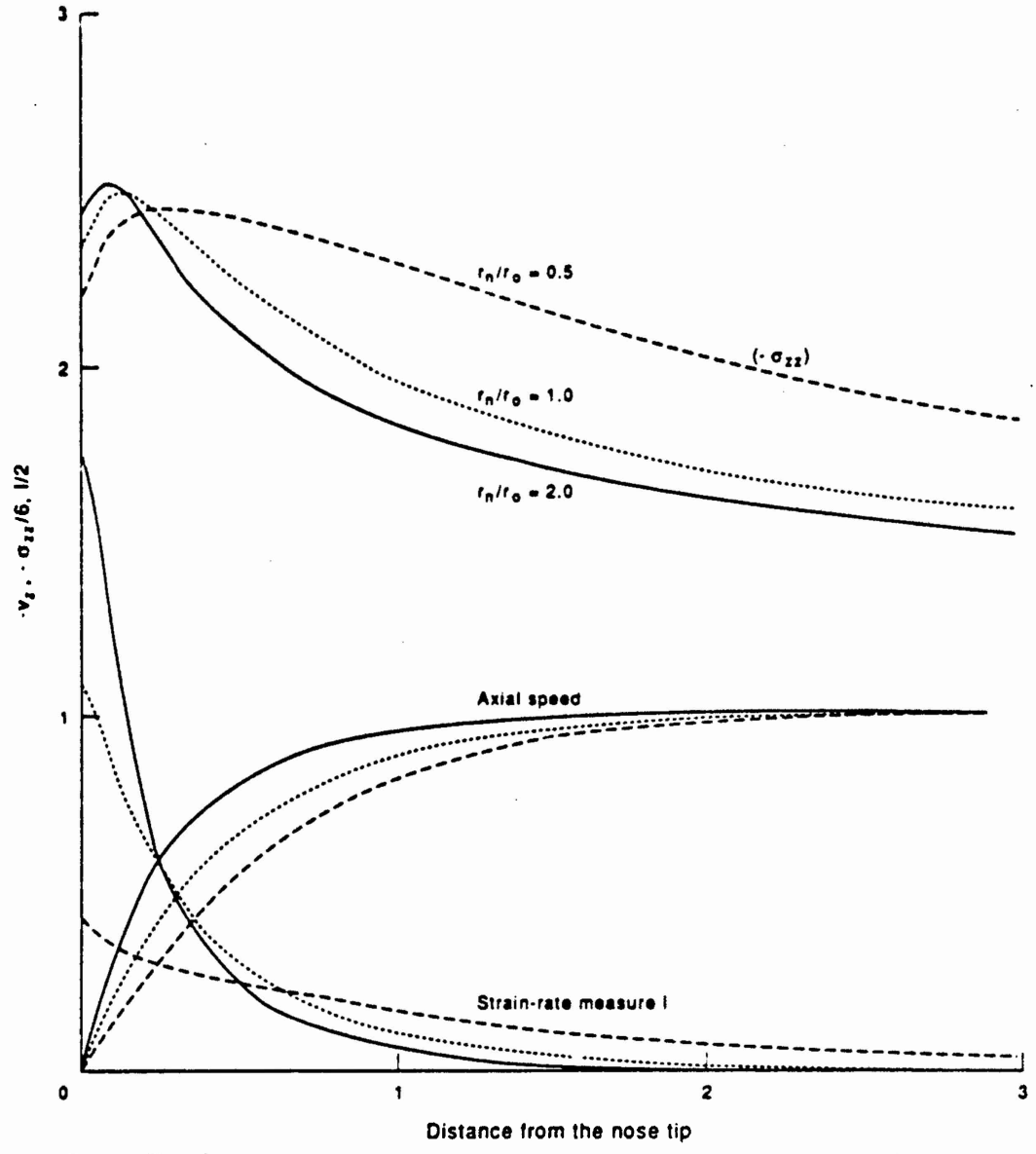

Fig. 11. Distribution of $(-\sigma_{zz})$, I, and the axial speed at target particles on the axial line for three different nose shapes.

The axial resisting force acting on the penetrator increases sharply as r_n/r_0 is decreased from 2.0 to 0.5; this is plotted in Fig. 5. Figure 12 depicts the variation of the axial speed of the target material flowing rearward and instantaneously lying on the planes $z = 0$ and $z = -1.0$. It is clear that the target material adjacent to the sides of the penetrator appears to extrude rearward as a uniform block that is separated from the bulk of the stationary target by a relatively narrow region with a sharp velocity gradient. This calculation of backward extrusion of a uniform block provides a partial justification to the velocity field assumed by Ravid and Bodner [7] in their work involving penetration of targets of finite thickness. There is no experimental data available in the open literature that proves or disproves the validity of results presented herein.

5. CONCLUSIONS

We have studied thermomechanical deformations of a thick viscoplastic target being penetrated by a long rigid cylindrical penetrator. Results computed when the target material is

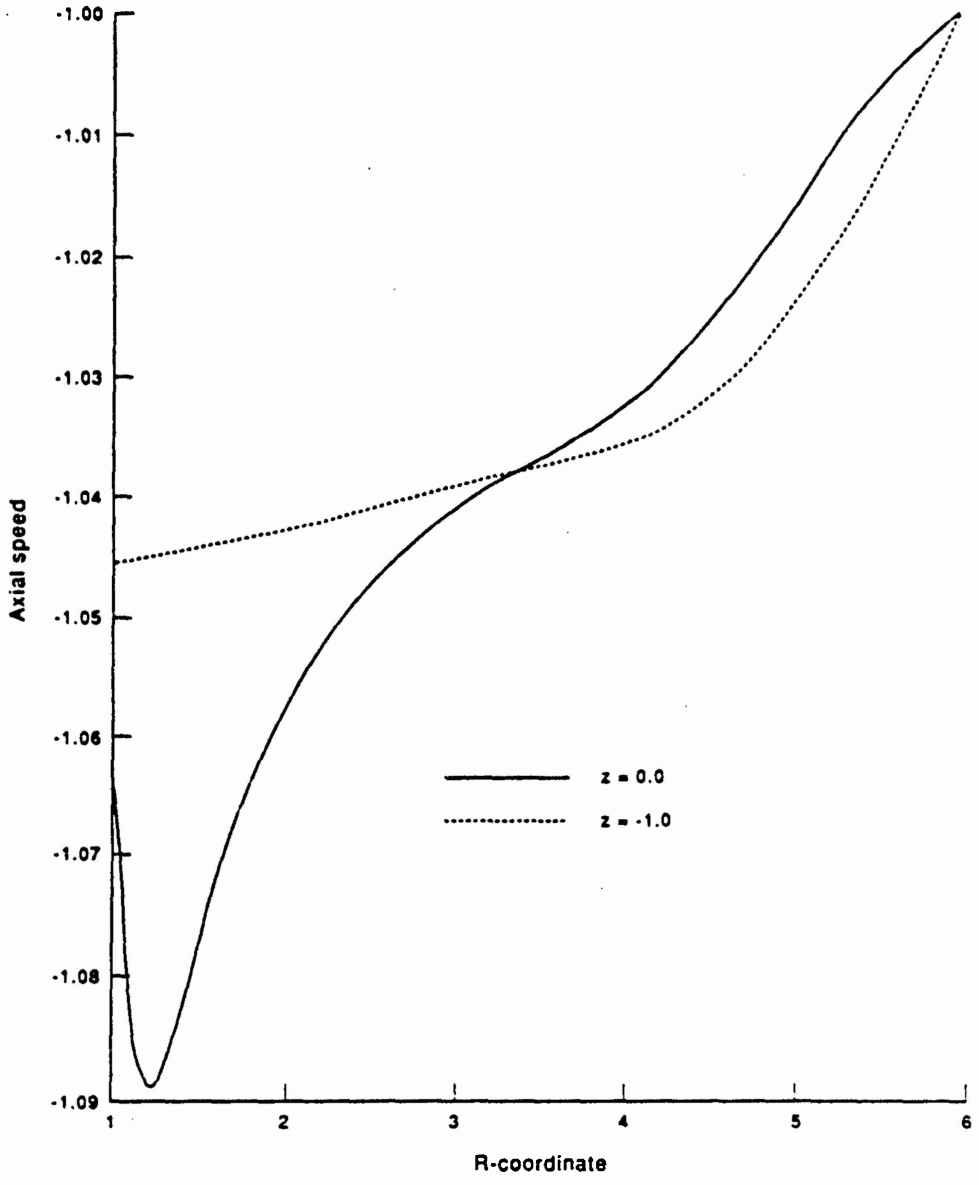

Fig. 12. Variation of the axial speed on planes $z = 0$ and $z = -1.0$.

modeled by the Litonski-Batra flow rule or the Bodner–Partom flow rule agree with each other qualitatively, but differ quantitatively. The material constants in the two constitutive relations were determined by requiring that the shear stress–shear strain curve in overall adiabatic simple shearing deformations of a block made of the target material were essentially similar. We note that the method used to determine the parameter values is not unique. The quantitative difference in the results computed with the two flow rules could also be due to the more complex state of deformations prevailing in the target than that in the simple shearing problem. The peak hydrostatic pressure for the Bodner–Partom flow rule is considerably more than that computed with the use of the Litonski–Batra flow rule.

We have also investigated the effect of the variation in the values of various parameters appearing in the Bodner–Partom flow rule. The range of values of parameters considered is more than that likely to be determined for one material. It is found that all of the parameters appearing in the Bodner–Partom flow rule influence strongly the deformations of the target. Significant deformations of the target occur at target particles ahead of the penetrator nose.

and distant less than one penetrator diameter from the penetrator nose surface. More severe deformations occur at target particles in the vicinity of the stagnation point for a long tapered nosed penetrator than for other nose shapes. However, for a blunt nosed penetrator, severest deformations occur at target particles near the nose periphery.

Acknowledgements—This work was supported by the U.S. Army Research Office Contract DAAL03-89-K-0050 to the University of Missouri-Rolla. Some of the computations were done on the NSF sponsored supercomputer center in Urbana, Illinois.

REFERENCES

[1] M. E. BACKMAN and W. GOLDSMITH, *Int. J. Engng Sci.* **16**, 1–99 (1978).
[2] T. W. WRIGHT and K. FRANK, *Approaches to Penetration Problems, SMIRT Symposium*, No. 14, *Impact*, Lausanne, Switzerland (1987).
[3] C. E. ANDERSON and S. R. BODNER, *Int. J. Impact Engng* **7**, 9–35 (1988).
[4] J. A. ZUKAS *et al.*, *Impact Dynamics*. Wiley-Interscience, New York (1982).
[5] T. Z. BLAZYNSKI, in *Materials at High Strain Rates* (Edited by T. Z. BLAZYNSKI). Elsevier, New York (1987).
[6] M. MACAULEY, *Introduction to Impact Engineering*. Chapman & Hall, London (1987).
[7] M. RAVID and S. R. BODNER, *Int. J. Engng Sci.* **21**, 577–591 (1983).
[8] M. RAVID, S. R. BODNER and I. HOLCMAN, *Int. J. Engng Sci.* **25**, 473–482 (1987).
[9] M. J. FORRESTAL, K. OKAJIMA and V. K. LUK, *J. Appl. Mech.* **55**, 755–760 (1988).
[10] A. TATE, *J. Mech. Phys. Solids* **15**, 387–399 (1967).
[11] A. TATE, *J. Mech. Phys. Solids* **17**, 141–150 (1969).
[12] V. P. ALEKSEEVSKII, *Comb. Expl. Shock Waves* **2**, 63–66 (1966). (Translation from Russian, Faraday Press, New York.)
[13] A. TATE, *Int. J. Mech. Sci.* **28**, 599–612 (1986).
[14] A. TATE, *Int. J. Engng Sci.* **16**, 858 (1978).
[15] P. H. PIDSLEY, *J. Mech. Phys. Solids* **32**, 315–333 (1984).
[16] R. C. BATRA and T. GOBINATH, *Int. J. Impact Engng* **11**, 1–31 (1991).
[17] R. C. BATRA and XINGJU CHEN, *Int. J. Engng Sci.* **28**, 1347–1358 (1990).
[18] S. R. BODNER and Y. PARTOM, *J. Appl. Mech.* **42**, 385–389 (1975).
[19] R. C. BATRA, *Comp. Mech.* **3**, 1–12 (1988).
[20] W. D. FARREN and G. I. TAYLOR, *Proc. R. Soc. London Ser. A* **107**, 422–429 (1925).
[21] J. LITONSKI, *Bull. Acad. Pol. Sci.* **25**, 7 (1977).
[22] R. C. BATRA and P. R. LIN, *Int. J. Impact Engng* **8**, 99–113 (1989).
[23] R. C. BATRA and D. S. LIU, *J. Appl. Mech.* **56**, 527 (1989).
[24] R. C. BATRA and X.-T. ZHANG, *Acta Mech.* **85**, 221–234 (1990).
[25] A. TATE, A theoretical estimate of temperature effects during rod penetration. *9th Ballistic Symposium*, pp. 2/307–2/314 (1987).
[26] J. F.BELL , *Physics of Large Deformation of Crystalline Solids*. Springer, New York (1968).
[27] M. R. LIN and R. H. WAGONER, *Scripta Met.* **20**, 143–148 (1986).
[28] U. S. LINDHOLM and G. R. JOHNSON, Strain-rate effects in metals at large strain rates. In *Material Behavior Under High Stresses and Ultrahigh Loading Rates* (Edited by V. WEISS), pp. 61–79. Plenum Press, New York (1983).
[29] R. C. BATRA, A comparison of solutions of the steady state thermoviscoplastic problem by the Petrov–Galerkin formulation and the introduction of artificial viscosity. *Computational Mechanics '89, Theory and Applications* (Edited by S. N. ATLURI and G. YAGAWA). Springer, Berlin (1989).
[30] R. C. BATRA and C. H. KIM, *J. Mech. Phys. Solids* **38**, 859–874 (1990).
[31] A. MARCHAND and J. DUFFY, *J. Mech. Phys. Solids* **36**, 251 (1988).

(Revision received 12 February 1991; accepted 15 March 1991)

Int. J. Impact Engng Vol. 12, No. 2, pp. 209–226, 1992
Printed in Great Britain

0734-743X/92 $5.00 + 0.00

EFFECT OF CONSTITUTIVE MODELS ON STEADY STATE AXISYMMETRIC DEFORMATIONS OF THERMOELASTIC–VISCOPLASTIC TARGETS

R. C. BATRA and R. JAYACHANDRAN

Department of Mechanical and Aerospace Engineering and Engineering Mechanics, University of Missouri-Rolla, Rolla, MO 65401-0249, U.S.A.

(*Received* 20 *October* 1991; *and in revised form* 20 *December* 1991)

Summary—We study the steady state axisymmetric deformations of a thick target being penetrated by a rigid cylindrical penetrator with a hemispherical nose and use three different constitutive relations, namely, the Litonski–Batra flow rule, the Bodner–Partom flow rule, and the Brown–Kim–Anand flow rule, to model the thermoelastic–viscoplastic response of the target. Each of these constitutive relations uses an internal variable to account for the microstructural changes in the body. The three flow rules are calibrated to give virtually identical effective stress–logarithmic strain curves during the overall adiabatic plane strain compression of a block of the target material deformed at an average strain rate of $3300\,s^{-1}$. It is found that the three constitutive relations give nearly the same value of the resisting force acting on the penetrator, temperature rise of material particles in the vicinity of the target–penetrator interface, and other macroscopic measures of deformation, such as the effective stress and logarithmic strain rate.

1. INTRODUCTION

During the penetration of a thick target by a fast moving cylindrical rod, severe deformations of the target and penetrator cause the temperature of the material particles in the vicinity of the target–penetrator interface to rise by a significant amount. Also, strain rates prevailing in this region are of the order of $10^6\,s^{-1}$. Constitutive relations that are valid over a wide range of strains, strain rates and temperatures are presently being developed by various research groups. This task is very challenging because different deformation mechanisms (for example, [1]) are active at various temperatures and strain rates, and the mechanisms themselves (e.g. thermally activated motion of dislocations, diffusion, phonon drag motion) are temperature and time dependent. Another complicating factor is the microstructural changes such as the generation annihilation of dislocations, development of texture, dynamic recovery and recrystallization, nucleation and growth of microcracks and voids, and the development of shear bands, that occur during the plastic deformation of the material. One way to account for these microstructural changes at a macroscopic level is to use the theory of internal variables proposed by Coleman and Gurtin [2]. Chan *et al.* [3] have summarized more than 10 such constitutive relations valid for small strains. Many more are given in the review article by Inoue [4] and the book by Lubliner [5].

Here we use three constitutive relations, namely, the Litonski–Batra flow rule [6], the Bodner–Partom flow rule [7], and the Brown–Kim–Anand flow rule [8] to model the thermoelastic–viscoplastic response of the elastic–viscoplastic target. For simplicity we assume that the penetrator is rigid, and steady state as seen by an observer situated at the penetrator nose tip has been reached. Each of the aforestated three flow rules employs an internal variable to account for the microscopic deformations, and does not employ a yield surface. The material parameters in these constitutive relations have been evaluated by solving numerically an initial-boundary-value problem corresponding to the plane strain compression of a block made of the target material being deformed at an average strain rate of $3300\,s^{-1}$ and ensuring that the effective stress–logarithmic strain curves for the three constitutive relations are nearly identical. With these values of material parameters, steady state axisymmetric deformations of the target have been analysed and various

quantities, such as the axial resisting force experienced by the penetrator and the pressure distribution on the penetrator nose surface, have been computed.

We note that Batra and Adam [6] conducted such a study for the Litonski–Batra and the Bodner–Partom flow rules. They evaluated the material parameters by comparing the response of the target material deformed in simple shear. With the values of material parameters so determined, they found that the Bodner–Partom law gave a very high value of the hydrostatic pressure at the target–penetrator interface as compared to that given by the Litonski–Batra flow rule. However, in the present study, all three flow rules give essentially the same value of the hydrostatic pressure and hence the axial resisting force experienced by the penetrator.

The present work is a continuation of the one initiated by Batra and Wright [9] with the goal of providing some guidelines for selecting and improving upon the previously used kinematically admissible fields in engineering models of penetration. Subsequently, Batra and co-workers [10–18] have analysed various aspects of the steady state penetration process. The reader should consult the review articles by Backman and Goldsmith [19], Wright and Frank [20], and Anderson and Bodner [21], and books by Blazynski [22], MaCauley [23] and Zukas *et al.* [24] to gain a comprehensive view of the work completed on the penetration problem. The engineering models proposed by Tate [25–28] and Alekseevskii [29] for the steady state penetration problem have been found very useful by ballisticians. Batra and Chen [30] selected a kinematically admissible field based upon the numerical studies of Batra *et al.* alluded to above, and proposed an engineering model of steady state deformations of a viscoplastic target.

2. FORMULATION OF THE PROBLEM

We use a cylindrical coordinate system with origin attached to the center of the hemispherical penetrator nose, moving with it at a uniform speed v_0, and positive z-axis pointing into the target, to describe the thermomechanical deformations of the target. We note that target deformations appear to be steady to an observer situated at the penetrator nose tip and moving with it. Equations governing the target deformations and written in the Eulerian description of motion are the following.

Balance of mass

$$\operatorname{div} \underline{v} = 0 \tag{1}$$

Balance of linear momentum

$$\operatorname{div} \underline{\sigma} = \rho(\underline{v}\cdot\operatorname{grad})\underline{v} \tag{2}$$

Balance of internal energy

$$-\operatorname{div} \underline{q} + tr(\underline{\sigma}\underline{D}^p) = \rho(\underline{v}\cdot\operatorname{grad})U \tag{3}$$

where
$$\underline{D} = (\operatorname{grad}\underline{v} + (\operatorname{grad}\underline{v})^T)/2, \quad \underline{W} = (\operatorname{grad}\underline{v} - (\operatorname{grad}\underline{v})^T)/2 \tag{4}$$

$$\underline{q} = -k \operatorname{grad}\theta \tag{5}$$

$$U = c\theta \tag{6}$$

$$\underline{\sigma} = -p\underline{1} + \underline{s} \tag{7}$$

$$\overset{\circ}{\underline{s}} = 2G(\underline{D} - \underline{D}^p) \tag{8}$$

$$\overset{\circ}{\underline{s}} = (\underline{v}\cdot\operatorname{grad})\underline{s} + \underline{s}\underline{W} - \underline{W}\underline{s} \tag{9}$$

$$\underline{s} = 2\mu(I, \theta, \psi)\underline{D}^p \tag{10}$$

$$I^2 = \tfrac{1}{2}tr(\underline{D}^{p2}). \tag{11}$$

Here $\underline{v}$ is the velocity of a material particle, $\underline{\sigma}$ the Cauchy stress tensor at the present location of a material particle, ρ the mass density, $\underline{q}$ the heat flux, $\underline{D}$ the stretching tensor,

and $\underset{\sim}{W}$ the spin tensor. Equation (5) is the Fourier law of heat conduction with k the thermal conductivity assumed here to be a constant, and θ the temperature of a material particle in °C. Equation (6) is the constitutive relation for U, and (8) for the deviatoric stress tensor $\underset{\sim}{s}$, defined by Eqn (7), where p is the hydrostatic pressure not determined by the history of the deformation, since the deformations are assumed to be isochoric. Equation (8) is Hooke's law written in the rate form, and is based on the assumption that the strain rate ($\underset{\sim}{D}$) has additive decomposition into elastic ($\underset{\sim}{D}^e$) and plastic ($\underset{\sim}{D}^p$) parts. The superimposed open circle on $\underset{\sim}{s}$ indicates its Jaumann derivative, which for steady state deformations is given by the right-hand side of (9). We recall that Pidsley [31] used the ordinary time derivative of $\underset{\sim}{s}$ in Eqn (8), which is not frame-indifferent, and equals the first term on the right hand side of (9) for steady state deformations. Equation (10) is the flow rule, and the expression for μ, wherein ψ is an internal parameter, depends upon the flow rule employed. In order to complete formulation of the problem, we need to specify the form of μ, the evolution equation for ψ, and the pertinent boundary conditions. We first give details of the three constitutive relations.

Litonski–Batra flow rule

$$2\mu(I,\theta,\psi) = \frac{\sigma_0}{\sqrt{3}I}(1+bI)^m(1-v\theta)\left(1+\frac{\psi}{\psi_0}\right)^n \tag{12.1}$$

$$\dot{\psi} = \frac{tr(\underset{\sim}{s}\underset{\sim}{D}^p)}{\sigma_0\left(1+\frac{\psi}{\psi_0}\right)^n}. \tag{12.2}$$

Bodner–Partom flow rule

$$2\mu(I,\theta,W) = \frac{Z_2}{\sqrt{3}I\left[\frac{2\hat{n}}{\hat{n}+1}\ln\left(\frac{D_0}{I}\right)\right]^{1/2\hat{n}}} \tag{13.1}$$

$$Z_2 = Z_1 + (Z_3 - Z_1)\exp(-\hat{m}W/Z_3) \tag{13.2}$$

$$\hat{n} = \frac{\hat{a}}{T}, \quad T = 273 + \theta \tag{13.3}$$

$$\dot{W} = tr(\underset{\sim}{s}\underset{\sim}{D}^p). \tag{13.4}$$

Brown–Kim–Anand flow rule

$$2\mu(I,\theta,g) = \frac{2g}{3I\xi}\sinh^{-1}(\phi^{\hat{m}}), \tag{14.1}$$

$$\phi = \left(\frac{I}{A}\right)\exp\left(\frac{Q}{RT}\right), \quad T = 273 + \theta \tag{14.2}$$

$$\dot{g} = h_0 I\left(\max\left(0,\left(1-\frac{g}{g^*}\right)^a\right)\right), \tag{14.3}$$

$$g^* = \tilde{g}\phi^{\hat{n}}. \tag{14.4}$$

The constitutive relation (12), proposed by Batra [14], incorporates and generalizes that suggested by Litonski [32] for simple shearing deformations. Batra and co-workers [6,14,16] have used it to study thermomechanical penetration problems, and the initiation and growth of shear bands in viscoplastic materials. In it σ_0 is the yield stress in a quasistatic simple compression test, the material parameters b and m characterize the strain rate sensitivity of the material, v its thermal softening, and ψ_0 and n the strain hardening of the material. With ψ interpreted as the plastic strain

$$\sigma = \sigma_0\left(1+\frac{\psi}{\psi_0}\right)^n \tag{15}$$

describes the stress–strain curve in a quasistatic simple compression test. In a dynamic test, the effect of the history of deformation upon the present state of deformation is accounted for through the parameter ψ. The linear dependence of the flow stress upon the temperature rise has been used by Tate [33] in the analysis of a penetration problem, and has been observed by Bell [34], Lin and Wagoner [35] and Lindholm and Johnson [36]. Should the temperature of a material point exceed $1/v$ so as to make μ negative, we set $\mu = 0$. Thus, the material point behaves like an incompressible fluid for $\theta \geq 1/v$. However, the latent heat required for the phase transformation to occur is not accounted for in our work. We add that for the problem studied herein, the maximum temperature at any point in the deforming target region never reached $1/v$.

In Eqns (13.1)–(13.4), T is the absolute temperature of a material particle, the internal variable W equals the plastic work done, D_0 is the limiting value of the plastic strain rate and is usually assigned a large value, the material parameter $\hat{m}$ characterizes the rate of work hardening and $\hat{n}$ is the strain rate sensitivity parameter. In Eqn (13.2), Z_3 equals the hardening at zero inelastic strain, and Z_1 is the limit or saturation value of the work hardening of the material. We set $\hat{a}$ equal to the melting temperature of the material, and we need to specify D_0, $\hat{a}$, Z_1, Z_3 and $\hat{m}$ to characterize the material. Once T equals $\hat{a}$, we set $\mu = 0$, analogous to what we did for the Litonski–Batra flow rule. However, for problems studied herein, the temperature at a point never reached the melting temperature of the material.

In the Brown–Kim–Anand flow rule described by Eqns (14.1)–(14.4), A is called the pre-exponential factor, Q the activation energy, R the gas constant, $\tilde{m}$ the strain rate sensitivity parameter, h_0 a constant rate of athermal hardening, and g^* equals the saturation value of g associated with a given temperature/strain rate pair. Thus, g never exceeds g^*. In order to characterize the material, we need to specify ξ, $\tilde{m}$, A, Q, R, h_0, g^*, $\tilde{a}$, $\tilde{g}$ and $\tilde{n}$.

We nondimensionalize variables by scaling stress-like quantities by σ_0, length variables by r_0, time by (r_0/v_0), and the temperature by the reference temperature θ_r, defined by

$$\theta_r \equiv \frac{\sigma_0}{\rho c}. \tag{16}$$

Here r_0 equals the radius of the cylindrical part of the penetrator. Substituting for $\hat{s}$ from (9) into (8), and rewriting the result and Eqns (1)–(3) in terms of nondimensional variables we arrive at the following set of equations.

$$\operatorname{div} \underline{v} = 0 \tag{17.1}$$

$$-\operatorname{grad} p + \operatorname{div} \underline{s} = \alpha(\underline{v}\cdot\operatorname{grad})\underline{v} \tag{17.2}$$

$$\underline{s} + \beta\gamma((\underline{v}\cdot\operatorname{grad})\underline{s} + \underline{s}\underline{W} - \underline{W}\underline{s}) = 2\beta\underline{D} \tag{17.3}$$

$$tr(\underline{s}\underline{D}^p) + \delta \operatorname{div}(\operatorname{grad}\theta) = (\underline{v}\cdot\operatorname{grad})\theta \tag{17.4}$$

where

$$\alpha = \frac{\rho v_0^2}{\sigma_0}, \quad \beta = \frac{\mu v_0}{\sigma_0 r_0}, \quad \gamma = \frac{\sigma_0}{G} \text{ and } \delta = \frac{k}{\rho c v_0 r_0} \tag{18}$$

are nondimensional numbers. Henceforth we will use nondimensional variables only. Note that α, γ and δ are constants for the given problem, but β varies from point to point in the deforming region. The value of α signifies the influence of inertia forces relative to the flow stress of the material, those of γ and δ give the effect of material elasticity and the heat conduction, respectively. For most metals, γ is of the order of 10^{-3}, and it equals zero for a rigid perfectly plastic material. The value of the Weissenberg number $(\beta\gamma)$ varies from 10^{-3} to 10^{4} in the deforming region. For typical penetration problems involving long rod penetrators, δ is of the order of 10^{-5}; hence, the target deformations may be considered adiabatic. The form of flow rules in terms of nondimensional variables remains unaltered.

Because of our inability to solve analytically nonlinear Eqns (17), we seek their approximate solution by the finite element method. Accordingly, we consider deformations

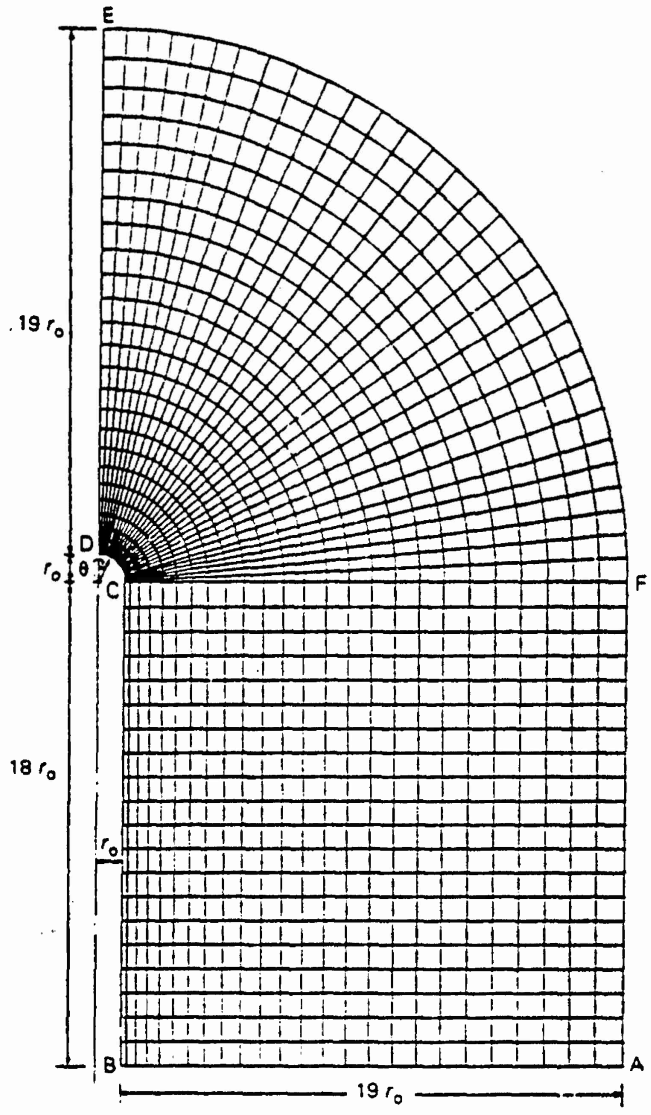

FIG. 1. The finite region studied and its discretization.

of the finite target region shown in Fig. 1 and impose on it the following boundary conditions.

$$\underline{t}\cdot(\underline{\underline{\sigma}}\underline{n}) = 0 \quad \text{on} \quad \Gamma_i, \tag{19.1}$$

$$\underline{v}\cdot\underline{n} = 0 \quad \text{on} \quad \Gamma_i, \tag{19.2}$$

$$\underline{q}\cdot\underline{n} = h_c(\theta - \theta_a) \quad \text{on} \quad \Gamma_i, \tag{19.3}$$

$$\sigma_{zz} = 0, \quad v_r = 0, \quad \frac{\partial\theta}{\partial z} = 0 \quad \text{on the surface AB.} \tag{20.1}$$

$$v_r = 0, \quad v_z = -1, \quad \theta = 0, \quad \psi = 0, \quad g = 1, \quad p = 0, \quad s_{rr} = 0, \quad s_{\theta\theta} = 0, \quad s_{zz} = 0, \quad s_{rz} = 0$$
on the bounding surface EFA. (20.2)

$$\sigma_{rz} = 0, \quad v_r = 0, \quad \frac{\partial\theta}{\partial r} = 0 \quad \text{on the axis of symmetry DE.} \tag{20.3}$$

Here $\underline{n}$ and $\underline{t}$ are, respectively, a unit normal and a unit tangent vector to the surface, θ_a is an average temperature of the penetrator, and h_c is the heat transfer coefficient between the penetrator and the target, and Γ_i denotes the target–penetrator interface. Equation

(19.1) implies that Γ_1 is smooth, and (19.2) ensures that there is no interpenetration of the target material into the penetrator and vice versa. The boundary conditions (20.3) are due to the axial symmetry of deformations. That the region R studied is adequate was established by increasing the size of the region in both r and z direction until the values of p, $\dot{\gamma}$, ξ, θ and ψ at points on Γ_1 differed by less than 5%.

Figure 1 depicts the final region R so obtained, and its finite element discretization used to compute the results presented below. We note that enlarging the region ahead of the penetrator from 19 to $20r_0$ changed the value of $\|\xi\|$ by a maximum of 4.7% and of pressure, p, by 2.7%, increasing the target region behind the penetrator nose from 17 to $18r_0$ resulted in a maximum variation in $\|\xi\|$ and p of 2.2%. The value of other variables changed by considerably smaller amounts. When the target region R was divided into 700, 900 and 1250 elements proportioned as shown in Fig. 1, the peak values of the temperature rise at any node, and the pressure and the strain rate measure I at the centroid of an element were found to be (12.07, 3.42, 1.38), (12.17, 3.69, 1.52) and (12.10, 3.67, 1.53), respectively. Results presented below are for a finite element mesh with 1250 elements.

We refer the reader to [37] for details of obtaining a finite element solution of the problem.

3. NUMERICAL RESULTS

3.1. *Determination of material parameters for the three flow rules*

In order to compute predictions from the three flow rules for the penetration problem, we first need to calibrate them against the same test. Since the experimental data for a typical target material over the ranges of strain rates and temperature changes likely to occur in a penetration problem is not available in the open literature, we consider a hypothetical simple compression test. The code developed by Batra and Liu [38] to analyse the plane strain thermomechanical deformations of a viscoplastic body obeying the Litonski–Batra flow rule was modified to include the Bodner–Partom and the Brown–Kim–Anand viscoplastic models. The same initial-boundary value problem corresponding to the plane strain simple compression of a viscoplastic block being deformed at an average strain rate of $3300\,s^{-1}$ was solved with each of the three flow rules. The value of each material parameter was changed in turn to assess the sensitivity of the effective deviatoric stress s_e vs strain ε_e curve. Here

$$s_e = \sqrt{\tfrac{3}{2}}\,tr(\xi\xi^T)^{1/2} \tag{21}$$

$$\varepsilon_e = \ln\left(\frac{l_0}{l}\right) \tag{22}$$

l and l_0 being the current and reference heights of the block. The values of material parameters determined so that the s_e vs ε_e curves for the three constitutive relations almost matched, as shown in Fig. 2, are listed below.

(a) The Litonski–Batra (LB) flow rule:

$$b = 10\,s, \quad v = 1.2 \times 10^{-3}/^{\circ}C, \quad \psi_0 = 0.1, \quad m = 0.01, \quad n = 0.13.$$

(b) The Bodner–Partom (BP) flow rule:

$$D_0 = 3.3 \times 10^6\,s^{-1}, \quad \hat{a} = 1800\,K, \quad Z_3 = 50\,MPa, \quad Z_1 = 650\,MPa, \quad \hat{m} = 0.05.$$

(c) The Brown–Kim–Anand (BKA) flow rule:

$$A = 6.346 \times 10^{15}\,s^{-1}, \quad Q = 275\,kJ/mole, \quad \tilde{g} = 405\,MPa, \quad h_0 = 5000\,MPa,$$

$$\xi = 3.25, \quad \tilde{m} = 0.1, \quad \tilde{n} = 0.002, \quad \tilde{a} = 1.5.$$

Values of geometric and other material parameters that are independent of the constitutive relation employed are:

$$\rho = 7860\,kg/m^3, \quad \sigma_0 = 405\,MPa, \quad G = 80\,GPa, \quad c = 473\,J/kg\,^{\circ}C, \quad k = 50\,W/m\,^{\circ}C,$$

$$h = 20\,W/m^2\,^{\circ}C, \quad \theta_a = 0, \quad r_0 = 10\,mm.$$

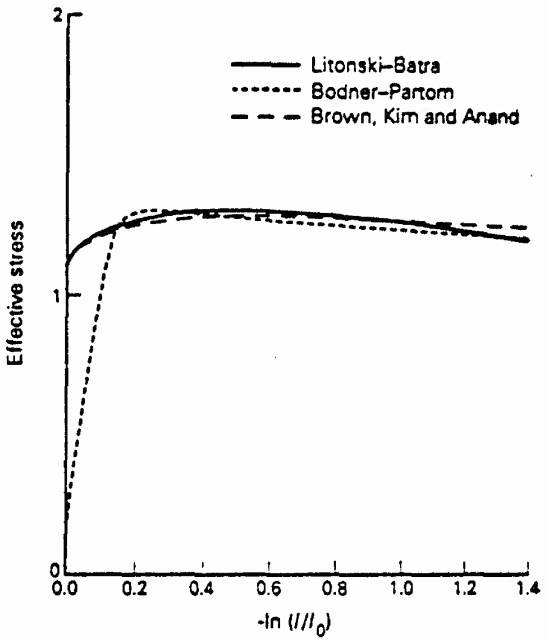

FIG. 2. The effective stress VS logarithmic strain curves for the three constitutive relations for a viscoplastic block deformed in plane strain compression at an average strain rate of 3300 s^{-1}.

We note that the initial-boundary-value problem solved to compute the s_e vs ε_e curve is highly nonlinear, and its solution may not be unique.

The aforestated values are used in studying the penetration problem whose results are discussed below.

3.2. *Comparison of results for the penetration problem from the three constitutive relations*

Figure 3 depicts the distribution of the normal stress, temperature rise and the tangential speed on the penetrator nose surface and the strain rate measure I at the centroids of elements abutting the nose surface for $\alpha = 10$, which corresponds to the penetrator speed of 718 m/s. In these and subsequent plots, the values of various quantities have been divided by a factor so that the curves fit on the same graph. For the values of material parameters used herein, the reference temperature θ_r, used to nondimensionalize the temperature rise, equals 108.9°C. The values of the tangential speed and the strain rate measure I for the three models are nearly the same. However, the value of the normal stress and the temperature rise computed with the BP model is more than that for the other two models. The value of the temperature rise at every point on the nose surface as computed with the BKA flow rule is more than that found with the LB model, but less than that determined by using the BP flow rule. The maximum difference between the temperature rise computed at any point on the nose surface with the three flow rules is nearly 30°C for an average temperature rise there of 400°C. One reason for the temperature being essentially uniform over the nose surface is that heat is transferred mainly by convection, since the value of δ in Eqn (17.4) equals 1.9×10^{-6}. The BP flow rule gives the highest value of the normal stress on the nose surface among the three flow rules because the pressure computed with it is the highest. For example, the pressure at the stagnation point equalled 12.07 and 12.67 for the LB and the BP flow rules, respectively. The nondimensional axial resisting force experienced by the penetrator was found to be 8.19, 8.84 and 8.26 for the LB, BP and BKA flow rules, respectively.

We recall that Batra and Adam [6] used the material parameters determined by Batra and Kim [39], who evaluated them by ensuring that the computed shear stress–shear strain curve during overall adiabatic simple shearing deformations of a viscoplastic block

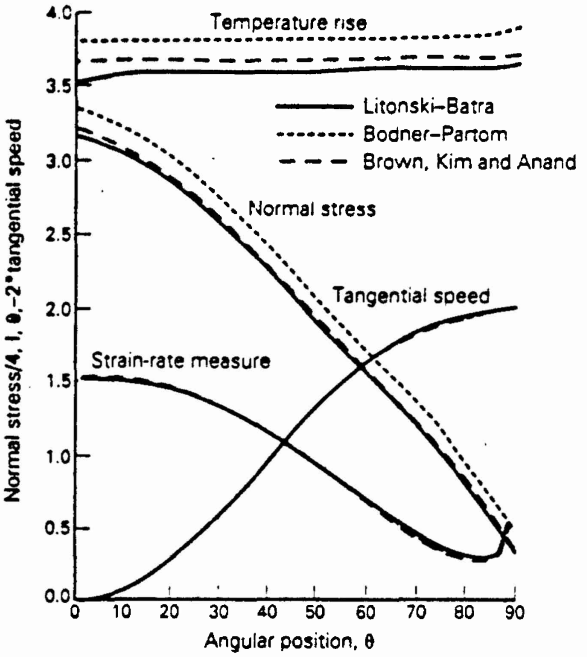

FIG. 3. Comparison of the variation of normal stress, strain rate measure, tangential speed, and the temperature rise at target particles abutting the penetrator nose surface for the three constitutive relations.

deformed at an average strain rate of $3300\,s^{-1}$ matched well with the experimental curve of Marchand and Duffy [40] for a HY-100 structural steel. Batra and Adam [6] found that for $\alpha = 4.5$, the peak pressure at or near the stagnation point equalled 18.71 and 30.16, respectively, for the LB and BP flow rules. Also, the values of the tangential speed and the strain rate measure I at points on the target–penetrator interface were not as close as that found in the present case. The BP flow rule predicted considerably higher values of the normal stress, mainly because of the significantly higher value of the hydrostatic pressure, and also of the temperature rise as compared to that for the LB flow rule. When G was set equal to infinity and material parameters assigned values used by Batra and Adam in the present code, the peak pressure with the BP flow rule was found to be twice that with the LB flow rule for $\alpha = 4.5$. We note that the target region analysed herein is more than that studied by Batra and Adam, and the problem formulation, as well as the finite element meshes used, is different.

We have plotted in Fig. 4 the variations of the axial stress $(-\sigma_{zz})$, the temperature rise θ, and the axial velocity $(-v_z)$ on the axial line, and the strain rate measure I at the centroids of elements adjoining the central line of symmetry for the three different constitutive relations studied herein. As for the distribution on the target–penetrator interface, the curves for the axial velocity and the strain rate measure are hardly distinguishable from each other for the three constitutive relations. There is not that much difference in the computed values of the temperature rise, but the axial stress computed with the BP model differs somewhat from that computed with the other two models, primarily due to the difference in the computed values of the hydrostatic pressure. These plots reveal that, at least along the axial line, significant deformations occur at target particles situated, at most, one penetrator diameter from the target–penetrator interface. The values of (I, θ) at the stagnation point, i.e. penetrator nose tip, are found to be (1.52, 3.53), (1.52, 3.80) and (1.53, 3.67) for the LB, BP and BKA flow rules, respectively. Since the nondimensional values of I need to be multiplied by (v_0/r_0) to get their dimensional counterparts, it is obvious that peak strain rates of the order of $1.1 \times 10^5\,s^{-1}$ occurred in the problem studied herein.

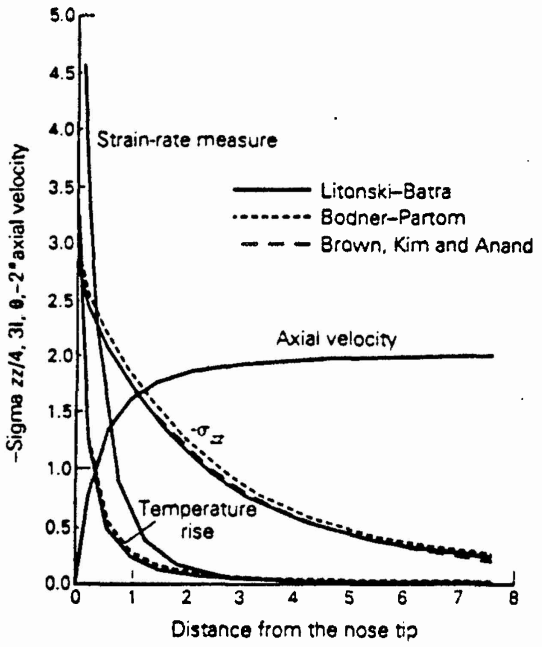

FIG. 4. Comparison of the variation of $(-\sigma_{zz})$, θ, I and $(-v_z)$ on the axial line for the three constitutive relations.

Along the axial line, uniaxial strain conditions prevail approximately. Thus, the magnitude of the deviatoric stress s_{zz} at a point on the axial line should equal 2/3 the effective flow stress defined as

$$\sigma_{eff} = 2\sqrt{3}\mu I. \tag{23}$$

The error e given by

$$e = 100\frac{|\frac{2}{3}\sigma_{eff} - |s_{zz}||}{\frac{2}{3}\sigma_{eff}} \tag{24}$$

is plotted in Fig. 5. The maximum error of 2.5% for the BP model suggests that the computed results satisfy $|s_{zz}| = 2/3\,\sigma_{eff}$ on the axial line reasonably well. The error decreases first as we move away from the stagnation point, but begins to increase at points distant $7r_0$ from the penetrator nose tip, probably because plastic deformations there are negligibly small.

An integration of the equation of motion (17.2) along the central streamline ($r = 0$) gives

$$\tfrac{1}{2}\alpha v^2 + p - s_{zz} - 2\int_0^z \frac{\partial \sigma_{rz}}{\partial r}\,dz = -\sigma_{zz}(0). \tag{25}$$

Figure 6 shows the contribution from the various terms for $\alpha = 10$. The three models give nearly the same value of the kinetic energy term ($\frac{1}{2}\alpha v^2$). The value of p for the BP model is uniformly more than that for the other two models. However, the value of s_{zz} for the three models is approximately the same. As noted by Pidsley [31] and Wright [41], there is a substantial contribution from transverse gradients of the shear stress, unlike that for a perfect fluid.

Setting $z = 0$ in Eqn (25) and comparing it with Tate's Eqn [27], we get

$$R_t = -\sigma^s_{zz} - \frac{\alpha}{2} \tag{26}$$

where R_t equals the strength parameter for the target in Tate's equation, and σ^s_{zz} is the

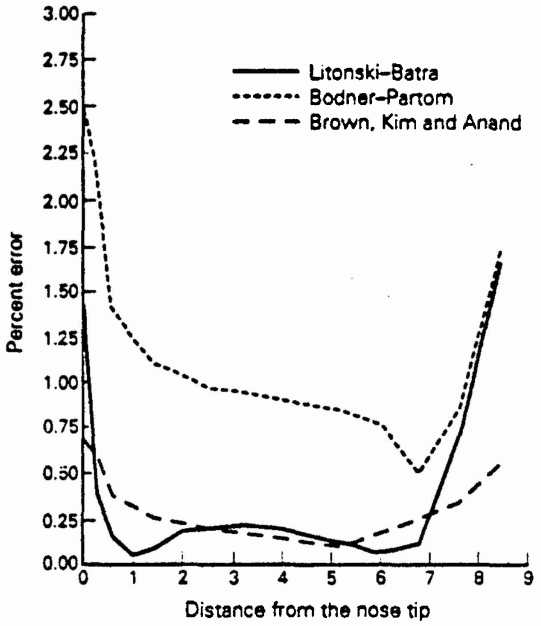

FIG. 5. Percentage error of s_{zz} in being equal to $2.3\,\sigma_{eff}$ on the axial line.

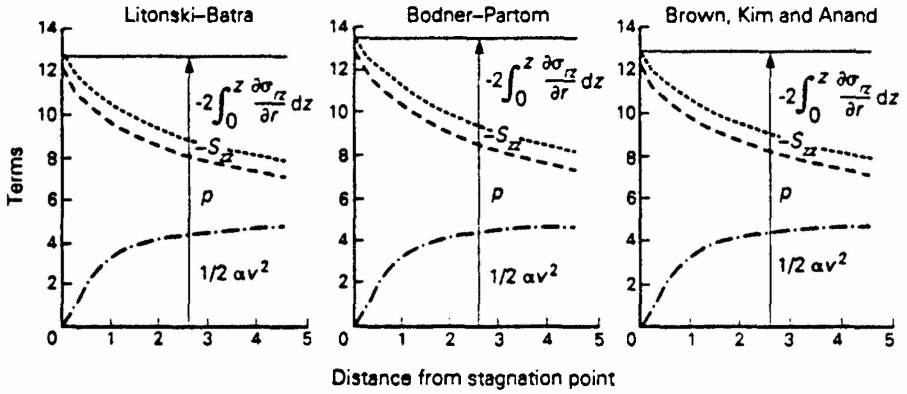

FIG. 6. Contribution of various terms in the nondimensionalized Bernoulli equation along the central stream line.

value of σ_{zz} at the stagnation point. Knowing σ^s_{zz} and α_e, we find R_t and arrive at the following

$$R_t = 8.13\,\sigma_{eff} = 7.713, \quad \text{for the LB model.} \tag{27.1}$$

$$R_t = 7.50\,\sigma_{eff} = 8.459, \quad \text{for the BP model.} \tag{27.2}$$

$$R_t = 6.57\,\sigma_{eff} = 7.886, \quad \text{for the BKA model.} \tag{27.3}$$

Tate [27] gave

$$R_t = \left[\frac{2}{3} + \ln\left(\frac{2}{3}\frac{E_t}{\sigma_0}\right)\right], \tag{28}$$

where E_t is Young's modulus for the target material. Equation (28) gives R_t equal to 6.64 for each one of the three flow rules. Thus, each one of the three models predicts a slightly higher value of R_t than that given by Tate. For an elastic perfectly plastic target, Jayachandran and Batra [10] found $R_t = 5.96$, and that its value depended weakly upon α.

We have plotted in Fig. 7 contours of the hydrostatic pressure in the deforming target

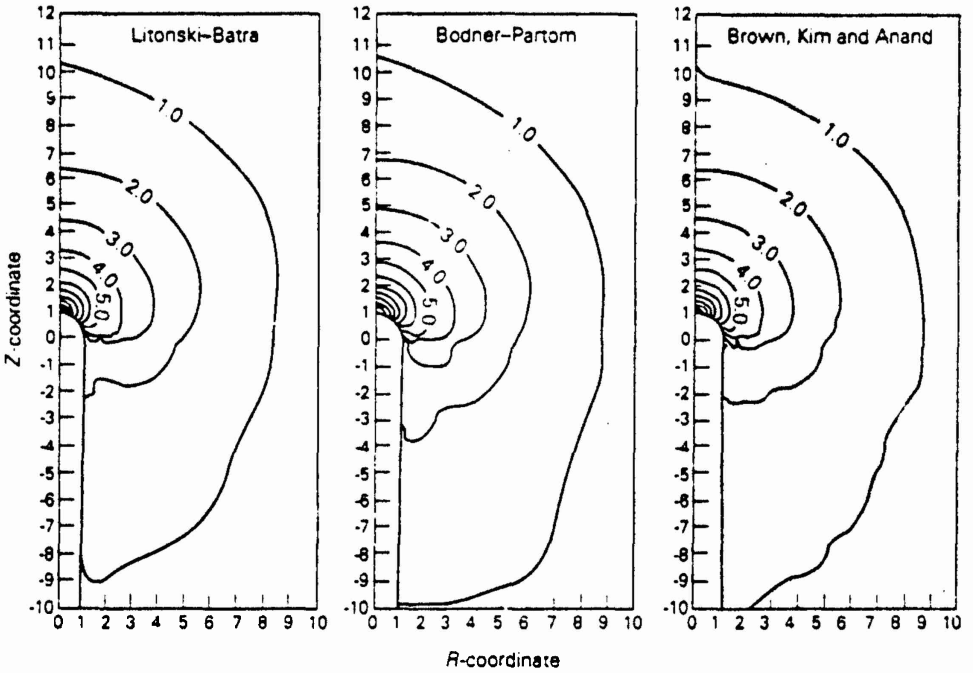

FIG. 7. Contours of the hydrostatic pressure in the deforming target region for three different flow rules.

region for the three flow rules. It is clear that along any radial line the pressure drops off more slowly for the BP model as compared to that for the other two flow rules. The contours are at an interval of 1.0 and the contour of the zero hydrostatic pressure is not plotted in order to concentrate on the region surrounding the target–penetrator interface. For each flow rule, the pressure drops off to nearly 3.0 at the nose periphery from its peak value of more than 12 at the nose tip. However, when the target material was modeled as elastic–perfectly plastic in [10], the pressure at the nose tip equalled at most 10 and dropped off to nearly 2.0 at the nose periphery. The consideration of strain-hardening, strain rate hardening, and thermal softening effects has resulted in an increase in the computed value of the hydrostatic pressure.

In the constitutive relations employed herein, it is tacitly assumed that a material point undergoes elastic and plastic deformations simultaneously. However, points on the bounding surface EFA where $\underset{\sim}{s} = \underset{\sim}{0}$ cannot be deforming plastically. Here we classify points for which the stress state satisfies the condition

$$tr(\underset{\sim}{s}^2) = \tfrac{2}{3}\sigma_{\text{eff}}^2 \tag{29}$$

as deforming plastically, and those for which the stress state lies inside the surface (29) as deforming elastically. The elastic–plastic boundary thus computed and obtained by joining points on the surface (29) by straight line segments is depicted in Fig. 8. Ahead of the penetrator nose surface, the elastic–plastic boundary extends farthest for the LB model. The distance 6.8 on the axial line of the elastic–plastic boundary for the BP and BKA models is about the same as that found when the target material is presumed to be elastic–perfectly plastic [10]. Tate [27], by using a solenoid flow model and assuming that a material point was deforming either elastically or plastically, found that the elastic–plastic boundary was located at an axial distance of 6.71, which compares well with the presently computed results.

For steady state problems, Tate [28] has proposed a method to compute the components of the finite strain tensor from a known velocity field. He found the contours of the circumferential strain to be nearly parallel to the crater surface, and the circumferential strain at a point distant r_0 from the crater tip equal to 0.05. Here we define a scalar measure

Int. J. Engng Sci. Vol. 28, No. 12, pp. 1347–1358, 1990 0020-7225/90 $03.00 + 0.00

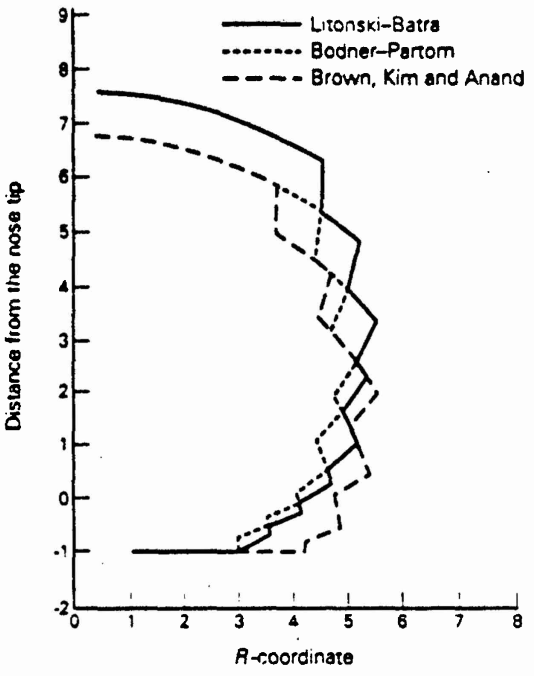

FIG. 8. Elastic-plastic boundary in the deforming target region for three different flow rules.

ε of strain by

$$\dot{\varepsilon} = \sqrt{\tfrac{2}{3}}[trD^2]^{1/2} = \frac{2}{\sqrt{3}}I \tag{30}$$

which, because of the steady state deformations, can be written as

$$(\mathbf{v}\cdot\text{grad})\varepsilon = \frac{2}{\sqrt{3}}I. \tag{31}$$

We note that ε does not equal an invariant of any finite strain tensor. We first compute I from the velocity field, and then ε as a solution of Eqn (31) with boundary condition $\varepsilon = 0$ on EFA. The contours of ε look alike for the three flow rules; those for the BP model are depicted in Fig. 9. The contours of ε are virtually parallel to the crater surface. On any radial line, ε drops off quite rapidly for a distance of r_0 from the crater surface, and then quite slowly. Comparing these contours of ε with the elastic-plastic boundary plotted in Fig. 8, one can conclude that $\varepsilon = 0.02$ on the elastic-plastic boundary. The contours of ε reveal that severe deformations of the target spread farther to the side than ahead of the penetrator nose. At points on the target-penetrator interface $\varepsilon = 3.0$. Since no failure criterion is included in our work, a material point can undergo an unlimited amount of deformation.

3.3. *Histories of field variables for target particles*

The results discussed heretofore have involved the spatial distribution of field variables. However, in order to establish testing regimes for target materials, it is useful to know the histories of stress, strain rate, temperature, etc. for a typical target particle. Accordingly, we discuss below the histories of field variables for three target particles. The results for the three models are quite similar to each other. Thus, we present results for the BKA model only; those for the LB model have been given by Lin and Batra [18]. The computer code developed by Lin and Batra has been used to first find streamlines originating from a spatial location, and then histories of field variables for that material particle. Henceforth, we identify the history of a field variable for the material particle that once occupied the place A as the history of the variable for the material particle A.

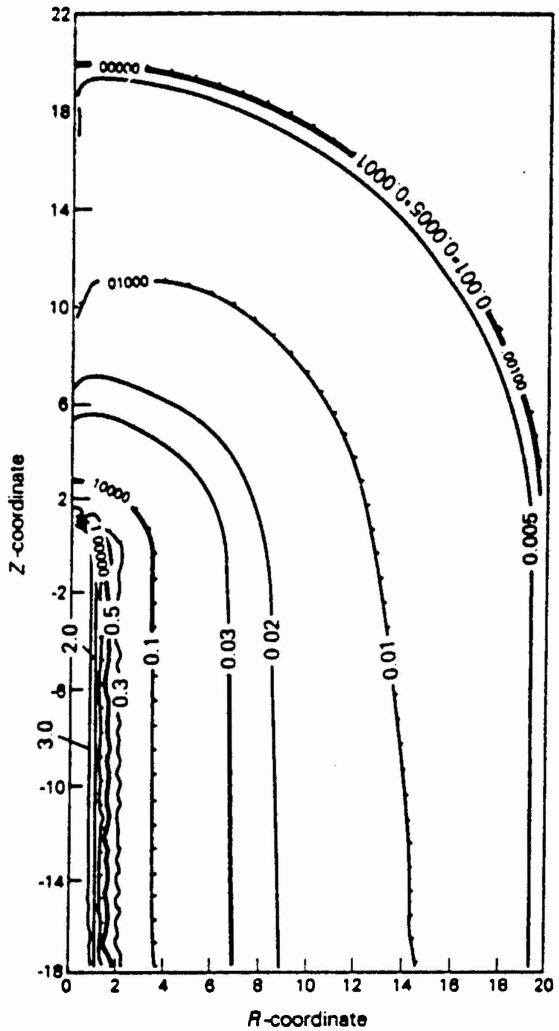

FIG. 9. Contours of strain in the deforming target region for the Bodner–Partom flow rule.

Figure 10 shows streamlines for three particles A(0.02, 8), B(0.05, 8) and C(0.1, 8). That the streamlines do not intersect should be clear from their enlarged view around the penetrator nose. Because of the different scales used along the vertical and horizontal axes, the nose shape appears flat rather than circular. The r- and z-coordinates of these three points at different times are given in Fig. 11, the time being measured from the instant these particles occupied the aforestated places. The particles reach a position near the nose tip at $t \approx 4.5$, and are near the nose periphery when $t \approx 7.25$. The time increment is computed by dividing the incremental distance a particle travels by its speed during that interval. The time history of the r- and z-components of the velocity of these three particles relative to that of the nose tip is depicted in Fig. 12. As these particles approach the penetrator nose, the r- and z-components of their absolute velocity increase. Whereas the peak values of v_r for these three particles are nearly equal, the maximum value of the z-component of the absolute velocity varies from 0.9 for particle A to 0.8 for particle C.

The time histories of the strain rate measure I and the spin are given in Fig. 13. Since the target deformations are assumed to be axisymmetric, there is only one non-zero component of spin. The small oscillations or bumps in the curves are due to numerical errors, possibly introduced because of taking larger time intervals in computing the time histories. The peak values of the spin for these three particles are nearly the same. However,

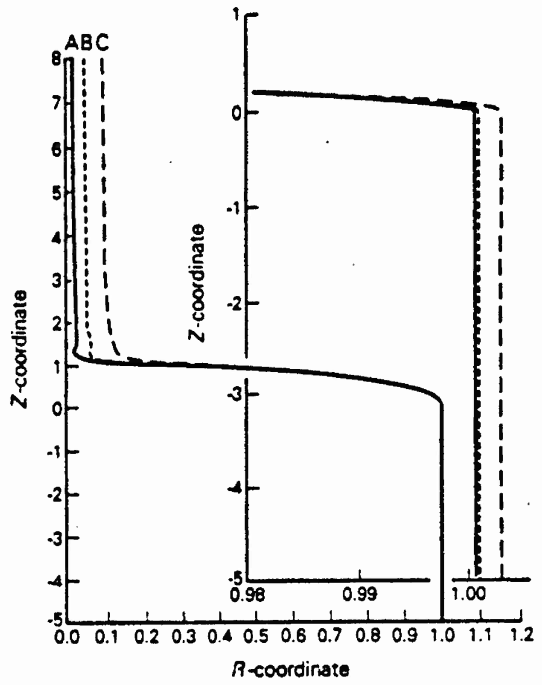

FIG. 10. Streamlines emanating from points A(0.01, 8), B(0.05, 8) and C(0.1, 8).

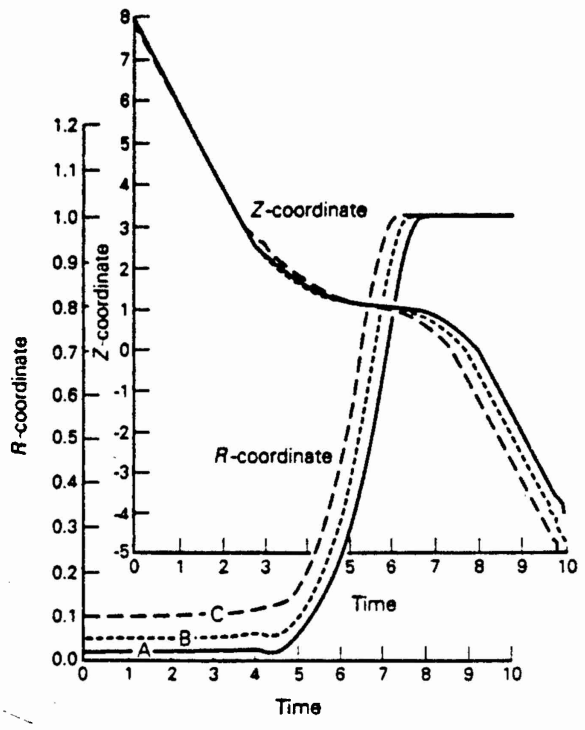

FIG. 11. The r- and z-coordinates of points A, B and C at different times.

the peak value of I for particle A is 2.1, and that for C is 1.9. For particle A, peak values of I and the spin occur when it is near the nose tip and the nose periphery, respectively. Figure 14 depicts the time histories of the temperature rise θ, hydrostatic pressure p, the internal variable g, and the effective stress σ_{eff} for these four particles. The value of g increases slowly till these particles reach near the penetrator nose tip and then stays

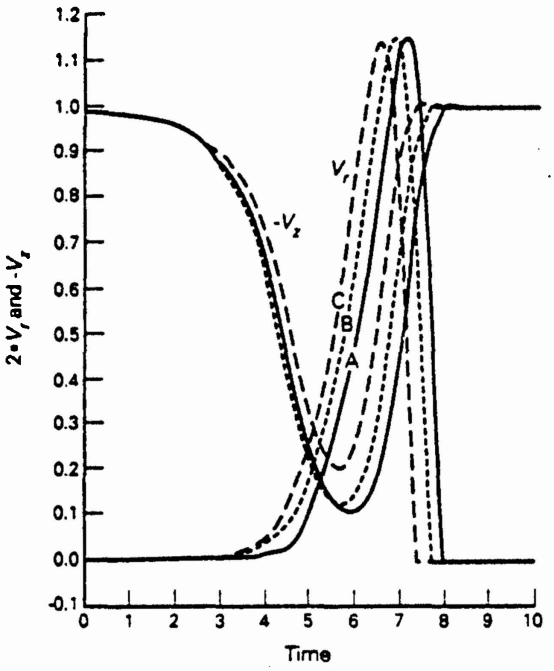

FIG. 12. The r- and z-components of the velocity of points A, B and C at different times.

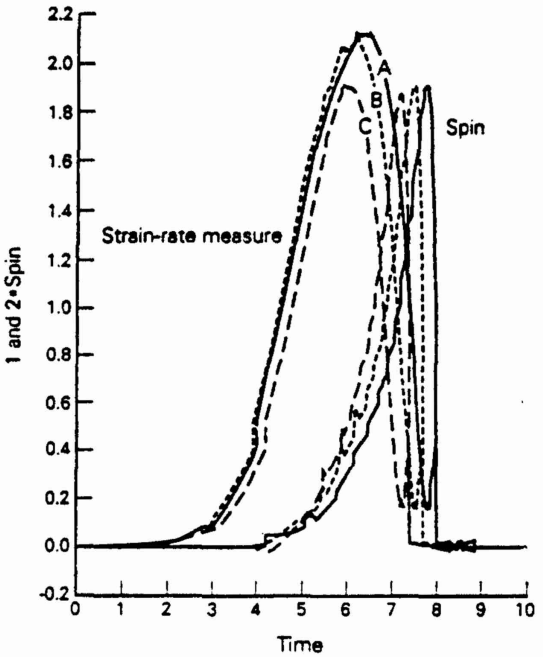

FIG. 13. Histories of the strain rate measure I and the spin for particles A, B and C.

essentially constant, suggesting that it has reached the saturation value. Nearly all of the temperature rise at a material particle occurs during the time it is going around the penetrator nose. The time histories of I, θ and σ_{eff} reveal that even though I and θ are increasing for $4 \leqslant t \leqslant 6$ for particle A, the effective stress σ_{eff} is decreasing during this time interval, implying that thermal softening exceeds the hardening caused by the strain rate and the evolution of the internal variable g. Whether or not this softening will lead to a

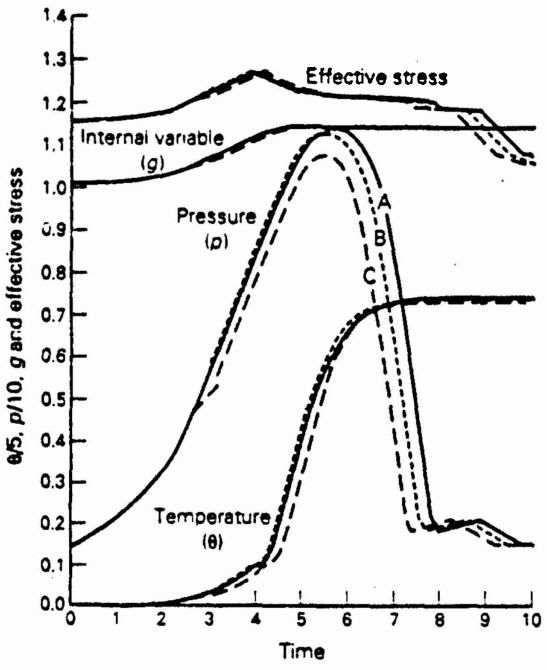

FIG. 14. Histories of the temperature rise, hydrostatic pressure, internal variable and the effective stress at points A, B and C.

material instability in the form of a shear band is unclear because of the complex state of deformations prevailing at points adjoining the target–penetrator interface.

4. CONCLUSIONS

We have analysed the steady state axisymmetric deformations of a viscoplastic target being penetrated by a rigid cylindrical hemispherical nosed penetrator. The thermomechanical response of the target material is modeled by three viscoplastic flow rules, namely, the Litonski–Batra, the Bodner–Partom and the Brown–Kim–Anand. Each of these flow rules is calibrated to give almost identical effective stress versus logarithmic strain curves for a block made of target material and deformed in plane strain compression at an average strain rate of $3300\,s^{-1}$. For the penetration problem, the BP model gives a slightly higher value of the hydrostatic pressure, and hence, normal stress on the penetrator nose surface as compared to that given by the use of the other two models. The pressure decays a little bit slowly for the BP model as one moves away from the penetrator nose surface as compared to the other two models. A comparison of the presently computed results with those obtained previously by Batra and Adam for the BP and LB models reveals that the models calibrated against a compression test give almost identical results for the penetration problem as compared to those calibrated against a simple shear test. The time histories of the field variables at three target particles initially close to the axis of symmetry suggest that they experience softening behavior, in the sense that even though the strain rate increases, the effective stress decreases. The peak values of the spin and the second invariant of the strain rate tensor are of the same order of magnitude, but a particle experiences these peak values when it is at different locations around the penetrator nose.

Acknowledgements—This work was supported by the U.S. Army Research Office Contract DAAL03-89-K-0050 to the University of Missouri, Rolla. Some of the computations were performed on the NSF sponsored supercomputer center at the University of Illinois at Urbana.

REFERENCES

1. H. J. Frost and M. F. Ashby. *Deformation Mechanism Maps*. Pergamon Press. New York (1982).
2. B. D. Coleman and M. E. Gurtin. Thermodynamics with internal state variables. *J. Chem. Phys.* **47**. 597 (1967).
3. K. S. Chan, U. S. Lindholm, S. R. Bodner and K. P. Walker. A survey of unified constitutive theories. *Proceedings of 2nd Symposium on Nonlinear Constitutive Relations for High Temperature Applications*. NASA Lewis Research Center. 15–17 June. (1984).
4. T. Inoue. Inelastic constitutive relationships and applications to some thermomechanical processes involving phase transformations. In *Thermal Stresses III* (edited by R. B. Hetnarski). North Holland. Amsterdam. pp. 192–278 (1989).
5. J. Lubliner. *Plasticity Theory*. MacMillan Publishing Company. New York (1990).
6. R. C. Batra and A. Adam. Effect of viscoplastic flow rules on steady state penetration of thermoviscoplastic targets. *Int. J. Engng Sci.* **29**. 1391–1408 (1991).
7. S. R. Bodner and Y. Partom. Constitutive equations for elastic-viscoplastic strain-hardening materials. *J. Appl. Mech.* **42**. 385–389 (1975).
8. S. B. Brown, K. H. Kim and L. Anand. An internal variable constitutive model for hot working of metals. *Int. J. Plasticity* **5**. 95–130 (1989).
9. R. C. Batra and T. W. Wright. Steady state penetration of rigid perfectly plastic targets. *Int. J. Engng Sci.* **24**. 41–54 (1986).
10. R. Jayachandran and R. C. Batra. Steady state penetration of elastic perfectly plastic targets. *Acta Mechanica*. in press.
11. R. C. Batra and T. Gobinath. Steady state axisymmetric deformations of a thermoviscoplastic rod penetrating a thick thermoviscoplastic target. *Int. J. Impact Engng* **11**. 1–31 (1991).
12. T. Gobinath and R. C. Batra. A steady state axisymmetric penetration problem for rigid perfectly plastic materials. *Int. J. Engng Sci.* **29**. 1315–1331 (1991).
13. R. C. Batra. Steady state penetration of viscoplastic targets. *Int. J. Engng Sci.* **25**. 1131–1141 (1987).
14. R. C. Batra. Steady state penetration of thermoviscoplastic targets. *Comp. Mech.* **3**. 1–12 (1988).
15. R. C. Batra and Pei-Rong Lin. Steady state deformations of a rigid perfectly plastic rod striking a rigid cavity. *Int. J. Engng Sci.* **26**. 183–192 (1988).
16. R. C. Batra and P. R. Lin. Steady state axisymmetric deformations of a thermoviscoplastic rod striking a hemispherical rigid cavity. *Int. J. Impact Engng* **8**. 99–113 (1989).
17. R. C. Batra and P. R. Lin. Histories of stress, temperature and spin in steady state deformations of a thermoviscoplastic rod striking a hemispherical rigid cavity. *Int. J. Engng Sci.* **28**. 93–98 (1990).
18. P. R. Lin and R. C. Batra. Histories of stress, strain-rate, temperature, and spin in steady state penetration problems. *Int. J. Engng Sci.* **27**. 1155–1165 (1989).
19. M. E. Backman and W. Goldsmith. The mechanics of penetration of projectiles into targets. *Int. J. Engng Sci.* **16**. 1–99 (1978).
20. T. W. Wright and K. Frank. Approaches to penetration problems. *SMIRT Symposium*. No. 14. Impact. Lausanne. Switzerland (1987).
21. C. E. Anderson and S. R. Bodner. The status of ballistic impact modeling. *Int. J. Impact Engng* **7**. 9–35 (1988).
22. T. Z. Blazynski. *Materials at High Strain Rates* (edited by T. Z. Blazynski). Elsevier Applied Science. Elsevier. London (1987).
23. M. MacCauley. *Introduction to Impact Engineering*. Chapman and Hall. London (1987).
24. J. A. Zukas, T. Nicholas, H. F. Swift, L. B. Greszczuk and D. R. Curran. *Impact Dynamics*. Wiley-Interscience. New York (1982).
25. A. Tate. A theory for the deceleration of long rods after impact. *J. Mech. Phys. Solids* **15**. 387–399 (1967).
26. A. Tate. Further results in the theory of long rod penetration. *J. Mech. Phys. Solids* **17**. 141–150 (1969).
27a. A. Tate. Long rod penetration models—part I. A flow field model for high speed long rod penetration. *Int. J. Mech. Sci.* **28**. 535–548 (1986).
27b. A. Tate. Long rod penetration models—part II. Extensions to the hydrodynamic theory of penetration. *Int. J. Mech. Sci.* **28**. 599–612 (1986).
28. A. Tate. A simple hydrodynamic model for the strain field produced in a target by the penetration of a high speed long rod projectile. *Int. J. Engng Sci.* **16**. 845–858 (1978).
29. V. P. Alekseevski. Penetration of a rod into a target at high velocity. *Comb. Expl. Shock Waves* **2**. 63–66 (1966). (Translation from Russian. Faraday Press. New York.)
30. R. C. Batra and Xinju Chen. An approximate analysis of steady state axisymmetric deformations of viscoplastic targets. *Int. J. Engng Sci.* **28**. 1347–1358 (1990).
31. P. H. Pidsley. A numerical study of long rod impact onto a large target. *J. Mech. Phys. Solids* **32**. 315–333 (1984).
32. J. Litonski. Plastic flow of a tube under adiabatic torsion. *Bull. Acad. Pol. Sci.* **25**. 7 (1977).
33. A. Tate. A theoretical estimate of temperature effects during rod penetration. *9th Ballistic Symposium*. pp. 2.307–2.314 (1987).
34. J. F. Bell. *Physics of Large Deformation of Crystalline Solids*. Springer-Verlag. New York (1968).
35. M. R. Lin and R. H. Wagoner. Effect of temperature, strain, and strain rate on the tensile flow stress of

I. F. steel and stainless steel type 310. *Scripta Metallurgica* **20**, 143–148 (1986).
36. U. S. LINDHOLM and G. R. JOHNSON, Strain rate effects in metals at large strain rates. In *Metal Behaviour Under High Stresses and Ultrahigh Loading Rates* (edited by V. WEISS). Plenum Press, New York, pp. 61–79 (1983).
37. R. JAYACHANDRAN and R. C. BATRA, Steady state axisymmetric deformations of a thick elastic-thermoviscoplastic target. *Int. J. Engng Sci.*, in press.
38. R. C. BATRA and D. S. LIU, Adiabatic shear banding in plane strain compression problems. *J. Appl. Mech.* **56**, 527 (1989).
39. R. C. BATRA and C. H. KIM, Effect of viscoplastic flow rules on the initiation and growth of shear bands at high strain rates. *J. Mech. Phys. Solids* **38**, 859–874 (1990).
40. A. MARCHAND and J. DUFFY, An experimental study of the formation process of adiabatic shear bands in a structural steel. *J. Mech. Phys. Solids* **36**, 251 (1988).
41. T. W. WRIGHT, A survey of penetration mechanics for long rods. In *Lecture Notes in Engineering*, Vol. 3. *Computational Aspects of Penetration Mechanics* (edited by J. CHANDRA and J. FLAHERTY). Springer-Verlag, New York (1983).

Int. J. Engng Sci. Vol. 28. No. 1. pp. 93–98. 1990
Printed in Great Britain.

0020–7225/90 $3.00 + 0.00

LETTERS IN APPLIED AND ENGINEERING SCIENCES

HISTORIES OF STRESS, STRAIN-RATE, TEMPERATURE, AND SPIN IN STEADY STATE DEFORMATIONS OF A THERMOVISCOPLASTIC ROD STRIKING A HEMISPHERICAL RIGID CAVITY

R. C. BATRA and PEI-RONG LIN

Department of Mechanical and Aerospace Engineering and Engineering Mechanics, University of Missouri–Rolla, Rolla, MO 65401, U.S.A.

Abstract—Given the velocity field and the values of a field variable f at a large number of discrete points in a bounded 2-dimensional domain, an algorithm has been developed to compute the streamline that passes through a desired point P in the domain, and the time histories of f at the material particle starting from the instant it occupied the point P. Time histories of the effective stress, second invariant of the strain-rate tensor, temperature and the spin for a few material particles in the steady state axisymmetric deformations of a thermoviscoplastic rod striking a rigid hemispherical cavity are presented. This information should help develop appropriate constitutive models for the penetrator material and establish desirable testing regimes for practical problems.

INTRODUCTION

The solution of any mechanics problem necessarily involves choosing for the material of the body a constitutive relation that adequately models its response over the range of deformations anticipated to occur in the problem. However, the computed values of various field variables depend, in a nontrivial way, upon the constitutive assumptions made to solve the problem. One possible resolution of this rather interesting problem is to choose a constitutive relation, solve the problem, check if the constitutive assumptions made are valid over the range of computed deformations, and, if necessary, redo the problem with the modified constitutive relation.

We note that many of the recently proposed theories (e.g. see [1–4]) of large deformation elastoplasticity are based on different kinematic assumptions thus necessitating the hypothesizing of constitutive relations for variables which may not be simply related to each other. In an attempt to determine the most appropriate theory for the analysis of penetration problems and to delimit the range of values of the variables for which the constitutive relation should be valid, we find the histories of the effective stress, second invariant of the strain-rate tensor, the temperature and the spin at a few typical particles on the penetrator. Only steady state axisymmetric deformations of a viscoplastic penetrator striking a rigid hemispherical cavity are studied. The solution of this problem reported earlier by Batra and Lin [5] is presumed to be given. It is hoped that the time histories of various field variables reported herein will help establish desirable testing regimes for practical problems, and assess the efficacy of different plasticity theories for the penetration problem.

Computed results reveal that material particles near the free surface suffer higher values of the peak plastic strain-rate as compared to those near the centroidal axis of the rod. Values of plastic spin are of the same order of magnitude as the second invariant of the strain-rate tensor. The effective stress at material particles initially near the undeformed centroidal axis decreases because of the rise in their temperature, even though the plastic-strain rate stays essentially uniform. This occurs when the particles reach near the cavity bottom. This drop of effective stress suggests that there is a greater likelihood of the formation of an adiabatic shear band near the stagnation point, and at points adjoining the cavity surface.

STATEMENT OF THE PROBLEM

Let f denote one of the quantities such as the second invariant of the strain-rate tensor, temperature or a component of the stress tensor. The problem studied herein may be stated as

follows: given the values of the velocity field $(V_x(x^\alpha, y^\alpha),\ V_y(x^\alpha, y^\alpha))$ and $f(x^\alpha, y^\alpha)$, $\alpha = 1, 2, \ldots, M$ at M discrete points (x^α, y^α) in a bounded 2-dimensional domain, find the history of f at a material particle that initially was at any arbitrary place (x_0, y_0). Needless to say, the accuracy with which the problem can be solved depends upon the value of M and the spatial distribution of points where the data is given. The optimum number of points and their spatial distribution required to solve the problem within a prescribed tolerance has not been determined yet. However, in the present case the data is given at numerous points since a very fine finite element mesh was used to solve the steady state penetration problem whose output serves as the data for the current problem.

The first step in the solution of the problem is to find the streamline that passes through the point $P(x_0, y_0)$. If the velocity field were given as a continuous function of position, then the streamline can be found by integrating the given ordinary differential equations and finding their solution that passes through P. However, for the present problem such is not the case. When the data is given at a discrete set of points, Lin and Batra [6] have developed an algorithm to compute the streamline through P and the time history of the field variable f for a material particle that once occupied the place (x_0, y_0). We use the same computer code to find the histories of the effective stress, second invariant of the strain-rate tensor, spin, hydrostatic pressure and the temperature for a few material particles during the steady state axisymmetric deformations of a penetrator striking a rigid hemispherical cavity.

RESULTS

Below we present streamlines and histories of various field variables for the steady state axisymmetric deformations of a thermoviscoplastic rod striking a hemispherical rigid cavity [5]. In cylindrical coordinates and in terms of non-dimensional variables, the governing equations are:

$$\operatorname{div}\mathbf{v} = 0,$$

$$\operatorname{div}\boldsymbol{\sigma} = \frac{\bar{\rho}v_0^2}{\sigma_0}(\mathbf{v}\cdot\operatorname{grad})\mathbf{v},$$

$$\operatorname{tr}(\boldsymbol{\sigma}\mathbf{D}) + \beta\operatorname{div}(\operatorname{grad}\theta) = (\mathbf{v}\cdot\operatorname{grad})\theta,$$

$$\frac{\operatorname{tr}(\boldsymbol{\sigma}\mathbf{D})}{(1+\psi/0.017)^{0.01}} = (\mathbf{v}\cdot\operatorname{grad})\psi,$$

where

$$\boldsymbol{\sigma} = -p\mathbf{1} + \frac{1}{\sqrt{3}\,I}\left(1 + 10^4\frac{v_0}{r_0}I\right)^{0.025}(1 - 0.00055\theta_0\theta)\left(1 + \frac{\psi}{0.017}\right)^{0.01},$$

$$2I^2 = \operatorname{tr}(\mathbf{D}^2), \qquad 2\mathbf{D} = \operatorname{grad}\mathbf{v} + (\operatorname{grad}\mathbf{v})^{\mathrm{T}},$$

$$\boldsymbol{\sigma} = \bar{\boldsymbol{\sigma}}/\sigma_0, \qquad p = \bar{p}/\sigma_0, \qquad \mathbf{v} = \bar{\mathbf{v}}/v_0, \qquad r = \bar{r}/r_0, \qquad z = \bar{z}/r_0,$$

$$\theta = \bar{\theta}/\theta_0, \qquad \beta = \bar{k}/(\bar{\rho}\bar{c}v_0r_0), \qquad \theta_0 = \sigma_0/(\bar{\rho}\bar{c}).$$

Here the dimensional quantities are indicated by a superimposed bar, $\boldsymbol{\sigma}$ is the Cauchy stress tensor, $\bar{\rho}$ is the mass density of a penetrator material particle, $\bar{k}$ is the thermal conductivity, σ_0 is the yield stress in a quasistatic simple tension or compression test, $\bar{c}$ is the specific heat, θ is the temperature rise, the internal parameter ψ describes the work hardening of the material, v_0 is the speed of the penetrator and r_0 its radius. Values assigned to different parameters are

$$\bar{c} = 473\ \text{J/kg °C}, \qquad \bar{k} = 48\ \text{W/m °C}, \qquad \bar{\rho} = 7800\ \text{kg/m}^3, \qquad \sigma_0 = 180\ \text{MPa},$$

$$v_0 = 340\ \text{m/s}, \qquad r_0 = 2.54\ \text{mm}.$$

This choice of values gives $\theta_0 = 48.9$°C. Results presented below are in terms of non-dimensional variables and the multiplying factors in order to obtain their dimensional counterparts are given in Table 1.

Figure 1 depicts the streamlines emanating from the points (0.05, 3.0), (0.10, 3.0), (0.90, 3.0) and (0.95, 3.0). We have not plotted the streamlines that start from the points (0.0, 3.0) and

Table 1

Quantity	Multiplying factor
Speed (m/s)	340
r or z-coordinate (mm)	2.54
Hydrostatic pressure (MPa)	180
Effective stress (MPa)	180
Strain-rate invariant (s^{-1})	1.34×10^5
Spin (s^{-1})	1.34×10^5
Temperature rise (°C)	48.9

(1.0, 3.0). The former coincides with the centroidal axis of the rod and the latter with the free surface. The shape of the free surface for different values of the penetrator speed is shown in Fig. 3 of the paper by Batra and Lin [5]. Whereas the streamlines passing through the points (0.90, 3.0) and (0.95, 3.0) stay essentially parallel to each other, the distance between those originating from (0.05, 3.0) and (0.10, 3.0) decreases sharply after they reach the area near the stagnation point and turn around. In Fig. 2 we have plotted the location of these material particles at different times and their speed, the time is reckoned from the instant these material particles were on the surface $z = 3$. The speed of particles near the free surface decreases from 1.0 to about 0.45 when they are at the bottom-most point on the free surface and then stays essentially constant. However, the speed of material particles initially near the centroid axis undergoes a significant change, their speed decreases from 1.0 to about 0.15 when they reach the area near the stagnation point and then increases gradually to about 0.74. As expected the speed of the particle initially closer to the centroidal axis decreases more than that of the particles initially farther from the centroidal axis.

Figure 3 shows the time histories of the spin and the second invariant I of the strain-rate tensor. Since we have neglected elastic deformations and studied the axisymmetric problem, there is only one non-zero component of the plastic spin tensor. These plots reveal that the values of the plastic spin and I are higher for material particles near the free surface as compared to those for material particles near the centroidal axis. Whereas the peak values of I for the four material particles considered are of the same order of magnitude those of the plastic spin are not. The maximum value of the plastic spin for the material particles near the centroidal axis is an order of magnitude lower than that of the particles near the free surface of the rod.

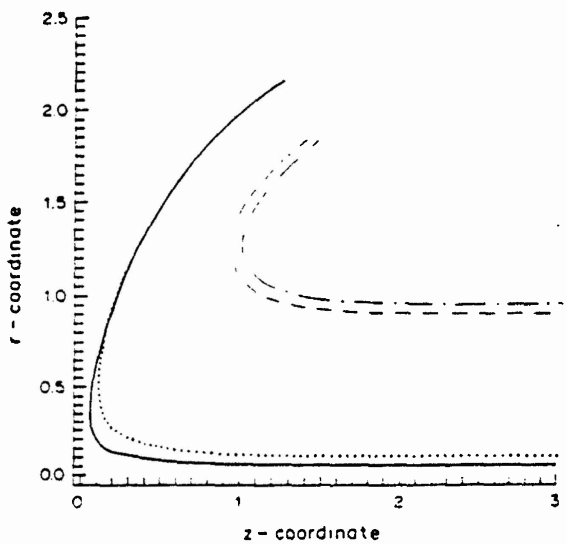

Fig. 1. Streamlines emanating from four points on the incoming penetrator. The originating point for the four curves are: —— (0.05, 3.0); . . . . . (0.10, 3.0); - - - - - - (0.90, 3.0); ——— (0.95, 3.0).

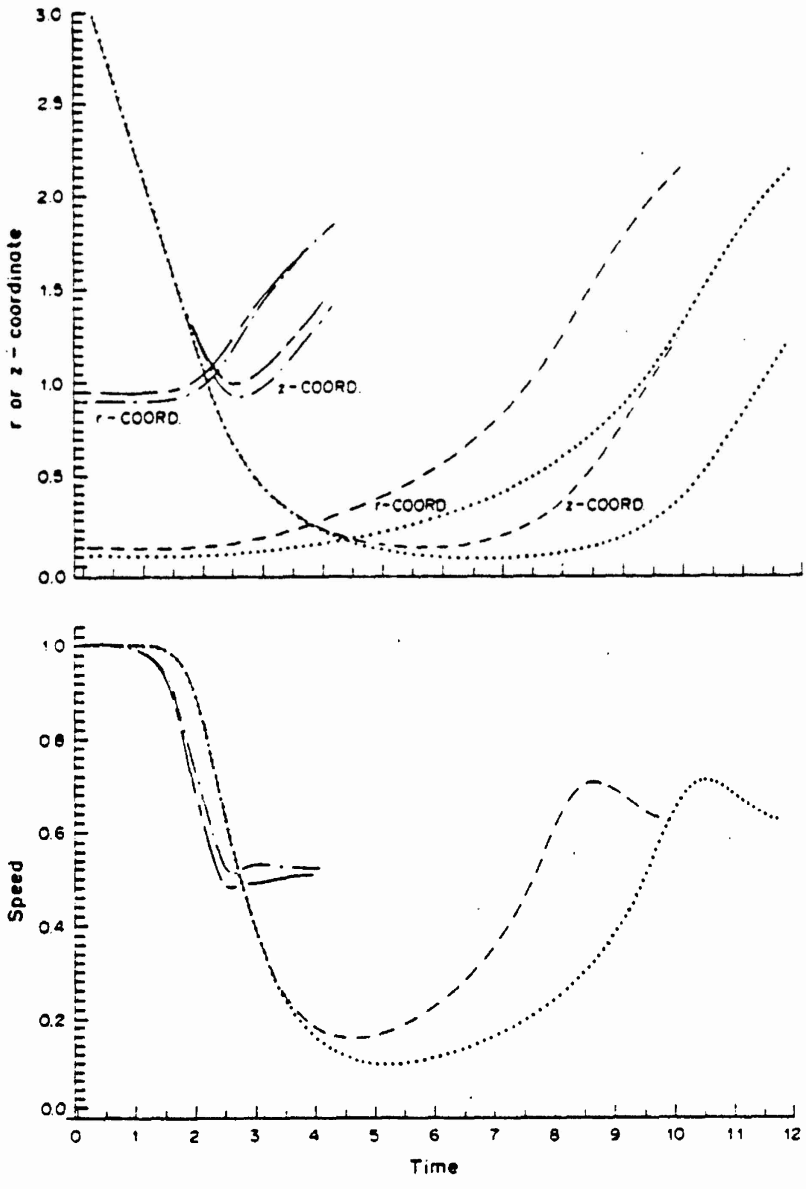

Fig. 2. The variation with time of the speed, and r-, z-coordinates of the four material particles. The initial location of the material particle for the four curves are: ——— (0.95, 3.0); — — — (0.80, 3.0); ------ (0.10, 3.0); ····· (0.05, 3.0).

The time histories of the temperature and the effective stress s_e defined as

$$s_e = \left(\frac{1}{2}\,\mathrm{tr}(\boldsymbol{\sigma} + p\mathbf{1})^2\right)^{1/2}$$

for the four material particles considered are plotted in Fig. 4. Note that the peak value of the effective stress experienced by the four material particles is essentially the same. However, the time histories of the temperature and I for these particles are noticeably different. The temperature rise for material particles near the free surface is considerably less as compared to that for material particles near the centroidal axis. The temperature rise for the latter particles is nearly one-third of the presumed melting temperature of the material. At a higher speed, these values will be even higher. The plots of the strain-rate invariant I in Fig. 3 and of the temperature rise and s_e in Fig. 4 reveal that the values of s_e for material particles near the

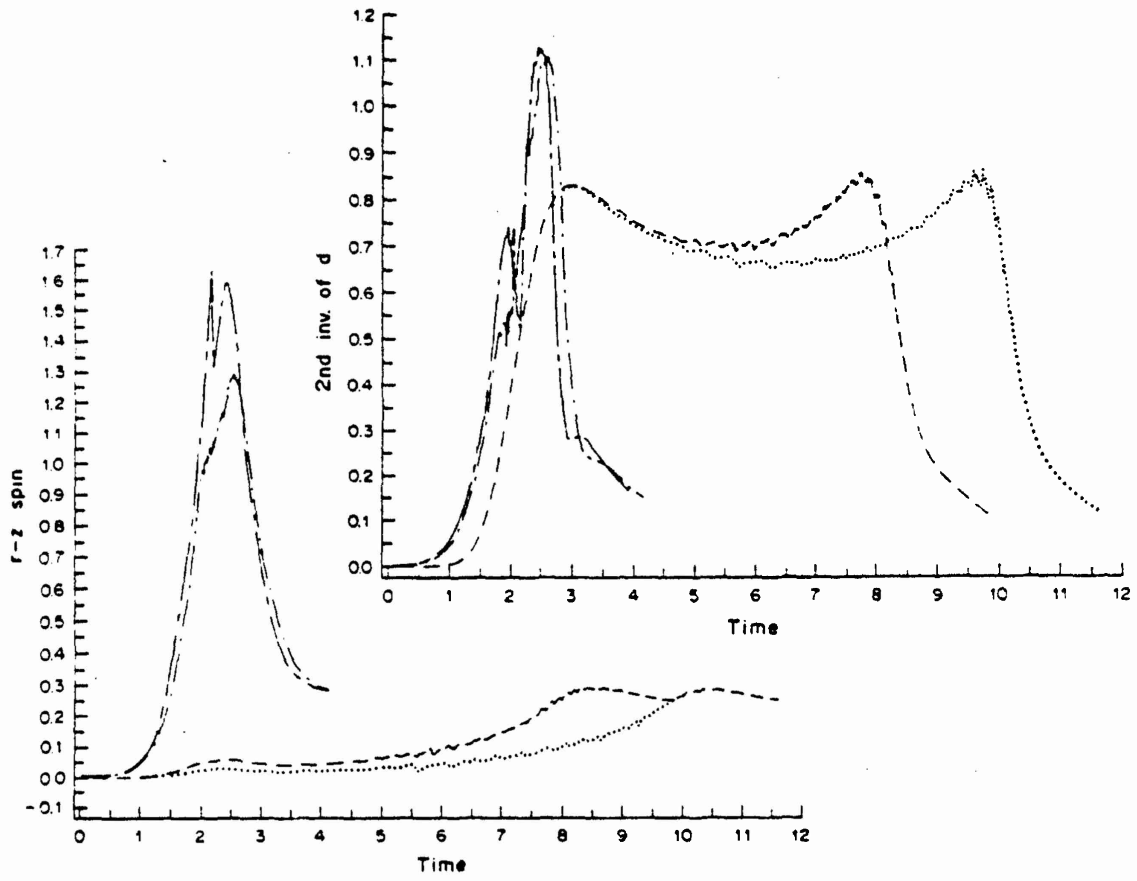

Fig. 3. Time histories of the spin and the second invariant of the strain-rate tensor for the four material particles. See Fig. 2 for explanations.

centroidal axis decrease due to the fact that softening of the material caused by its heating has overcome the combined effects of strain-rate and work hardening. The effect of work-hardening represented herein by the parameter ψ is not that significant because of the relatively small value (0.01) of the exponent selected in the constitutive relation. That is why we have not included the time history of ψ in our results. If plotted, the time histories of ψ for these material particles mimic those of the temperature rise except for a change of scale. The results of Fig. 4 suggest that, in this problem, a shear band is likely to form near the cavity surface for higher values of the penetrator speed.

CONCLUSIONS

During the steady state axisymmetric thermomechanical deformations of a viscoplastic rod striking a rigid hemispherical cavity, the plastic spin for material particles near the free surface is an order of magnitude higher than that for material particles near the centroidal axis. The values of the second invariant of the strain-rate tensor at these particles are not that much different and are of the same order of magnitude as the peak value of the plastic spin. Material particles initially near the centroidal axis of the rod are heated considerably more than those near the free surface of the rod. The time histories of the temperature, strain-rate invariant I and the effective stress seem to suggest that there is a greater likelihood of the formation of an adiabatic shear band near the cavity surface.

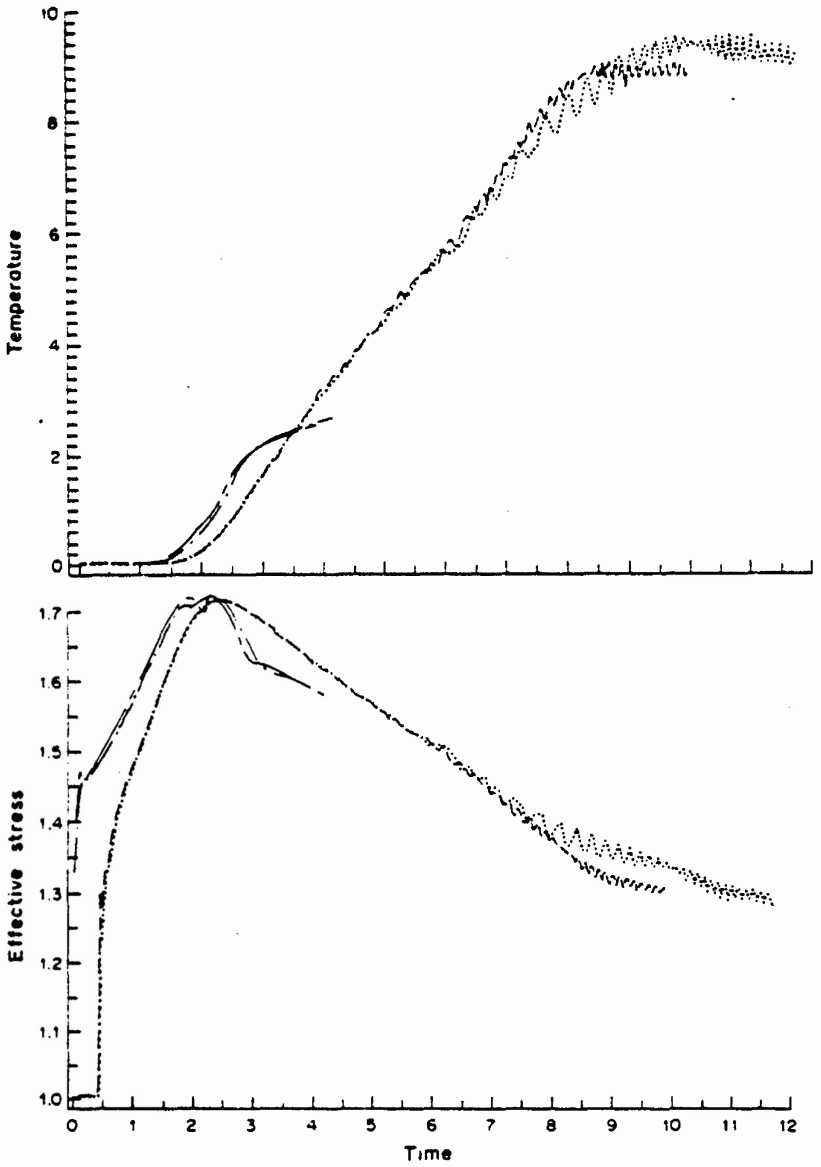

Fig. 4. Time histories of the temperature and the effective stress for the four material particles. See Fig. 2 for explanations.

Acknowledgement—This work was supported by the U.S. Army Research Office contract DAAL 03-89-0050 to the University of Missouri-Rolla.

REFERENCES

[1] E. H. LEE, Elastic-plastic deformations at finite strains. *J. Appl. Mech.* **36**, 1 (1969).
[2] L. ANAND, Constitutive equations for rate-independent, isotropic, elastic-plastic solids exhibiting pressure-sensitive yielding and plastic dilatancy. *J. Appl. Mech.* **47**, 439 (1980).
[3] S. NEMAT-NASSER, Micromechanically based finite plasticity. *Proc. Symp. Plasticity Today* (Edited by A. SAWCZUK). Elsevier, Amsterdam (1983).
[4] Y. F. DAFALIAS, Issues on the constitutive formulation at large elasto-plastic deformations. *Acta Mech.* **69**, 119–138 (1987).
[5] R. C. BATRA and PEI-RONG LIN, Steady state axisymmetric deformations of a thermoviscoplastic rod striking a rigid cavity. *Int. J. Impact Engng* **8**, 99–113 (1989).
[6] PEI-RONG LIN and R. C. BATRA, Histories of the stress, strain-rate, temperature, and spin in steady state penetration problems. *Int. J. Engng. Sci.* **27**, 1155–1165 (1989).

(*Received* 15 *March* 1989)

Int. J. Engng Sci. Vol. 28, No. 12, pp. 1347–1358, 1990
Printed in Great Britain.

0020–7225/90 $3.00 + 0.00

AN APPROXIMATE ANALYSIS OF STEADY STATE AXISYMMETRIC DEFORMATIONS OF VISCOPLASTIC TARGETS

R. C. BATRA and XINGJU CHEN

Department of Mechanical and Aerospace Engineering and Engineering Mechanics, University of Missouri-Rolla, Rolla, MO 65401-0249, U.S.A.

Abstract—Steady state axisymmetric deformations of a viscoplastic target being penetrated by a rigid cylindrical penetrator with a hemispherical nose are analyzed. The presumed kinematically admissible velocity field satisfies all of the boundary conditions on the target/penetrator interface, and also the balance of mass. The unknown parameters appearing in the admissible velocity field are found by minimizing the error in satisfying the balance of linear momentum. The solution so obtained is found to be very close to the finite element solution of the problem. An advantage of the present technique is the enormous savings in the computational effort and resources required to analyze the problem.

1. INTRODUCTION

In recent years, emphasis has been placed on kinetic energy penetrators, which for terminal ballistic purposes may be considered as long metal rods traveling at high speeds. For impact velocities in the range of 2–10 km/s, incompressible hydrodynamic flow equations can be used to describe adequately the impact and penetration phenomena, because large stresses occurring in hypervelocity impact permit one to neglect the rigidity and compressibility of the striking bodies. Models, which require the use of the Bernoulli equation or its modification to describe this hypervelocity impact, have been proposed by Birkhoff *et al.* [1] and Pack and Evans [2]. At ordnance velocities (0.5–2 km/s), the material strength becomes an important parameter. Allen and Rogers [3] modified the Pack and Evans [2] flow model by representing the strength as a resistive pressure. This idea was taken further by Alekseevskii [4] and Tate [5, 6], who considered separate resistive pressures for the penetrator and the target. These resistive pressures are empirically determined quantities, and the predicted results depend strongly upon the assumed values of these pressures. As described by Wright [7] in his survey article on long rod penetrators, Tate's model is difficult to use for quantitative purposes, because the strength parameters depend upon the velocity of impact and the particular combination of materials involved. Wright and Frank [8] in their reexamination of Tate's theory, have derived expressions for the resistive pressures in terms of mass densities, yield strengths of the penetrator and target material, and penetrator speed.

The paper by Backman and Goldsmith [9] is an authoritative review of the open literature on ballistic penetration, containing 278 reference citations from the 1800s to 1977. They describe different physical mechanisms involved in the penetration and perforation processes, and also discuss a number of engineering models. Jonas and Zukas [10] reviewed various analytical methods for the study of kinetic energy projectile–armor interaction at ordnance velocities and placed particular emphasis on three-dimensional numerical simulation of perforation. Anderson and Bodner [11] have recently reviewed engineering models for penetration and some of the major advances in hydrocode modeling of penetration problems. Two books [13, 14], published during the past few years, include extensive discussions of the engineering models, experimental techniques and analytical modeling of ballistic perforation.

Awerbuch [15], Awerbuch and Bodner [16], Ravid and Bodner [17], and Ravid *et al.* [18] have developed models to analyze the normal perforation of metallic plates by projectiles. The penetration process is presumed to occur in several interconnected stages, with plug formation and ejection being the principal mechanism of plate perforation. They presumed a kinematically admissible flow field and found the unknown parameters by minimizing the plastic dissipation. They characterized the procedure as being a modification of the upper bound theorem of plasticity to include dynamic effects. These authors have included the dependence of the yield stress upon the strain rate and studied a purely mechanical problem.

Jones *et al.* [19] have modified the one-dimensional eroding-rod penetration theory of Tate by accounting for the mass transfer from the rigid end of the rod into the plastic region, and the mushroom strain at the deforming end of the rod. Their results suggest that the latter factor has a substantial effect on calculated penetrations. Woodward [20] has proposed a one-dimensional model of penetration which regards both penetrator and target as mushrooming cylinders and the target flow stress is increased to account for the lateral constraint. A finite difference formulation is used for both target and projectile to divide them into a series of elements. The projectile elements which enter the target are subjected to lateral constraint and a shear stress if their diameter is sufficient to touch the edges of the hole. Forrestal *et al.* [21] have used the cavity expansion model to predict the penetration depths for relatively rigid projectiles striking deformable semi-infinite targets.

The one-dimensional theories ignore the lateral motion, plastic flow and the detailed dynamic effects. In an attempt to understand better the approximations made in simpler theories of penetration, Batra and Wright [22] studied the problem of a rigid cylindrical rod with a hemispherical nose penetrating into a rigid/perfectly plastic target. The target deformations, as seen by an observer moving with the penetrator nose tip, were presumed to be steady. Subsequently Batra and his coworkers [23–28] studied the effect of nose shape, strain hardening, strain-rate hardening and thermal softening characteristics of the target material and also analyzed the steady state axisymmetric deformations of a rod striking a rigid cavity. Guided by the results given in [22, 23] we presume a kinematically admissible velocity field to analyze the steady state axisymmetric deformations of a viscoplastic target being penetrated by a rigid hemispherical nosed cylindrical rod. The approximate solution obtained herein compares favorably with the finite element solution and requires less than one-hundredth of the computational resources in terms of the CPU time and the storage requirements.

2. FORMULATION OF THE PROBLEM

We use the Eulerian description of motion and a cylindrical coordinate system with origin at the center of the hemispherical nose and moving with it at a uniform speed v_0 to describe the deformations of the target. The positive z-axis is taken to point into the target. We work in terms of non-dimensional variables indicated below by a superimposed bar.

$$\bar{\boldsymbol{\sigma}} = \boldsymbol{\sigma}/\sigma_0, \qquad \bar{p} = p/\sigma_0, \qquad \alpha = \rho_0 v_0^2/\sigma_0,$$
$$\bar{\mathbf{v}} = \mathbf{v}/v_0, \qquad \bar{r} = r/r_0, \qquad \bar{z} = z/r_0, \tag{1}$$

where $\boldsymbol{\sigma}$ is the Cauchy stress tensor, p the hydrostatic pressure not determined by the deformation history since the deformations are assumed to be isochoric, $\mathbf{v} = (v_r, v_z)$ is the velocity of a material particle, the pair (r, z) describe the current position of a material particle, r_0 is the radius of the undeformed cylindrical portion of the rod, ρ_0 equals the mass density of a target material and σ_0 is the yield stress of the target material in a quasistatic simple compression test. The non-dimensional parameter α equals the magnitude of the inertia forces relative to the flow stress of the material.

Hereafter, we drop the superimposed bars. Equations governing the deformations of the target are

$$\operatorname{div} \mathbf{v} = 0, \tag{2.1}$$

$$\operatorname{div} \boldsymbol{\sigma} = \alpha(\mathbf{v} \cdot \operatorname{grad})\mathbf{v}, \tag{2.2}$$

$$\boldsymbol{\sigma} = -p\mathbf{1} + \frac{(1 + bI)^m}{\sqrt{3I}}\mathbf{D}, \tag{2.3}$$

$$2\mathbf{D} = \operatorname{grad} \mathbf{v} + (\operatorname{grad} \mathbf{v})^T, \tag{2.4}$$

$$2I^2 = \operatorname{tr}(\mathbf{D}^2). \tag{2.5}$$

Equations (2.1) and (2.2) express, respectively, the balance of mass and the balance of linear momentum. Equation (2.3) is the constitutive relation for the rigid/viscoplastic target material.

It may be written as

$$S_e = \left(\frac{1}{2}\mathrm{tr}(\mathbf{s}^2)\right)^{1/2} = (1 + bI)^m/\sqrt{3}, \tag{3.1}$$

$$\mathbf{s} = \boldsymbol{\sigma} + p\mathbf{1}. \tag{3.2}$$

The kinetic equation (3.1) is of a specific overstress form—roughly similar to that proposed by Cowper–Symonds–Bodner and generalized by Perzyna. The parameters b and m describe the strain-rate hardening characteristics of the material. $\mathbf{D}$, given by equation (2.4), is the strain-rate tensor and I is its second invariant. Equation (2.1) and the one obtained by substituting (2.3) into (2.2) are the nonlinear partial differential equations to be solved for $\mathbf{v}$ and p under the prescribed boundary conditions.

At the target/penetrator interface, we impose the boundary conditions

$$\mathbf{t} \cdot (\boldsymbol{\sigma}\mathbf{n}) = 0, \tag{4.1}$$

$$\mathbf{v} \cdot \mathbf{n} = 0, \tag{4.2}$$

where $\mathbf{n}$ and $\mathbf{t}$ are, respectively, a unit normal and a unit tangent to the surface. The boundary condition (4.2) ensures that there is no interpenetration of the target material into the penetrator, and the boundary condition (4.1) states that the target/penetrator interface is smooth. This seems reasonable because a thin layer of material at the interface either melts or is severely degraded by adiabatic shear. At points far away from the penetrator,

$$|\mathbf{v} + \mathbf{e}| \to 0 \quad \text{as} \quad |\mathbf{x}| = (r^2 + z^2)^{1/2} \to \infty, \qquad z > -\infty, \tag{5.1}$$

$$|\boldsymbol{\sigma}\mathbf{n}| \to 0 \quad \text{as} \quad z \to -\infty, \tag{5.2}$$

where $\mathbf{e}$ is a unit vector in the positive z-direction. The boundary condition (5.1) states that target particles far away from the penetrator appear to be moving with a uniform speed with respect to it. Equation (5.2) states that far to the rear the traction field vanishes. Note that the governing equations (2.1)–(2.3) are nonlinear in $\mathbf{v}$ and their solution, if there exists one, will depend on the rates at which quantities in (5) decay to zero.

3. AN APPROXIMATE SOLUTION

Guided by the finite element solutions [22, 23] of the corresponding problem, we divide the deforming target region shown in Fig. 1 into two subregions: region I and region II. We assume that in region I the target material extrudes rearward as a uniform block. Thus, the velocity of

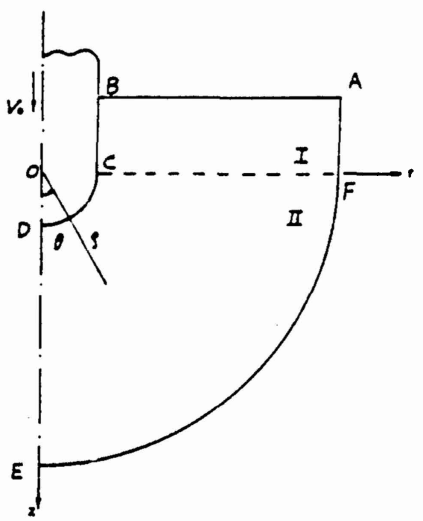

Fig. 1. The problem studied.

material particles in this region is along the axis of the rod. We note that a similar assumption was made by Ravid and Bodner [17] in their analysis of the perforation of thick plates. In order to describe the velocity field in region II, we introduce a new coordinate system (ρ, θ) where

$$\rho = (r^2 + z^2)^{1/2}, \tag{6.1}$$

$$\theta = \tan^{-1}(r/z). \tag{6.2}$$

Thus

$$v_\theta = v_r \cos\theta - v_z \sin\theta, \tag{7.1}$$

$$v_\rho = v_r \sin\theta + v_z \cos\theta. \tag{7.2}$$

Equation (2.1), and the boundary conditions (4.2) and (5.1) take the form

$$\frac{\partial v_\rho}{\partial \rho} + \frac{1}{\rho}\frac{\partial v_\theta}{\partial \theta} + \frac{2v_\rho}{\rho} + \frac{v_\theta}{\rho}\frac{\cos\theta}{\sin\theta} = 0, \tag{8}$$

$$v_\rho = 0 \quad \text{on CD and } v_\theta = 0 \text{ on DE}, \tag{9.1}$$

$$v_z \to -1, \qquad v_r = 0 \quad \text{as} \quad \rho \to \infty. \tag{9.2}$$

We also need to ensure that on CF

$$\mathbf{v}_{\mathrm{I}} = \mathbf{v}_{\mathrm{II}}, \tag{10.1}$$

and

$$(\boldsymbol{\sigma}\mathbf{n})_{\mathrm{I}} = (\boldsymbol{\sigma}\mathbf{n})_{\mathrm{II}}. \tag{10.2}$$

If the boundary EF is far enough from the noise tip D, then condition (9.2) is a reasonable approximation to (5.1). The condition (9.1) on DE follows from the assumption that the deformations are axisymmetric.

A velocity field that satisfies equation (8), boundary conditions (9.1) and (9.2), and the continuity condition (10.1) and exhibits characteristics similar to that found by the finite element solution is given below. In region II,

$$v_\theta = \left(1 - \frac{1}{\rho^{n+1}} + \frac{1}{\rho^n}\right)\sin\theta + \sum_{m,k} C_{mk}\rho^m \sin^k 2\theta, \tag{11.1}$$

$$v_\rho = \left[\left(\frac{1}{\rho^2} - 1\right)\cos\theta - \frac{2}{1-n}\left(\frac{1}{\rho^2} - \frac{1}{\rho^{n+1}}\right)\cos\theta + \frac{2}{2-n}\left(\frac{1}{\rho^2} - \frac{1}{\rho^n}\right)\cos\theta\right] - \sum_{m,k}\frac{C_{mk}}{m+2}\left(\frac{1}{\rho^2} - \rho^m\right)\sin^{k-1}2\theta((2k+1)\cos 2\theta + 1), \tag{11.2}$$

and in region I

$$v_z = -\left(1 - \frac{1}{r^{n+1}} + \frac{1}{r^n}\right), \qquad v_r = 0. \tag{12}$$

In equation (11), the constants n and C_{mk} are yet to be determined. The natural boundary conditions (4.1) and (5.1), and that on the axis of symmetry DE can be written as

$$\sigma_{\rho\theta} = 0 \qquad \text{on DC}, \tag{13.1}$$

$$|\boldsymbol{\sigma}\mathbf{n}| \to 0 \qquad \text{as } \rho \to \infty, \tag{13.2}$$

$$\sigma_{rz} = 0 \qquad \text{on DE}. \tag{13.3}$$

Recalling the constitutive relation (2.3), we see that boundary conditions (13.1) and (13.3) are equivalent to

$$\frac{\partial v_\theta}{\partial \rho} + \frac{1}{\rho}\frac{\partial v_\rho}{\partial \theta} - \frac{v_\theta}{\rho} = 0 \qquad \text{when } \rho = 1 \text{ or } \theta = 0. \tag{14}$$

This is satisfied if we choose

$$m \le -3, \qquad k \ge 3, \qquad \sum_m C_{mk}(m-1) = 0, \qquad k = 3, 4, \ldots \tag{15}$$

The satisfaction of the boundary condition (13.2) requires that

$$|p| \to 0, \quad \text{as} \quad \rho \to \infty. \tag{16}$$

In order to determine the hydrostatic pressure p, we use the balance of linear momentum (2.2). Substitution from (11), (7) and (2.3) into (2.2) gives

$$\frac{\partial p}{\partial r} = f(r, z), \tag{17.1}$$

$$\frac{\partial p}{\partial z} = g(r, z), \tag{17.2}$$

where f and g are known functions of r and z. Their expressions are quite long and are omitted. Since it is hard to choose n and C_{mk} such that the integrability condition

$$\frac{\partial f}{\partial z} - \frac{\partial g}{\partial r} = 0 \tag{18}$$

is satisfied, we find n and C_{mk} by ensuring that the functional

$$J(n, C_{mk}) = \int_{\Omega} \left(\frac{\partial f}{\partial z} - \frac{\partial g}{\partial r} \right)^2 d\Omega \tag{19}$$

takes on the minimum value. Knowing n and C_{mk}, the pressure is found by integrating equation (17) and the constant of integration is determined by setting $p = 0$ at $\rho = 1$, $\theta = 90°$. This condition is also taken from the finite element solution of the problem. The computed pressure field does satisfy (16). However, no attempt was made to achieve the rate of decay of p equal to that obtained in a finite element solution of the problem.

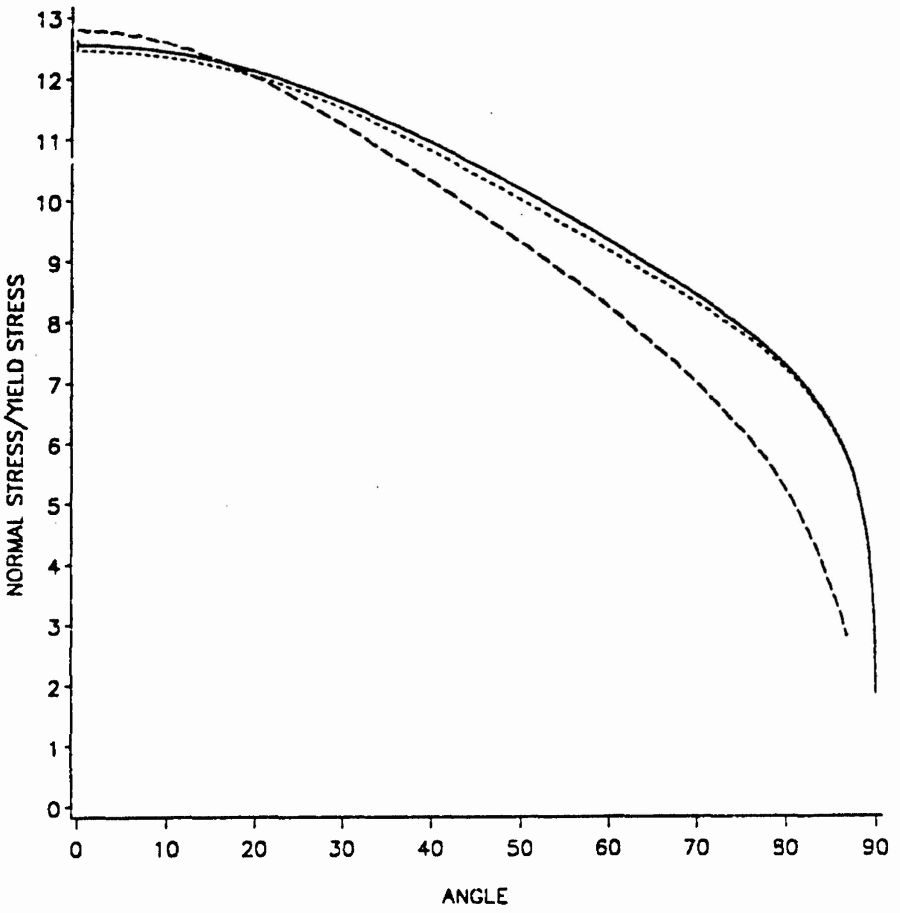

Fig. 2. Distribution of the normal traction on the penetrator nose. —— One term solution; ----- three terms solution; – – – FEM solution.

Having determined σ in region II we can use the balance of linear momentum, boundary conditions (10.2) and (5.2) to compute the stress field in the region I. However, the computation of this stress field is not necessary in order to compute various quantities of practical interest.

4. DISCUSSION OF RESULTS

In order to compare the solution obtained with the present method with that computed by the finite element method, we set $b = 10^4$ s, $m = 0.03$ and $\alpha = \rho_0 v_0^2/\sigma_0 = 6.15$. Whenever different values of b, m and α are used, these are stated in the figure captions. Figure 2 depicts the distribution of the normal traction on the penetrator nose. The solution computed with the leading term in equation (11) differs very little from that found by also including the next two terms in the series. These two solutions match well with the finite element solution for $0 \leq \theta \leq 25°$. For $\theta > 25°$, the presently computed solution differs noticeably from the finite element solution. Because of very little difference between the leading term solution and the three terms solution, it was felt that the consideration of the additional terms in the series will not result in any significant improvement in the solution. The variation of the second invariant I of the strain-rate tensor **D** along the axial line, plotted in Fig. 3, reveals that the results obtained with the present method are very close to the finite element solution of the problem. In this case, the three terms solution and the one term solution overlapped each other. However, the computed values of σ_{zz} on the axial line, shown in Fig. 4, do not agree that well

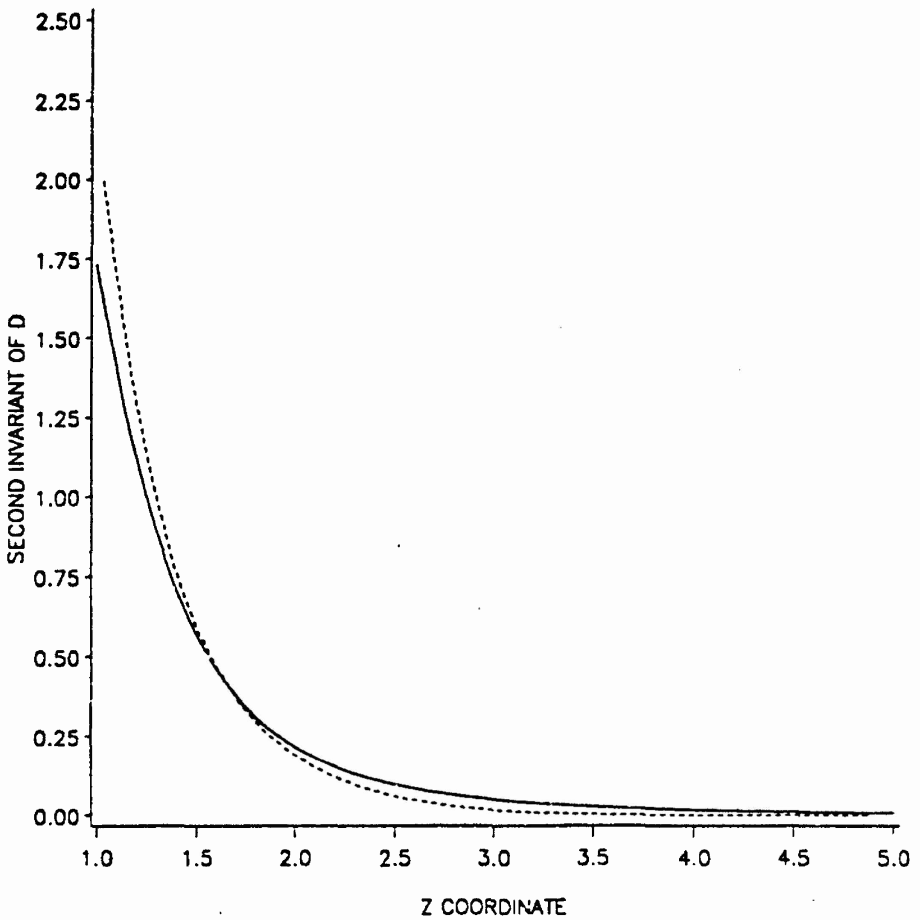

Fig. 3. Variation of the second invariant I of the strain-rate tensor on the axial line. —— Present solution; - - - - - finite element solution.

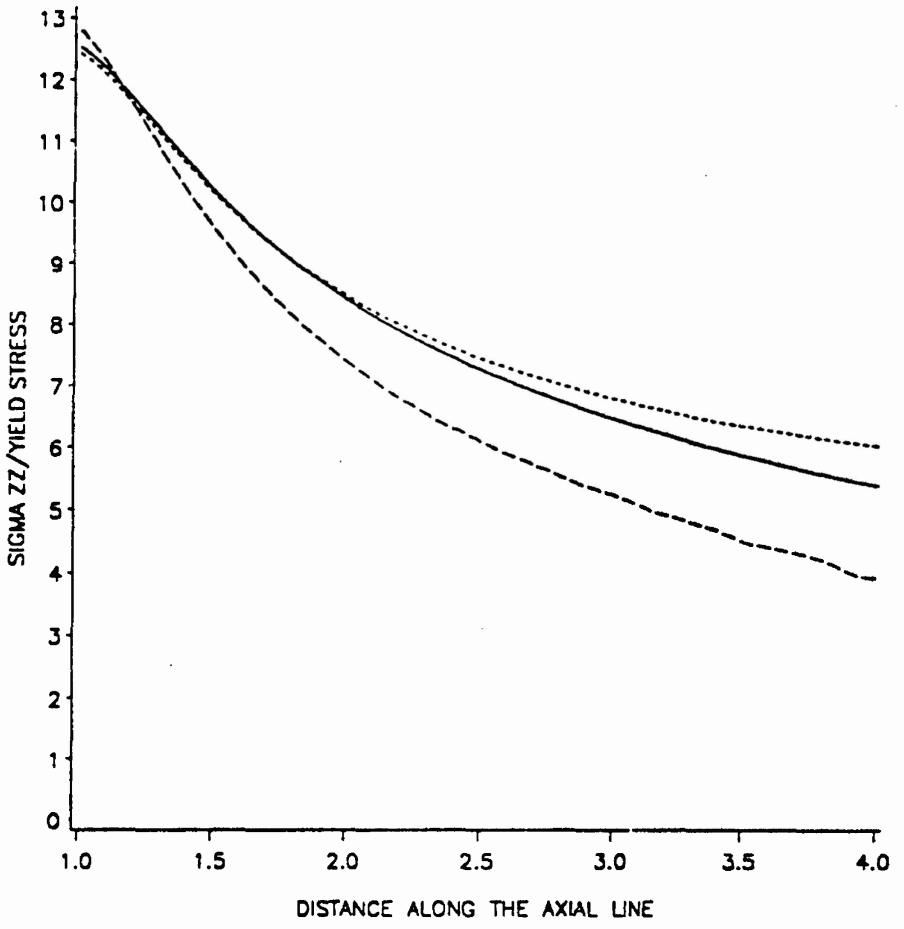

Fig. 4. Variation of σ_{zz} on the axial line.

with the finite element solution except near the nose tip. Three sets of curves show similar trends in that σ_{zz} decreases gradually as we move away from the nose tip. The decrease is more for the finite element solution as compared to the solution with the present method. Since the hydrostatic pressure is a major contributor to the value of σ_{zz}, the difference between the present solution and the finite element solution can be attributed to the different rates of decay of p. We note that many results of practical importance computed with the present method, as outlined below, are close to those obtained from the finite element solution.

On the axial line, the Bernoulli equation, as modified by Tate [5, 6] is

$$\frac{1}{2}\rho_0 v_s^2 + R_t = -\sigma_{zz}(1, 0) \tag{20}$$

where R_t accounts for the strength of the target material. Having computed σ_{zz} and knowing $\rho_0 v_s^2$, we can find R_t. The value of R_t thus computed equals 9.43 σ_0 with the present method and 9.63 σ_0 with the finite element method. From Fig. 3, we see that at the nose tip I = 1.75. Since $v_0/r_0 = 1.48 \times 10^5\ s^{-1}$, therefore, at the nose tip

$$\sigma_D = \sigma_0(1 + 10^4(1.75 \times 1.48 \times 10^5))^{0.03} = 1.916\sigma_0 \tag{21}$$

where σ_D is the value of the flow stress for the target material at a strain-rate of $2.59 \times 10^5\ s^{-1}$. Thus $R_t = 4.92\sigma_D$ for the presently computed solution. The non-dimensional axial resisting

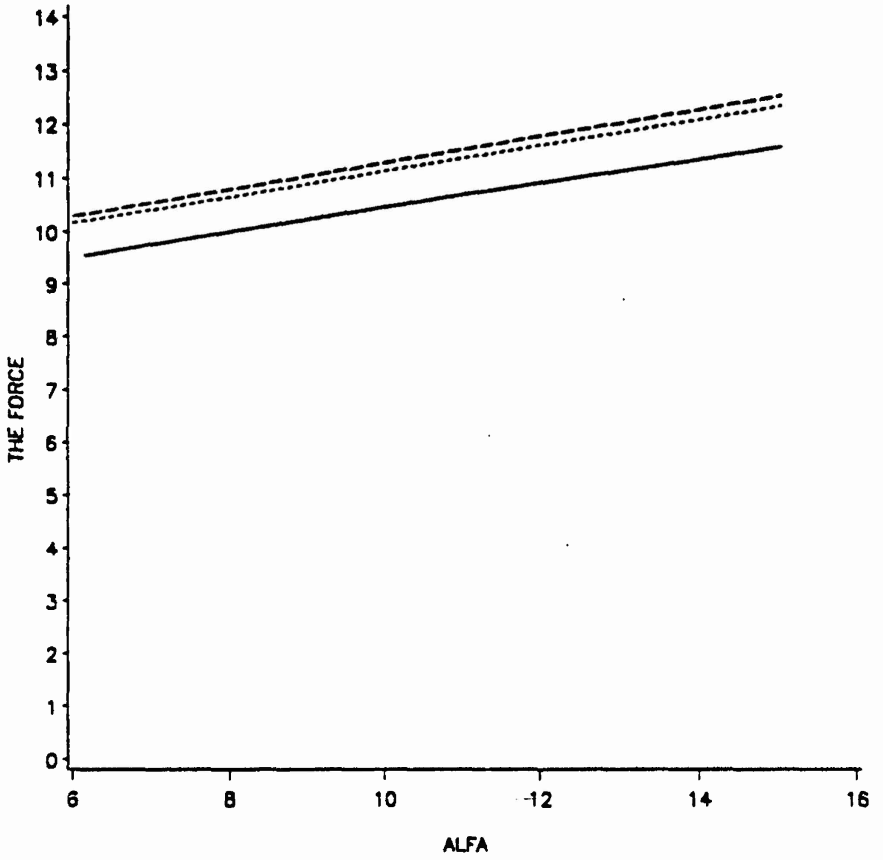

Fig. 5. Dependence of the axial resisting force upon α. —— Finite element solution; - - - - - one term solution; – – – three terms solution.

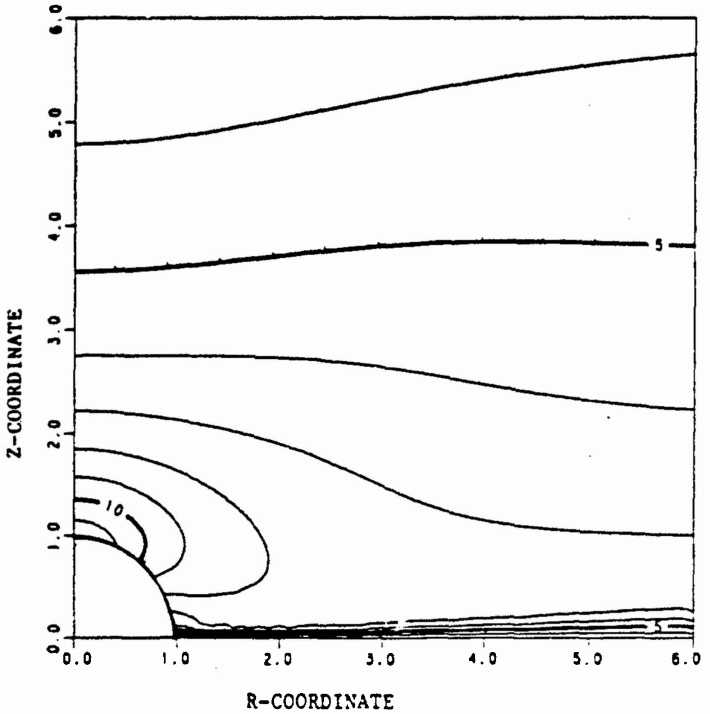

Fig. 6. Contours of the hydrostatic pressure in the deforming target region.

force F experienced by the penetrator is given by

$$F = \int_0^{\pi/2} (\mathbf{n} \cdot \boldsymbol{\sigma}\mathbf{n}) \sin 2\theta \, d\theta. \tag{22}$$

The dimensional values of the resisting force equal $\pi r_0^2 \sigma_0 F$. Figure 5, which is a plot of F vs α, shows that the dependence of F upon α is rather weak. Equations of straight lines fitted by the least squares method to the computed data are

$$F = 8.575 + 0.197\alpha, \text{ FEM solution,} \tag{23.1}$$

$$F = 8.717 + 0.243\alpha, \text{ Present 3 terms solution.} \tag{23.2}$$

Thus the two methods yield virtually identical values of F. The weak dependence of F upon α indicates why the choice of the constant target resistance in the simple theory of Tate [5, 6] gives good qualitative results.

The contours of the hydrostatic pressure p plotted in Fig. 6 indicate that the pressure near the nose tip is very high and it drops off rather slowly as we move away from the nose tip. It is thus obvious that the hydrostatic pressure near the penetrator nose makes a significant contribution to the normal traction acting on the nose tip and hence to the axial resisting force experienced by the penetrator. In Fig. 7, we have plotted the distribution of the normal traction on the penetrator nose for different values of α. As expected, the normal traction at a point on the penetrator nose increases with α. In the finite element solution [22] of the problem, the normal traction at $\theta = 45°$ was unaffected by the value of α. It seems that this was

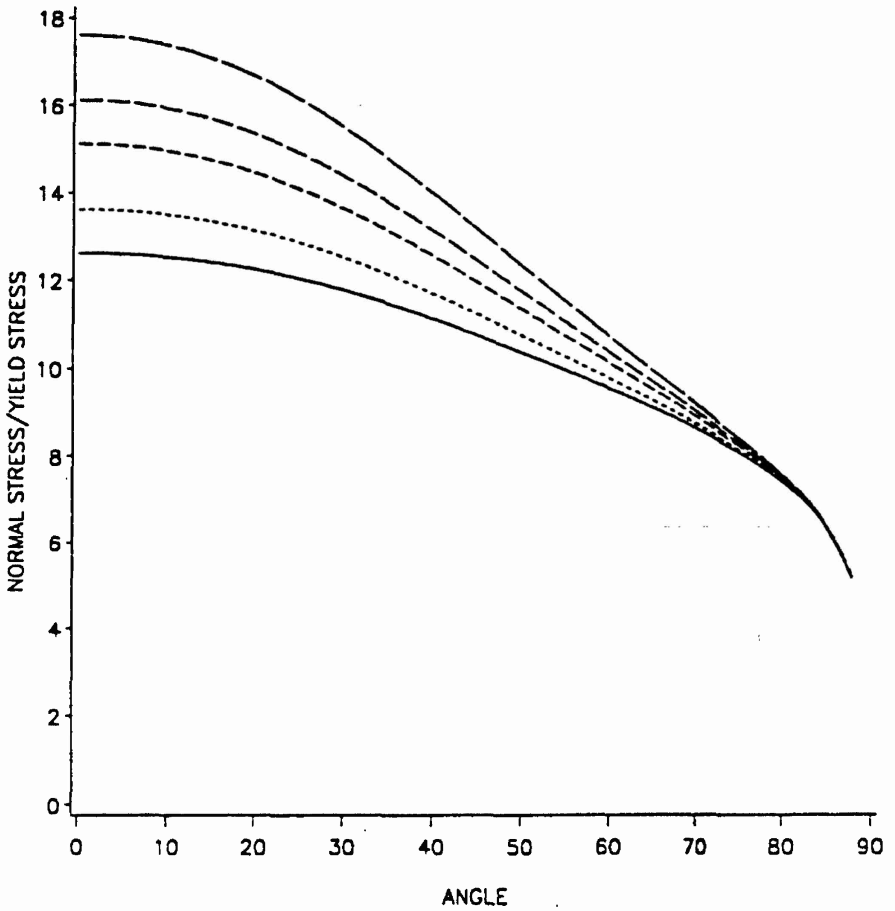

Fig. 7. Dependence of the normal traction on the penetrator nose upon α. —— $\alpha = 5$; - - - - - $\alpha = 7$; - - - $\alpha = 10$; —— —— $\alpha = 12$, —— —— $\alpha = 15$. $m = 0.05$.

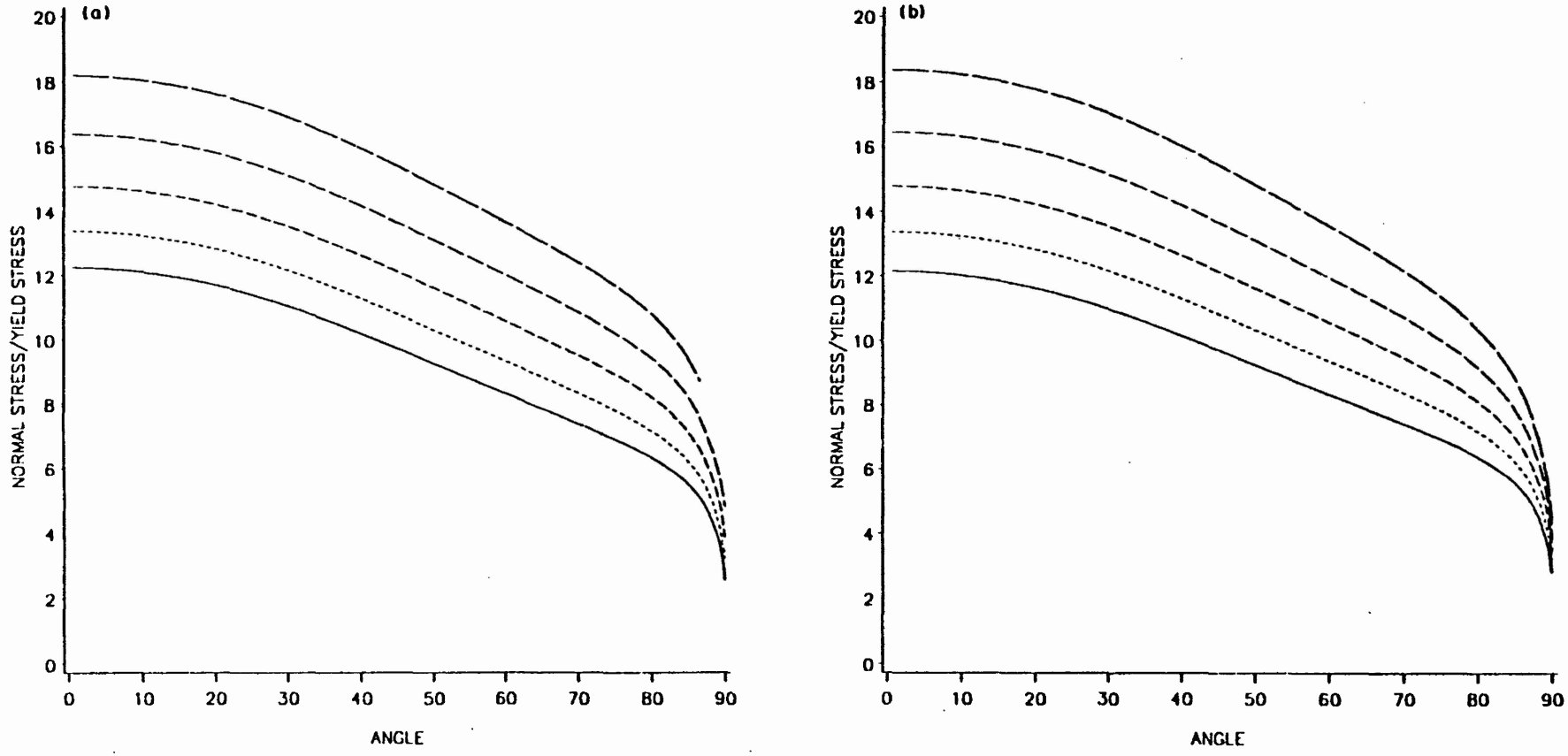

Fig. 8. Dependence of the normal stress acting on the penetrator nose upon the values of b and m. (a) —— $b = 10^2$; - - - - - $b = 10^4$; - - - $b = 10^6$; —— $b = 10^8$; —— —— $b = 10^{10}$; $\alpha = 8$, $m = 0.03$. (b) —— $m = 0.01$; - - - - - $m = 0.03$; - - - $m = 0.05$; - - - - $m = 0.07$; —— $m = 0.09$; $\alpha = 8$.

due to the coarse mesh used. Since at $\theta = 0°$, the normal traction on the penetrator nose equals $(-\sigma_{zz})$, and the deviatoric part of the stress equals 0.667 for the rigid/perfectly plastic target material and a little bit more for the viscoplastic target material, the hydrostatic pressure at the nose tip increases significantly with the increase in the value of α.

Figures 8(a) and (b) depict respectively the dependence of the normal stress on the penetrator nose upon the values of b and m that characterize the viscoplastic response of the target material. It is obvious that the normal stress on the penetrator nose and hence the axial resisting force acting on the penetrator depend strongly upon the values of b and m. As the value of either b or m is increased, the normal stress at a point on the penetrator nose, except near the periphery of the nose, increases sharply. Recall that at $\theta = 90°$, p is set equal to 0 during the solution of the problem. The dependence of the axial resisting force upon m and b is depicted in Fig. 9. These plots show that F depends strongly upon b and m as was also found to be the case in the finite element solution of the problem.

We note that Forrestal *et al.* [29] have given the depth of penetration of hemispherical nosed steel rods penetrating into aluminum targets impacted at different speeds. From their data, it is hard to estimate the resisting force experienced by the rod during the steady state portion of the penetration process. Also the assumption in our work that the contact at target/penetrator interface is smooth should be modified to account for the frictional forces acting on the interface. Since the assumed kinematically admissible velocity field gives zero tangential tractions at the contact surface, the consideration of frictional forces there necessitates that we modify the velocity field.

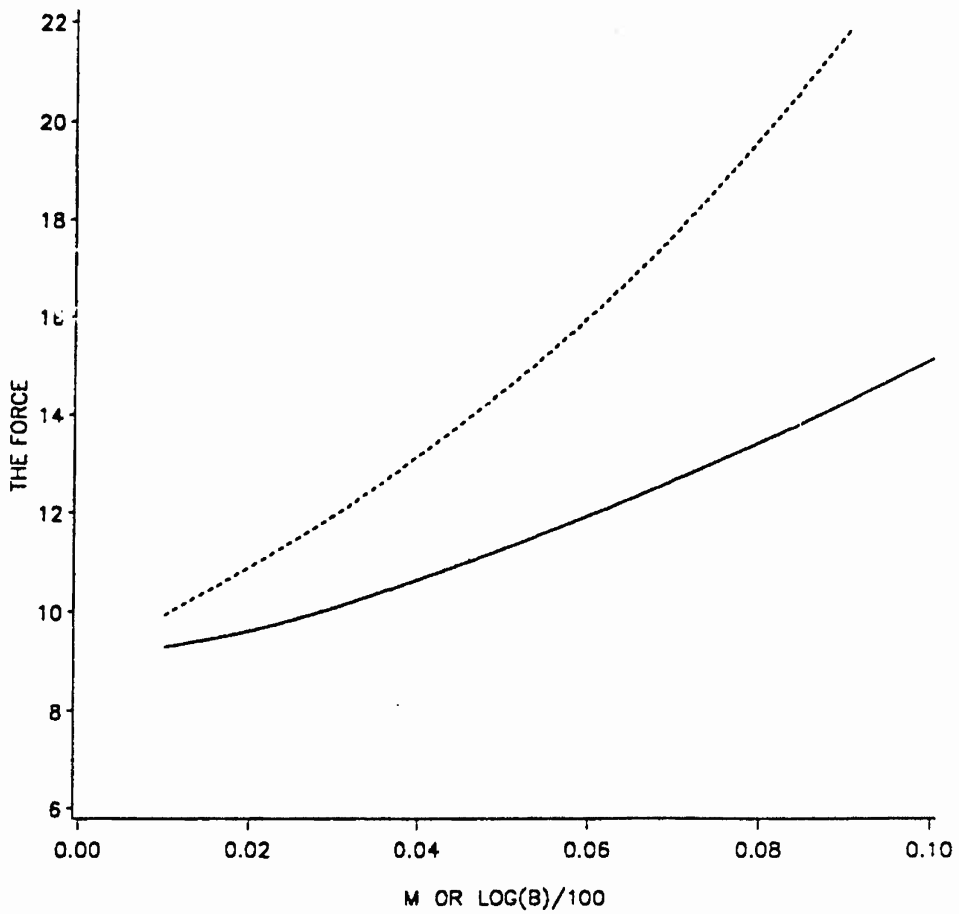

Fig. 9. Dependence of the axial resisting force experienced by the penetrator upon the values of b and m. —— b; - - - - m; $\alpha = 8.0$.

5. CONCLUSIONS

A simple approximate solution to the problem of analyzing axisymmetric steady state deformations of a rigid-viscoplastic target being penetrated by a long rigid cylindrical rod with a hemispherical nose is presented. A kinematically admissible velocity field that satisfies the balance of mass, all of the essential boundary conditions, and traction boundary conditions on the axis of symmetry and the target/penetrator interface is proposed. The various parameters in the presumed velocity field are found by minimizing the error in the satisfaction of the balance of linear momentum. The computed results reveal that the leading term in the proposed velocity field gives a good solution that is reasonably close to the finite element solution [22, 23]. The axial resisting force experienced by the penetrator is found to depend weakly upon the square of the penetrator speed but strongly upon the strain-rate hardening exponent for the target material. The value of the resisting force term suggested by Tate [5, 6] in the modified Bernoulli equation is found to be 9.43 σ_0 or 4.92σ_D where σ_D is the dynamic flow stress for the target material at a value of the strain-rate equal to that prevailing at the stagnation point.

Acknowledgement–This work was supported by the U.S. Army Research Office Contract DAAL03-89-K-0050 to the University of Missouri-Rolla.

REFERENCES

[1] G. BIRKHOFF, D. P. MCDOUGALL, E. M. PUGH and G. TAYLOR, *Proc. Phys. Soc. Lond.* **57**, 147 (1945).
[2] D. C. PACK and W. M. EVANS, *Proc. Phys. Soc. Lond.* **B64**, 298 (1951).
[3] W. A. ALLEN and J. W. ROGERS, *J. Franklin Inst.* **272**, 275 (1961).
[4] V. P. ALEKSEEVSKII, *Combust. Explo. Shock Waves* **2**, 63 (1966).
[5] A. TATE, *J. Mech. Phys. Solids* **15**, 387 (1967).
[6] A. TATE, *J. Mech. Phys. Solids* **17**, 141 (1969).
[7] T. W. WRIGHT, *Lecture Notes in Engineering*, Vol. 3, *Computational Aspects of Penetration Mechanics* (Edited by J. CHANDRA and J. FLAHERTY). Springer, New York (1984).
[8] T W. WRIGHT and K. FRANK, BRL Technical Report No. 2957 (1988).
[9] M. E. BACKMAN and W. GOLDSMITH, *Int. J. Engng Sci.* **16**, 1 (1978).
[10] G. H. JONAS and J. A. ZUKAS, *Int. J. Engng Sci.* **16**, 879 (1978).
[11] C. E. ANDERSON and S. R. BODNER, *Int. J. Impact Engng* **7**, 9 (1988).
[12] E. W. BILLINGTON and A. TATE, *The Physics of Deformation and Flow*. McGraw–Hill, New York (1981).
[13] J. A. ZUKAS, T. NICHOLAS, H. F. SWIFT, L. B. GRESZCZUK and D. R. CURRAN, *Impact Dynamics*. Wiley, New York (1982).
[14] M. MACAULEY, *Introduction to Impact Engineering*. Chapman & Hall, London (1987).
[15] J. AWERBUCH, Technion–Israel Institute of Technology, MED Report No. 28 (1970).
[16] J. AWERBUCH and S. R. BODNER, *Int. J. Solids Struct.* **10**, 671 (1974).
[17] M. RAVID and S. R. BODNER, *Int. J. Engng Sci.* **21**, 577 (1983).
[18] M. RAVID, S R. BODNER and I. HOLCMAN, *Int. J. Engng Sci.* **25**, 473 (1987).
[19] S. E. JONES, P. O. GILLIS and J. C. FOSTER, *J. Mech. Phys. Solids* **35**, 121 (1987).
[20] R. L. WOODWARD, *Int. J. Mech. Sci.* **24**, 73 (1982).
[21] M. J. FORRESTAL, K. OKAJIMA and V. K. LUK, *Proc. 1st Joint SES/ASME-AMD Conf.*, Univ. of California at Berkeley (1988).
[22] R. C. BATRA and T. W. WRIGHT, *Int. J. Engng Sci.* **24**, 41 (1986).
[23] R. C. BATRA, *Int. J. Engng Sci.* **25**, 1131 (1987).
[24] R. C. BATRA, *Comp. Mechs.* **3**, 1 (1988).
[25] R. C. BATRA and PEI-RONG LIN, *Int. J. Engng Sci.* **26**, 183 (1988).
[26] R. C. BATRA and PEI-RONG LIN, *Int. J. Impact Engng* **8**, 99 (1989).
[27] R. C. BATRA and T. GOBINATH, *Int. J. Engng Sci.* **26**, 741 (1988).
[28] PEI-RONG LIN and R. C. BATRA, *Int. J. Engng Sci.* **27**, 1155 (1989).
[29] M. J. FORRESTAL, N. S. BRAR and V. K. LUK, *Computational Techniques for Contact, Impact, Penetration and Perforation of Solids* (Edited by L. E. SCHWER, N. J. SALAMON and W. K. LIU), pp. 215–222. ASME Press, New York (1989).

(Revision received and accepted 21 June 1990)